



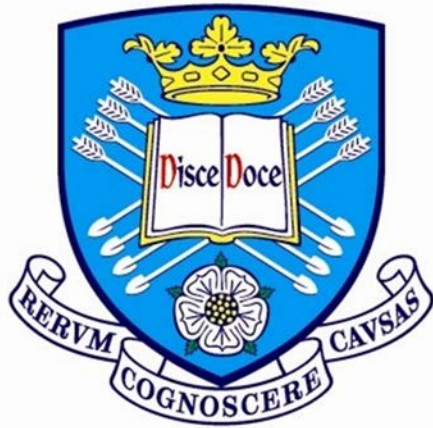
The
University
Of
Sheffield.

Access to Electronic Thesis

Author: Marzook Alshammary
Thesis title: Optical and Magneto-Optical Properties of Doped Oxides
Qualification: PhD

This electronic thesis is protected by the Copyright, Designs and Patents Act 1988. No reproduction is permitted without consent of the author. It is also protected by the Creative Commons Licence allowing Attributions-Non-commercial-No derivatives.

If this electronic thesis has been edited by the author it will be indicated as such on the title page and in the text.



The
University
Of
Sheffield.

Department of Physics and Astronomy

**Optical and Magneto-Optical Properties
of Doped Oxides**

Marzook S. Alshammary

Thesis submitted to the University of Sheffield for the degree of
Doctor of Philosophy
December 2011

Index

Abstract.....	v
Publications.....	vi
Papers in Preparation	vi
Conferences.....	vii
Acknowledgements.....	viii
Chapter 1 – Introduction and Thesis Structure.....	1
1.1 Introduction.....	1
1.2 Thesis Structure	2
1.3 References.....	4
Chapter 2 – Dilute Magnetic Semiconductors.....	6
2.1 Introduction.....	6
2.2 Magnetic Moments of Electrons and Atoms	6
2.3 Diamagnetism	8
2.4 Paramagnetism of Independent Moments and Atoms	9
2.5 Ferromagnetism	10
2.6 Anti-Ferromagnetism.....	10
2.7 Band Theory.....	11
2.8 Metallic Magnetism in Transition Elements.....	12
2.9 Spin-Based Electronics (Spintronics)	12
2.10 History of Spin-Based Electronics (Spintronics).....	13
2.11 Magneto-Optics.....	16
2.12 Magneto-Optics in Terms of Dielectric Tensors	19
2.13 Kramers-Kronig Relations	21
2.14 Pure In ₂ O ₃	22
2.15 Sn doped In ₂ O ₃	32
2.16 TM doped Oxides	35
2.17 Energy Levels of Oxygen Vacancies.....	38
2.18 References.....	41

Chapter 3 –Experimental Setup and Techniques	52
3.1 Introduction.....	52
3.2 Magneto-Optics Setup and the Principles of the Technique.....	52
3.3 Absorption Spectroscopy and the Principles of the Technique	56
3.4 Developments of Magneto-Optics and Absorption Systems	59
3.5 Systems Automation Method.....	60
3.5.1 Install Software and Drivers	60
3.5.2 Connect and Set Up Hardware.....	61
3.6 Growth of In ₂ O ₃ Thin Films	63
3.7 Suitable and Measurement of Thin Film Thickness	66
3.8 Dektak Surface Profiler.....	67
3.9 Aluminium Oxide Substrate	68
3.10 Swanepoel Method.....	71
3.11 References.....	76
Chapter 4 –Pure In₂O₃.....	80
4.1 Introduction.....	80
4.2 Experiment Details, Results, and Discussion	80
4.3 Conclusion	91
4.4 References.....	92
Chapter 5 –Maxwell-Garnett Theory	93
5.1 Introduction.....	93
5.2 Co Nanoparticles.....	93
5.3 Fe ₃ O ₄ Nanoparticles.....	98
5.4 Conclusion	105
5.5 References.....	106
Chapter 6 – Co Doped In₂O₃.....	107
6.1 Introduction.....	107
6.2 Experiment Details, Results, and Discussion	107
6.3 Conclusion	128
6.4 References.....	129

Chapter 7 – Fe Doped In₂O₃	131
7.1 Introduction.....	131
7.2 Experiment Details, Results, and Discussion	131
7.3 Conclusion	153
7.4 References.....	155
Chapter 8 – Multiferroic GdMnO₃	156
8.1 Introduction.....	156
8.2 Literature Review.....	156
8.3 Experiment Details, Results, and Discussion	160
8.4 Conclusion	167
8.5 References.....	168
Chapter 9 –Conclusions	170
9.1 Thesis Review	170
9.2 Future work.....	171
Appendix A –Development of computer program	173
A.1 Introduction.....	173
A.2 Program Structure	174
A.3 Program Code	175
A.4 References.....	181
Appendix B –Abbreviations	182

Abstract

This study aimed to understand the optical and magneto-optical properties of pure, transition metals doped, and tin and transition metals co-doped In_2O_3 thin films grown in various growth conditions, and aimed to investigate the role of the oxygen defect states in every situation. Indium oxide doped with magnetic transition metals is a promising material for spintronics. This study presents results on the magnetic, transport, optical and magneto-optical properties of thin films of pure and transition metal (Fe,Co) doped In_2O_3 investigated at different transition metal concentrations and at different growth conditions.

The optical and magneto-optical measurements at low temperature confirmed the formation of the defect states associated with oxygen vacancies within the forbidden range of the optical band gap energy of In_2O_3 and located below the conduction band. The density of the donor states is tuned using the oxygen partial pressure to give oxygen vacancies or by doping with tin; this gives control over the carrier concentration in the system as well as affecting the magnetic properties.

This study developed optical and magneto-optical systems and undertook the world's first optical and magneto-optical measurements of In_2O_3 . A new lab-based alternative technique to the Extended X-ray Absorption Fine Structure was developed to identify the existence of magnetic nanoparticles in addition to provide the fraction and the contribution of these nanoparticles to the magnetisation and magneto-optical properties. The Maxwell-Garnett analysis of magnetic circular dichroism was used to obtain quantitative measures of the amount of defect phases present for Co metal. Similar to Maxwell-Garnett analysis, a new equation for Fe_3O_4 nanoparticles was developed in this study. This magneto-optical method was found to be more precise than EXAFS in determining the fraction and the contribution of nanoparticles to the total response of the system. However, these nanoparticles disappeared when thin films were co-doped with tin, indicating that doping with Sn not only introduced more carriers but also inhibited the growth of defect phases in semi magnetic semiconductor thin films. Finally, this study identified the origin of the magnetism in the class of magnetic oxides where ferromagnetism originated from the polarized electrons in localized donor states associated with the oxygen vacancy defect.

Publications

Throughout the duration of my PhD studies, I have been involved in several publications or future publications, which are listed below, and have participated in many conference events.

Hakimi A., **Alshammari M.** et al., *Donor-band ferromagnetism in cobalt-doped indium oxide*, Phys. Rev. B **84**, 085201, (2011).

David S Score, **Alshammari M.** et al., *Magneto-optical properties of Co/ZnO multilayer films*, J. Phys.: Conf. Ser. **200** 062024, (2010).

Gehring, G. A., **Alshammari M.** et al., *Using Magnetic and Optical Methods to Determine the Size and Characteristics of Nanoparticles Embedded in Oxide Semiconductors*, Magnetics, IEEE Transactions on **46**(6): 1784-1786, (2010).

Feng-Xian Jiang, **Alshammari M.** et al., *Room temperature ferromagnetism in metallic and insulating $(In_{1-x}Fe_x)_2O_3$ thin films*, J. Appl. Phys. **109**, 053907 (2011).

Al Qahtani M., **Alshammari M.** et al., *Magnetic and Optical properties of strained films of multiferroic $GdMnO_3$* , submitted to Journal of Physics, (2011).

Papers in Preparation

The title may change before submission.

“*Optical and magneto-optical studies of Fe doped In_2O_3 containing Fe_3O_4 nanoparticles*”, **Marzook Alshammari**, Mohammed S Al-Qahtani, A Mark Fox, S. Alfahaid, M. Alotaibi, Gillian A Gehring

“*Temperature dependence of the optical absorption of In_2O_3* ”, **Marzook Alshammari**, A Mark Fox, S. Alfahaid, M. Alotaibi, A Alyamani, Gillian A Gehring

“Enhanced magnetic properties in ZnCoAlO caused by exchange-coupling to Co nanoparticles”, David S Score, James R Neal, Anthony J Behan, Abbas Mokhtari, Feng Qi, **Marzook S Alshammari**, Mohammed S Al-Qahtani, Harry J Blythe, A Mark Fox, Roy W Chantrell, Steve M Heald, Gillian A Gehring

Conferences

Score D., **Alshammari M.** et al., *Magneto-optical properties of Co/ZnO multilayer films*, The International Conference on Magnetism (ICM) in Karlsruhe, July 26 - 31, 2009. Germany.

Alshammari M. et al., *Influence of oxygen pressure on the magnetic and transport properties of Fe-doped In_2O_3 thin films*, Condensed Matter and Materials Physics CMMP09, at the University of Warwick, 2009, Dec. 15-17, UK.

Alshammari M., Score D., et al., *Magneto-Optical studies of doped In_2O_3* , Uk semiconductor 2010 Sheffield, 7-8 July 2010, UK.

Alshammari M. et al., *Magneto-Optical studies of Fe-doped In_2O_3 thin films*, Condensed Matter and Material Physics Conference (CMMP) 2010, University of Warwick, 2010, Dec. 14-16, UK.

Acknowledgments

I am eternally indebted to Prof. Gillian Gehring and Prof. Mark Fox, my supervisors, for their unending patience, invaluable guidance and generous support throughout this research. I would also like to thank all faculty and staff members who provided support for this research, especially Dr. Harry Blythe, Mr. Chris Vickers and Mr. Pete Robinson for their experimental support with liquid helium, and who were so generous with their valuable advice and helpful remarks.

I wish to express my appreciation to my colleagues David Score, Mohammed Al-Qatani, Qi Feng, and Ali Hakimi for their support and encouragement, and for sharing the wealth of information that enriched the content of this research.

Thanks are also due to the father, the brother, and the friend, the Prince Turki bin Saud bin Mohammad Al Saud, Vice President of KACST for Research Institutes, for his unlimited encouragement and support. Also, I would like to thank the engineers of the national center of nanotechnology in KACST, especially, S. Alfahid for the growth of some of the samples used in this thesis. My work in Sheffield was funded by KACST and managed by the Saudi cultural bureau in London for which I am very grateful.

I should also show my deep gratitude to the external and internal examiners; Professor C.F. McConville and Dr Dan A Allwood who, in their valuable comments and recommendations, brought my study to the required standard.

Finally, I would like to express my sincere gratitude to my mother, Dehla, and my wife, Hulailah, for their patience and continuous support.

Chapter 1 – Introduction and Thesis Structure

1.1 Introduction

Silicon integrated circuit technology and data storage technology are considered to be among the most successful technologies ever. The integrated circuits operate using the charge of carriers in the influence of externally applied electric fields. In the absence of electric power, the Si integrated circuit loses its stored data. In magnetic data storage, the spin of the electron is used to store data within magnetic materials rather than using electric charge or current flows, where, the magnetic polarization in magnetic circuits does not leak over time. This means that, even when there is no power, the data remain stored. These advantages make spin-based electronics one of the most important topics of investigation in the field of new functional semiconductor devices [1, 2].

A new generation of spintronic materials, called dilute magnetic semiconductors, has attracted a great deal of attention for their potential applications. TM-doped semiconductor oxides, such as ZnO, SnO₂ and TiO₂, are predicted to be good candidates. Among the semiconductor oxides is In₂O₃ semiconductor. In₂O₃ (IO) is known to be one of the best transparent semiconductors used in optoelectronic applications. In₂O₃ has a wide band gap energy combined with a large electron carrier density when doped with Sn, and doping In₂O₃ with a transition element (TM) leads to a combination of the magnetism, optical and transport properties into a single material, which leads to the making of multi-functional devices. The only thing that prevents In₂O₃ from being considered in theoretical calculations is its complex structure. Lately, research on the structure, transport, and magnetic properties of TM-doped In₂O₃ has been initialized. Room temperature ferromagnetism has been observed for all 3*d* transition metals (V, Cr, Fe, Co, Ni, Cu) doped In₂O₃ [3-16]. The ferromagnetism has been attributed to the interaction between the host In₂O₃ *s*, *p* band carriers and the localized 3*d* electrons in doped transition metal elements. Several theoretical models have been suggested based on the *s(p)-d* interactions feature [17-22]. In general, the ferromagnetism in oxide magnetic semiconductors is induced by clustered magnetic impurities [23] or is attributed to the oxygen vacancy defects where the ferromagnetic exchange interaction is mediated by shallow donor electrons

trapped in oxygen vacancy defects [24, 25]. The work reported in this study confirmed the importance of oxygen defect states for magnetism.

However, all previous studies in this field agreed that the density of oxygen defect states, the structure, the transport, the magnetic, the optical, and the magneto-optical properties of TM-doped semiconductor oxides are very sensitive to the growth conditions of the samples.

This work was carried out at the University of Sheffield and aimed to understand the optical and magneto-optical properties of pure, TM-doped, and Sn-TM- co-doped In_2O_3 thin films grown in various growth conditions and to investigate the role of the oxygen defect states in every situation. In addition, this study undertook the first optical and magneto-optical measurements of In_2O_3 .

1.2 Thesis Structure

Chapter Two gives the background physics required to understand the work and the results obtained in this thesis. It discusses the diluted magnetic semiconductors in more detail and introduces the history of spin-based electronics. It covers some of the magnetic properties related to our work, such as paramagnetism, ferromagnetism, and anti-ferromagnetism and discusses band theory and the related optical properties. It gives an introduction about the transition element, the In_2O_3 semiconductor, and the theory of magneto-optics.

Chapter Three outlines the experimental techniques used in this work with some details and the background physics behind the work; it also discusses how the work was carried out. It gives some of the concepts and ideas that were used to improve the performance of these systems and explains how these systems were upgraded and improved. Also, it presents the Swanepoel method and the new software programs in order to use the Swanepoel method for low temperature measurement.

Chapter Four explores the optical properties of pure In_2O_3 , and discusses the effect varying the growth conditions have on these properties. It investigates the origin of the optical transitions occur within the forbidden range of the optical band gap energy of In_2O_3 and the role of the oxygen vacancies in these transitions. In addition, it studies the influence of tin doping on the optical properties of pure In_2O_3 .

Chapter Five introduces a lab-based alternative to EXAFS and develop a new method for identifying the existence of magnetic nanoparticles. This chapter presents the Maxwell-Garnett (M-G) theory and represents and derives equations to determine the fraction of metallic Co and Fe_3O_4 nanoparticles in the semiconductor host material, and to determine the contribution of Co and Fe_3O_4 nanoparticles to the magnetic and magneto-optical properties.

Chapter Six investigates the impact of Co-doping on the optical and magneto-optical properties of In_2O_3 . It examines the influence of Co concentration, followed by a study of the effect of different growth conditions on the optical and magneto-optical properties of Co-doped In_2O_3 thin films. Also, the optical and magneto-optical properties investigated in the case of the presence of metallic Co and the Maxwell-Garnett theory are used to calculate the magneto-optical response of Co nanoparticles and to estimate the fraction of metallic Co in these thin films. Chapter Five also includes a study of the influence of tin content on the optical and magneto-optical properties of Co-doped In_2O_3 in the presence and absence of Co nanoparticles.

Chapter Seven studies the influence of Fe-doping on the optical and magneto-optical properties of In_2O_3 . It investigates the influence of Fe concentration, the growth conditions, and tin doping on the optical and magneto-optical properties of Fe-doped In_2O_3 thin films. Also, it investigates the optical and magneto-optical properties in the existing of Fe_3O_4 nanoparticles. The Maxwell-Garnett theory is used to determine the fraction of Fe_3O_4 nanoparticles in the semiconductor host material and to determine the magnetic and magneto-optical response related to the Fe_3O_4 nanoparticles. Also, chapter seven covers the influence of tin content on the optical and magneto-optical properties of Fe-doped In_2O_3 .

Chapter Eight investigates the optical and magneto-optical properties of multiferroic GdMnO_3 in order to obtain detailed information on the magnetic polarization of the electronic states. It gives an introduction about the Rare-earth elements, multiferroic materials, and the magnetoelectric effect and discusses the role of strain in these thin films.

Chapter Nine gives a summary of the results and conclusions along with some suggestions for future work.

1.3 References

1. S. A. Wolf, D. D. Awschalom, R. A. Buhrman, J. M. Daughton, S. V. Molnar, M. L. Roukes, A. Y. Chtchelkanova and D. M. Treger, *Science* **294**, 1488-1495 (2001).
2. S. J. Pearton, Y. D. Park, C. R. Abernathy, M. E. Overberg, G. T. Thaler, J. Kim, F. Ren, J. M. Zavada and R. G. Wilson, *Thin Solid Films* **447-448**, 493-501 (2004).
3. N. H. Hong, J. Sakai, N. T. Huong, and V. Brize, *Appl. Phys. Lett.* **87**, 102505 (2005).
4. N. H. Hong, J. Sakai, A. Ruyter and V. Brize, *J. Phys.: Condens. Matter* **18**, 6897 (2006).
5. N. H. Hong, *J. Magn. & Magn. Mater.* **303**, 338 (2006).
6. T. Ohno, T. Kawahara, H. Tanaka, T. Kawai, M. Oku, K. Okada and S. Kohiki, *Jpn. J. Appl. Phys.* **45**, L957 (2006).
7. G. Peleckis, X. Wang, and S. X. Dou, *Appl. Phys. Lett.* **89**, 022501 (2006).
8. G. Peleckis, X. Wang, and S. X. Dou, *IEEE Trans. Magn.* **42**, 2703 (2006).
9. G. Peleckis, X. Wang, and S. X. Dou, *Appl. Phys. Lett.* **88**, 132507 (2006).
10. G. Peleckis, X. Wang, and S. X. Dou, *J. Magn. & Magn. Mater.* **301**, 308 (2006).
11. A. Gupta, H. Cao, K. Parekh, K. V. Rao, A. R. Raju, and U. V. Waghmare, *J. Appl. Phys.* **101**, 09N513 (2007).
12. J. He, *Appl. Phys. Lett.* **86**, 052503 (2005).
13. Y. K. Yoo, *Appl. Phys. Lett.* **86**, 042506 (2005).
14. Z. G. Yu, J. He, S. Xu, Q. Xue, O. M. J. Van't Erve, B. T. Jonker, M. A. Marcus, Y. K. Yoo, S. Cheng, and X. Xiang, *Phy. Rev. B* **74**, 165321 (2006).
15. J. Philip, A. Punnoose, B. I. Kim, K. M. Reddy, S. Layne, J. O. Holmes, B. Satpati, P. R. LeClair, T. S. Santos and J. S. Moodera, *Nat Mater* **5**, 298-304 (2006).
16. S. Kohiki, M. Sasaki, Y. Murakawa, K. Hori, K. Okada, H. Shimooka, T. Tajiri, H. Deguchi, S. Matsushima, M. Oku, T. Shishido, M. Arai, M. Mitome and Y. Bando, *Thin Solid Films* **505**, 122-125 (2006).
17. T. Dietl, H. Ohno and F. Matsukura, *Physical Review B* **63**, 195205 (2001).
18. T. Dietl, A. Haury, and D. A. Merle, *Physical Review B* **55**, R3347 (1997).

19. H. Akai, Physical Review Letters **81**, 3002 (1998).
20. D. Gennes, P. G., Physical Review **118**, 141 (1960).
21. M. V. Schilfgaarde, and O. N. Mryasov, Physical Review B **63**, 233205 (2001).
22. P. W. Anderson, and H. Hasegawa, Physical Review **100**, 675 (1955).
23. J. Y. Kim, J. H. Park, B. G. Park, H. J. Noh, S. J. Oh, J. S. Yang, D. H. Kim, S. D. Bu, T. W. Noh, H. J. Lin, H. H. Hsieh and C. T. Chen, Physical Review Letters **90**, 017401 (2003).
24. J. M. D. Coey, A. P. Douvalis, C. B. Fitzgerald and M. Venkatesan, Applied Physics Letters **84**, 1332-1334 (2004).
25. J. M. D. Coey, M. Venkatesan and C. B. Fitzgerald, Nat Mater **4**, 173-179 (2005).

Chapter 2 – Dilute Magnetic Semiconductors

2.1 Introduction

Understanding the principles of magnetism is an essential step in order to gain a better insight into the origins of magnetic circular dichroism (MCD) in semi magnetic semiconductors (SMS). This chapter introduces the SMS and provides some brief but basic information regarding magnetism in order to facilitate an understanding of the topics covered through this thesis. An introduction to magnetism, optics, magneto-optics, transition elements (TM), and the In_2O_3 semiconductor are provided with the aim of explaining the background theory behind our study. This introduction was obtained from referring to the following text books: *The Optical Properties of Solid and Quantum Optics: An Introduction* by Mark Fox [1, 2], *Introduction to Magnetic Materials* by B. D. Cullity [3], *Physics of Magnetism and Magnetic Materials* by K. H. J. Buschow [4], *Spintronic Materials and Technology* by Y. B. Xu [5], *Electronic Structure and Magneto-Optical Properties of Solids* by V. Antonov [6], *Magnetic Materials: Fundamentals and Applications* by N. A. Spaldin [7].

2.2 Magnetic Moments of Electrons and Atoms

It is well known that the electron spins about its own axis and moves in its own orbit around the atom. Therefore, the electron has two kinds of motion: spin (s) and orbital (l). Each motion of the electron has a definite amount of magnetic moment associated with it.

$$\vec{\mu}_l = -\frac{eh}{4\pi m} \vec{l} = -\mu_B \vec{l} \quad , \quad \vec{\mu}_s = -g_e \mu_B \vec{s} \quad \text{Equation(2.1)}$$

where μ_B is the *Bohr* magneton $\mu_B = 9.27 \times 10^{-24} \text{J/Tesla}$ [8], e and m are the electron charge and mass respectively, h is Planck's constant, and g_e is the spectroscopic splitting factor.

When a free atom has many electrons, the total orbital angular moment \vec{L} and the total spin angular moment \vec{S} have to be considered, which is defined as

$$\vec{L} = \sum_i \vec{l} \quad , \quad \vec{S} = \sum_i \vec{s} \quad \text{Equation(2.2)}$$

The total orbital angular momentum \vec{L} and the total spin angular momentum \vec{S} are coupled through the spin-orbit interaction to form the orbital dipole moment $\vec{\mu}_L$, the spin dipole moment $\vec{\mu}_S$, the total dipole moment $\vec{\mu}_{total}$, and the total angular momentum \vec{J} .

$$\vec{\mu}_L = -\mu_B \vec{L}, \quad \vec{\mu}_S = -g_e \mu_B \vec{S}, \quad \vec{\mu}_{total} = \vec{\mu}_L + \vec{\mu}_S \quad \text{Equation(2.3)}$$

$$\vec{J} = \vec{L} + \vec{S} \quad \text{Equation(2.4)}$$

Therefore, the magnetic properties are determined by the atomic moment through the formula,

$$\vec{\mu} = \vec{\mu}_{total} \cos \theta = -g_l \mu_B J \quad \text{Equation(2.5)}$$

where $J = (L - S)$ if the shell is less than half full or $J = (L + S)$ if the shell is more than half full, θ is the angle between $\vec{\mu}_{total}$ and \vec{J} , and g_l is the Lande spectroscopic g-factor.

$$g_l = 1 + \frac{J(J+1) + S(S+1) - L(L+1)}{2J(J+1)} \quad \text{Equation(2.6)}$$

The atomic moment $\vec{\mu}$ gives the magnetization of the system through the formula

$$M = -N \vec{\mu} \quad \text{Equation(2.7)}$$

where N is the number of the participating atoms.

The magnetization of the system is a result of the sum of all the net magnetic moment of its atoms. Each atom has a net magnetic moment presented from the sum of all the electronic moments in that atom. Therefore, if the magnetic moments of the electrons are oriented in such a way that they cancel each other out, then the net magnetic moment of the atom is zero, which leads to a diamagnetic system. However, if the magnetic moments of the electrons are oriented in such a way that they only partially cancel each other out, then the net magnetic moment of the atom is not zero. The sum of the net magnetic moments of all the atoms in any particular system reflects the type of that system and dominates all its physical properties. The theoretical calculation of the net magnetic moment of a system is impossible due to its complexity. However, the determination of the net magnetic moment is possible experimentally. The above formulae work very well for free ions, where the magnitude of their magnetic moment, m , calculated theoretically using Equ.8 is in agreement with what is measured experimentally.

$$m = g_l \mu_B \sqrt{J(J+1)} \quad \text{Equation(2.8)}$$

and the total magnetization depends on m . In solids, the situation is slightly different as, in transition elements, the magnetic moment calculated theoretically is in agreement with what is measured experimentally only when the orbital angular momentum of the electrons is completely ignored. This effect is due to the electric field generated by the surrounding ions in the solid, which forces the orbitals to couple strongly to the lattice of the crystal. As a result, they cannot react to any applied magnetic field and they do not contribute to the observed magnetic moment. In contrast, the spins are not coupled to the lattice of the crystal except through the spin orbit coupling to the orbit. Therefore, they react to any applied magnetic field, and they do contribute to the observed magnetic moment. This phenomenon in general is known as the quenching of the orbital angular momentum. Measured magnetic moments for some of the transition-metal ions used in this thesis are shown in Table 2.1.

**Removed
by the author
for copyright reasons**

Table 2.1: Measured magnetic moments for some transition-metal ions [7, 9].

2.3 Diamagnetism

The theory of diamagnetism was presented by the French physicist Paul Langevin in 1905. Diamagnetic materials react to an externally applied field by exhibiting negative magnetism even though they are made of atoms with no net magnetic moment. The classical theory considers that the externally applied field arouses each single electron in the atom to produce the magnetic moment opposing the applied field. The sum of the opposing magnetic moments of all the electrons in

the atom makes the atom react against the applied field independently of the others. The atoms that have no net magnetic moment are composed of closed-shell electronic structures. Thus, all the noble gases are diamagnetic. The process of molecule formation of other gases like H₂, N₂, etc., or the process of bonding in ionic solids like NaCl, leads to filled electron shells and no net magnetic moment. Materials with covalent bonding by sharing electrons, which usually end up with a closed shells, and elements such as Si, diamond, and Ge, are diamagnetic. All normal insulators like Al₂O₃ and un-doped semiconductors like In₂O₃ are diamagnetic. Diamagnetism is present in all materials and the crystal shows diamagnetic behaviour if it is not paramagnetic.

2.4 Paramagnetism of Independent Moments and Atoms

The classical theory of paramagnetism by Langevin is based on the assumption that each atom has the same net magnetic moment and points at a random direction, and that the atoms cancel one another out, meaning there is no interaction between different atoms. Therefore, the sum of the net magnetic moment or the magnetization of this material is zero. When an external magnetic field is applied and no opposing force acts, each magnetic moment tends to turn toward the direction of the applied magnetic field. When the magnetic moments of all the atoms are aligned in the same direction of the applied field, the material exhibits a large magnetization in the direction of the field. However, the thermal agitation opposes the tendency of the atoms and tends to keep their magnetic moments pointed at random. As a result, a partial alignment occurs in the field direction, and the ability of a material to become magnetized is small. The ability of a material to become magnetized is called the susceptibility. The susceptibility is calculated as the ratio of the material's magnetic moment per unit volume M and the field H .

$$M = \chi H \quad \text{Equation(2.9)}$$

Paramagnetic materials have a small positive susceptibility and exhibit low temperature dependence. However, the susceptibility of paramagnetic materials shows temperature dependence through the Curie-Weiss law when there is no interaction between moments.

$$\chi = \frac{C}{T} \quad \text{Equation(2.10)}$$

where C is the Curie constant. Detection of the para susceptibility obtained from the data is corrected by subtracting the diamagnetic contribution. Sometimes, this correction is ignored because it is small in comparison to the paramagnetic term.

2.5 Ferromagnetism

According to the localized moment theory, ferromagnetism originates from the electrons. In a magnetic insulator, the electrons and their magnetic moments of any atom are localized in their atom and cannot move in the crystal, and there is an exchange force among these electrons in each atom to cause a parallel spin alignment. In the band theory, the ferromagnetism originates from the whole crystal electrons. These electrons are not localized and are able to move from one atom to another. In an applied magnetic field, the magnetization of the system achieves its maximum and is saturated at a point known as the saturation magnetization M_s . When the external magnetic field goes to zero, the magnetization does not vanish, as in paramagnetic materials; rather, the ferromagnetic materials exhibit a permanent magnetization called the remaining magnetization, or remanence M_r . Therefore, the magnetic field required to eliminate the remaining magnetization is called the coercive field or coercively H_c . The saturation magnetization M_s is a temperature-dependent quantity and reaches its minimum below the Curie temperature and its maximum at absolute zero. The Curie temperature, T_C , is a characteristic property related to the ferromagnetic materials. Below the Curie temperature, these materials show ferromagnetic behaviour and above the Curie temperature, the materials revert to their original state, which is paramagnetic with susceptibility, in the form:

$$\chi = \frac{C}{T-T_c} \quad \text{Equation(2.11)}$$

2.6 Anti-Ferromagnetism

In anti-ferromagnetic materials, the interaction between the magnetic moments tends to align adjacent moments antiparallel to each other. These materials do not hold a permanent magnetization like ferromagnetic material does. Antiferromagnetic materials exhibit anomalous paramagnetic susceptibility with temperatures. The susceptibility of antiferromagnetic materials increases with decreases in temperature to a maximum point called the Néel temperature T_N .

Below T_N , the material is antiferromagnetic and above it, the material is paramagnetic. The susceptibility of the antiferromagnetic materials at $T > T_N$ is

$$\chi = \frac{c}{T+\theta} \quad \text{Equation(2.12)}$$

**Removed
by the author
for copyright reasons**

Figure 2.1: (I) Typical magnetization curves at $T < T_c$ of (a) a diamagnet; (b) a paramagnet or antiferromagnet; and (c) a ferromagnet. (II) Typical temperature dependence of susceptibility inverse in ferromagnetic, paramagnetic, and antiferromagnetic at $T > T_c, T_N$.

2.7 Band Theory

In atoms, the electrons occupy discrete energy levels called orbitals. When these atoms are combined to form a solid, the electronic configuration of these atoms is altered to form wide energy bands. In semiconductor materials and at absolute zero temperature, the electrons occupy the energy levels starting with those of the lowest energy and working upwards; the last band to be filled is called the valence band. Then, there is a gap in energy called the band gap E_g to the next band, called the conduction band, which is entirely empty. As the temperature is increased from absolute zero, a certain number of electrons can be excited from the valence band to the conduction band, and the Fermi energy level, E_F is shifted up. The energy levels at the Fermi energy level are identical for spin up and spin down electrons. When a magnetic field is applied, these energy levels split. The down spin states are lowered by an amount of energy $-\mu_o\mu_B H$, and the up spin states are raised by an amount of energy $+\mu_o\mu_B H$ which leads to a spill-over of electrons from up-spin levels to down-spin levels until the new Fermi energy levels for up- and down-spin are equal. This phenomenon causes the Magneto-optics effects to occur.

2.8 Metallic Magnetism in Transition Elements

The diamagnetism in metals comes from the positive ions and free electrons of the metal. The positive ions are made of closed shells, which lead to diamagnetism; it is important to remember that the orbital motion of an electron causes a diamagnetic reaction when an external field is applied. The free conduction electrons move in curved paths in the presence of an external magnetic field leading to an additional diamagnetic contribution. The paramagnetism in metal originates from the conduction electrons. There are one or more conduction electrons per atom and each electron has a spin magnetic moment of one Bohr magneton. Nevertheless, the resulting paramagnetism is very weak. The sum of all these effects presents the susceptibility of the metal. Thus, if the diamagnetic contribution is stronger, the metal is diamagnetic, like copper. If the paramagnetic contribution is stronger, the metal is paramagnetic, like aluminium.

Incomplete inner shells, like in transition metal ions, exhibit a large net magnetic moment. The net magnetic moment of the transition metal ions is entirely due to the spin components, and the orbital contribution to the net magnetic moment is mostly quenched due to the strong coupling of the orbitals to the crystal lattice. The density of state of the *d*-electron bands is much higher than that of the *s*- and *p*- bands, which also explains why band magnetism is restricted to the transition metal elements that have a partially empty *d* band.

2.9 Spin-Based Electronics (Spintronics)

Spin-based electronics technology forms the basis for information technology in the modern age by exploiting both the charge and spin of electrons in semiconductor devices through introducing a high concentration of magnetic elements into nonmagnetic semiconductors to make them ferromagnetic and to form dilute magnetic semiconductor materials (DMS). When the power of the integrated circuits that exist today is switched off, the stored data in these circuits disappears while in magnetic circuits, the magnetic polarization does not leak over time like an electric charge does; as a result, the data are stored even when the power is switched off. No known wearing out mechanism exists, since switching the magnetic polarization does not involve any real movement of electrons or atoms.

The semiconductor devices based on spintronics technology or the spintronics devices have the advantages of non-volatility, increased data processing speed, decreased electric power consumption and increased integration densities when compared to classical semiconductor devices [10]. These advantages make spin-based electronics one of the most important topics of investigation in the field of new functional semiconductor devices [10, 11].

Spin-based devices have many potential applications, such as the spin field effect transistor (spin-FET), the spin resonant tunnelling device (spin-RTD), spin light-emitting diodes (spin-LEDs), optical switches operating at terahertz frequencies, encoders, decoders, modulators, and quantum bits for quantum computation and communication [10-13]. However, there are many challenges regarding the practical application of spintronic devices, such as spin injection, transport, manipulation and detection on the nano scale; these need to be addressed, and finding appropriate ferromagnetic semiconductors has become a major issue.

2.10 History of Spin-Based Electronics (Spintronics)

There is a long history of research into magnetic semiconductor materials. The first generation of these materials are the europium chalcogenides and ternary chalcogenides of chromium [14, 15]. The difference in lattice structure among these materials prevents their growth, and this has stopped any further research work on these materials. When it was discovered that doping the semiconductors with impurities led to a change in their properties, usually to p-type or n-type, the second generation began.

**Removed
by the author
for copyright reasons**

Figure 2.2: Three types of semiconductors: (A) a non-magnetic semiconductor, (B) a magnetic semiconductor; and (C) a dilute magnetic semiconductor (DMS), which is an alloy of non-magnetic and magnetic elements [16].

The second generation of magnetic semiconductor materials are the II-VI based, where a semiconductor can be made magnetic by introducing magnetic elements into its matrix. Such semiconductor materials are called dilute magnetic semiconductors (DMSs) [17]. Theoretical calculations of the Curie temperature (T_c) for a variety of wide bandgap semiconductor materials have been presented by Dietl based on the mean-field Zener Model [18]. Dietl considered Mn-doped ZnO and GaN to be the two most promising materials for practical spintronic devices with room temperature ferromagnetism. This prediction inspired extensive research into magnetically doped oxides and nitrides.

Removed
by the author
for copyright reasons

Figure 2.3: Computed values of the Curie temperature T_c for a range of wide bandgap semiconductors containing 5% of Mn and 10^{20} holes per cm^3 [18].

Studies of DMSs and their heterostructures have concentrated on II-VI semiconductors, such as CdTe, ZnO and ZnSe. Theoretically, Dietl et al. [18] and Sato et al. [19] found that ZnO doped with V, Cr, Fe, Co and Ni would be ferromagnetic at room temperature without additional carrier doping. Therefore, doped ZnO was the focus of most of the attention and was widely investigated. A comprehensive review of ZnO material and related devices was performed by Özgür et al. [20]. The Özgür review gives an exhaustive discussion of the mechanical, chemical, electrical, and optical properties of ZnO in addition to the technological issues such as growth, defects, p-type doping, band-gap engineering, devices, and nanostructures. However, the major obstacle to the development of ZnO was the lack of reproducibility and the low-resistivity p-type ZnO, as lately discussed by Look and

Claflin [21]. $\text{Cd}_{1-x}\text{Mn}_x\text{Te}$ received some attention due to its ability to accommodate as high as 77% of Mn atoms, and its suitable energy gap for optical applications. However, some difficulties, such as the impossibility of doping II-VI based DMSs to create a p-type and an n-type, and the interaction between the localized magnetic moments of the Mn spins being dominated by antiferromagnetic exchange, which leads to the paramagnetic, antiferromagnetic, or spin-glass behaviour. Another difficulty is when the ferromagnetic II-VI DMS are demonstrated at temperatures below 2K [22]. Also, the transition metal elements show low solubility in these host semiconductors and demonstrate a lack of reproducibility. All of these difficulties led to a loss of interest in the development of the II-VI material and in its use for practical applications.

The third generation materials are III-V based diluted semiconductors, such as $\text{In}_{1-x}\text{Mn}_x\text{As}$ and $\text{Ga}_{1-x}\text{Mn}_x\text{As}$. The magnetic properties of these materials are strongly dependent on the carrier concentration [23-25]. These materials exhibit magnetic, electric and/or optical properties, but because of the difficulties in growing good quality single crystals of these materials, it became necessary to produce uniform III-V based dilute magnetic semiconductor alloys under non-equilibrium conditions. Therefore, the molecular beam epitaxy, (MBE), was introduced into the area of research and several Mn-doped III-V semiconductors, such as $\text{In}_{1-x}\text{Mn}_x\text{As}$ [26, 27], $\text{Ga}_{1-x}\text{Mn}_x\text{As}$ [25, 28], $\text{Ga}_{1-x}\text{Mn}_x\text{P}$ [29], $\text{Ga}_{1-x}\text{Mn}_x\text{N}$ [11] and $\text{Ga}_{1-x}\text{Mn}_x\text{Sb}$ [30], have been successfully demonstrated. Since the Curie temperature, T_c , is proportional to the density of holes and the Mn ion concentration, Dietl's calculations suggested that a T_c value above room temperature is achievable for cubic (zinc-blende) $\text{Ga}_{1-x}\text{Mn}_x\text{N}$ containing 5% of Mn and 3.5×10^{20} holes per cm^3 . The T_c value for cubic (zinc-blende) GaN is 6% greater than that calculated for the hexagonal (wurtzite) structure [18]. Therefore, an interest in developing p-type $\text{Ga}_{1-x}\text{Mn}_x\text{N}$ ferromagnetic semiconductors began.

The electrical properties of p-type cubic $\text{Ga}_{1-x}\text{Mn}_x\text{N}$ films at room temperature were reported and a ferromagnetic signal over 400 K was detected at carrier concentrations higher than 10^{18} cm^{-3} where the $\text{Ga}_{1-x}\text{Mn}_x\text{N}$ layers had been grown by plasma assisted molecular beam epitaxy (PA-MBE) [31-33]. Hysteresis loops and p-type conductivity were also reported for all cubic $\text{Ga}_{1-x}\text{Mn}_x\text{N}$ samples

grown by PAMBE following the implantation of Mn^+ ions and annealing at $950\text{ }^\circ\text{C}$ for 1–5 min, and ferromagnetism was detected up to room temperature [34, 35]. However, this generation of materials was not suitable for spintronic devices applications because of their low Curie temperatures and the difficulty of integrating Mn magnetic elements into the semiconductor matrix.

In_2O_3 is one of the materials that Dietl did not consider in his calculations. Lately, several studies on doping In_2O_3 with small amounts of transition metals have been initialized [36-40]. Room temperature intrinsic ferromagnetism, ferromagnetism from extrinsic transition metal clusters and no ferromagnetism at all have been reported. The controversy among these results led to a conclusion that the magnetic properties of transition metal doped In_2O_3 are very sensitive to the growth conditions. This thesis focuses mainly on un-doped and doped In_2O_3 . Therefore, a review of the literature about In_2O_3 material is presented in section 1.14 and the investigation of the influence of the growth conditions and doping on optical and magneto-optical properties of In_2O_3 is covered.

2.11 Magneto-Optics

Magneto-optics is a spectroscopic method used to specify the source of ferromagnetism. It shows whether the ferromagnetism is intrinsic due the incorporation of TM ions into the lattice of the host material or is due to secondary impurity phases. Such information cannot be provided by any other method. It was also used by our group to determine the size, fraction, and characteristics of nanoparticles embedded in oxide semiconductors [41]. Magneto-optics uses light to investigate the splitting of electronic levels under the influence of internal or applied magnetic fields. Maxwell describes the light beam as an electromagnetic wave comprising two components: the electric field and the magnetic field. The direction of the electric field of an electromagnetic wave is called the polarization. There are several different types of polarization, such as Linear, Circular, Elliptical and Unpolarized [2]. In free space, the polarization of a wave is constant as it propagates. When the electric field vector, E , points along a constant direction, the polarization in this case is linear. Light has a wavevector k and an angular frequency ω related to the refractive index through the formula

$$k = \frac{n\omega}{c} = \frac{2\pi}{\lambda/n} \quad \text{Equation(2.13)}$$

This formula is valid for transparent materials. When the light passed through an absorbing medium, the absorption vector of this material needs to be included and the complex refractive index has to be considered. Therefore, Equ.13 becomes

$$k = \frac{\tilde{n}\omega}{c} \quad \text{Where,} \quad \tilde{n} = n + i\kappa \quad \text{Equation(2.14)}$$

where κ is called the extinction coefficient and relates to the absorption coefficient α and the wavelength λ through the relation

$$\kappa = \frac{\alpha c}{2\omega} = \frac{\alpha\lambda}{4\pi} \quad \text{Equation(2.15)}$$

Linearly polarized light comprises two components: the left circularly polarized light (LCP) and the right circularly polarized light (RCP). In a magnetic medium, the refractive index based on these components is rewritten as

$$\tilde{n}_{\pm} = n_{\pm} - i\kappa_{\pm} \quad \text{Equation(2.16)}$$

where (+) and (-) signs refer to RCP and LCP respectively.

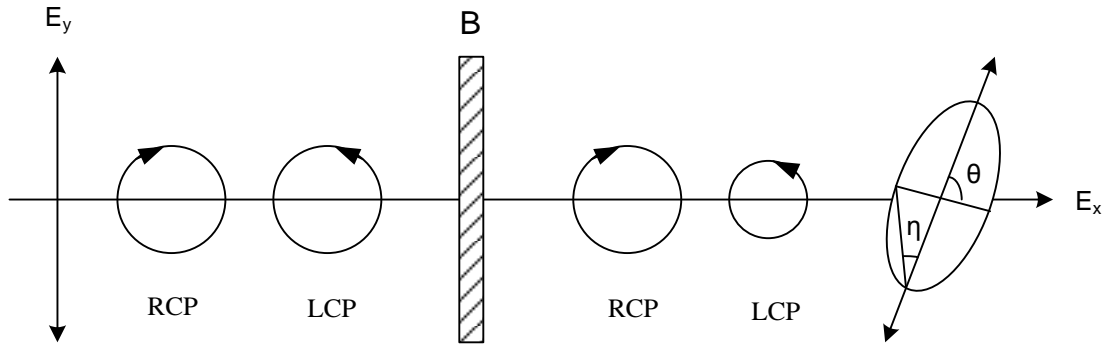


Figure 2.4: RCP and LCP components of linearly-polarized light emerges with a different phase and amplitude when they passes through a perpendicularly magnetized thin film.

The RCP and LCP components are always equal unless the linearly polarized light passes through a magnetic medium and propagates in a direction parallel to the direction of an applied magnetic field. In such a case, the RCP and LCP components are not equal, the refractive indices of the circularly polarized light components are not the same, $n_+ \neq n_-$, and a phase shift between LCP and RCP takes place indicating a magnetic circular birefringence, known as the Faraday rotation:

$$\theta_F = \frac{\omega l}{2c} \Delta n = \frac{\omega l}{2c} (n_+ - n_-) \quad \text{Equation(2.17)}$$

where c is the speed of the light, and l is the thickness of the magnetic medium. If the magnetic medium is absorbing light, the extinction coefficient comprises two components. The extinction coefficient components for RCP and LCP are κ_+ and κ_- respectively. The difference between the extinction coefficient components κ_+ and κ_- leads to elliptically polarized light, which gives the magnetic circular dichroism ‘MCD’.

$$\eta_F = \frac{\omega l}{2c} \Delta k = \frac{\omega l}{2c} (\kappa_+ - \kappa_-) \quad \text{Equation(2.18)}$$

As a result, the transmitted or reflected light will be elliptically polarized and rotated. This phenomenon is called the Faraday effect for transmitted light and the Kerr effect for reflected light.

Fundamentally, the magneto optical effect is a result of the splitting of energy levels in an external or spontaneous magnetic field. The absorption and the refractive index are a result of the electric dipole transitions between the magnetically quantized electronic states. Therefore, some spin-orbital coupling is necessary for the orbital moment to reflect information about the magnetism. If the spin-orbit coupling is weak, then the selection rules become $\Delta m_s = 0$ and $\Delta m_l = \pm 1$ [5].

The difference between the extinction coefficient components κ_+ and κ_- can happen when the valence and or the conduction bands are split or there is a difference in the orbital state populations. When band splitting occurs, the light transitions for LCP and RCP light happen at different energies but at the same orbital state population. The difference between the absorption components κ_+ and κ_- leads to a dispersive feature in the MCD spectra known as a diamagnetic line shape, as shown in Fig.2.5 (a).

When the occupation of orbital states is not equal, the transitions for LCP and RCP light occur at the same energy, but with different strengths. The difference between the absorption components κ_+ and κ_- leads to a dispersive feature in MCD spectra known as paramagnetic line shape, as shown in Fig.2.5 (b).

Removed by the author for copyright reasons

Figure 2.5: (a) Diamagnetic line shape and (b) Paramagnetic line shape of left and right circularly polarized light transitions [42].

Paramagnetic and diamagnetic line shapes are historical labels unrelated to earlier discussions in paramagnetism or diamagnetism. These line shapes could be used to check whether the detected MCD signal is real or just an unreal signal caused by a sample absorbing strongly at its band edge. This check could be performed by examining the way in which a peak in the Faraday rotation is seen at the zero point of an MCD signal and vice versa [43, 44].

Magneto-optical effects can occur at X-ray absorption edges, or resonances due to the excitation of electrons in the conduction band enhanced by transitions from atomic core levels to selected valence states; this kind of magneto optics is called the XMCD [6].

2.12 Magneto-Optics in Terms of Dielectric Tensors

The propagation of electromagnetic waves is described by the dielectric tensor $\tilde{\epsilon}$ or the conductivity tensor $\tilde{\sigma}$, which characterize the band-structure and describe the electric displacement field in the material through $\vec{D} = \tilde{\epsilon}\epsilon_0 \cdot \vec{E}$.

The dielectric tensor describes the interaction of the different components of an electromagnetic wave with the isotropic material through the dielectric tensor form shown below:

$$\tilde{\epsilon} = \begin{pmatrix} \tilde{\epsilon}_{xx} & 0 & 0 \\ 0 & \tilde{\epsilon}_{xx} & 0 \\ 0 & 0 & \tilde{\epsilon}_{xx} \end{pmatrix} \quad \text{Equation(2.19)}$$

If the material exhibits magnetic properties, the off diagonal components of the dielectric tensor are activated; therefore, the propagation of electromagnetic waves can be completely described by considering the complex dielectric tensor form shown below:

$$\tilde{\epsilon} = \begin{pmatrix} \tilde{\epsilon}_{xx} & -i\tilde{\epsilon}_{xy} & 0 \\ i\tilde{\epsilon}_{xy} & \tilde{\epsilon}_{xx} & 0 \\ 0 & 0 & \tilde{\epsilon}_{xx} \end{pmatrix} \quad \text{Equation(2.20)}$$

In general, if the absorption of the material is not zero, the components of the dielectric tensor became complex by considering the absorption vector component and are given by

$$\tilde{\epsilon}_{ij} = \epsilon'_{ij} + i\epsilon''_{ij} \quad \text{Equation(2.21)}$$

The diagonal and off diagonal components of the dielectric tensor are expressed in terms of the experimentally measured refractive index, absorption, Faraday MCD and rotation through the formula

$$\tilde{\epsilon}_{xx} = (n - i\kappa)^2 \quad \text{Equation(2.22)}$$

$$\epsilon'_{xy} = \frac{2c}{\omega l} (n\theta_F - \kappa\eta_F) \quad \text{Equation(2.23)}$$

$$\epsilon''_{xy} = \frac{2c}{\omega l} (\kappa\theta_F + n\eta_F) \quad \text{Equation(2.24)}$$

The diagonal and off diagonal components of the dielectric tensor can be related to each other through the formulae

$$\tilde{n}_{\pm}^2 = \tilde{\epsilon}_{xx} \pm \tilde{\epsilon}_{xy} \quad \text{Equation(2.25)}$$

$$\tilde{n}_{\pm} = \sqrt{\tilde{\epsilon}_{xx}} \pm \frac{\tilde{\epsilon}_{xy}}{2\sqrt{\tilde{\epsilon}_{xx}}} \quad \text{Equation(2.26)}$$

In the case of $\tilde{\epsilon}_{xx} \gg \tilde{\epsilon}_{xy}$, magneto-optic effects are given in terms of the difference between left- and right circular polarizations and therefore depend on

$$\tilde{n}_+ - \tilde{n}_- = \frac{\tilde{\epsilon}_{xy}}{\sqrt{\tilde{\epsilon}_{xx}}} \quad \text{Equation(2.27)}$$

The Faraday rotation, θ_F , and MCD, η_F , in a sample of thickness l_o are given in terms of the real and imaginary parts, n_{\pm} and κ_{\pm} , by:

$$\theta_F = \text{Re} \left(\frac{\omega l_o}{2c} (\tilde{n}_+ - \tilde{n}_-) \right) = \frac{\omega l_o}{2c} (n_+ - n_-) \quad \text{Equation(2.28)}$$

$$\eta_F = \tan \left(\text{Im} \left(\frac{\omega l_o}{2c} (\tilde{n}_+ - \tilde{n}_-) \right) \right) = \tan \left(\frac{\omega l_o}{2c} (\kappa_+ - \kappa_-) \right) \quad \text{Equation(2.29)}$$

which is equivalent to Equ.17 and Equ.18 mentioned previously.

2.13 Kramers-Kronig Relations

Kramers–Kronig relations are mathematical properties that connect the real and imaginary parts of any complex response function. The Kramers–Kronig relations allow us to calculate the real (n) part of the complex refractive index (\tilde{n}) from the imaginary (κ) part (if known) at all frequencies, and vice versa [1]. Kramers-Kronig relations are used to calculate the reflectivity $R(\omega)$ from experimental $\varepsilon'(\omega)$ and $\varepsilon''(\omega)$ [45-47]. From another point of view, Kramers-Kronig transformations are used to calculate the effective electron density and the imaginary part of the dielectric constant from known $R(\omega)$ [48, 49]. Kramers-Kronig analysis has been widely used by others [49-52].

The Kramers-Kronig relations for the two components of the complex dielectric function are [6]:

$$\varepsilon'_{ij}(\omega) = 1 + \frac{2}{\pi} P \int_0^\infty \frac{\omega' \varepsilon''_{ij}(\omega')}{\omega'^2 - \omega^2} d\omega' \quad \text{Equation(2.30)}$$

$$\varepsilon''_{ij}(\omega) = -\frac{2}{\pi \omega} P \int_0^\infty \frac{\omega'^2 [\varepsilon'_{ij}(\omega') - 1]}{\omega'^2 - \omega^2} d\omega' \quad \text{Equation(2.31)}$$

The Kramers–Kronig relations of the optical conductivity are as follows:

$$\sigma'_{ij}(\omega) = \frac{2}{\pi} P \int_0^\infty \frac{\omega' \sigma''_{ij}(\omega')}{\omega'^2 - \omega^2} d\omega' \quad \text{Equation(2.32)}$$

$$\sigma''_{ij}(\omega) = -\frac{2\omega}{\pi} P \int_0^\infty \frac{\sigma'_{ij}(\omega')}{\omega'^2 - \omega^2} d\omega' \quad \text{Equation(2.33)}$$

where σ'_{ij} (σ''_{ij}) is the real (imaginary) part of the $\tilde{\sigma}_{ij}$ respectively [53]. The useful forms related between the real and imaginary parts of the complex refractive index \tilde{n} are written as [1, 45]

$$n(\omega) = 1 + \frac{2}{\pi} P \int_0^\infty \frac{\omega' \kappa(\omega')}{\omega'^2 - \omega^2} d\omega' \quad \text{Equation(2.34)}$$

$$\kappa(\omega) = -\frac{2}{\pi\omega} P \int_0^\infty \frac{\omega'^2 [n(\omega') - 1]}{\omega'^2 - \omega^2} d\omega' \quad \text{Equation(2.35)}$$

where P indicates the Cauchy principal value of the integral [1, 53].

2.14 Pure In₂O₃

Indium oxide, In₂O₃, is a transparent material belonging to the wide band gap, n-type semiconductors [54]. In₂O₃ grown in a low oxygen environment has a high electron carrier concentration (between 10¹⁸ and 10²⁰ cm⁻³) [55, 56]. In₂O₃ is used extensively in the semiconductor industry, especially in optoelectronics, including displays, photovoltaics and light emitting diodes [57, 58]. Introducing tin to the In₂O₃ gives the form indium-tin-oxide, ITO, which is used widely as transparent electrodes in liquid crystal display (LCD), and organic light emitting diode (OLED) devices [59, 60]. In₂O₃ crystallizes in a complex cubic bixbyite structure under the condition of O-deficiency and high temperature. Otherwise, it will crystallize in an amorphous structure. The complex cubic bixbyite structure contains 80 atoms in a unit cell with a lattice parameter of 10.118Å [40, 56, 62, 65, 68, 73-75]. The complexity of the structure originates from an array of unoccupied tetrahedral oxygen anion sites, which can be viewed as surrounding face-centred in sites having a periodicity of one-half the unit cell, or 5.059Å [76-79]. However, the cubic structure of In₂O₃ allows it to be grown easily on low-cost substrates, such as MgO or Al₂O₃ for real applications [38]. In₂O₃ shows optical transitions from about 3.6 eV [61], 3.75eV [56, 62, 63], 3.5 - 4.3 eV [64-67] and transitions from about 2.62 eV [61, 64, 68-70] attributed to indirect electronic transitions. However, the actual direct and indirect band gap energies of In₂O₃ are remains contentious. Paul Erhart *et al* [71] and using density functional theory calculations concluded that the experimental observations cannot be related to the electronic structure of the defect free bulk material of In₂O₃. Aron Walsh *et al* [68] found experimentally and theoretical agreement to set an upper limit of 2.9 eV for the fundamental gap of In₂O₃ where the fundamental band gap 0.81 eV lower in energy than the onset of strong optical absorption observed experimentally. The calculated band structure of In₂O₃ is shown in Fig.2.6 (a), and the difference between the fundamental and the optical energy gap are shown in Fig. 2.6 (b).

Removed by the author for copyright reasons

Figure 2.6: a) Band structure of In_2O_3 [68], b) Schematic diagrams for the fundamental and the optical energy gap with the forbidden and allowed transitions in In_2O_3 .

Fig.2.6 illustrated the band structure and Schematic diagrams for the fundamental and optical energy gap with the forbidden and allowed transitions in In_2O_3 . Walsh report that, the optical transitions to the conduction band from all the states above the $\Gamma_8(T_u)$ state are forbidden because they have even parity. The optical gap is 0.81eV higher than the real band gap which is observed by HXPS, which is supported by Novkovski *et al* [72]. However there is a weak absorption was seen by King et al. This might be because the transition was allowed because of defects or because it was allowed because of phonons. We have seen a similar tail to the absorption which depends on the oxygen vacancies. In our case, we believe that is arises from transitions to the defect band because it is spin polarised as is seen in the MCD. In addition, Novkovski *et al* reported several transitions from a direct forbidden at 3.29 eV which is supported by F. Fuchs *et al* [69] and three indirect allowed transitions at 2.09 eV, 3.42 eV and 3.58 eV. Therefore, the high conductivity seen in In_2O_3 is due to the generation of carriers by transitions from the two lowest maxima of the conduction band located within the valence band, going along with a high transmission in the visible range, up to the photon energies above 4 eV, at which direct allowed transitions occur, leading to strong absorption [72].

Studies on pure In_2O_3 thin films grown by various deposition techniques, such as direct current (DC) reactive magnetron sputtering [80, 81], chemical vapour deposition [82], reactive thermal evaporation [83], ion beam sputtering [84], and pulsed laser deposition (PLD) [85], have revealed that the method of preparation and growth conditions of complex oxide thin films play significant roles in their magnetic, electrical and optical properties. For example, Qiao *et al.* deposited In_2O_3 films using vacuum sputtering at a substrate temperature of 300K. The In_2O_3 films had an amorphous structure and had low transparency and high resistivity [86]. Hichou *et al.* deposited In_2O_3 films using pulse laser deposition (PLD) both at room temperature and at 373 K. The In_2O_3 films deposited at room temperature showed an amorphous structure whereas the In_2O_3 films deposited at 373 K had a cubic bixbyite structure and the transmission factor increased with an increase in the deposition temperature [87]. In addition, increasing the oxygen pressure led to an increase in the optical transmission factor [88] and the optical transmission increased or decreased with an impurity concentration [89], depending on the impurity type. The microstructure of the In_2O_3 film changed with an increase in thickness, which led to some improvements in the film's properties. It was found that with an increase in thickness, the electrical carrier density increases and the electrical resistivity decreases [86].

A previous study by Kaleemulla *et al.* about the influence of oxygen partial pressure (P_{O_2}) on the physical properties of pure In_2O_3 revealed that the atomic ratio of oxygen atoms to indium atoms decreased with a decrease in oxygen partial pressure [90]. As a result, films prepared at low oxygen partial pressure are rich in indium and oxygen vacancies. The grain size of pure In_2O_3 was found to decrease with an increase in oxygen partial pressure, as reported by Ryzhikov *et al.* [91]. Ovadyahu *et al.* found that the films tend to show a dendritic growth and create too many grain boundaries at low oxygen partial pressure [92]. Subramanyam *et al.*, using the X-ray diffraction, and Kaleemulla *et al.*, using the EDAX spectrum analysis, reported that the crystallinity of thin films increased with an increase in oxygen partial pressure regardless of the material type or the growth method used [90, 93].

The transport properties of pure In_2O_3 at different oxygen partial pressures were investigated by many groups. Choopun *et al.* reported that for thin films deposited in an oxygen-rich environment, the carrier concentration and conductivity were found to decrease with an increase in oxygen partial pressure due to the drop in

defect density [94]. Thin films deposited at low oxygen partial pressure usually fall into the metallic regime where the carrier concentration reaches approximately 10^{20} electrons/cm³. Das *et al.*, Bielz *et al.*, Gupta *et al.*, and others found that the electrical resistivity and the Hall mobility increase with an increase in oxygen partial pressure [90, 95-97]. Such variations in carrier concentration and electrical resistivity with oxygen partial pressure were observed in Tin-doped indium oxide (ITO), as reported by Kim *et al.* and Dekkers *et al.* [67, 98]. Kim found that the carrier density of the ITO films increases from 2×10^{20} to 11×10^{20} cm⁻³ when the oxygen deposition pressure is decreased from 50 to 10 mTorr. This variation was confirmed by others such as Ukah *et al.* [99], Liang *et al.* [100], and Subramanyam *et al.* [101].

Kaleemulla *et al.* found that the optical transmittance spectra increase with increases of oxygen partial pressure. The enhancement in transmittance with an increase in the oxygen partial pressure is also reported by other studies, such as H. Kim *et al.* and B. Tahar *et al.* [102, 103]. Variations in the optical absorption coefficient with oxygen partial pressure were found to increase with decreases in the oxygen partial pressure due to the increase of oxygen vacancy defects density. Another way to control the density of oxygen vacancy defects for already prepared thin films is to use the annealing process approach. Many types of annealing process have been used to enhance the physical properties of oxide thin films. Annealing in a vacuum, in air, or in a specific gas environment are some of the annealing types that are usually used. Annealing a thin film in air enhances the crystallization of the film while annealing in a vacuum increases the oxygen vacancy density and, accordingly, increases the carrier density. Increasing or decreasing the carrier density affects many of the physical properties of thin films. The Fermi energy level may shift up or down, and thin films may become insulator, semiconductors or metallic. It is widely believed that the annealing process enhances the properties of thin films. However, while this is true for un-doped materials, for doped materials, the annealing process is not always desirable, as we will find in the following chapters. Vickraman *et al.* prepared pure indium oxide (In₂O₃) thin films at the same growth conditions at base pressure using an electron beam evaporation system [104]. Then, the thin films were annealed in air at different temperatures, from 350 to 550 °C. The Variations in grain size and lattice constant with annealing temperatures in air is shown in Fig.2.7.

Removed by the author for copyright reasons

Figure 2.7: Variations in grain size and lattice constant with annealing temperatures in air, (Data plotted)[104].

Fig.2.7 illustrated the increase in grain size with an increase in the annealing temperature which is due to the sufficient increase in the supply of thermal energy for crystallization. The lattice constant was found to increase with an increase in the annealing in air temperature, as shown in Fig.2.7 due to the decrease in oxygen vacancies. The dislocation density and strain, were found to decrease with an increase in the annealing in air temperature, as shown in Fig.2.8.

Removed by the author for copyright reasons

Figure 2.8: Variations in dislocation density and strain with annealing temperatures, (data plotted) [104].

The electrical resistivity was found to decrease with an increase in the annealing temperature in air. The electrical conductivity of In_2O_3 films was found to increase with an increase in the annealing temperature. These results show that the mobility and/or carrier density increases with an increase in the annealing temperature due to the fact that the free electrons are trapped in the grain boundaries. When the grain size increases, as observed in Fig.2.7, the density of the grain boundaries

decreases; therefore, fewer carriers are trapped, leading to a higher carrier density or an increased amount of released free carriers, which means higher conductivity and lower resistivity [105]. Variations of the optical transmittance spectrum and the optical band gap energy with annealing temperature are shown in Fig.2.9.

Removed
by the author
for copyright reasons

Figure 2.9: Variations in transmission spectrum and the optical band gap energy of pure In_2O_3 with annealing temperatures in air,(Data plotted) [104].

The transmission spectrum of pure In_2O_3 film was found to increase with an increase in the annealing temperature due to the enhancement in the crystallinity of the films, which was also observed by Han *et al.* in ITO thin films [106]. The optical band gap energy was found to increase with an increase in the annealing temperature, as shown in Fig.2.9. The optical band gap shifted toward higher energy from 3.65 to 3.86 eV with an increase in the annealing temperature due to Burstein–Moss Effect. Variations in the In_2O_3 index of refraction with annealing temperatures in air are shown in Fig.2.10.

Removed
by the author
for copyright reasons

Figure 2.10: Variations in the index of refraction of In_2O_3 with annealing temperatures in air (Data plotted) [104].

The increase of index of refraction from 1.84 to 1.91 with an increase in the annealing temperature in air, implies that the stress in the lattice of In_2O_3 thin film increases with increases in the annealing temperature. Growth of thin films in high oxygen partial pressure or annealing them in air leads to fill up the empty positions in the lattice with oxygen atoms. Therefore, the physical properties of pure In_2O_3 are affected directly or indirectly, as shown in previous reviews in each case. The transmission depends on reflection; absorption and scattering, therefore, reduction in transmission not always mean that, the thin film is absorbing, where the absorption is depend on defect levels but can be due to the increases of the scattering, where the scattering depend on the grain size. A comparison between the variations in some of the physical properties of pure In_2O_3 with an increase in oxygen partial pressure and with an increase in the annealing temperature in air is shown in Table.2.1.

Parameter	Increases of oxygen partial pressure	Increases of annealing temperature in Air.
Atomic Ratio of O_2 atoms	Increase	Increase
Grain Size	Decrease	Increase
Carrier concentration	Decrease	Increase
Resistivity	Increase	Decrease
Mobility	Increase	Increase
Transmission	Increase	Increase
Absorption	Decrease	Decrease
Band gap energy	Decrease	Increase

Table 2.1 : Comparison between the influence of increases in oxygen partial pressure and the influence of increases in the annealing temperature in air on the physical properties of pure In_2O_3 .

Both methods show the same effect on most of the physical properties of pure In_2O_3 . The difference between them occurs in the grain size, the carrier concentration, the conductivity, and the resistivity. The carrier concentration and the grain size decrease with increases in oxygen partial pressure, whereas they increase with the annealing process in air; however, the mobility increases in both cases. The reason for this variation is that, in the case of oxygen partial pressure, the carriers related to the oxygen vacancy density are dominant while in the case of the annealing process in air, the free electrons released from the grain boundaries with an increase in grain size are dominant. When this phenomenon is saturated, then, the carrier density starts to decrease due to the insertion of oxygen atoms in the lattice. However, the effect of

oxygen vacancy density in this case is much lower than that in case of oxygen partial pressure.

The sample thickness is another growth variable that has a large impact on the structural, electrical, magnetic, optical, and magneto-optical properties of oxide thin films. Increasing the thickness of a thin film is not always the right way to enhance its properties. Determination of the thicknesses of a group of samples is essential in order to investigate the effect of any physical parameter per volume and to compare these samples. The influence of thickness on the physical properties of pure and doped In_2O_3 has been investigated by many groups, whose findings will be summarized in the following literature review. This section has been added in order to find out the suitable thickness, for optical measurements, of thin films in the case of pure In_2O_3 and TM-doped In_2O_3 .

Previous studies by Muranaka *et al.* and Kim *et al.* on the influence of thickness on the physical properties of pure In_2O_3 revealed that the grain size of In_2O_3 thin films increase with an increase in thickness. The increment in grain size leads to a reduction in the grain boundary scattering; consequently, the electrical resistivity of the In_2O_3 thin film decreases [102, 107]. Liang *et al.* reported that the surface roughness of In_2O_3 thin film increases with the increase in thickness due to the increment in grain size, and the orientation of the film is an effective element to control the roughness and, consequently, the grain size of In_2O_3 thin film [108, 109]. Qiao *et al.* found the strain that exists at the early stages of the growth process decreases with an increase in thickness of In_2O_3 thin film [86].

The influence of thickness on the transport properties of In_2O_3 thin films was investigated by several groups. Gupta *et al.* and Prathap *et al.* found that the carrier concentration and mobility of In_2O_3 thin films increase with an increase in the thickness [110, 111]. Al-Dahoudi *et al.* and Tak *et al.* reported the same results for ITO thin films [109, 112]. The variations in resistivity, mobility and the carrier concentration of un-doped In_2O_3 and Tin-doped In_2O_3 with thickness are shown in Fig.2.11.

Removed by the author for copyright reasons

Figure 2.11: the variations in resistivity (ρ), carrier concentration (n), and mobility (μ) with thickness of IO film (left) [110, 111], ITO film (right)[112].

Increases in the carrier density with increases in thickness due to increase of oxygen vacancy density [113]. It has been reported that in thin films with a thickness greater than 100nm, the carrier concentration decreases with an increase in thickness. The reason given for this is that during the growth of the films, a large lattice strain is presented by the mismatch between the substrate and the film, which causes many defects. These defects act as traps and trap free electrons; as a result, the carrier concentration decreases. Another reason given is because the oxygen vacancy density decreases with an increase in thickness [113]. Liang *et al.* investigated the influence of film thickness on the electro-optical properties of indium tin oxide films. They found that the absorption coefficient increases rapidly with thickness due to the increase in the carrier concentration. The optical absorption edge of Sn-doped In_2O_3 was found to shift towards higher energy with an increase in thickness. The variations in optical band gap energy with an increase in thickness are also reported by Liang *et al.* The optical band gap energy increased with increases in film thickness up to 500nm, and stabilized afterwards.

To date, there has been no optical study that considers the temperature dependence of the absorption and transmittance for pure In_2O_3 . Several optical studies of un-doped In_2O_3 as a function of different growth conditions have been reported, but all these studies have been taken at room temperature. Thus, the following literature review discusses the optical properties of pure In_2O_3 at room temperature through a published study about the substrate temperature dependence of optical properties of un-doped In_2O_3 . However, the dependence of other growth conditions will be covered in this thesis. Prathap *et al.* investigated the optical properties of un-doped In_2O_3 at

different substrate temperatures in the range 300-400 °C. This gives us an indication about the properties of our samples grown at 550 °C. The pure thin films of In₂O₃ were grown by spray pyrolysis technique [114] and the optical properties acquired were at room temperature. The transmission spectra of pure In₂O₃ thin films deposited at different substrate temperature and measured in the wavelengths between 300 and 2500 nm are shown in Fig.2.12.

Removed
by the author
for copyright reasons

Figure 2.12: Transmittance spectra of pure In₂O₃ films deposited at different substrate temperatures[114].

The optical transmission decreases sharply near the absorption band edge of In₂O₃. The absorption edge of In₂O₃ shifts towards higher energy with the increases in the deposition temperature, indicating the widening of the band gap energy. In the transparent region below the absorption edge, where $\lambda > 400 \text{ nm}$, the spectra of the film deposited at 400 °C displayed a transmittance higher than 80%. This suggests that the density of defects decreases with an increase in the deposition temperature. The absorption seen below the band gap edge for films deposited at 300 °C and 350 °C in Fig.2.14 was attributed to the formation of defects. The defects presented in these thin films are the oxygen vacancies, where there are no TM ions introduced to the In₂O₃ matrix. Prathap *et al.* found the optical band gap and the index of refraction varies with the temperature of the substrate, as shown in Fig.2.13.

Removed by the author for copyright reasons

Figure 2.13: Variations in the optical band gap energy and the refractive index of pure In_2O_3 with the substrate temperatures [114].

The optical band gap energy of un-doped In_2O_3 thin film deposited at a substrate temperature higher than $400\text{ }^\circ\text{C}$ exceeds 3.60eV of energy. The optical band gap energy shifts toward higher energy with an increase in the substrate temperature. In Fig.2.13, the shoulder area below the band gap edge and located between 3.2eV and 3.6eV for the thin film grown at $400\text{ }^\circ\text{C}$ is the smallest compared with the other shoulders, which confirmed the decrease in the density of defects with an increase in the deposition temperature. The refractive index of pure In_2O_3 thin film deposited at a substrate temperature higher than $400\text{ }^\circ\text{C}$ is shown to be weakly energy dependent and falls in the range of 1.8-1.95. The accurate refractive index spectrum of pure In_2O_3 thin film is very important in understanding the Faraday rotation and in achieving correct results in many magneto-optics theoretical calculations, as we are going to find out in the following chapters.

2.15 Sn doping In_2O_3 (ITO)

As we mentioned earlier, the crystal structure of pure In_2O_3 shows a cubic bixbyite structure. X-ray diffraction (XRD) and transmission electron microscopy (TEM) analyses reported by J. Popovicre *et al.* and S. Kim *et al.* revealed that doping In_2O_3 with tin has no effect on the structure of In_2O_3 ; Sn-doped indium oxide samples show a cubic bixbyite structure. The grain size decreases with increases in Sn doping levels, but the lattice strain was found to increase with an increase in Sn content, as shown in Fig.2.14 [115, 116].

Removed by the author for copyright reasons

Figure 2.14: Variations in grain size and lattice strain with Sn content, (Data plotted)[115].

The lattice constant was found to decrease with an increase in Sn concentration until it reaches a minimum, and then it increases again. The minimum value of the lattice constant is located at the point where the concentration of Sn shows the lowest resistivity and highest carrier density. That concentration of Sn is called the Critical Sn content.

The critical Sn content value increases or decreases according to the growth conditions and the material type. The critical Sn content value for ITO was reported to be 5% [118], 7.5% [119], 8% [120], and 10% [121]. Also, for other materials, it was reported to be 2.9% for TCO or Sn doped CdO [122]. The reduction of the lattice constant with the increase in Sn content to the minimum value indicates that the smaller Sn ions substitute the larger In ions in the lattice. Above the critical Sn content value, the lattice constant increases with increases in Sn content, indicating an increase in the repulsion between Sn ions. In addition, the interstitial Sn ions increases and acts as scattering centres and cause a decrease in the Hall mobility, as reported by H. Tomonaga and T. Morimoto [120]. The resistance of Tin doped In_2O_3 thin films was found to decrease as the concentration of Sn increased.

El Hichou *et al.* and G. Frank *et al.* found that the maximum solubility of Sn atoms in the In_2O_3 lattice reaches 5% [87, 123]. Therefore, for Sn content lower than 5%, when Sn^{4+} ions substitute In^{3+} ions, the Sn atoms act as n type donors. For Sn content higher than 5%, no more Sn atoms can be embedded in the In_2O_3 lattice; consequently, the interstitial Sn atoms in the lattice act as charged trapping centres for the electrons [78, 87].

H. Metzner *et al.* investigated the optical transmission spectra of In_2O_3 films doped with different Sn concentrations in the wavelength region of 300–1000 nm. The optical transmission of pure In_2O_3 increases with increase of tin content. However, a study by V. Senthilkumar *et al.* found that the transmittance decreases with an increase in Sn concentration for films grown in the same oxygen environment and under similar processing conditions [117]. In fact, the decrease in optical transmission may not be associated with the loss of light due to oxygen vacancies, but it is associated with the loss of light due to the increase in the density of the scattering centres. The increase in density of the scattering centres is due to an increase in grain boundaries associated with the increase in Sn dopant concentration [117]. The variations in the optical band gap energy and index of refraction at 550nm with tin content are shown in Fig.2.15.

**Removed
by the author
for copyright reasons**

Figure 2.15: Variations in optical band gap energy and refractive index at 550nm of In_2O_3 thin films with Sn content, (Data plotted)[117].

The estimated values of the optical band gap were found to increase with an increase in Sn concentration in the In_2O_3 lattice as shown in Fig.2.15, due to the increase in carrier density with tin content. The index of refraction at 550nm as a function of tin content was found to decrease with an increase in tin content as shown in Fig.2.16, implying that the refractive index of tin-doped thin films is smaller than that of the pure In_2O_3 thin films. The decrease in the refractive index was attributed to the lowering in the value of grain size of the ITO film with an increase in Sn content [117].

2.16 TM doped Oxides

Transition metal (TM) -doped semiconductor oxides have been found to show ferromagnetism at room temperature [39, 124-132]. The ferromagnetism in semi magnetic semiconductors (SMS) is usually attributed to the interaction between the host s , p bands carriers and the localized $3d$ electrons in doped transition metal elements. Several theoretical models have been suggested based on the $s(p)$ - d interactions feature, and these fall into two categories: the first category is the carrier-mediated models like the Zener model and the Ruderman-Kittel-Kasuya-Yosida (RKKY) model [133, 134]. In the carrier-mediated models, the coupling between magnetic ions is achieved through the mobile carriers, i.e., holes in the valence band or electrons in the conduction band. The second category is the super exchange models like the double-exchange model [135-138]. In super exchange models, the coupling is achieved between magnetic ions through the localized carriers.

The ferromagnetism in oxide magnetic semiconductors usually is induced by clustered magnetic impurities [139] or attributed to the oxygen vacancy defects where the ferromagnetic exchange interaction is mediated by shallow donor electrons trapped in oxygen vacancy defects [125, 140]. The presence of metallic TM is always expected, especially for Co-, and Fe-doped In_2O_3 . Cobalt (Co) is one of the TMs that show high total magnetic moments induced by each Co magnetic ion in the In_2O_3 matrix. The structural, magnetic, and electrical transport properties of Co-doped indium oxide and indium-tin oxide thin films have been studied by several groups. J. Stankiewicz *et al.* found different contributions of metallic Co and oxidized Co^{2+} to the observed ferromagnetism and the uniform substitution of Co atoms seen in ITO thin films doped with less than 7 % of Co [141, 142].

L. M. Huang *et al.* studied theoretically the magnetic and electronic properties of the transition metal (V, Cr, Mn, Fe, Co, Ni, Cu) doped In_2O_3 and found that when two TM ions of TM-TM are placed far from each other, only Co, Ni and Cu ions still prefer the ferromagnetic orientation and the $3d$ bands show strong hybridization with the host valence band formed mainly by the oxygen $2p$ state, while V, Cr, or Mn ions prefer antiferromagnetic ordering and the $3d$ bands are merged with the conduction band and show less hybridization with the host valence band [143].

Removed
by the author
for copyright reasons

Figure 2.16: The triangles represent the total magnetic moments induced by each magnetic ion; the squares represent the local magnetic moments on TM sites [143].

To the best of our knowledge, there is no published research about the optical and magneto-optical properties of Co-doped In_2O_3 except our paper [144]. However, the optical and magneto-optical properties of cobalt as a doping material in other semiconductors like ZnO have been reported. Saito *et al.* discussed these properties for $\text{Zn}_{1-x}\text{Co}_x\text{O}$ and found a dip in the optical transmission spectrum around 620nm (2.0eV) [145]. This dip is a localized absorption band due to Co^{2+} $d-d$ transitions.

Removed
by the author
for copyright reasons

Figure 2.17: The optical transmission and the optical absorption coefficient spectra of $\text{Zn}_{1-x}\text{Co}_x\text{O}$ [145].

The localized absorption band of Co^{2+} $d-d$ transitions in $\text{Zn}_{1-x}\text{Co}_x\text{O}$ is sharp when compared with the localized absorption band of Mn^{2+} $d-d$ transitions of Mn-based DMS, such as $\text{Zn}_{1-x}\text{Mn}_x\text{O}$ [145, 146] and $\text{Cd}_{1-x}\text{Mn}_x\text{Te}$ [145, 147, 148].

The MCD spectrum of $\text{Zn}_{1-x}\text{Co}_x\text{O}$ shows an MCD spectral shape near 2.0 eV. The MCD signal at 2.0eV for Co-doped semiconductors is related to the $\text{Co}^{2+} d - d$ transitions [145, 149-151]. Also, there is an MCD peak near the absorption edge of the host semiconductor. The MCD spectrum of $\text{Zn}_{1-x}\text{Co}_x\text{O}$ is strongly temperature dependent. The MCD peak near the absorption edge of $\text{Zn}_{1-x}\text{Co}_x\text{O}$ is negative at low temperatures, and its magnitude rapidly decreases with an increase in temperature, which reflects the paramagnetism of Co^{2+} ions in the host material; this, in turn, is confirmed by XMCD measurements by Hakimi *et al.* in cobalt-doped indium tin oxide thin films [152].

Removed
by the author
for copyright reasons

Figure 2.18: MCD of $\text{Zn}_{1-x}\text{Co}_x\text{O}$ [145].

The polarity of the MCD and Faraday effect in real units can be used to reveal whether the $p-d$ interaction in DMS materials is ferromagnetic or antiferromagnetic. It has been reported that $\text{Cd}_{1-x}\text{Mn}_x\text{Te}$ has a negative MCD peak polarity; therefore, the $p-d$ exchange interaction in $\text{Cd}_{1-x}\text{Mn}_x\text{Te}$ is antiferromagnetic [153]. This result is adapted in $\text{Zn}_{1-x}\text{Co}_x\text{O}$ where $\text{Zn}_{1-x}\text{Co}_x\text{O}$ also has a negative MCD peak polarity; as a result, the $p-d$ exchange interaction in $\text{Zn}_{1-x}\text{Co}_x\text{O}$ is antiferromagnetic, which is in accordance with the results for other Co-based II–VI diluted magnetic semiconductors such as $\text{Cd}_{1-x}\text{Co}_x\text{Se}$ [154, 155] and $\text{Cd}_{1-x}\text{Co}_x\text{S}$ [155] that have negative MCD peak polarity, and confirms that the $p-d$ exchange interaction in these materials is antiferromagnetic. Most of the doped transition metals were found to exhibit very low solubility in the host semiconductor's lattice. Among them, Fe as a doping material for In_2O_3 semiconductor exhibits an exceptional electrical conductivity, high Curie

temperature, high optical transparency, and high thermodynamic solubility reaching more than 20% of Fe in the host matrix [156], which makes any observed ferromagnetism intrinsic rather than originating in Fe clusters or any other magnetic impurity phases [157]. Therefore, Fe doped In_2O_3 is considered to be one of the most promising candidates for optoelectronics and spintronics applications.

An experimental study by D. Bérardan *et al.* on bulk Fe-doped In_2O_3 shows that bulk Fe-doped In_2O_3 is paramagnetic due to Fe^{3+} ions, and the dominant interactions are antiferromagnetic. For high iron content, a cluster glass or superparamagnetic behaviour is observed [65]. S. Kohiki *et al.* investigated Fe-doped In_2O_3 thin films and found that Fe-doped In_2O_3 thin films show antiferromagnetic behaviour, which is attributed to the super exchange interaction between Fe^{3+} ions at p and d sites [74]. Studies on Fe-doped In_2O_3 thin films by Yoo *et al.* and Peleckis *et al.* show that Fe-doped In_2O_3 thin films exhibit ferromagnetic behaviour at room temperature, which is attributed to the mixed valence of Fe^{2+} and Fe^{3+} [158, 159]. Another theoretical study by Hu *et al.* on the magnetic properties of Fe doped In_2O_3 shows that without oxygen vacancies, the doped Fe ions tend to display antiferromagnetic spin ordering, and with oxygen vacancies, a shallow donor state is induced and mediates the stable ferromagnetic exchange interaction [160]. Therefore, the ferromagnetism observed in low-dimensionality samples in thin films or nanocrystalline thin films is linked to different surface/volume ratios and therefore to different oxygen vacancy concentrations.

2.17 Energy Levels of Oxygen Vacancies

Oxygen vacancies are found in any material that has oxygen atoms as a part of its structure. The density of the oxygen vacancies varies based on the growth conditions of that material. In an In_2O_3 crystal, the oxygen vacancy density increases when the In_2O_3 crystal is grown at low oxygen pressure, as will be discussed later. Sometimes, In_2O_3 crystals exhibit different crystallization qualities due to the different amounts of oxygen vacancies and defects generated during growth. Such differences lead to different transition paths. Therefore, In_2O_3 crystals show different colours [161]. The oxygen vacancies in semiconductors induce the formation of new energy levels within the band gap.

Removed by the author for copyright reasons

Figure 2.19: The PL spectrum of In_2O_3 nanowires at (a) as-grown In_2O_3 nanowires; (b) oxidized in air at 850 °C for 3h; (c) deoxidized at 750 °C for 1 h [162].

Annealing in an oxygen rich atmosphere or reducing the atmosphere is an easy way to change the concentration of surface oxygen vacancies. Wu *et al.* found that oxidization and deoxidization of In_2O_3 by annealing the samples in air or in a vacuum leads to the creation of energy levels due to the formation of oxygen vacancies [162].

The shallow oxygen vacancy states have been observed experimentally by many groups [163-165]. The energy levels within the band gap induced by the oxygen vacancies can be divided into two broad categories: near-band-edge (NBE) states and deep-level (DL) states [166]. The DL states are ~ 0.6 eV below the conduction band edge [167] and are reported to be 1.33eV below the conduction band edge [168]. Hauser *et al.* reported an oxygen vacancy transition at 0.3 eV below the conduction band edge [169]. The NBE states are just below the conduction band edge. Cao *et al.* reported that In_2O_3 nanowires formed NBE states at 0.01eV below the conduction band edge [166]. Cao *et al.* found that the annealing process in air at a high temperature (~ 600 °C for un-doped In_2O_3) decreases the impurities and structure defects, such as oxygen vacancies. This leads to a high NBE emissions-to-DL-emissions ratio [166]. Magdas *et al.* confirmed that In_2O_3 shows cathodoluminescence spectra (CL) at 1.9, 2.6 eV as shown in Fig.2.20. The CL spectra at 1.9, 2.6 eV attributed to DL oxygen deficiency states and the CL spectra at 3.1 eV attributed to NBE oxygen deficiency states. After the annealing of samples in high vacuum conditions, the high NBE emissions-to-DL-emissions ratio increases [170]. For doped In_2O_3 , the energy levels within the induced band gap may not be related to the oxygen vacancies. G.W. Pabst *et al.* reported trap ionization energy of 0.65–0.8 eV, which corresponds to the ionization of Fe^{2+} ions [171].

Removed by the author for copyright reasons

Figure 2.20: a) Cathodoluminescence (CL) spectrum of untreated In_2O_3 powder. b) CL spectrum after annealing at 600 °C for 5 h. c) CL spectrum after annealing at 600 °C for 10 h. b) and c) annealed in high vacuum conditions [170].

In this thesis, some of the Fe and Co doped In_2O_3 showed DL states found to be related to the Fe_3O_4 and Co nanoparticles, which was confirmed by the XAFS measurements. In fact, there are two methods to confirm the origin of the NBE states and DL states. The first method is to use the XAFS measurement to check if there are any nanoparticles. The second method is to anneal the samples in air. If the DL states decrease with annealing, that implies that the DL states observed are due to the oxygen vacancies. However, if the DL states increase, that implies that nanoparticles of the doped material are formed and contribute to the physical properties detected.

2.18 References

1. M. Fox, *Optical properties of solids*. Oxford master series in condensed matter physics 2001, Oxford ; New York: Oxford University Press. xii, 305 p.
2. M. Fox, *Quantum optics : an introduction*. Oxford master series in physics 2006, Oxford ; New York: Oxford University Press. xvii, 378 p.
3. B. D. Cullity, and C. D. Graham, *Introduction to magnetic materials*. 2nd ed 2009, Hoboken, N.J.: IEEE/Wiley. xvii, 544 p.
4. K. H. J. Buschow, and F. R. D. Boer, *Physics of magnetism and magnetic materials* 2003, New York: Kluwer Academic/Plenum Publishers. vii, 182 p.
5. Y. B. Xu, and S.M. Thompson, *Spintronic materials and technology*. Series in materials science and engineering 2007, New York: Taylor & Francis. 423 p.
6. V. Antonov, B. Harmon and A. Yaresko, *Electronic structure and magneto-optical properties of solids* 2004, Dordrecht ; Boston: Kluwer Academic Publishers. xiii, 528 p.
7. N. A. Spaldin, *Magnetic materials : fundamentals and device applications* 2003, Cambridge, Uk ; New York: Cambridge University Press. ix, 213 p.
8. Y. Liu, D. Shind and D. J. Sellmyer, *Handbook of advanced magnetic materials* 2006, New York, Beijing: Springer ; Tsinghua University Press.
9. C. Kittel, *Introduction to solid state physics*. 7th ed 1996, New York: Wiley. xi, 673 p.
10. S. A. Wolf, D. D. Awschalom, R. A. Buhrman, J. M. Daughton, S. V. Molnar, M. L. Roukes, A. Y. Chtchelkanova and D. M. Treger, *Science* **294**, 1488-1495 (2001).
11. S. J. Pearton, Y. D. Park, C.R. Abernathy, M. E. Overberg, G. T. Thaler, J. Kim, F. Ren, J. M. Zavada and R. G. Wilson, *Thin Solid Films* **447-448**, 493-501 (2004).
12. S. J. Pearton, C. R. Abernathy, D. P. Norton, A. F. Hebard, Y. D. Park, L. A. Boatner and J.D. Budai, *Materials Science and Engineering: R: Reports* **40**, 137-168 (2003).
13. A. H. MacDonald, P. Schiffer and N. Samarth, *Nat Mater* **4**, 195-202 (2005).

14. K. Sato, K. Sato, Y. Furukawa and K. Nakajima, *Crystal growth and characterization of magnetic semiconductors*, in *Advances in Crystal Growth Research* 2001, Elsevier Science B.V.: Amsterdam. p. 303-319.
15. T. Kasuya, and A. Yanase, *Reviews of Modern Physics* **40**, 684 (1968).
16. H. Ohno, *Science* **281**, 951-956 (1998).
17. J. K. Furdyna, *J. Appl. Phys.* **64**, R29-R64 (1988).
18. T. Dietl, H. Ohno, F. Matsukura, J. Cibert and D. Ferrand, *Science* **287**, 1019-1022 (2000).
19. K. Sato, and H. Katayama-Yoshida, *Physica E: Low-dimensional Systems and Nanostructures* **10**, 251-255 (2001).
20. U. Ozgur, Y. I. Alivov, C. Liu, A. Teke, M. A. Reshchikov, S. Dogan, V. Avrutin, S. J. Cho and H. Morkoc, *J. Appl. Phys.* **98**, 041301 (2005).
21. D. C. Look, B. Claflin, *physica status solidi (b)* **241**, 624-630 (2004).
22. A. Haury, A. Wasiela, A. Arnoult, J. Cibert, S. Tatarenko, T. Dietl and Y. M. d'Aubigné, *Phys. Rev. Lett.* **79**, 511 (1997).
23. H. Ohno, *J. Magn. Magn. Mater.* **200**, 110-129 (1999).
24. Y. Iye, A. Oiwa, A. Endo, S. Katsumoto, F. Matsukura, A. Shen, H. Ohno and H. Munekata, *Materials Science and Engineering B* **63**, 88-95 (1999).
25. H. Ohno, A. Shen, F. Matsukura, A. Oiwa, A. Endo, S. Katsumoto and Y. Iye, *Appl. Phys. Lett.* **69**, 363-365 (1996).
26. H. Ohno, H. Munekata, S. V. Molnar and L. L. Chang. *New III-V diluted magnetic semiconductors (invited)*. 1991. AIP.
27. H. Munekata, H. Ohno, S. V. Molnar, A. Segmüller, L. L. Chang and L. Esaki, *Phys. Rev. Lett.* **63**, 1849 (1989).
28. F. Matsukura, H. Ohno, A. Shen and Y. Sugawara, *Phys. Rev. B* **57**, R2037 (1998).
29. M. E. Overberg, B. P. Gila, C. R. Abernathy, S. J. Pearton, N. A. Theodoropoulou, K. T. McCarthy, S. B. Arnason and A. F. Hebard, *Appl. Phys. Lett.* **79**, 3128-3130 (2001).
30. X. Chen, M. Na, M. Cheon, S. Wang, H. Luo, B.D. McCombe, X. Liu, Y. Sasaki, T. Wojtowicz, J. K. Furdyna, S. J. Potashnik and P. Schiffer, *Appl. Phys. Lett.* **81**, 511-513 (2002).

31. K. W. Edmonds, S. V. Novikov, M. Sawicki, R. P. Champion, C. R. Staddon, A. D. Giddings, L. X. Zhao, K. Y. Wang, T. Dietl, C. T. Foxon and B. L. Gallagher, *Appl. Phys. Lett.* **86**, 152114 (2005).
32. S. V. Novikov, K. W. Edmonds, A. D. Giddings, K. Y. Wang, C. R. Staddon, R. P. Champion, B. L. Gallagher and C. T. Foxon, *Semicond. Sci. Technol.* L13 (2004).
33. T. S. Cheng, L. C. Jenkins, S. E. Hooper, C. T. Foxon, J. W. Orton and D. E. Lacklison, *Appl. Phys. Lett.* **66**, 1509-1511 (1995).
34. V. A. Chitta, J. A. H. Coaquira, J. R. L. Fernandez, C. A. Duarte, J. R. Leite, D. Schikora, D. J. As, K. Lischka and E. Abramof, *Appl. Phys. Lett.* **85**, 3777-3779 (2004).
35. D. Schikora, M. Hankeln, D. J. As, K. Lischka, T. Litz, A. Waag, T. Buhrow and F. Henneberger, *Phys. Rev. B* **54**, R8381 (1996).
36. J. Philip, A. Punnoose, B. I. Kim, K. M. Reddy, S. Layne, J. O. Holmes, B. Satpati, P. R. LeClair, T. S. Santos and J. S. Moodera, *Nat Mater* **5**, 298-304 (2006).
37. R. P. Panguluri, P. Kharel, C. Sudakar, R. Naik, R. Suryanarayanan, V. M. Naik, A. G. Petukhov, B. Nadgorny and G. Lawes, *Phys. Rev. B* **79**, 165208 (2009).
38. N. H. Hong, J. Sakai, N. T. Huong and V. Brize, *Appl. Phys. Lett.* **87**, 102505-3 (2005).
39. G. Peleckis, X. Wang and S. X. Dou, *Appl. Phys. Lett.* **89**, 022501 (2006).
40. N. H. Hong, J. Sakai, N. T. Huong and V. Brizé, *J. Magn. Magn. Mater.* **302**, 228-231 (2006).
41. G.A. Gehring, H. J. Blythe, F. Qi, D. S. Score, A. Mokhtari, M. Alshammari, M.S. Al Qahtani and A.M. Fox, *Magnetics, IEEE Transactions on* **46**, 1784-1786 (2010).
42. A. Behan, *Characterisation of Doped ZnO Thin Films for Spintronic Applications*, in *Department of Physics and Astronomy 2008*, The University of Sheffield
43. J. Suits, *Magnetics, IEEE Transactions on* **8**, 95-105 (1972).
44. S. Wittekoek, T. J. A. Popma, J. M. Robertson and P. F. Bongers, *Phys. Rev. B* **12**, 2777 (1975).

45. F. Wooten, *Optical properties of solids* 1972, New York,: Academic Press. xii, 260 p.
46. E. D. Palik, *Handbook of optical constants of solids*. Academic Press handbook series 1985, Orlando: Academic Press. xviii, 804 p.
47. J. R. McBride, L. R. Miller and W. H. Weber, *Phys. Rev. B* **49**, 12224 (1994).
48. S. Tajima, H. Ishii, T. Nakahashi, T. Takagi, S. Uchida, M. Seki, S. Suga, Y. Hidaka, M. Suzuki, T. Murakami, K. Oka and H. Unoki, *Journal of the Optical Society of America B: Optical Physics* **6**, 475-482 (1989).
49. A. I. Kozlov, S. G. K., and V. V. Sobolev, *Moldavian Journal of the Physical Sciences* **4**, 5 (2005).
50. F. J. Kahn, P. S. Pershan and J. P. Remeika, *Phys. Rev.* **186**, 891 (1969).
51. W. Beckenbaugh, J. Evers, G. Güntherodt, E. Kaldis and P. Wachter, *J. Phys. Chem. Solids* **36**, 239-248 (1975).
52. S. K. Park, T. Ishikawa and Y. Tokura, *Phys. Rev. B* **58**, 3717 (1998).
53. H. Czichos, T. Saito and L.R. Smith, *Springer handbook of materials measurement methods* 2006, [Germany]: Springer. xxvi, 1208 p.
54. D. Zhang, C. Li, S. Han, X. Liu, T. Tang, W. Jin and C. Zhou, Vol. **82**. 2003: AIP. 112-114.
55. J. Stankiewicz, F. Villuendas and R. Alcala, *Appl. Phys. Lett.* **96**, 192108 (2010).
56. S. J. Pearton, C. R. Abernathy, M. E. Overberg, G. T. Thaler, D. P. Norton, N. Theodoropoulou, A. F. Hebard, Y. D. Park, F. Ren, J. Kim and L. A. Boatner, *J. Appl. Phys.* **93**, 1-13 (2003).
57. C. N. D. Carvalho, G. Lavareda, A. Amaral, O. Conde and A.R. Ramos, *Journal of Non-Crystalline Solids* **352**, 2315-2318 (2006).
58. J. H. Lee, S. Y. Lee and B. O. Park, *Materials Science and Engineering: B* **127**, 267-271 (2006).
59. H. Han, J. W. Mayer and T. L. Alford, *J. Appl. Phys.* **99**, 123711 (2006).
60. H. Han, D. Adams, J. W. Mayer and T. L. Alford, *J. Appl. Phys.* **98**, 083705 (2005).

61. D. Beena, K. J. Lethy, R. Vinodkumar, V. P. M. Pillai, V. Ganesan, D. M. Phase and S. K. Sudheer, *Applied Surface Science* **255**, 8334-8342 (2009).
62. F. X. Jiang, X. H. Xu, J. Zhang, H. S. Wu and G.A. Gehring, *Applied Surface Science* **255**, 3655-3658 (2009).
63. I. Hamberg, C. G. Granqvist, K. F. Berggren, B. E. Sernelius and L. Engström, *Phys. Rev. B* **30**, 3240 (1984).
64. R. L. Weiher, and R. P. Ley, *J. Appl. Phys.* **37**, 299-302 (1966).
65. D. Bérardan, and E. Guilmeau, *J. Phys.: Condensed Matter* **19**, 236224 (2007).
66. H. Kim, A. Pique, J. S. Horwitz, H. Mattoussi, H. Murata, Z. H. Kafafi and D. B. Chrisey, *Appl. Phys. Lett.* **74**, 3444-3446 (1999).
67. H. Kim, C. M. Gilmore, A. Pique, J. S. Horwitz, H. Mattoussi, H. Murata, Z. H. Kafafi and D. B. Chrisey, *J. Appl. Phys.* **86**, 6451-6461 (1999).
68. A. Walsh, J. L. F. Da Silva, S. H. Wei, C. Körber, A. Klein, L. F. J. Piper, A. DeMasi, K. E. Smith, G. Panaccione, P. Torelli, D. J. Payne, A. Bourlange and R. G. Egdell, *Phys. Rev. Lett.* **100**, 167402 (2008).
69. F. Fuchs, and F. Bechstedt, *Phys. Rev. B* **77**, 155107 (2008).
70. P. D. C. King, T. D. Veal, D. J. Payne, A. Bourlange, R. G. Egdell and C. F. McConville, *Phys. Rev. Lett.* **101**, 116808 (2008).
71. P. Erhart, A. Klein, R. G. Egdell and K. Albe, *Phys. Rev. B* **75**, 153205 (2007).
72. N. Novkovski, and A. Tanuševski, *Semicond. Sci. Technol.* **23**, 095012 (2008).
73. M. Marezio, *Acta Crystallographica* **20**, 723-728 (1966).
74. S. Kohiki, M. Sasaki, Y. Murakawa, K. Hori, K. Okada, H. Shimooka, T. Tajiri, H. Deguchi, S. Matsushima, M. Oku, T. Shishido, M. Arai, M. Mitome and Y. Bando, *Thin Solid Films* **505**, 122-125 (2006).
75. J. Chandradass, M. Balasubramanian, S. Kumar, D. S. Bae and K. H. Kim, *Current Appl. Phys.* **10**, 333-336 (2010).
76. F. O. Adurodija, H. Izumi, T. Ishihara, H. Yoshioka, H. Matsui and M. Motoyama, *Appl. Phys. Lett.* **74**, 3059-3061 (1999).

77. E. J. Tarsa, J. H. English and J. S. Speck, *Appl. Phys. Lett.* **62**, 2332-2334 (1993).
78. I. Hamberg, and C. G. Granqvist, *J. Appl. Phys.*, 1986. **60**, R123-R160 DOI: 10.1063/1.337534.
79. T. B. Hur, I. J. Lee, H. L. Park, Y. H. Hwang and H. K. Kim, *Solid State Commun.* **130**, 397-400 (2004).
80. A. N. H. Al-Ajili, and S. C. Bayliss, *Thin Solid Films* **305**, 116-123 (1997).
81. S. Kasiviswanathan, and G. Rangarajan, *J. Appl. Phys.* **75**, 2572-2577 (1994).
82. S. Suh, and D.M. Hoffman, *Journal of the American Chemical Society* **122**, 9396-9404 (2000).
83. C. A. Pan, and T. P. Ma, *Appl. Phys. Lett.* **37**, 163-165 (1980).
84. J. S. Cho, K. H. Yoon and S. K. Koh, *J. Appl. Phys.* **89**, 3223-3228 (2001).
85. E. J. Tarsa, J. H. English and J. S. Speck, *Appl. Phys. Lett.* **62**, 2332-2334 (1993).
86. Z. Qiao, R. Latz and D. Mergel, *Thin Solid Films* **466**, 250-258 (2004).
87. A. El Hichou, A. Kachouane, J. L. Bubendorff, M. Addou, J. Ebothe, M. Troyon and A. Bougrine, *Thin Solid Films* **458**, 263-268 (2004).
88. S. H. Kim, N.M. Park, T. Kim and G. Sung, *Thin Solid Films* **475**, 262-266 (2005).
89. S. M. Rozati, and T. Ganj, *Renewable Energy* **29**, 1671-1676 (2004).
90. S. Kaleemulla, A. S. Reddy, S. Uthanna and P.S. Reddy, *Journal of Alloys and Compounds* **479**, 589-593 (2009).
91. A. S. Ryzhikov, R. B. Vasiliev, M. N. Romyantseva, L. I. Ryabova, G. A. Dosovitsky, A. M. Gilmutdinov, V. F. Kozlovsky and A. M. Gaskov, *Materials Science and Engineering B* **96**, 268-274 (2002).
92. Z. Ovadyahu, B. Ovrin and H.W. Kraner, *Journal of The Electrochemical Society* **130**, 917-921 (1983).
93. T. K. Subramanyam, B. S. Naidu and S. Uthanna, *Appl. Surf. Sci.* **169-170**, 529-534 (2001).
94. S. Choopun, R. D. Vispute, W. Noch, A. Balsamo, R. P. Sharma, T. Venkatesan, A. Iliadis and D. C. Look, *Appl. Phys. Lett.* **75**, 3947-3949 (1999).

95. R. Das, K. Adhikary and S. Ray, *Appl. Surf. Sci.* **253**, 6068-6073 (2007).
96. T. Bielz, H. Lorenz, W. Jochum, R. Kaindl, F. Klauser, B. Klötzer and S. Penner, *J. Phys. Chem. C* **114**, 9022-9029 (2010).
97. R. K. Gupta, K. Ghosh, S. R. Mishra and P. K. Kahol, *Appl. Surf. Sci.* **254**, 4018-4023 (2008).
98. J. M. Dekkers, G. Rijnders and D. H. A. Blank, *Appl. Phys. Lett.* **88**, 151908-3 (2006).
99. N. B. Ukah, R. K. Gupta, P.K. Kahol and K. Ghosh, *Appl. Surf. Sci.* **255**, 9420-9424 (2009).
100. Y. C. Liang, and Y. C. Liang, *Appl. Phys. A: Materials Science & Processing* **97**, 249-255 (2009).
101. T. K. Subramanyam, B. R. Krishna, S. Uthanna, B. S. Naidu and P. J. Reddy, *Vacuum* **48**, 565-569 (1997).
102. H. Kim, J. S. Horwitz, G. P. Kushto, S. B. Qadri, Z. H. Kafafi and D. B. Chrisey, *Appl. Phys. Lett.* **78**, 1050-1052 (2001).
103. R. B. H. Tahar, T. Ban, Y. Ohya, and Y. Takahashi, *J. Appl. Phys.* **83**, 2631 (1998).
104. V. Senthilkumar, and P. Vickraman, *Current Appl. Phys.* **10**, 880-885 (2010).
105. H. R. Fallah, M. Ghasemi, A. Hassanzadeh and H. Steki, *Materials Research Bulletin* **42**, 487-496 (2007).
106. H. Han, J. W. Mayer and T. L. Alford, *J. Appl. Phys.* **100**, 083715 (2006).
107. S. Muranaka, and N. Hayashi, *Journal of Materials Science* **44**, 3315-3318 (2009).
108. C. H. Liang, S. C. Chen, X. Qi, C. S. Chen and C. C. Yang, *Thin Solid Films* **519**, 345-350 (2010).
109. Y. H. Tak, K. B. Kim, H. G. Park, K. H. Lee and J. R. Lee, *Thin Solid Films* **411**, 12-16 (2002).
110. R. K. Gupta, K. Ghosh, R. Patel and P. K. Kahol, *Appl. Surf. Sci.* **255**, 3046-3048 (2008).
111. P. Prathap, N. Revathi, K. T. R. Reddy and R. W. Miles, *Thin Solid Films* **518**, 1271-1274 (2009).
112. N. Al-Dahoudi, and M. A. Aegerter, *Thin Solid Films* **502**, 193-197 (2006).

113. K. Vanheusden, , C. H. Seager, W. L. Warren, D. R. Tallant and J. A. Voigt, *Appl. Phys. Lett.* **68**, 403-405 (1996).
114. P. Prathap, Y. P. V. Subbaiah, M. Devika and K. T. R. Reddy, *Materials Chemistry and Physics* **100**, 375-379 (2006).
115. J. Popovic, B. Grzeta, E. Tkalcec, A. Tonejc, M. Bijelic and C. Goebbert, *Materials Science and Engineering: B* **176**, 93-98 (2011).
116. S. M. Kim, K. H. Seo, J. H. Lee, J. J. Kim, H. Y. Lee and J. S. Lee, *Journal of the European Ceramic Society* **26**, 73-80 (2006).
117. V. Senthilkumar, P. Vickraman, M. Jayachandran and C. Sanjeeviraja, *Vacuum* **84**, 864-869 (2010).
118. S. M. A. Durrani, E. E. Khawaja, J. Shirokoff, M. A. Dams, G. D. Khattak, M. A. Salim and M. S. Hussain, *Solar Energy Materials and Solar Cells* **44**, 37-47 (1996).
119. J. Kanazawa, T. Haranoh and K. Matsumoto, *Vacuum* **41**, 1463-1465 (1990).
120. H. Tomonaga, and T. Morimoto, *Thin Solid Films* **392**, 243-248 (2001).
121. M. J. Alam, and D. C. Cameron, *Thin Solid Films* **377-378**, 455-459 (2000).
122. B. J. Zheng, J. S. Lian, L. Zhao and Q. Jiang, *Vacuum* **85**, 861-865 (2011).
123. G. Frank, H. Köstlin and A. Rabenau, *physica status solidi (a)* **52**, 231-238 (1979).
124. N. H. Hong, J. Sakai, W. Prellier and A. Hassini, *J. Phys.: Condensed Matter* **17**, 1697 (2005).
125. J. M. D. Coey, A. P. Douvalis, C. B. Fitzgerald and M. Venkatesan, *Appl. Phys. Lett.* **84**, 1332-1334 (2004).
126. S. B. Ogale, R. J. Choudhary, J. P. Buban, S. E. Lofland, S. R. Shinde, S. N. Kale, V. N. Kulkarni, J. Higgins, C. Lanci, J. R. Simpson, N. D. Browning, S. D. Sarma, H. D. Drew, R. L. Greene and T. Venkatesan, *Phys. Rev. Lett.* **91**, 077205 (2003).
127. M. Venkatesan, C. B. Fitzgerald, J. G. Lunney and J. M. D. Coey, *Phys. Rev. Lett.* **93**, 177206 (2004).
128. N. H. Hong, J. Sakai, W. Prellier, A. Hassini, A. Ruyter and F. Gervais, *Phys. Rev. B* **70**, 195204 (2004).

129. Z. Wang, J. Tang, L. D. Tung, W. Zhou and L. Spinu, *J. Appl. Phys.* **93**, 7870-7872 (2003).
130. G. Peleckis, X. L. Wang and S. X. Dou, *J. Magn. Magn. Mater.* **301**, 308-311 (2006).
131. P. F. Xing, Y. X. Chen, M. J. Tang, S. S. Yan, G. L. Liu, L. M. Mei and J. Jun, *Chinese Physics Letters* **26**, 117503 (2009).
132. X. Meng, L. Tang and J. Li, *J. Phys. Chem. C* **114**, 17569-17573 (2010).
133. T. Dietl, H. Ohno and F. Matsukura, *Phys. Rev. B* **63**, 195205 (2001).
134. T. Dietl, A. Haury, Y. M. d'Aubign, *Phys. Rev. B* **55**, R3347 (1997).
135. H. Akai, *Phys. Rev. Lett.* **81**, 3002 (1998).
136. P. G. D. Gennes, *Phys. Rev.* **118**, 141 (1960).
137. M. V. Schilfgaard, and O. N. Mryasov, *Phys. Rev. B* **63**, 233205 (2001).
138. P. W. Anderson, and H. Hasegawa, *Phys. Rev.* **100**, 675 (1955).
139. J. Y. Kim, J. H. Park, B. G. Park, H.J. Noh, S. J. Oh, J. S. Yang, D. H. Kim, S. D. Bu, T. W. Noh, H. J. Lin, H. H. Hsieh and C. T. Chen, *Phys. Rev. Lett.* **90**, 017401 (2003).
140. J. M. D. Coey, M. Venkatesan and C. B. Fitzgerald, *Nat Mater* **4**, 173-179 (2005).
141. G. Subías, J. Stankiewicz, F. Villuendas, M. P. Lozano and J. García1, *Phys. Rev. B* **79**, 094118 (2009).
142. J. Stankiewicz, F. Villuendas and J. Bartolomé, *Phys. Rev. B* **75**, 235308 (2007).
143. L. M. Huang, C. M. Araújo and R. Ahuja, *EPL (Europhysics Letters)* **87**, 27013 (2009).
144. A. M. H. R. Hakimi, M. G. Blamire, S. M. Heald, M. S. Alshammari, M. S. Alqahtani, D. S. Score, H. J. Blythe, A. M. Fox and G. A. Gehring, *Phys. Rev. B* **84**, 085201 (2011).
145. K. Ando, H. Saito, Z. Jin, T. Fukumura, M. Kawasaki, Y. Matsumoto and H. Koinuma, Vol. **78**. 2001: AIP. 2700-2702.
146. T. Fukumura, Z. Jin, A. Ohtomo, H. Koinuma and M. Kawasaki, Vol. **75**. 1999: AIP. 3366-3368.
147. K. Ando, *Phys. Rev. B* **47**, 9350 (1993).

148. Y. R. Lee, and A. K. Ramdas, *Solid State Commun.* **51**, 861-863 (1984).
149. H. A. Weakliem, Vol. **36**. 1962: AIP. 2117-2140.
150. J. M. Baranowski, J. W. Allen and G. L. Pearson, *Phy. Rev.* **160**, 627 (1967).
151. K. Ando, A. Chiba and H. Tanoue, Vol. 83. 1998: AIP. 6545-6547.
152. Hakimi, A. M. H. R., F. Schoofs, R. Bali, N. A. Stelmashenko, M. G. Blamire, S. Langridge, S. A. Cavill, G. V. D. Laan and S. S. Dhesi, *Phys. Rev. B* **82**, 144429 (2010).
153. K. Ando, and H. Akinaga, *J. Magn. Magn. Mater.* **140-144, Part 3**, 2029-2030 (1995).
154. M. Nawrocki, F. Hamdani, J. P. Lascaray, Z. Golacki and J. Deportes, *Solid State Commun.* **77**, 111-114 (1991).
155. U. Gennser, X. C. Liu, T. Q. Vu, D. Heiman, T. Fries, Y. Shapira, M. Demianiuk and A. Twardowski, *Phys. Rev. B* **51**, 9606 (1995).
156. Z. G. Yu, J. He, S. Xu, Q. Xue, O. M. J. van't Erve, B. T. Jonker, M. A. Marcus, Y. K. Yoo, S. Cheng and X. D. Xiang, *Phys. Rev. B* **74**, 165321 (2006).
157. P. F. Xing, Y. X. Chen, S. S. Yan, G. L. Liu, L. M. Mei, K. Wang, X. D. Han and Z. Zhang, *Appl. Phys. Lett.* **92**, 022513 (2008).
158. Y. K. Yoo, Q. Xue, H. C. Lee, S. Cheng, X. D. Xiang, G. F. Dionne, S. Xu, J. He, Y. S. Chu, S. D. Preite, S. E. Lofland and I. Takeuchi, *Appl. Phys. Lett.* **86**, 042506 (2005).
159. G. Peleckis, X. L. Wang and S. X. Dou, *Appl. Phys. Lett.* **88**, 132507-3 (2006).
160. S. J. Hu, S. S. Yan, X. I. Lin, X. X. Yao, Y. X. Chen, G. I. Liu and L. M. Mei, *Appl. Phys. Lett.* **91**, 262514-3 (2007).
161. C. P. Chu, T. S. Ko, Y. C. Chang, T. C. Lu, H. C. Kuo and S. C. Wang, *Materials Science and Engineering: B* **147**, 276-279 (2008).
162. W. Ping, Q. Li, X. Zou, W. Cheng, D. Zhang, C. Zhao, L. Chi and T. Xiaoand, *J. of Physics: Conference Series* **188**, 012054 (2009).
163. C. Wang, M. Takahashi, H. Fujino, X. Zhao, E. Kume, T. Horiuchi and S. Sakai, *J. Appl. Phys.* **99**, 054104 (2006).

164. H. Yang, M. Jain, N. A. Suvorova, H. Zhou, H. M. Luo, D. M. Feldmann, P. C. Dowden, R. F. DePaula, S. R. Foltyn and Q. X. Jia, *Appl. Phys. Lett.* **91**, 072911 (2007).
165. H. W. Jang, S. H. Baek, D. Ortiz, C. M. Folkman, C. B. Eom, Y. H. Chu, P. Shafer, R. Ramesh, V. Vaithyanathan and D. G. Schlom, *Appl. Phys. Lett.* **92**, 062910 (2008).
166. H. Cao, X. Qiu, Y. Liang, Q. Zhu and M. Zhao, *Appl. Phys. Lett.* **83**, 761-763 (2003).
167. S. J. Clark, and J. Robertson, *Appl. Phys. Lett.* 2009. **94**, 022902.
168. Z. Zhang, P. Wu, L. Chen and J. Wang, *Appl. Phys. Lett.* **96**, 232906 (2010).
169. A. J. Hauser, J. Zhang, L. Mier, R. A. Ricciardo, P. M. Woodward, T. L. Gustafson, L. J. Brillson and F. Y. Yang, *Appl. Phys. Lett.* **92**, 222901-3 (2008).
170. D. A. Magdas, A. Cremades and J. Piqueras, *Appl. Phys. Lett.* **88**, 113107 (2006).
171. G. W. Pabst, L. W. Martin, Y. H. Chu and R. Ramesh, *Appl. Phys. Lett.* **90**, 072902 (2007).
172. A. Y. Polyakov, A. V. Govorkov, N. B. Smirnov, N. Y. Pashkova, G. T. Thaler, M. E. Overberg, R. Frazier, C. R. Abernathy, S. J. Pearton, J. Kim and F. Ren, *J. Appl. Phys.* **92**, 4989-4993 (2002).
173. R. Y. Korotkov, J. M. Gregie and B. W. Wessels, *Appl. Phys. Lett.* **80**, 1731-1733 (2002).
174. P. G. Baranov, I. V. Ilyin, E. N. Mokhov and A. D. Roenkov, *Semicond. Sci. Technol.* **11**, 1843 (1996).
175. M. A. Khan, D. T. Olson, J. N. Kuznia, W. E. Carlos and J. A. Freitas, *J. Appl. Phys.* **74**, 5901-5903 (1993).
176. J. Baur, K. Maier, M. Kunzer, U. Kaufmann and J. Schneider, *Appl. Phys. Lett.* **65**, 2211-2213 (1994).
177. J. Baur, K. Maier, M. Kunzer, U. Kaufmann, J. Schneider, H. Amano, I. Akasaki, T. Detchprohm and K. Hiramatsu, *Appl. Phys. Lett.* **64**, 857-859 (1994).
178. E. Burstein, *Phys. Rev.* **93**, 632 (1954).

Chapter 3 – Experimental Setup and Techniques

3.1 Introduction

This chapter explores the experimental techniques employed in this work and the procedures followed to analyze the presented data. The samples used in this thesis were grown by our group here in the University of Sheffield or obtained through the collaboration of our group with many groups in same field. These groups are Xiao-Hong Xu's group from Shanxi Normal University, China; A. M. H. R. Hakimi from the University of Cambridge; KACST group from Saudi Arabia; and Ya. Mukovskii's group from the National University of Science and Technology "MISiS", Russia. The source of the samples will be mentioned in every section throughout this thesis. My main duty in our group was to investigate the optical and magneto-optics properties of the samples that we grew or obtained. The first section of this chapter deals with the magneto-optics spectroscopy technique. It covers the fundamentals and the operational principle of the magneto-optical spectroscopy. Also, it explains the procedures used to measure the magneto-optics properties of the samples. The second section deals with the absorption spectroscopy technique and gives an overview of the absorption spectroscopy. Also, it explains the procedures used to measure the optical properties of the samples, such as the transmission, reflection, and absorption. It explains how these data were used to determine the band gap energy of the sample. The third section describes the growth techniques used to fabricate the samples and the last section describes the procedures used to determine the film thickness and the refractive index of the samples.

3.2 Magneto-Optics Setup and the Principles of the Technique

Katsuaki Sato [1] developed the measurements of magneto-optical spectra by using a Piezo-Birefringent Modulator. This approach is considered one of the most advanced magneto-optical techniques and is widely used [2-16]. Sato's technique allows the simultaneous determination of magnetic circular dichroism (MCD) and

rotation, and provides a sensitivity of 0.002° for Kerr rotation at a wavelength of 500 nm with 12 nm resolution.

Magneto-optical effects were measured using the Piezo-Birefringent Modulator method cover a wavelength region from 300 to 2500 nm. This gives magneto-optical spectra, and magneto-optical hysteresis loops at different wavelengths. Measurements were taken for ellipticity, which is also known as the Faraday ellipticity η_F or the Kerr ellipticity η_k , and for rotation, which is also known as the Faraday rotation θ_F or the Kerr rotation θ_k . This classification is based on the setup geometry used during the measurement. If the sample is high absorbing and not transmitting light, Kerr geometry is the most appropriate geometry to use whereas if the sample is transparent, the Faraday is the most appropriate geometry to be used, as in this case. The setup can be altered between Kerr and Faraday geometries by detecting the reflected light instead of the transmitted light, as shown in Fig.3.1.

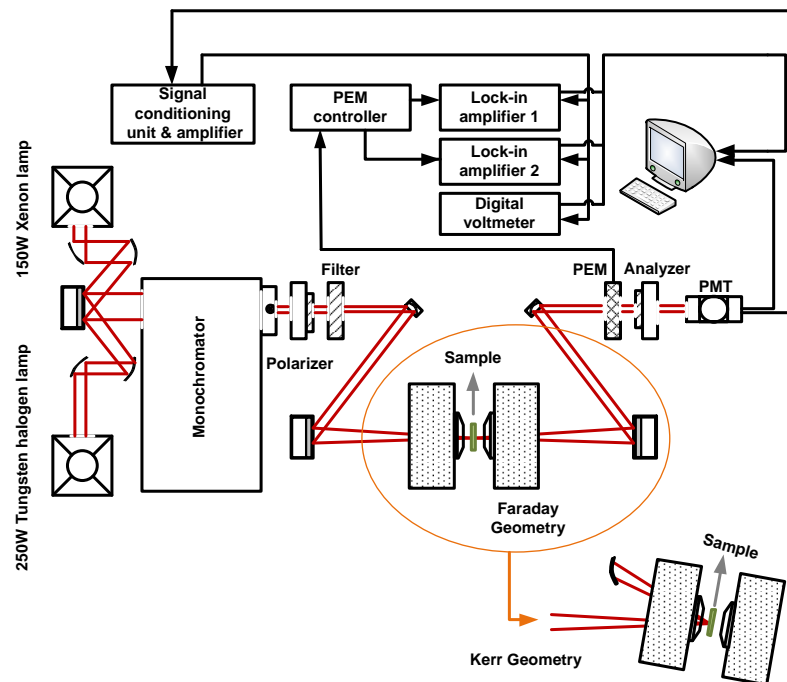


Figure 3.1: An illustration of the system used to measure the magneto-optical properties of the samples discussed in this thesis.

Two high power lamps were used to cover a wide range of spectra. A Xenon lamp with a power of 150 Watt was used to cover a spectral range between 1.5 and

4.5 eV, and a tungsten lamp with a power of 250 Watt was used to cover a spectral range between 0.6 and 3.8 eV [17]. The light produced from the lamp was passed through a Spectro-275 spectrometer to produce monochromatic light with the required wavelength by choice of the right grating. Then, the light was filtered using a bandpass filter to remove unwanted wavelengths that may have distorted the desired wavelength of the light. The passed light was polarised using a Glan-Taylor UV prism polarizer and focused onto the sample using manoeuvre mirrors and lenses to achieve the optimal alignment for the light beam and reduce the prospect of light scattering.

The sample was mounted on a sample holder with an aperture to allow the light to pass through it. The sample was vertically placed between electromagnet poles, as shown in Fig.1, under the influence of an applied magnetic field of 1.8 Tesla at room temperature or of 0.5 Tesla when the cryostat was used for low-temperature measurements. The low temperature measurements between 4K and 400K were achieved using liquid helium and the cryostat was evacuated to reduce the possibility of thermal contact between the sample and the cryostat surface. When the light is either reflected from or transmitted through the sample, it passes through a photoelastic modulator (PEM). The PEM produces a signal in proportion to the ellipticity and rotation of the light. In the PEM, a birefringent crystal is mounted on a piezo-vibrator with frequency, f . The vibration of the birefringent crystal causes advancement and retardation of the transversing light phase parallel to the vibration direction. Setting the modulation of the retardation at a quarter of the light wavelength and setting the vibration direction of the birefringent crystal at 45° to the polarizer means the emerging light alternates between RCP or LCP light with a frequency f . After the PEM, the light passes through an analyzer towards a photomultiplier tube detector. The photomultiplier tube detector converts the light intensity into an electrical signal and sends it to a signal conditioning unit to amplify the signal and split it into the AC and DC components. The AC component is sent to two Signal Recovery lock-in amplifiers to record it. In this study, a Keithley voltmeter was used to read and display the DC voltage component, which can be controlled by the PMT gain. The voltmeter and lock-in amplifiers (one and two) were used to measure $I_1(0)$, $I_2(f)$ and $I_3(2f)$ intensities respectively. $I_2(f)$ and $I_3(2f)$ Intensities remain equal when the sample shows no magneto-optics effect. However, when a magneto-

optics effect exists, the two intensities will differ. $I_1(0)$, $I_2(f)$ and $I_3(2f)$ intensities were calculated with the following equations [1].

$$I_1(0) = I_0 T [1 + J_0(\delta_0) \sin(\Delta\theta + 2\phi)] \quad \text{Equation(3.1)}$$

$$I_2(f) = I_0 \Delta T J_1(\delta_0) \quad \text{Equation(3.2)}$$

$$I_3(2f) = 2I_0 T J_2(\delta_0) \sin(\Delta\theta + 2\phi) \quad \text{Equation(3.3)}$$

$$\Delta T = (t_+^2 - t_-^2) \quad \text{Equation(3.4)}$$

$$T = \frac{1}{2}(t_+^2 + t_-^2) \quad \text{Equation(3.5)}$$

where δ_0 denotes the amplitude of the retardation; J_0 , J_1 and J_2 terms are the Bessel functions used to determine the optimal PEM retardation; t_{\pm} are the Fresnel coefficients that represent RCP and LCP light; I_0 is the intensity constant; ϕ is the analyzer angle; and $\Delta\theta$ is the difference in LCP and RCP rotation.

**Removed
by the author
for copyright reasons**

Figure 3.2: Bessel functions J_0 , J_1 and J_2 . The optimum value for all measurements (ellipticity and rotation) is at $\delta_0 = 0.3832$ (indicated as red vertical line)[18].

The ideal PEM retardation value is 0.383, as shown in Fig.3.2. At this value, J_0 is zero, which indicates insensitivity to changes in light intensity, while J_1 and J_2 are near their maximum values, which indicates a maximum magneto-optics sensitivity.

The values of Faraday ellipticity η_F and Faraday rotation θ_F can be inferred from the measurement of $I_1(0)$, $I_2(f)$ and $I_3(2f)$ intensities, as shown by Sato's formulae [18]:

$$\theta_F = -\frac{1}{2}\Delta\theta \quad \text{Equation(3.6)}$$

$$\eta_F = \frac{1}{4}\left(\frac{\Delta T}{T}\right) \quad \text{Equation(3.7)}$$

The ratios of (I_2/I_1) and (I_3/I_1) related to the ellipticity and rotation were calculated using the following equations[18]:

$$\frac{I_2(f)}{I_1(0)} = A \frac{J_1(\delta_0) \Delta T/T}{1+J_0(\delta_0)\text{Sin}(\Delta\theta+2\phi)} = AJ_1(\delta_0) \Delta T/T \approx \eta_F \quad \text{Equation(3.8)}$$

$$\frac{I_3(2f)}{I_1(0)} = B \frac{2J_2(\delta_0) \text{Sin}(\Delta\theta+2\phi)}{1+J_0(\delta_0)\text{Sin}(\Delta\theta+2\phi)} = 2BJ_2(\delta_0) \Delta\theta \approx \theta_F \quad \text{Equation(3.9)}$$

The values of ellipticity and rotation obtained by Sato's formulas were in arbitrary units. In order to convert them into real units, the ellipticity and rotation were calibrated by rotating the analyzer over a few degrees, and measuring the resulting change in $I_3(2f)/I_1(0)$. Then the calibration factor C was determined and used to calculate the ellipticity and rotation in real units (degree) using the following equations [18]:

$$\eta_F = -1.20 C \frac{I_2(f)}{I_1(0)} \quad \text{Equation(3.10)}$$

$$\theta_F = C \frac{I_3(2f)}{I_1(0)} \quad \text{Equation(3.11)}$$

This process can be repeated using an automated computer system to reduce measurements errors.

3.3 Absorption Spectroscopy and the Principles of the Technique

Absorption spectroscopy is one of the most versatile and widely used techniques to investigate the electronic structures of materials. It introduces the transmission and reflection spectra of the samples, which provide rich information about the electronic structures of these samples. The transmission or reflection coefficient describes either the intensity or the amplitude of transmitted or reflected light relative to an incident light. The measurement can be taken at room temperature or low temperature using liquid helium down to 5K and covers the Infra-Red, visible and Ultra-Violet portions of the electromagnetic spectrum, precisely from 1.7 eV to 4.5 eV or 275nm to 730nm. The setup can be changed between transmission and

reflection measurement geometry by detecting the reflected light rather than the transmitted light, as shown in Fig.3.3.

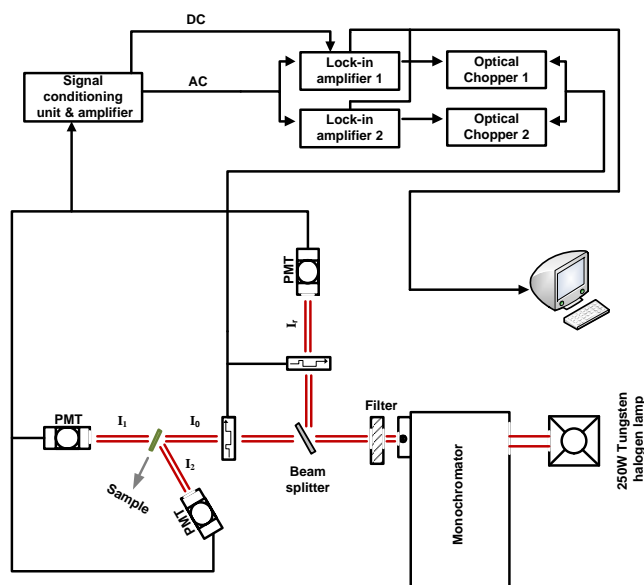


Figure 3.3: An illustration of the absorption spectroscopy system used to measure the optical properties of the samples discussed in this thesis.

A tungsten lamp with a power of 250 Watts was used to cover the desired range of spectra. The light produced passes through a Spectro-275 spectrometer to produce monochromatic light at the required wavelength. The monochromatic light is filtered using a bandpass filter and splits in two beams of light with intensities of 50-50 using a beam splitter device. One of these beams, called the reference beam, passes through an optical chopper with a frequency of 370 MHz before it is detected by a reference photomultiplier tube detector (PMT). The photomultiplier tube (PMT) detector converts the light intensity to an electrical signal before it is sent to the signal conditioning unit. The other beam passes through another optical chopper with a frequency of 310 MHz. Then, it is transmitted through or reflected from the sample based on the running measurement. The transmitted or reflected light is detected by another photomultiplier tube detector. The PMT also sends the electrical signal to the signal conditioning unit. The signal conditioning unit amplifies the signal and then splits it into the AC and DC components. In this study, two Signal Recovery lock-in amplifiers were used to record the AC measurements for the reference beam and the transmitted or reflected light beam. Mirrors and lenses were used to focus the light

beam onto the sample and detectors, and to reduce the possibility of light scattering. Lock-in amplifiers (one and two) were used to measure I_0, I_1, I_2 and I_r intensities for incident, transmitted, reflected and reference light respectively. Transmission and reflection coefficients can be calculated using the following the equations.

$$T = \frac{I_1}{I_0} \quad , \quad R = \frac{I_2}{I_0} \quad \text{Equation(3.12)}$$

The absorption coefficient can be calculated after determining the thickness of sample l , using the Moss relationship [19, 20].

$$T = (1 - R_1)e^{-\alpha l}(1 - R_2) \quad \text{Equation(3.13)}$$

With an assumption that there is no reflection from the back surface ($R_2 = 0$), the absorption coefficient can be calculated using the following equation [21, 22]

$$\alpha = \frac{1}{l} \ln\left(\frac{1-R}{T}\right) \quad \text{Equation(3.14)}$$

If reflection from the back surface is included ($R_2 = R_1 = R$), then the absorption coefficient can be calculated using the following equation [21-24].

$$\alpha = \frac{1}{l} \ln\left(\frac{(1-R)^2}{T}\right) \quad \text{Equation(3.15)}$$

If the cryostat is used at low-temperature measurements, a combination of multiple internal reflections occurs. These reflections come from the substrate, the film, and the cryostat windows. Therefore, using the earlier methods would not lead to an accurate result. Consequently, only the transmittance data were used to obtain the absorption coefficient using the Swanepoel method [25], and the reflection measurement was not required.

Determining the absorption coefficient α led to the estimation of the absorption index through the relation [26, 27].

$$\kappa = \frac{\lambda\alpha}{4\pi} \quad \text{Equation(3.16)}$$

and the optical band gap E_g by plotting αhv vs hv from the formula

$$\alpha hv = A(hv - E_g)^{\frac{1}{2}} \quad \text{Equation(3.17)}$$

where A is a constant, hv is the photon energy and E_g is the optical band gap energy.

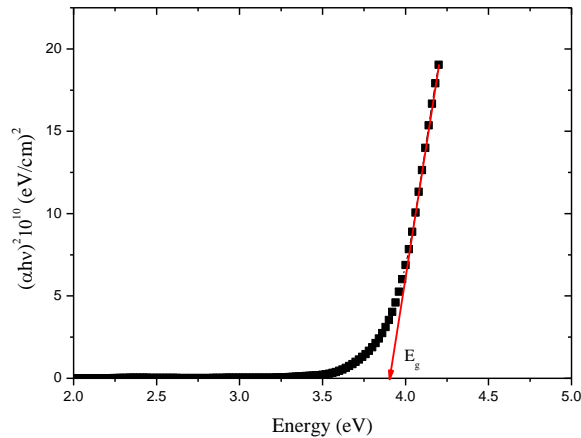


Figure 3.4: Tauc plot method used to estimate the optical band gap energy E_g of semiconductors.

The intersection on the $h\nu$ axis from the plot of α^2 versus $h\nu$ in the linear region in Fig.3.4 gives the optical band gap energy E_g [20]. This method is known as the Tauc plot [28] and has been used successfully by others [29-33].

3.4 Developments of Magneto-Optics and Absorption Systems

The magneto-optics and the absorption systems were put together by Dr Neal of the University of Sheffield, with Prof. Kucera of Charles University [17]. Both systems have been improved over the years by Anthony Behan and David Score. Their steps were followed in order to add further enhancements to these systems.

The Magneto-optics system and the absorption system are greatly improved when more optical pieces are supplemented to both systems in order to improve the resolution and accuracy of the measurements and to handle low temperature measurement. Instead of filters being changed manually during the measurement, filters were automated and integrated within the setup software. Filters drivers were programmed from scratch using the C++ command and Microsoft.Net framework and fitted within the LabView program. The LabView program was used to manage both systems, control the measurements, and acquire data. The Magneto-optic system LabView program was upgraded. Consequently, most of the equipment's old LabView drivers failed to perform with the new version of the software. Therefore, the equipment's LabView drivers were reprogrammed to be compatible with the new

version. Both the Magneto-optics LabVIEW programs in the field and at remanence were reprogrammed and combined in one LabVIEW Magneto-optics program. Fig.3.5 show the transmittance data measured using the absorption system before and after the improvement for the same sample.

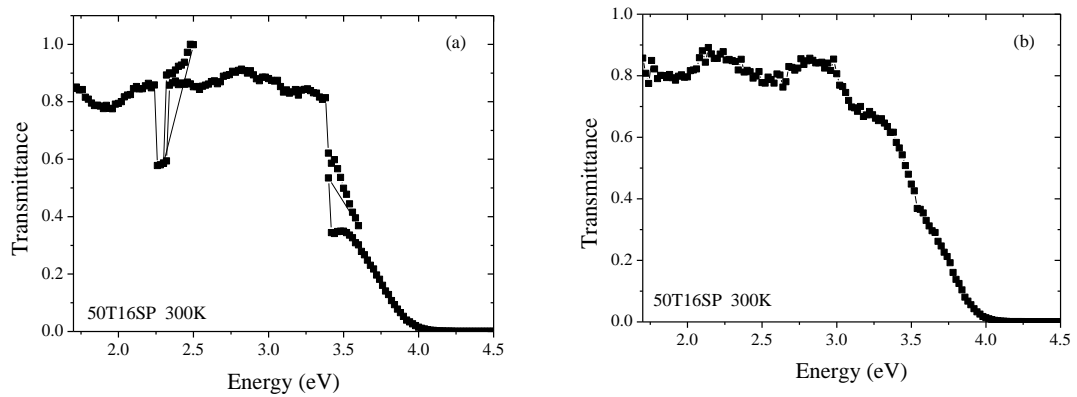


Figure 3.5: Transmittance a) before, and after b) improvement.

Changing the filter position manually created cut off points around 2.2 eV and 3.4 eV, as shown in Fig.5. After improvement, Fig.6 shows no cut off points and the interference oscillation between the film and the substrate appears. This oscillation could not be seen clearly before the improvement.

3.5 Systems Automation Method

There are several steps must be followed to acquire data using an instrument:

1. Install Software and Drivers.
2. Connect, Set Up, and configure Hardware.
3. Learn LabVIEW Basics.
4. Begin Your Application.

3.5.1 Install Software and Drivers

The first step to acquire data is to choose the right hardware platforms, and then install the proper software and drivers for your application. There are several

platforms provided by National Instruments Corporation such as Data Acquisition, CompactRIO, and Instrument Control. Data Acquisition platform is including LabVIEW software and DAQmx driver, which support all USB, CompactDAQ, PCI/PCI Express, PXI/PXI Express, Ethernet, and wireless data acquisition (DAQ) devices. CompactRIO platform is including LabVIEW software, Real-Time, and FPGA Modules, and RIO driver to program a CompactRIO programmable automation controller (PAC). Instrument Control platform is including LabVIEW software, NI-VISA, and NI-488.2 software to enable communication with any instrument via USB, GPIB, Ethernet/LAN, or Serial bus. The Instrument Control platform is the option that we used to automated our systems. LabVIEW software, NI-VISA software, and NI-488.2 software can be bought from National Instruments Corporation. After installing LabVIEW software on the lab computer, NI-VISA software needs to be installed to facilitate communication with the instrument. Then NI-488.2 needs to be installed also to be able to use NI GPIB device in your application and help Windows to detect any installation of any new NI GPIB hardware devices. The software package from National Instruments comes with NI Device Drivers DVD which includes a complete steps guide to install NI-488.2 and NI-VISA. When the software and drivers installed, the next step is to physically connect and setup the instruments hardware.

3.5.2 Connect and Set Up Hardware

Based on the platform used, there is a different method to connect and to setup the hardware and there is a user manual for each case can be downloaded from “www.ni.com” which explains every step in details. We have used the Instrument Control platform, therefore, the instrument have to support GPIB or USB or serial to be able to use GPIB or USB or serial connection method. Every instrument has a user manual which includes everything about the instrument. The instrument user manual contains the connection method that the instrument support and the commands used to communicate with the instrument. There are many connection methods that instruments support to be automated, such as GPIB, USB, Ethernet/LAN, and Serial. Also, there are many connection methods can be used to connect the instrument to the computer such as, GPIB-USB Controllers, PCI/PCI Express GPIB Controllers, GPIB-

ENET/100, PXI-GPIB and PXI-8232 Controllers, ExpressCard-GPIB Controllers, PCMCIA-GPIB Controllers, AT-GPIB/TNT (PnP) Controllers, PMC-GPIB Controllers, direct connection via GPIB, direct connection via USB, direct connection via Ethernet/LAN, direct connection via Serial. Every connection method has different instructions to properly install and configure the instrument.

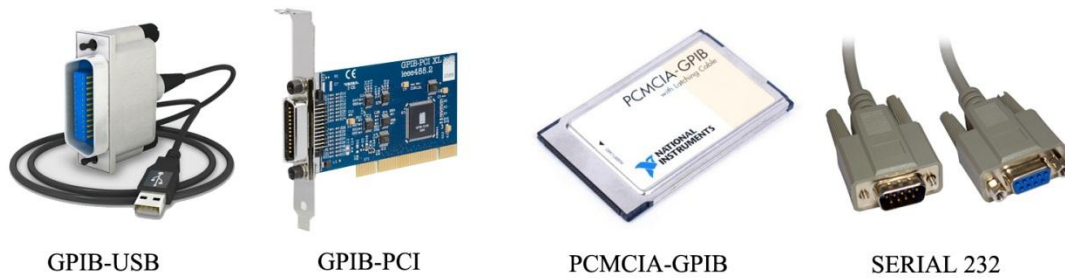


Figure 3.6: Different types of connection methods used to connect the instrument to the computer.

In magneto-optical and absorptions systems, the GPIB and Serial 232 methods used to connect the instruments to the computer. After switching the instrument on and connect it to the computer, there is an utility installed with the NI-488 driver called The Measurement and Automation (MAX). MAX provides tools to search for connected instruments, and send and receive communication with the instrument. MAX can be opened from the computer by going to Start >> Programs >> National Instruments >> Measurement & Automation. Then, by clicking on “Scan For Instruments” and then, expanding the “Devices and Interfaces” subdirectory below “My System”, the name and address of the GPIB controller will appear in main window if it is connected properly. In case of Serial connections, expanding “Serial & Parallel” will show all the computer serial ports (COM1, COM2, ...etc). MAX will establish a VISA communication with the GPIB or Serial port instrument. The communication with the instrument can be initialized by clicking on “Communicate with Instrument” or “Open VISA Test Panel” and both will open VISA Interactive Control panel. The VISA Interactive Control utility used to communicate (read, write, serial poll, etc.) with the instruments. When communicate with an instruments, each instrument has an identification (ID) string. The instrument can be queried for its identification by sending it “*IDN?”. Usually, the Instrument will respond with the manufacturer’s name, model name, and various alphanumeric characters that the

manufacturer uses to track firmware revision. At this point, transition from interactive mode to programming mode using LabVIEW software is necessary.

Laboratory Virtual Instrumentation Engineering Workbench (LabVIEW) is a system design platform and development environment for a visual programming language to create and deploy measurement and control systems. LabVIEW works on a variety of platforms including Microsoft Windows, Linux, UNIX, and Mac OS X. A quick introduction about basic concepts of LabVIEW is essential to program software to control, communicate and run the instruments using their commands.

3.6 Growth of In₂O₃ Thin Films

This section has been added to clarify the conditions associated with the growth process, because most of the following chapters investigate the influence of these growth conditions on the optical and magneto-optical properties of our doped and un-doped In₂O₃ samples. I worked very closely with KACST engineers during the installation of their new PLD system. All the growth conditions, such as oxygen partial pressure, laser power, target and substrate separation, substrate temperature, etc. were investigated in order to run the system correctly; the addition of this section does not mean that I was involved in any of the growth processes. In fact, there is a lack of structural data for our samples; therefore, we are facing difficulties in comparing different samples sets.

The first step in producing a thin film is to make a target. The target consisted of mixed amounts of In₂O₃ and the desired dopant. The target was prepared by a widely used standard ceramic technique [34], where the powder component's mass is calculated and weighed then mixed and ground using a pestle. The mixture is sintered at the preferred temperature for some time to form the right oxide syntheses. The process of grinding the composition and sintering it is usually repeated several times in order to eliminate any impurity phases and un-reacted components and to deliver a high quality thin film. Then, the composition is compressed in vacuum by a high-pressure press to 25000 kPa on a copper disc. As a result, a high-density target is formed with a 25 mm diameter and 5 mm thickness. This method helps to reduce the problem of particulate contamination of laser-deposited films [35]. The target is

sintered again to increase the quality and reduce the strain. Reducing the strain is necessary to avoid any cracks that may occur before or during the usage of the target in the laser ablation chamber.

The next step is the film growth technique. Several deposition techniques are used to develop high quality thin films and multilayers. These techniques include a direct current (DC) reactive magnetron sputtering [36, 37], chemical vapour deposition [38], reactive thermal evaporation [39], molecular beam epitaxy [40, 41], ion beam sputtering [42], and pulsed laser deposition (PLD) [43-45].

Pulsed laser deposition was thought to be the best technique to produce magnetic oxide thin films because of the simplicity, the low cost, the direct production method and the flexibility in producing films in different ambient gases and pressures. Also, it is possible to produce multilayer films by moving different targets in and out of the beam's focal point. The main disadvantage with PLD is the “splashing” which can lead to defects on the substrate [46]. Another disadvantage is the roughening of the target [47]. Many solutions to these problems have been suggested, including using velocity filters [48], rotating the target or the substrate or rotating both the target and the substrate [49, 50] or polishing the surface of the target before starting the deposition.



Figure 3.7: Picture of the PLD system used to prepare some of the thin films discussed in this thesis.

The PLD system is in the national centre of nanotechnology, KACST.

The PLD system consists of two main parts: the laser and the deposition chamber. The laser is a UV laser with 248 nm wavelength attached directly to the

chamber, as shown in Fig.3.8 with its beam focused directly at the surface of the target. The laser pulse repetition rate is 10Hz with energy of 250 mJ per pulse. The deposition chamber is a stainless-steel high vacuum compartment containing the target and the substrate holders. The substrate holder can be heated to the desired temperature and kept constant during ablation. The target holder can hold up to six targets at the same time and rotate them during the ablation process using an electric motor. This is particularly useful for the multilayer deposition process.

The substrate was cleaned with ethanol, clamped onto the substrate holder, and maintained at the desired temperature during the ablation process. The substrate temperature during the ablation process has a strong influence on the structural, optical and electrical properties of the thin film. Thus, the substrate temperature may vary. A high substrate temperature leads the transition metal ions to form isolated clusters [51, 52].

Before the ablation starts, the deposition chamber is closed and pumped down to the desired pressure. The oxygen pressure can be controlled by evacuating the chamber to a minimum base pressure of 10^{-8} Torr. Then, through a controlled gas-valve, oxygen, nitrogen and helium can be introduced into the chamber.

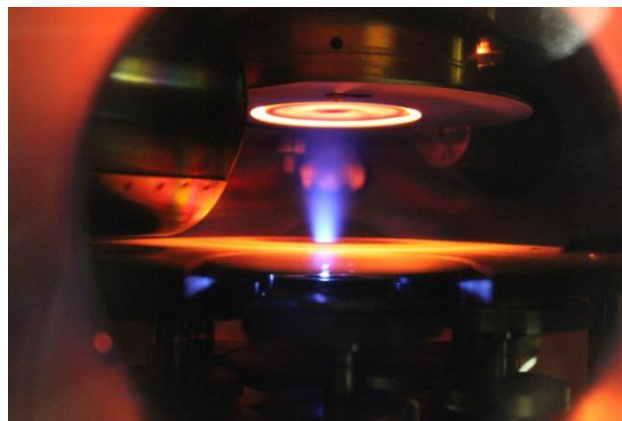


Figure 3.8: The plasma plume during the deposition where the substrate was clamped onto the holder above the target, KACST.

When the target starts to rotate, it is pulsed by the laser beam. The target surface absorbs the beam. Molecules, ions, atoms, and electrons evaporate in the form of a plasma plume and are deposited on the surface of the substrate to achieve the desired thin film.

When the deposition process is finished, the film and substrate are cooled down to room temperature before they are released from the substrate holder. For this study, the produced film was designed with free areas in every corner of the substrate. These areas were used as a reference when measuring the film's thickness using the Dektak surface profiler. Then, the produced thin film named with a dissimilar name in order to distinguish it among the other thin films and its specifications and growth conditions written down and linked to its name as shown in Table. 3.1.

SAMPLE Name	CONTENT	TIME (Min)	d (nm)	T & S sep. (mm)	S.TEMP. (°C)	PRESS. mTorr	LASER.E (mJ)	DEPOSITION METHOD	Annealing for 30 min	SUBSTRATE
489T71SP	In ₂ O ₃ / (5% NiO)	35	156	32	600	2x10 ⁻³	300	PLD	-	Al ₂ O ₃ (0001)
490T71SP		34	153	32	600	2x10 ⁻³			500 C°	
491T71SP		34	141	32	600	2x10 ⁻³			400 C°	
492T71SP		38	158	32	600	2x10 ⁻³			300 C°	

Table 3.1: The method used to order to distinguish between the grown thin films.

Where the name of the samples 489T71SP, includes the sample number (489), the target number (T71) and the substrate type (SP) which is sapphire. Time is pointed to the deposition time, *d* is the thickness in *nm* unit, (T & S sep.) is the target and the substrate separation distance in *mm* unit, (S.TEMP.) is the substrate temperature, (PRESS.) is the pressure inside the chamber during the growth process, (LASER.E) is the laser power used to prepare the thin film, and then, the growth method which is PLD system in the case shown in table 3.1.

3.7 Suitable and Measurement of Thin Film Thickness

We investigated the influence of thickness on the optical and magneto-optical properties of pure In₂O₃ thin films and found that for pure In₂O₃ thin films, the suitable thicknesses are between 400nm to 500nm. For TM-doped In₂O₃ thin films, the suitable thickness is around 200nm. This result was taken into account in all our pure and TM-doped In₂O₃ thin films. However, there are two methods can be used to determine the thickness of thin films. The first method is by fitting the transparent

area of the transmission or reflection spectra. The transparent area is where the absorption coefficient is nearly zero. If the refractive index is known and the transmission or reflection spectrum shows oscillations ($nd > \lambda$), then the thickness of the thin film can be determined. This method is perfect for thin films of pure materials where the refractive index as a function of wavelength is well known. In contrast, in doped materials, the refractive index is affected by doping, especially when the doping amount is higher than 5%. In this case, the first method is not an accurate way to determine the thickness, but it is an accurate method to determine the refractive index itself. The first method will be explained in detail in the next chapter. The second method to measure the thickness is to use the Dektak surface profiler. Most of the samples thicknesses in this study were measured using this method unless otherwise stated.

3.8 Dektak Surface Profiler

The Dektak surface profiler is an instrument used to measure the thickness of thin films by moving the Dektak stylus along the film surface in a vertical direction. The Dektak surface profiler has a video camera to provide a real-time viewing of the scan in progress. The vertical movement of the stylus is recorded and converted to a height and plotted as a function of horizontal distance as the stylus moves along the sample.

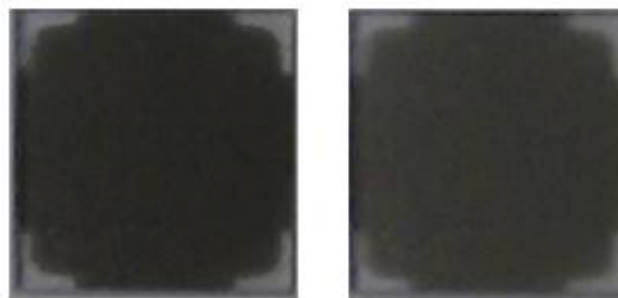


Figure 3.9: LaSrMnO_3 and $(\text{InFe})_2\text{O}_3$ thin films deposited on sapphire substrate, where the free areas in the substrate corners used as a step in Dektak thickness measurement.

Usually, the Dektak stylus is positioned on the middle of the film and directed toward one of the four corners of the substrate where the free part of the film is located. During the movement of the stylus, the stylus steps from the film surface to the substrate surface (Fig.3.9); this step can be measured to obtain the thickness value. In this study, four measurements were recorded, and an average calculated.

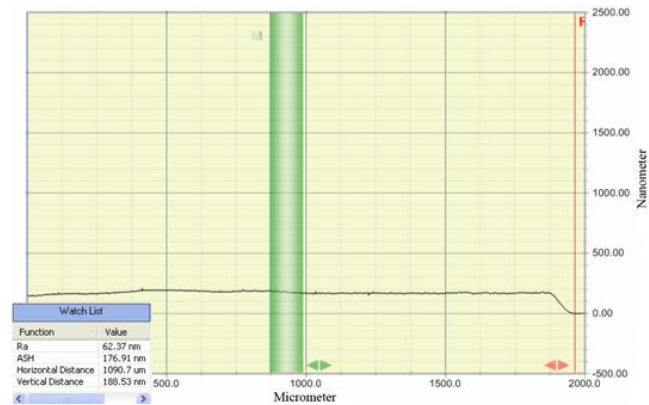


Figure 3.10: Dektak surface profiler data show the red line located on the zero point where the free area of the substrate is. The green line is located on the top of the thin film surface. The thickness is the difference between these two lines; in the table it is 176.91 nm.

Dektak can perform a long scan with a range of up to 200 mm with a maximum of 60,000 data points per scan. This gives a resolution or a horizontal distance between data points of up to 1 angstrom. In order to increase the resolution, more data points need to be taken during a given scan length. Therefore, the shortest scan range provides the best possible horizontal resolution. Also, scan duration and scan speed determine the horizontal resolution of the Dektak. When measuring thick films or very rough or curved samples, use of a low resolution is recommended [53, 54]. Dektak can also be used for measuring the film stress to avoid any deformation, cracking, delamination, and other failures during the production of high quality thin films and devices [55].

3.9 Aluminium Oxide Substrate

Al_2O_3 , or sapphire, has a corundum structure with a lattice constant of 4.758 Å, which is close to the lattice constant of most of the semiconductor materials. This

match in lattice constant between sapphire and the semiconductor materials reduces the strain problem in the early stage of the growth process. Sapphire is transparent in the region of the band gap of all the semiconductor materials (0 to 6eV). Therefore, sapphire has been widely used as a substrate of single or multi layer semiconductor thin films. Almost all our samples were grown on a sapphire substrate. Therefore, the optical and magneto-optical properties of the sapphire substrate will be discussed briefly in this section.

A sapphire substrate looks transparent and colourless to the naked eye. We obtain it as a single side or double side polished. Thus, the transmission between these types differs, and so the index of refraction of each type needed to be calculated separately. Nearly all the sapphire substrates used in this study were double side polished sapphire. The transmission spectra of the sapphire between 1.7eV and 4.5eV are shown in Fig.3.11.

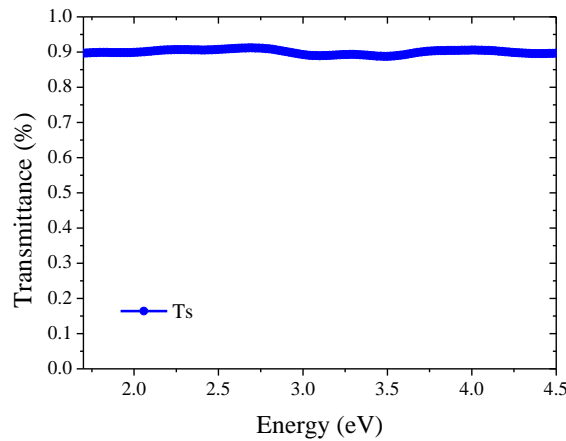


Figure 3.11: The optical transmission spectrum of sapphire as a function of energy measured at RT.

Fig.3.11 illustrates the acquired transmittance spectrum for the sapphire substrate alone. The maximum transmission is limited by the reflection of the incident light from the sapphire's surface. The index of refraction of the sapphire substrate was determined using a method developed by Swanepoel [25] through the interference-free transmission spectra for the sapphire substrate, which is given by

$$T_s = \frac{(1-R)^2}{1-R^2} \quad \text{Equation(3.18)}$$

$$R = \left(\frac{s-1}{s+1}\right)^2 \quad \text{Equation(3.19)}$$

where R denotes the reflection coefficient. Combining Equ.3.17 and Equ.3.18 leads to the maximum transmission for the sapphire substrate.

$$T = \frac{2s}{s^2+1} \quad \text{Equation(3.20)}$$

At $T=0.89$, the refractive index of our sapphire substrate was $s = 1.64$ which was in agreement with same values obtained by General Ruby and Sapphire [56]. Other values of the index of refraction of the sapphire substrate 1.76, and 1.77 have also been reported [57]. Sapphire substrates exhibit ellipticity and rotation. The MCD and the rotation of a blank substrate measured at 300K and in a field of 1.8T is shown in Fig.3.12.

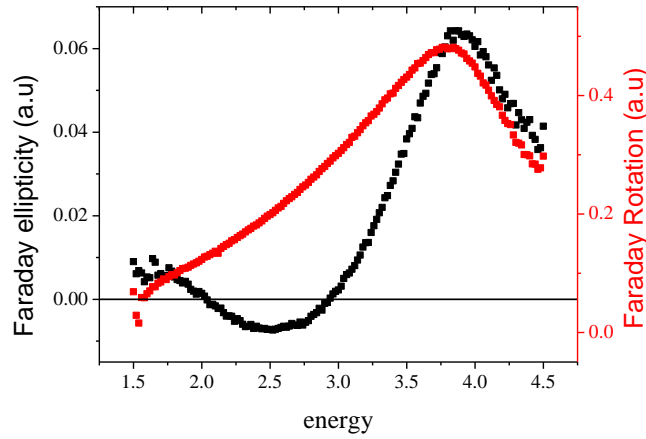


Figure 3.12: The MCD and rotation spectra of a sapphire substrate measured at RT and 1.8Tesla.

The MCD and the rotation of the sapphire substrate are weakly temperature dependent and larger than that of the thin film. Therefore, in order to acquire the MCD and the rotation of a thin film deposited on a sapphire substrate, the substrate's contribution has to be subtracted. Neal *et al.* reported similar MCD data for un-doped ZnO thin film deposited on a sapphire substrate in a shorter range of energy from 1.5 to 3.7eV due to the restriction of the absorption band edge of ZnO. Their MCD data were taken at 0.45 Tesla and were dominated by the contribution of the sapphire substrate [58].

3.10 Swanepoel Method

The thickness, the index of refraction as a function of energy, and the absorption coefficient spectra of a thin film can be determined through the transmission spectrum alone using a method developed by Swanepoel [25]. In this method, the transmission spectrum is divided into three different regions. The first region is the transparent region where the absorption coefficient is $\alpha d \ll 1$. The second region is the weak and medium absorption region where $\alpha d > 1$. The third region is the strong absorption region, where $\alpha d \gg 1$. In the transparent region ($\alpha d \ll 1$), the transmittance is given by Equ.3.21.

$$T = \frac{Ax}{B - Cx \cos \varphi + Dx^2} \quad \text{Equation(3.21)}$$

where

$$A = 16n^2s \quad \text{Equation(3.22)}$$

$$B = (n + 1)^3(n + s^2) \quad \text{Equation(3.23)}$$

$$C = 2(n^2 - 1)(n^2 - s^2) \quad \text{Equation(3.24)}$$

$$D = (n - 1)^3(n - s^2) \quad \text{Equation(3.25)}$$

$$\varphi = 4\pi d/\lambda \quad \text{Equation(3.26)}$$

$$x = \exp(-\alpha d) = 1 - \gamma \quad \text{Equation(3.27)}$$

s and n are the substrate and the film refractive indices respectively; d is thickness of the thin film. The substrate index of refraction s is calculated using the method explained previously in section 3.8.

When there is no absorption or $\varphi = 2n\pi$, the transmittance in Equ.1 is equal to the transmittance from the substrate alone, $T = \frac{2s}{s^2+1}$.

The thickness of the thin film d is measured using the Dektak surface profiler as a primary step and the thin film index of refraction n as a function of wavelength calculated using the Cauchy formula as a primary step too [59, 60].

$$n(\lambda) = A + B/\lambda^2 + C/\lambda^4 \quad \text{Equation(3.28)}$$

where λ is the wavelength of the light used in (μm) unit. A , B and C are the Cauchy's parameters. The values of Cauchy's parameters can be affected easily by the growth conditions, such as the substrate temperature, the oxygen pressure, the

thickness of the film, the strain, etc. Hence, these parameters will have initial values of $A = 1.63632$, $B = 0.0971308$, and $C = -0.0032811$. The values of Cauchy's parameters will be modified during the fitting process so that they are treated as fitting parameters. The value of s and the spectrum of n as a function of energy are obtained from Equ.3.28. The actual spectrum of the index of refraction n and the thickness d can be obtained by fitting the experimentally acquired transmission data using Equ.3.21 within the transparent region of the thin film where $\alpha d \ll 1$ and $x \approx 1$.

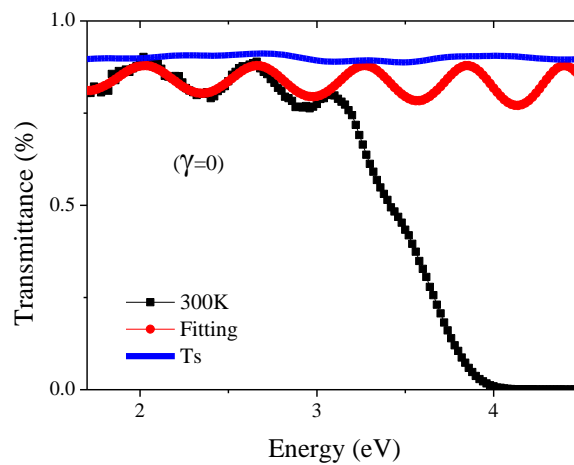


Figure 3.13: The experimental transmission spectrum of pure In_2O_3 fitted within the transparent region (1.7eV-3.0eV), Ts represents the transmission of the sapphire substrate.

The index of refraction n as a function of energy of pure In_2O_3 thin film obtained in this example is shown in Fig. 3.14.

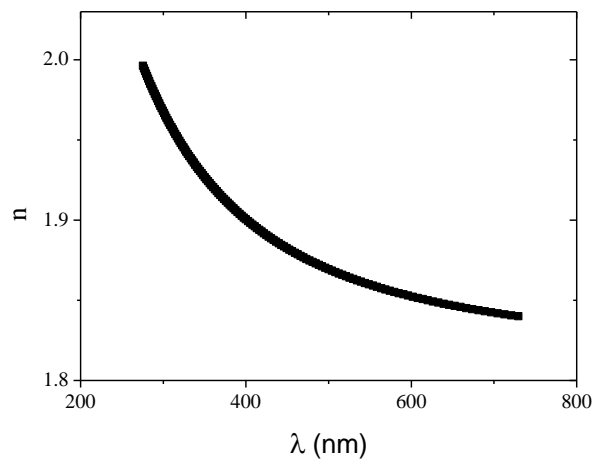


Figure 3.14: The refractive index n as a function of the wavelength, achieved from fitting the transmission spectrum only using the Swanepoel method.

The refractive index as a function of energy achieved using the Swanepoel method is equivalent to that measured for pure In_2O_3 thin film reported by Prathap *et al.* [61]. In the absorption region ($\alpha \neq 0$, $x < 1$), the index of refraction as a function of energy n and the thickness of the thin film d were determined previously. Therefore, Equ.3.21 was fitted again for the value of γ , where γ is related to x using Equ.3.27.

With the aim of achieving an accurate fitting, the Python programming language was used to program the fitting software. The software was developed in a modular structure and consisted of multi-inner loops in order to fit the data and find out the values of γ at every single point of the wavelength. The inner loops of the software perform multiple operations, being able to read data, solve an equation, then record the results, and so on. The modular structure of the software is shown in Fig.3.15.

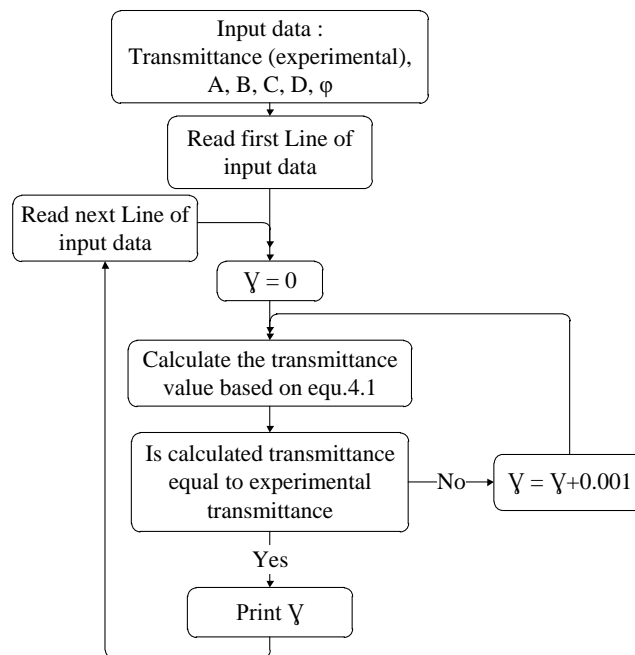


Figure 3.15: The modular structure used to develop the fitting software using the Swanepoel method.

The fitting software code is added in Appendix A. The coefficients A, B, C, D, ϕ , and X are wavelength dependent. Therefore, Equ.3.22 to Equ.3.27 are used to calculate the values of these coefficients as a function of energy by using Microsoft Excel® program. The fitting software starts by assuming $\gamma = 0$, and takes the first

values of the wavelength λ and the coefficients A, B, C, D, φ , and X . The software then computes the value of transmittance based on Equ.1. If the value of the calculated transmittance is equivalent to the value of the transmittance that was measured experimentally, then the software records the value of γ at that wavelength and then proceeds to the next point on the wavelength. If the computed and measured transmittance values are not equal, then the value of γ will increase by a step of $\gamma = \gamma_0 + 0.001$ until the values of the calculated and the measured transmittance become equal; then, the value of γ is saved, and so on. The resultant is a γ spectrum as a function of energy.

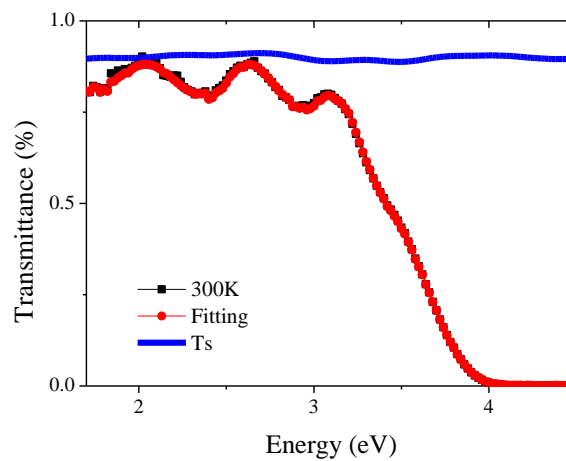


Figure 3.16: The complete fitted of the transmittance spectrum of pure In_2O_3 using the fitting software, where the value of γ at every energy point is completely determined.

Using Equ.3.27, the γ spectrum can be used to generate the spectrum of the optical absorption coefficient α as a function of energy.

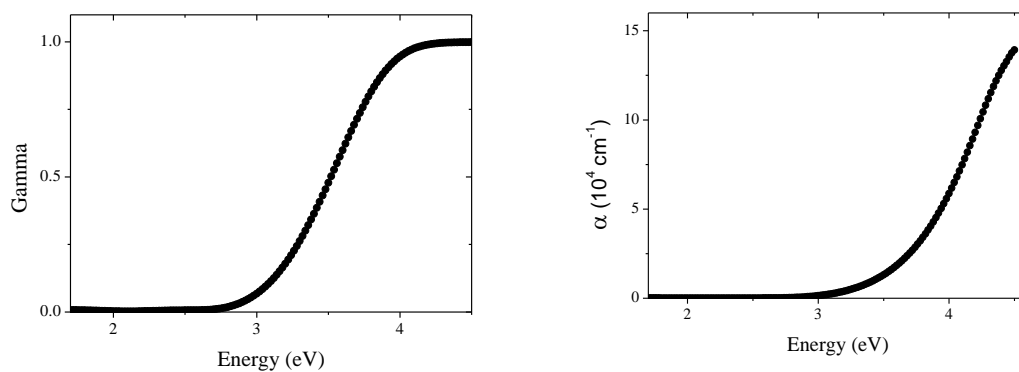


Figure 3.17: γ spectrum and the absorption coefficient spectra α as a function of energy of pure In_2O_3 .

Obtaining the absorption coefficient spectra α as a function of energy paves the way to determining the optical band gap of the system using a Tauc plot [28], as explained previously in section 3.3. This method is very accurate in determining the optical absorption coefficient spectrum where it is not affected by any changes in the fitting parameters, such as the thickness and the index of refraction. The Swanepoel method is used in the following chapters to deal with any transmission data taken at low temperature; otherwise, Equ.3.15 is used and the reflection spectrum is considered.

3.11 References

1. K. SATO, Jpn. J. Appl. Phys. **20**, 2403-2409 (1981).
2. K. Ohgushi, Y. Okimoto, T. Ogasawara, S. Miyasaka and Y. Tokura, J. Phys. Soc. Jpn. **77**, (2008).
3. T. Ishibashi, Z. Kuang, S. Yufune, T. Kawata, M. Oda, T. Tani, Y. Iimura, K. Sato, Y. Konishi, K. Akahane, X. Zhao and T. Hasegawa, J. Appl. Phys. **100**, (2006).
4. P. T. Chiu, and B. W. Wessels, Appl. Phys. Lett. **89**, (2006).
5. H. L. Liu, K. S. Lu, M. X. Kuo, L. Uba, S. Uba, L.M. Wang and H. T. Jeng, J. Appl. Phys. **99**, (2006).
6. K. Ohgushi, T. Ogasawara, Y. Okimoto, S. Miyasaka and Y. Tokura, Phys. Rev. B **72**, (2005).
7. D. A. Smith, Y. A. Barnakov, B. L. Scott, S. A. White and K. L. Stokes. *Magneto-optical spectra of closely spaced magnetite nanoparticles*. in *49th Annual Conference on Magnetism and Magnetic Materials*. 2004. Jacksonville, FL.
8. K. J. Kim, J. H. Lee and S. H. Lee, J. Magn. Magn. Mater. **279**, 173-177 (2004).
9. D. A. Allwood, G. Xiong, M. D. Cooke and R. P. Cowburn, J. Phys. D-Appl. Phys. **36**, 2175-2182 (2003).
10. G. P. Moore, J. Ferre, A. Mougin, M. Moreno and L. Daweritz, J. Appl. Phys. **94**, 4530-4534 (2003).
11. K. J. Kim, H. S. Lee, M. H. Lee and S. H. Lee, J. Appl. Phys. **91**, 9974-9977 (2002).
12. S. Lee, S. Park and C.M. Falco. *Magnetic properties of ultra-thin MBE-grown multilayers*. in *4th International Symposium on Metallic Multilayers*. 2001. Aachen, Germany.
13. K. J. Kim, S. J. Lee, T. A. Wiener and D. W. Lynch, J. Appl. Phys. **89**, 244-248 (2001).
14. T.L. Cheeks, M. Brasil, T. Sands, J. P. Harbison, D. E. Aspnes, V. G. Keramidis and S. J. Allen, Appl. Phys. Lett. **60**, 1393-1395 (1992).
15. S. T. Purcell, M. T. Johnson, N. W. E. McGee, J. J. Devries, W. B. Zeper and W. Hoving, J. Appl. Phys. **73**, 1360-1367 (1993).

16. K. Sato, H. Hongu, H. Ikekame, Y. Tosaka, M. Watanabe, K. Takanashi and H. Fujimori, *Jpn. J. Appl. Phys. Part 1-Regular Papers Short Notes & Review Papers* **32**, 989-995 (1993).
17. A. Behan, *Characterisation of Doped ZnO Thin Films for Spintronic Applications*, 2008, University of Sheffield.
18. W. P. Van Drent, and T. Suzuki, *J. Magn. Magn. Mater.* **175**, 53-62 (1997).
19. M. Fox, *Optical properties of solids*. Oxford master series in condensed matter physics 2001, Oxford ; New York: Oxford University Press. xii, 305 p.
20. N. G. Patel, and B. H. Lashkari, *Journal of Materials Science* **27**, 3026-3031 (1992).
21. J. I. Pankove, *Optical processes in semiconductors*. Prentice-Hall electrical engineering series Solid state physical electronics series 1971, Englewood Cliffs, N.J.,: Prentice-Hall. xvii, 422 p.
22. A. A. Bahgat, M. M. El-Desoky, A. Al-Hajry, A. Al-Mogeeth and M. S. Al-Assiri, *Optics & Laser Technology* **42**, 994-1003 (2010).
23. B. Radha Krishna, T. K. Subramanyam, B. S. Naidu and S. Uthanna, *Opt. Mater.* **15**, 217-224 (2000).
24. C. Xu, C. Ouyang, R. Jia, Y. Li and X. Wang, *J. Appl. Polym. Sci.* **111**, 1763-1768 (2009).
25. R. Swanepoel, *J. Phys. E: Scientific Instruments* **16**, 1214 (1983).
26. J. Sánchez-González, A. Díaz-Parralejo, A. L. Ortiz and F. Guiberteau, *Appl. Surf. Sci.* **252**, 6013-6017 (2006).
27. P. Dirk, and S. P. Frederic, *J. Phys. D: Appl. Phys.* **36**, 1850 (2003).
28. J. Tauc, *Amorphous and liquid semiconductors* 1974, London, New York,,: Plenum. ix, 441 p.
29. Y. Ohhata, F. Shinoki and S. Yoshida, *Thin Solid Films* **59**, 255-261 (1979).
30. M. J. Alam, and D. C. Cameron, *Thin Solid Films* **377-378**, 455-459 (2000).
31. H. Han, J. W. Mayer and T. L. Alford, *J. Appl. Phys.* **100**, 083715 (2006).
32. D. Beena, K. J. Lethy, R. Vinodkumar, V. P. M. Pillai, V. Ganesan, D. M. Phase and S. K. Sudheer, *Appl. Surf. Sci.* **255**, 8334-8342 (2009).
33. H. Han, J. W. Mayer and T. L. Alford, *J. Appl. Phys.* **99**, 123711-123711-7 (2006).
34. G. H. Jonker, and J. H. V. Santen, *Physica* **16**, 337-349 (1950).

35. J. F. Lawler, J. M. D. Coey, J. G. Lunney and V. Skumryev, *J. Phys.: Condensed Matter* **8**, 10737 (1996).
36. A. N. H. Al-Ajili, and S. C. Bayliss, *Thin Solid Films* **305**, 116-123 (1997).
37. S. Kasiviswanathan, and G. Rangarajan, *J. Appl. Phys.* **75**, 2572-2577 (1994).
38. S. Suh, and D. M. Hoffman, *Journal of the American Chemical Society* **122**, 9396-9404 (2000).
39. C. A. Pan, and T. P. Ma, *Appl. Phys. Lett.* **37**, 163-165 (1980).
40. C. H. Shih, I. Lo, W. Y. Pang and C. H. Hsieh, *J. Phys. Chem. Solids* **71**, 1664-1668 (2010).
41. K. Umeno, Y. Furukawa, N. Urakami, R. Noma, S. Mitsuyoshi, A. Wakahara and H. Yonezu, *Physica E: Low-dimensional Systems and Nanostructures* **42**, 2772-2776 (2010).
42. J. S. Cho, K. H. Yoon and S. K. Koh, *J. Appl. Phys.* **89**, 3223-3228 (2001).
43. E. J. Tarsa, J. H. English and J. S. Speck, *Appl. Phys. Lett.* **62**, 2332-2334 (1993).
44. S. P. Sena, R. A. Lindley, H. J. Blythe, C. Sauer, M. Al-Kafarji and G. A. Gehring, *J. Magn. Magn. Mater.* **176**, 111-126 (1997).
45. W. Svendsen, J. Schou, B. Thestrup and O. Ellegaard, *Appl. Surf. Sci.* **96-98**, 518-521 (1996).
46. D. B. Chrisey, and G. K. Hubler, *Pulsed laser deposition of thin films 1994*, New York: J. Wiley. xxviii, 613 p.
47. E. van de Riet, U. K. P. Biermann and J. Dieleman, *Thin Solid Films* **241**, 134-137 (1994).
48. D. Lubben, S. A. Barnett, K. Suzuki, S. Gorbalkin and J. E. Greene, *Journal of Vacuum Science & Technology B: Microelectronics and Nanometer Structures* **3**, 968-974 (1985).
49. J. A. Greer, *High quality YBCO films grown over large areas by pulsed laser deposition*. 1992. AVS.
50. S. R. Foltyn, R.E. Muenchausen, R. C. Dye, X. D. Wu, L. Luo, D. W. Cooke and R. C. Taber, *Appl. Phys. Lett.* **59**, 1374-1376 (1991).
51. P. Sharma, A. Gupta, K. V. Rao, F. J. Owens, R. Sharma, R. Ahuja, J. M. O. Guillen, B. Johansson and G. A. Gehring, *Nat Mater* **2**, 673-677 (2003).

52. A. K. Pradhan, K. Zhang, S. Mohanty, J. B. Dadson, D. Hunter, J. Zhang, D. J. Sellmyer, U. N. Roy, Y. Cui, A. Burger, S. Mathews, B. Joseph, B. R. Sekhar and B. K. Roul, Appl. Phys. Lett. **86**, 152511 (2005).
53. nuance.northwestern. Available from:
<http://www.nuance.northwestern.edu/media/keckii%20pdf/dektak.pdf>.
54. Veeco. Available from: http://www.veeco.com/pdfs/datasheets/B509-RevA3-Dektak_150+_Surface_Profiler-Brochure.pdf.
55. Rpi. Available from:
http://www.rpi.edu/dept/cie/mncr/documents/AN516_Dektak_Stress_Measure.pdf.
56. G. R. S. Co, 2011; Available from:
<http://www.generalaruby.com/sapphire.html>.
57. R. Reed, 1998; Available from:
<http://hypertextbook.com/facts/2007/GaryChang.shtml>.
58. J. R. Neal, A. J. Behan, R. M. Ibrahim, H. J. Blythe, M. Ziese, A. M. Fox and G. A. Gehring, Phys. Rev. Lett. **96**, 197208 (2006).
59. B. P. Chandra, and S. C. Bhaiya, American J. Phys. **51**, 160-161 (1983).
60. S. A. Khodier, Optics & Laser Technology **34**, 125-128 (2002).
61. P. Prathap, Y. P. V. Subbaiah, M. Devika and K. T. R. Reddy, Materials Chemistry and Physics **100**, 375-379 (2006).

Chapter 4 – Pure In₂O₃

4.1 Introduction

Variations in the oxygen partial pressure during the deposition process of thin films affect not only the structure, but also the physical properties of these films. Oxygen partial pressure has been found to be a key parameter in order to increase or decrease the density of oxygen vacancies. The oxygen vacancies act as donors, which leads to an increment in the carrier concentration. Variations in carrier concentration have a major impact on most of the physical properties of the materials. Therefore, by altering the oxygen partial pressure during the growth process, it is possible to archive the desired structure, surface, interface, and many other physical properties of the films while maintaining high-quality epitaxy. Understanding the variations in the absorption and refractive index of an un-doped system with oxygen partial pressure is an essential step towards understanding the behaviour of the MCD and rotation of that system, and providing background knowledge for TM-doped systems. This chapter investigates the behaviour of oxygen impurity bands formed within the band gap energy of the host In₂O₃ in the absence of any effect originating from the TM *3d* impurity band and related transitions. This will help us to predict and understand the impact of TM-doping and other growth conditions on In₂O₃ semiconductors. In addition, this chapter introduces a study about the tin-doping dependence of the optical and magneto-optical properties of pure In₂O₃. Tin doping affects the In₂O₃ thin films because Sn⁴⁺ ions substitute In³⁺ ions and release an electron. Therefore, the carrier density increases with tin doping. Variations in the carrier concentration have a major impact on most of the physical properties. They can change the thin film from an isolator to a metallic material through the semiconductor regime.

4.2 Experiment Details, Results, and Discussion

In order to investigate the influence of oxygen partial pressure on the optical properties of pure In₂O₃, ten thin films of pure In₂O₃ were prepared on sapphire substrates at 550 °C using the PLD system with laser energy of 250 mJ. The oxygen partial pressure within the growth chamber was varied between 20x10⁻³ mTorr and 100 mTorr. These thin films were obtained through collaboration with A. Alyamani's

group from KACST. The results given are just for two representative thin films. The growth details of these two films are shown in Table 4.1.

Sample	Content	Thickness (nm)	Substrate Temp. (c)	Oxygen Partial Pressure (mTorr)	Deposition Method	Substrate
46T16SP	Pure In ₂ O ₃	440	550	20x10 ⁻³	PLD	Al ₂ O ₃ (0001)
53T16SP	Pure In ₂ O ₃	448	550	10		

Table 4.1: Growth details of pure In₂O₃ thin films at different oxygen pressures.

The optical transmission spectra were measured over a range of energy of 1.7eV to 4.5eV at room temperature using the absorption system. The acquired transmission data of un-doped In₂O₃ are shown in Fig.4.1.

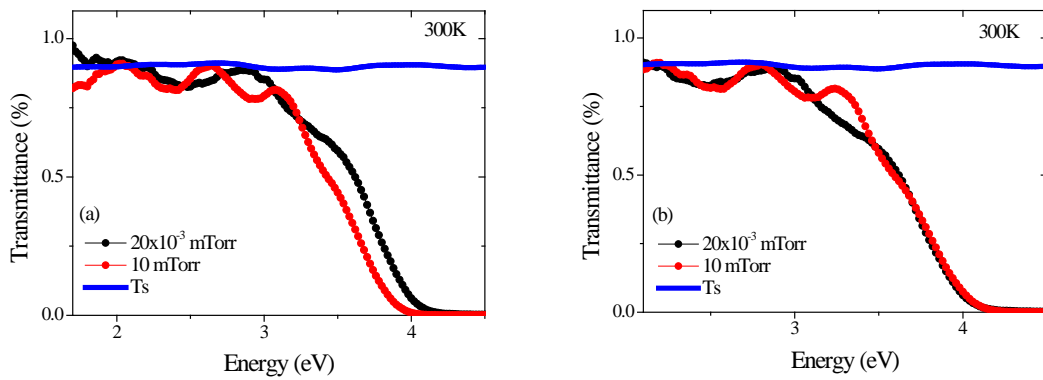


Figure 4.1: a) The optical transmission spectrums of pure In₂O₃ thin films deposited at 20x10⁻³ and 10mTorr. b) Scaled transmission spectrums. Ts is the optical transmission spectrum of a blank sapphire substrate.

Fig.4.1 (a), illustrates the transmission spectra of pure In₂O₃ thin films deposited at oxygen partial pressure of 20x10⁻³ mTorr and 10 mTorr. Both samples display high transparency and perfect interference fringes in the infrared and visible region of the electromagnetic spectrum. The thicknesses of the samples were measured using DekTack and were found to be 440nm and 448nm, which are nearly identical. Interference fringes were observed in the infrared and visible region of the spectra (1.7eV -3.0eV), suggesting that both films were smooth; the difference in the interference fringes, which was 0.19eV, indicated that the indices of refraction of

these samples were not equal. It is notable that the absorption edge was shifted to high energy for the sample deposited at low oxygen partial pressure with a step size of 0.14eV, which explains the difference seen in the interference fringes, which were due to the shift in the optical band edge plus the variations in the index of refraction with oxygen partial pressure. If the absorption edges of both samples are scaled so that they lie over each other, it will be clear that the transmittance spectra between 3.0eV and the optical absorption edge decrease with decreases in the oxygen partial pressure, as shown in Fig.4.1 (b), which is in agreement with what has been previously reported by Kaleemulla *et al.* and H. Kim *et al.* For the thin film deposited at low oxygen pressure of 20×10^{-3} mTorr, the decreases in the optical transmission spectrum between 3.0eV and the optical absorption edge imply that oxygen impurity bands were formed and concentrated at 3.3eV. The Swanepoel Method [1] explained in section 3.9 was used to calculate the indices of refraction and the optical absorption coefficient of these samples. The fitted transmission spectra of pure In_2O_3 thin films deposited at 10 mTorr and 20×10^{-3} mTorr are shown in Fig.4.2.

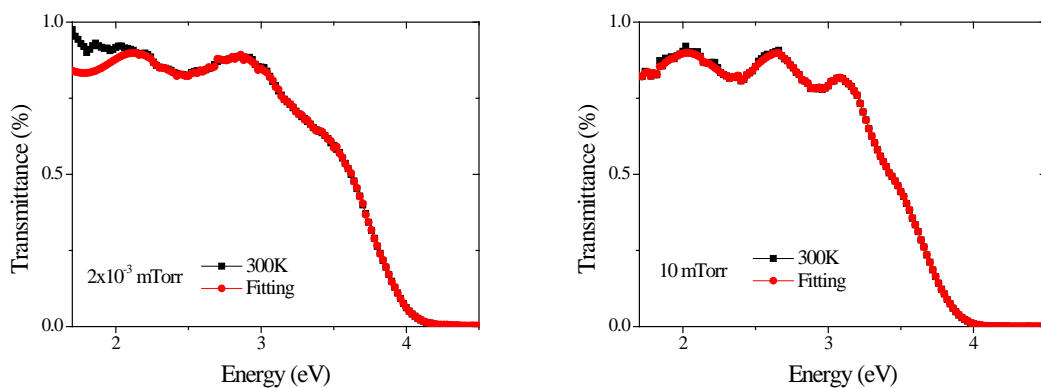


Figure 4.2: Fitted transmission spectrums of pure In_2O_3 thin films deposited at 20×10^{-3} and 10mTorr.

The thicknesses determined from the fitting were 496 nm and 475 nm for pure In_2O_3 thin films deposited at 10 mTorr and 20×10^{-3} mTorr respectively. These values are similar to those found from the Dektak but different. The difference can be used to estimate the errors on these measurements. The variations in the indices of refraction and optical absorption coefficient with oxygen partial pressure at RT are shown in Fig.4.3 (a) and Fig.4.3 (b) respectively.

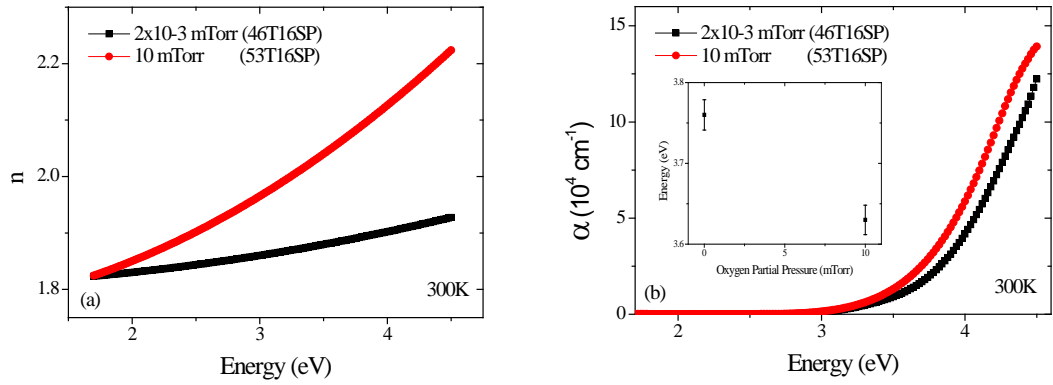


Figure 4.3: Variations in a) the indices of refraction, b) the optical absorption coefficient, with oxygen partial pressure of pure In₂O₃ thin films deposited at 20×10^{-3} and 10mTorr. Inset of (b) shows variations in the optical band gap energy with oxygen partial pressure.

Fig.4.3 (a), illustrated the index of refraction of pure In₂O₃ thin film deposited at 10mTorr was higher than that for the sample deposited at 20×10^{-3} mTorr, which implies that at a certain point of energy, the refractive index increases with an increase in oxygen partial pressure. The index of refraction of the thin film deposited at base pressure is less energy dependent especially in the visible range of the spectrum in comparison with the pure In₂O₃ thin film deposited at 10mTorr. Fig.4.3 (b), shows that both thin films had measurable non-zero absorption at the same point of energy 3.15eV. Then, the optical absorption edge shifted to higher energy for the pure In₂O₃ thin film deposited at low oxygen partial pressure while the non-zero absorption point remained constant, which implies that the density of oxygen impurity bands and the density of oxygen vacancy defects increase with decreases in oxygen partial pressure. As a result, the carrier concentration increased, the optical band gap expanded, and the optical band gap energy shifted to higher energy, as shown in the inset of Fig.4.3 (b).

In order to investigate the origin of the transitions that occur within the optical band gap, the cryostat was used to cool down the samples and to acquire the reflection spectra of a thin film. Using the cryostat led to a combination of multiple internal reflections involved in the final reflection spectrum, which affected the accuracy of the result. Therefore, in order to overcome this issue, the Swanepoel method discussed in section 3.9 was used. The optical transmission of pure In₂O₃ film

deposited at 10mTorr as a function of temperature was performed and the Swanepoel method was used. Variations in the transmission spectrum of pure In_2O_3 thin film deposited at 10mTorr and, at 20×10^{-3} mTorr are shown in Fig.4.4 (a) and Fig.4.4 (b) respectively.

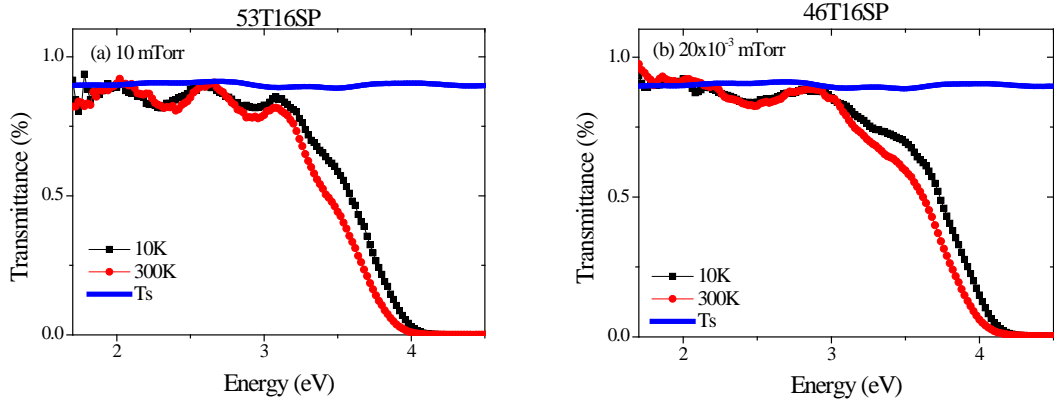


Figure 4.4: Variations in the transmission spectrum of pure In_2O_3 thin film deposited at a) 10mTorr, b) 20×10^{-3} mTorr, with temperature.

Fig.4.4 illustrated the transmission spectrums of un-doped In_2O_3 film grown in a (a) high and (b) low oxygen environment measured at 10K and RT exhibit high transparency in the region between 1.7eV and 3.0eV. Perfect interference fringes are observed indicating no scattering and no absorption below 3eV. The transmission spectrum of the substrate was measured and found to be temperature independent. The substrate transmittance spectrum at room temperature is shown in the blue line with $T_s = 0.89$ and $s = 1.64$. The transmission spectrum does not show any evidence of impurity band formation above the valance band. However, the thin film grown in high oxygen environment Fig.4.4 (a) shows a very thin impurity band formed below the conduction band around 3.2eV. The difference between 10K and RT transmission spectra at 3.2eV is 0.04%, which reflects the small spectral weight from the oxygen impurity band. The disagreement seen in the interference fringes of the transmission spectra measured at 10K and 300K indicates that the index of refraction is temperature dependent. Fig.4.4 (b) of the thin film grown in low oxygen environment illustrates a thick layer of NBE levels of oxygen vacancies was formed compared with what we observed in the highly oxygenated sample. The oxygen impurity band is located at 3.25eV. The difference between 10K and RT transmission

spectra at this energy is 0.08%, and it is this difference that gives the thickness of the oxygen impurity band. The density of the oxygen vacancy states increases toward the optical absorption edge. Any photon of light with energy higher than the band gap energy was highly absorbed. The absorption edge shifted toward high energy with the decrease in the temperature implying that the band gap energy increases with a decrease in temperature. After fitting the transmission spectrums of both thin films of pure In_2O_3 film measured at 10K and 300K, the variations in the index of refraction of pure In_2O_3 film grown at 10mTorr and, at 20×10^{-3} mTorr are shown in Fig.4.5 (a) and Fig.4.5 (b) respectively.

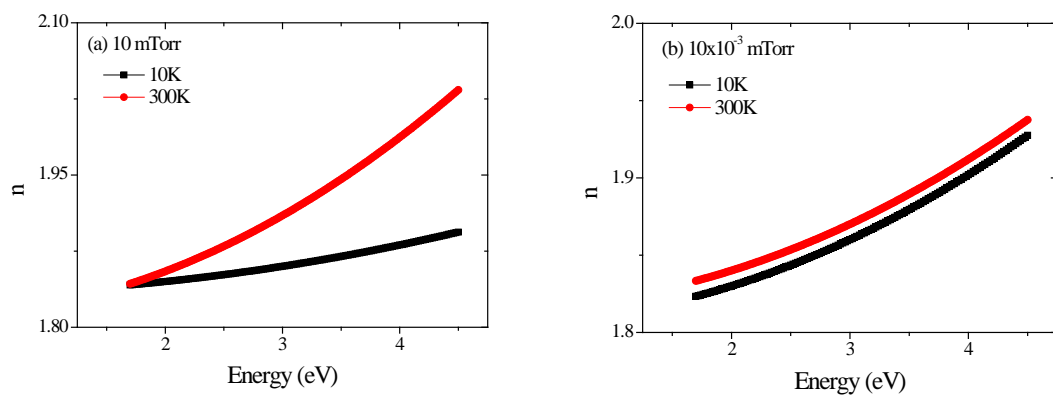


Figure 4.5: Variations in the index of refraction of un-doped In_2O_3 deposited at a) 10mTorr, b) 20×10^{-3} mTorr, with temperature.

Fig.4.5 shows the refractive index for un-doped In_2O_3 varied between 1.84 and 2.04, which is comparable with the index of refraction of In_2O_3 thin film deposited at a substrate temperature of 400°C shown in Fig.2.16. The index of the refraction spectra shows temperature dependent behaviour. For thin film grown at 10 mTorr, It increases sharply with the increase in temperature, indicating that the stress of the pure In_2O_3 increases gradually with the increase in temperature [4, 6]. Another explanation is that the index of refraction is volume dependent; therefore, any changes to the volume of the lattice due to the thermal expansion affect the refractive index.

The index of refraction of un-doped In_2O_3 deposited at 20×10^{-3} mTorr shows weak temperature dependence in the whole range of measured energy. The refractive index increases slightly with increases of temperature indicating that the low oxygenated In_2O_3 thin film resists any changes to the lattice volume initiated

thermally. The optical absorption coefficient spectrum as a function of temperature of pure In_2O_3 film grown at 10mTorr and, at 20×10^{-3} mTorr are shown in Fig.4.6 (a) and Fig.4.7 (b) respectively.

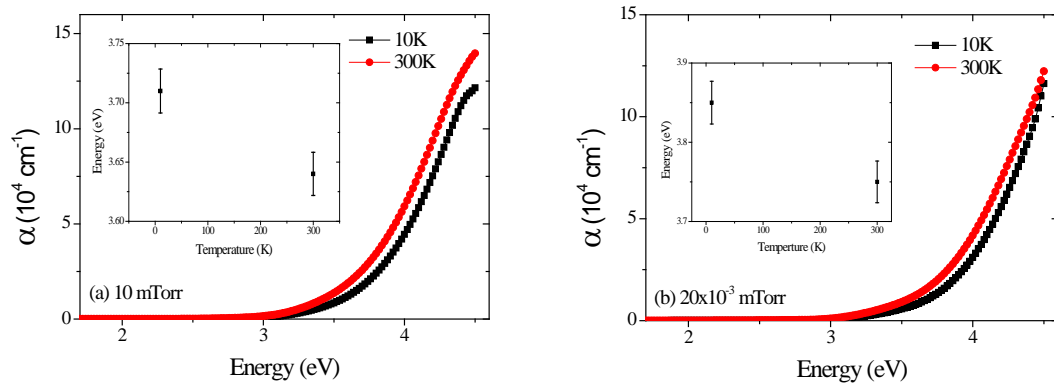


Figure 4.6: Variations in the optical absorption coefficient of un-doped In_2O_3 deposited at a) 10mTorr, b) 20×10^{-3} mTorr, with temperature; the inset shows the optical band gap as a function of temperature.

Fig.4.6 illustrates the absorption coefficient spectra as a function of temperature for un-doped In_2O_3 thin film deposited in (a) a high and (b) a low oxygen environment. The spectra show no energy band below 3.0eV, which clarifies the transparent region of In_2O_3 . In the range between 3.0eV and the optical absorption edge, a layer of NBE levels of oxygen vacancies was formed. The density of the oxygen vacancy states increased toward the optical absorption edge of the In_2O_3 thin film. The optical absorption edge shifted toward high energy as the temperature decreased. The optical band gap energy as a function of temperature is shown in an inset of Fig. 4.6. The optical band gap at room temperature is consistent with what is expected of thin film deposited at a substrate temperature higher than 400°C , as shown in Fig.2.15. The optical band gap energy increases with decreases in temperature, which is consistent with what is expected for variations in optical band gap energy with the temperature of the semiconductor, following the Varshni formula [7]. When the shift in energy between the optical absorption edges at 10K and RT is eliminated, then the optical absorption coefficient spectra are shown to be temperature independent. The scaled temperature dependence of the optical absorption coefficient spectra of pure In_2O_3 film grown at 10mTorr and, at 20×10^{-3} mTorr are shown in Fig.4.7 (a) and Fig.4.7 (b) respectively.

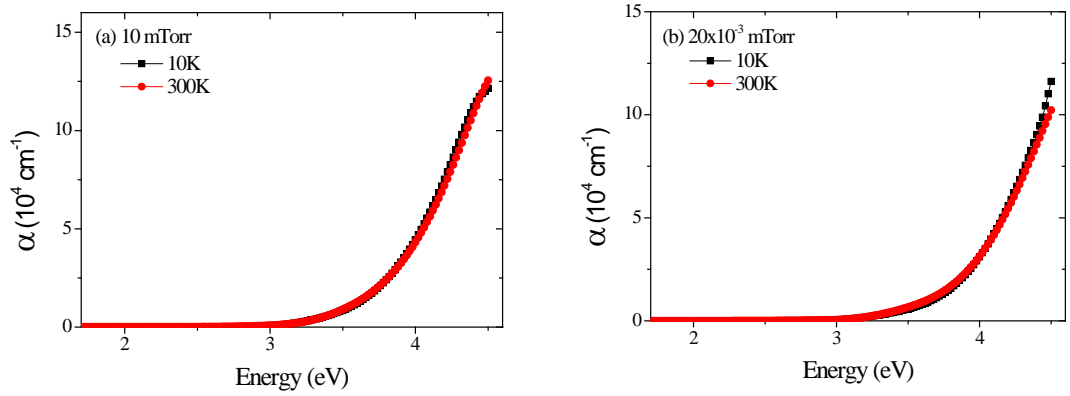


Figure 4.7: Scaled optical absorption coefficient spectra of un-doped In_2O_3 deposited at a) 10mTorr, b) 20×10^{-3} mTorr, with temperature; shows temperature independent behaviour.

Fig.4.7 illustrated that, scaled optical absorption coefficient spectra of un-doped In_2O_3 show temperature independent behaviour. This result shows that the transitions seen within the forbidden band gap energy of high oxygenated pure In_2O_3 are due to transitions from the valance band to the impurity band formed by defect just below the optical band edge and are not due to the phonon-assisted transitions.

In order to investigate the influence of Tin doping upon the optical properties of pure indium oxide, three thin films of $(\text{In}_{1-x}\text{Sn}_x)_2\text{O}_3$, with $x=0, 0.05$ and 0.10 , were grown by A. M. H. R. Hakimi from the University of Cambridge using dc magnetron sputtering in a highly oxygen deficient environment. These sputtering samples were completely different from the previous thin films grown in KACST using the PLD system. Therefore, it is possible that the optical properties may have varied due to the difference of the growth techniques used. The growth details of the Sn-doped In_2O_3 thin films are summarized in Table 4.2.

SAMPLE	CONTENT	THICKNESS (nm)	PRESSURE (mTorr)	TEMPERATURE (°C)	DEPOSITION METHOD	SUBSTRATE Al_2O_3 (0001)
					dc. magnetron sputtering	
020	In_2O_3	200	0.56	330	dc. magnetron sputtering	Al_2O_3 (0001)
017	$(\text{In}_{0.95}\text{Sn}_{0.05})_2\text{O}_3$	200	0.56			
018	$(\text{In}_{0.90}\text{Sn}_{0.10})_2\text{O}_3$	200	0.56			

Table 4.2: Growth details of pure In_2O_3 doped with different concentrations of Tin.

As a part of the cooperation between our group and others, the EXAFS measurement was performed by S. M. Heald from the Advanced Photon Source, Argonne National Laboratory, USA, and it was found that these thin films had many small grains and disordered sites. Mr. Hakimi measured the transport properties of these thin films. The variations in carrier concentration and in the Hall mobility with tin concentration for pure In_2O_3 samples doped only with tin are shown in Fig.4.8.

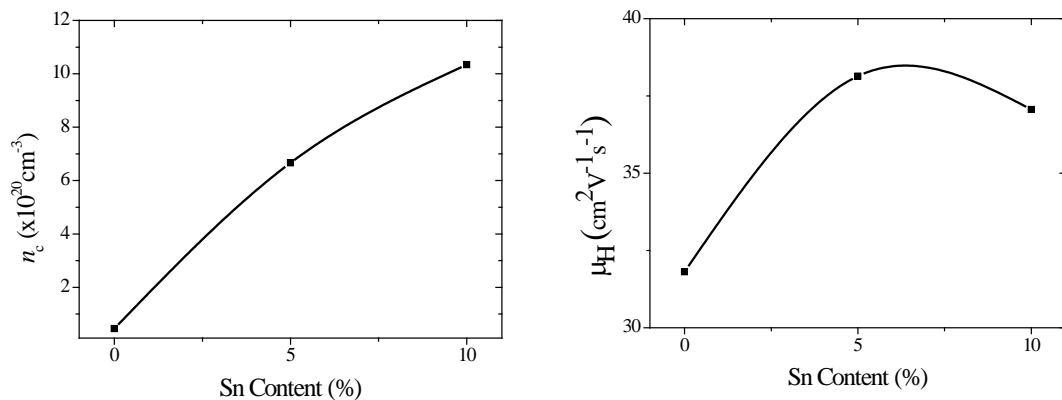


Figure 4.8: Variations in carrier concentration (n_c) and mobility (μ) with Sn content of pure In_2O_3 thin films.

The carrier concentration of un-doped In_2O_3 was $4.5 \times 10^{19} \text{ cm}^{-3}$; with the addition of tin, the carrier concentration n_c increased to $6.3 \times 10^{20} \text{ cm}^{-3}$ and $1.03 \times 10^{21} \text{ cm}^{-3}$ with 5% and 10% of tin respectively. As a result, the semiconductor un-doped In_2O_3 sample became a metallic sample after being doped with tin content above 5%. The Hall mobility increased with increases in tin to a maximum of around 5% of tin; then, it decreased, which means that the critical Sn content value is around 5% of tin. Then, by increasing the Sn content, the repulsion between Sn ions increases due to the increase in interstitial Sn ions that act as scattering centres, and this causes a decrease in the Hall mobility, as shown in Fig.4.8.

Optical transmission and reflection was measured at room temperature. The variations in transmission and the reflection with an increase in tin content are shown in Fig.4.9.

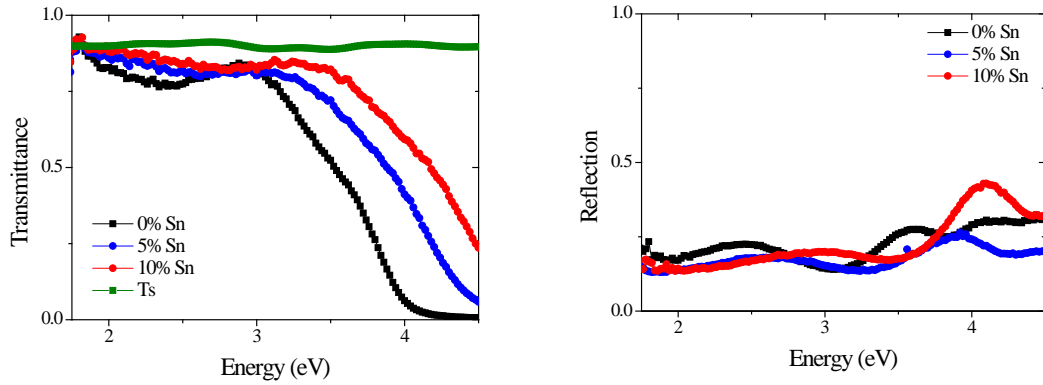


Figure 4.9: Variations in transmission and reflection spectra as a function of Sn content of pure In_2O_3 thin films.

Fig.4.9 shows that, the transmission spectrum increased with an increase in tin concentration especially in the violet and ultraviolet range from 3.0eV to 4.5 eV (413nm-275nm) and the absorption edge shifted toward high energy. The amplitude of the interference fringes decreased with an increase in tin content due the increase in the absorption of the thin films with tin content. The reflection spectrum shows a decrease in the maximum to minimum peak with an increase in tin concentration especially in the visible range (1.7-3.5eV) and a decrease in intensity compared with the un-doped sample. Since the thicknesses of the samples were equal, the shift of the maximum or minimum peaks shown in the reflection spectra indicated that the refractive indices of the samples were affected by the tin concentration and they were not the same. The variations in transmission at 550 nm are shown in Fig.4.10 (a).

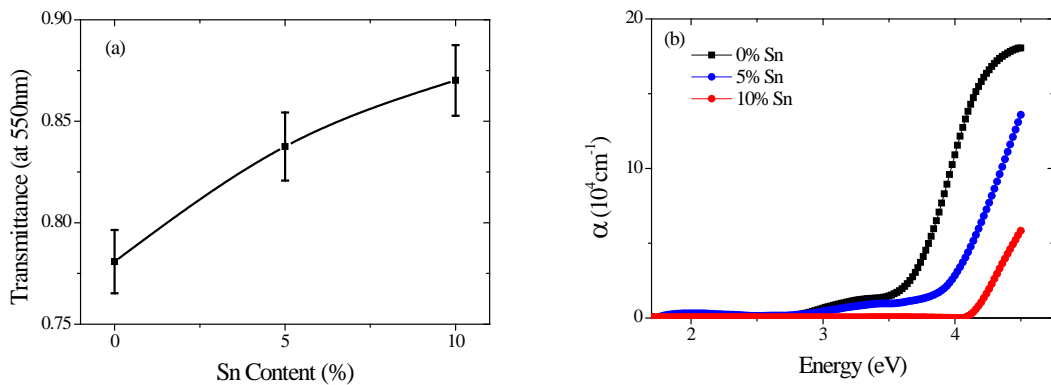


Figure 4.10: Variations in the a) optical transmittance, and b) optical absorption coefficient, of pure In_2O_3 at 550nm with Sn content of pure In_2O_3 thin films.

Fig.4.10 (a) illustrated that, the optical transmittance increases with increase of tin content. Fig.4.10 (b) shows that, the optical absorption coefficient spectrum decreases with increases in tin content. The absorption coefficient spectrum of pure In_2O_3 here is different from what we saw before in Fig.4.6 although both thin films were grown at low oxygen partial pressure. This variation is due to the different systems and growth processes used to prepare these thin films. The area under the shoulder below the band gap energy expanded with an increase in tin content up to 5% then decreased. Adding more tin resulted in more energy states by defects being generated within the band gap energy and some energy levels were formed around 2.0eV related to the Sn ions. The decrease in the optical absorption coefficient with an increase in tin implies the increase in the transparency of the thin film with tin doping and explains the increase in the transmission spectrum with tin content. The absorption band edge was shifted towards higher energy with an increase in tin content. The variations in the absorption coefficient squared and the optical band gap energy with tin concentration are shown in Fig.4.11.

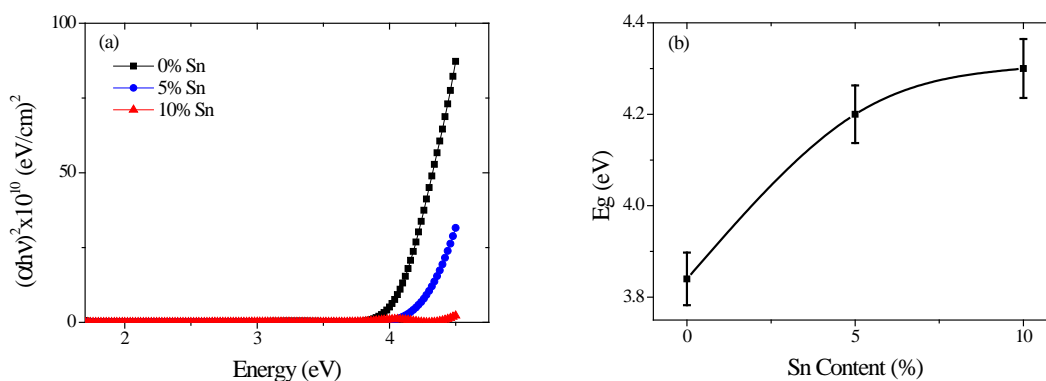


Figure 4.11: Variations in the a) optical absorption coefficient squared and b) the optical band gap energy with tin content of pure In_2O_3 thin films.

Figure 4.11 (b) illustrated that, the optical band gap energy increases with increases in tin content due to the increases in carrier concentration, as shown in Fig.4.8 (a). An investigation of the MCD spectra does not show any MCD peak or variation with tin content due to a low MCD signal, which is out of the detection range of our M-O system.

4.3 Conclusion

This chapter investigated the influence the oxygen partial pressure and tin doping on the optical properties of pure In_2O_3 thin films. Variations in oxygen partial pressure during the growth process lead to the formation or disappearance of oxygen impurity bands located below the optical absorption edge. Decreasing the oxygen partial pressure leads to the development of oxygen impurity bands, an increase in the carrier density, and the shifting of the optical band gap towards higher energy. The transmission drops in the range of energy located below the optical band gap energy, which is supported by the increases in the absorption coefficient in the same range of energy, indicating that the transitions between the valance band and some bands within the optical band gap are established. The origin of these transitions was explored through the measurements of the optical properties as a function of temperature. The few optical studies of In_2O_3 thin films reported to date have been at room temperate and this is the first optical study has considered the temperature dependence for doped or un-doped In_2O_3 . These investigations included thin films prepared in high and low oxygen partial pressure atmospheres. Both showed and confirmed that the transitions seen within the forbidden band gap energy are temperature independent and due to the transitions from the valance band to the donor levels by defects (oxygen impurity bands) and not due to the thermal activation of phonons. Therefore, the oxygen impurity bands are an active partner in any MCD signal that may exist between 3.0eV and the optical band gap energy of In_2O_3 .

The influence of tin doping on the optical properties of pure In_2O_3 was also discussed. We found that doping with tin leads to an increase in the carrier density and the density of the donor bands. Therefore, the carrier density and the density of the oxygen impurity bands can be increased by growing thin films at low oxygen pressure, through the vacuum annealing process, or by doping with tin; the low oxygen pressure method is more effective than the annealing process method. In the case of TM-doped In_2O_3 , this situation may change as some of these methods may lead to the formation of TM nanoparticles, as we are going to find out in the next chapters.

4.4 References

1. R. Swanepoel, J. Phys. E: Scientific Instruments **16**, 1214 (1983).
2. B. P. Chandra, and S. C. Bhaiya, American J. Phys. **51**, 160-161 (1983).
3. S. A. Khodier, Optics & Laser Technology **34**, 125-128 (2002).
4. P. Prathap, Y. P. V. Subbaiah, M. Devika and K. T. R. Reddy, Mater. Chem. Phys. **100**, 375-379 (2006).
5. J. Tauc, *Amorphous and liquid semiconductors* 1974, London, New York,: Plenum. ix, 441 p.
6. H. Poelman, D. Poelman, D. Depla, H. Tomaszewski, L. Fiermans and R. De Gryse, Surface Science **482-485**, 940-945 (2001).
7. S. Adachi, *Physical properties of III-V semiconductor compounds : InP, InAs, GaAs, GaP, InGaAs, and InGaAsP* 1992, New York: Wiley. xviii, 318 p.

Chapter 5 – Maxwell-Garnett Theory

5.1 Introduction

The ferromagnetism in oxide magnetic semiconductors usually induced by clustered magnetic impurities [1] or attributed to the oxygen vacancy defects [2, 3] or attributed to the formation of TM nanoparticles. The presence of metallic or nanoparticles TM is always expected, especially for Co-, and Fe-doped In₂O₃. This chapter develop a lab-based alternative to EXAFS and represent and use the Maxwell-Garnett (M-G) theory to determine the fraction and the contribution of TM nanoparticles to the total magnetic and magneto-optical properties of TM-doped In₂O₃ thin films where the existence of TM nanoparticles is confirmed.

5.2 Co Nanoparticles

C. Clavero *et al.* investigated the optical and magneto-optical properties of Co nanoparticles embedded in ZrO₂ in the spectral range from 1.4 to 4.3 eV[4]. They used the effective medium approximation [5], which takes into account the Co concentration dependence for the Co nanoparticles with a size much smaller than the wavelength of the incident light, and they used the Maxwell-Garnett approximation, which was originally an effective-medium theory but was developed by Maxwell-Garnett for a composite composed of particles embedded in a host on the assumption that the total polarization would be the same as the sum of the polarization contributions from the embedded particles. Therefore, the Maxwell-Garnett approximation calculates the effective dielectric tensor $\tilde{\epsilon}^{eff}$. The effective dielectric tensor represents a composite material consisting of particles randomly distributed in a matrix depending on the dielectric tensors of the particles and matrix, and the concentration and shape of the particles[6].

The expression for the elements of the dielectric tensor for cobalt metal is in the form

$$\hat{\epsilon} = \begin{pmatrix} \epsilon_1 & +i\gamma & 0 \\ -i\gamma & \epsilon_1 & 0 \\ 0 & 0 & \epsilon_2 \end{pmatrix} \quad \text{Equation(5.1)}$$

where all the elements are complex. The theoretical expressions for these elements are given using a Drude theory [7] as follows:

$$\varepsilon_1^{Co} = 1 + i \frac{(1 - i\omega\tau)\omega_p^2\tau}{\omega[(1 - i\omega\tau)^2 + (\omega_c\tau)^2]} \quad \text{Equation(5.2)}$$

$$\gamma^{Co} = \frac{\omega_c(\omega_p\tau)^2}{\omega[(1 - i\omega\tau)^2 + (\omega_c\tau)^2]} \quad \text{Equation(5.3)}$$

where $\omega_c = \frac{eB}{mc}$ is the cyclotron frequency, $\omega_p^2 = \frac{ne^2}{\varepsilon_0 m}$ is the plasma frequency, n being the conduction band electron density and m the electron effective mass. τ is the relaxation time of the electrons, which depends on the electron-electron, electron-phonon, and electron-defect scattering contributions [8].

Since the $(\omega_c\tau)^2 \ll (1 - i\omega\tau)^2$ in the range of spectrum that we are interested in, therefore, the expressions of the elements of the dielectric tensor of cobalt become:

$$\varepsilon_1^{Co} = 1 + i \frac{\omega_p^2\tau}{\omega(1 - i\omega\tau)} = 1 + i \frac{\omega_p^2\tau(1 + i\omega\tau)}{\omega(1 + \omega^2\tau^2)} \quad \text{Equation(5.4)}$$

$$\gamma^{Co} = \frac{\omega_c(\omega_p\tau)^2}{\omega(1 - i\omega\tau)^2} = \frac{\omega_c(\omega_p\tau)^2[1 - \omega^2\tau^2 + 2i\omega\tau]}{\omega[(1 - \omega^2\tau^2)^2 + 4\omega^2\tau^2]} \quad \text{Equation(5.5)}$$

by putting the elements of the dielectric tensor of cobalt in their real and imaginary parts, as follows:

$$\varepsilon_1^{Co} = a + ib \quad \text{Equation(5.6)}$$

$$\gamma^{Co} = c + id \quad \text{Equation(5.7)}$$

where the parameters $a, b, c,$ and d have the following expressions:

$$a = \text{Re}(\varepsilon_1^{Co}) = 1 - \frac{\omega_p^2\tau^2}{1 + (\omega\tau)^2} \quad \text{Equation(5.8)}$$

$$b = \text{Im}(\varepsilon_1^{Co}) = \frac{\omega_p^2\tau}{\omega[1 + (\omega\tau)^2]} \quad \text{Equation(5.9)}$$

$$c = \text{Re}(\gamma^{Co}) = \frac{\omega_c(\omega_p\tau)^2(1 - \omega^2\tau^2)}{\omega(1 + \omega^2\tau^2)^2} \quad \text{Equation(5.10)}$$

$$d = \text{Im}(\gamma^{co}) = \frac{2\omega_c\omega_p^2\tau^3}{(1 + \omega^2\tau^2)^2} \quad \text{Equation(5.11)}$$

These equations were derived by my supervisor Gillian Gehring for metallic Co. The parameters $\omega_p, \omega_c,$ and τ were obtained by Krinchik for Co [9-11]. The values of these parameters for Co were $\omega_p = 9.74\text{eV}, \omega_c = 0.089\text{eV},$ and $\tau = 0.632\text{eV}^{-1}$. These values were used to plot the expressions of Equ.5.10 and Equ.5.11 in the energy range of (1.5eV to 4.2eV). The real and imaginary parts of the off diagonal elements of the dielectric tensor of cobalt are shown in Fig.5.1.

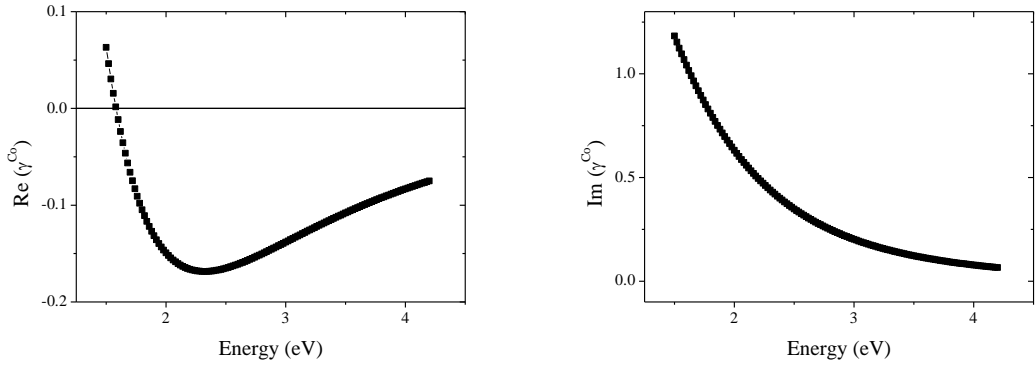


Figure 5.1: The real and imaginary parts of the Off diagonal elements of the dielectric tensor of cobalt.

These data are in agreement with those calculated for cobalt by Krinchik [9] and Clavero [11]. However, the real and imaginary parts of off diagonal elements calculated for bulk cobalt by Clavero were switched; he used a different definition for the off diagonal elements with ϵ_{xy} and $-\epsilon_{xy}$ rather than $i\gamma$ and $-i\gamma$, as follows:

$$\tilde{\epsilon} = \begin{pmatrix} \epsilon_{xx} & -\epsilon_{xy} & 0 \\ \epsilon_{xy} & \epsilon_{xx} & 0 \\ 0 & 0 & \epsilon_{zz} \end{pmatrix} \quad \text{Equation(5.12)}$$

The Maxwell-Garnett theory was used to calculate the expected response of cobalt nanoparticles in a non-magnetic In_2O_3 medium. The effective dielectric tensor γ^{eff} in terms of the parameters $a, b, c,$ and d is:

$$\frac{\gamma^{eff}}{f} = \frac{\gamma^{Co}}{\left[1 + (1-f)L_x \left(\frac{\epsilon_1^{Co}}{\epsilon_1^{In_2O_3}} - 1\right)\right]^2} = \frac{c + id}{\left[1 + (1-f)L_x \left(\frac{a + ib}{\epsilon_1^{In_2O_3}} - 1\right)\right]^2} \quad \text{Equation(5.13)}$$

where f represents the volume fraction of metallic Co embedded in the host material. L_x represents the shape factors, which have been reported for Co nanoparticles in the MgO host as $L_x = L_y = 0.236$ and $L_z = 0.527$ [11].

$$\frac{\gamma^{eff}}{f} = \frac{c + id}{1 + 2(1-f)L_x \left(\frac{a + ib}{\epsilon_1^{In_2O_3}} - 1\right) + \delta} \quad \text{Equation(5.14)}$$

$$\delta = (1-f)^2 L_x^2 \left(\frac{a^2 - b^2 + 2iab}{(\epsilon_1^{In_2O_3})^2} - 2\left(\frac{a + ib}{\epsilon_1^{In_2O_3}}\right) + 1\right) \quad \text{Equation(5.15)}$$

By considering new parameters α and β , where

$$\alpha = 1 + 2(1-f)L_x \left(\frac{a}{\epsilon_1^{In_2O_3}} - 1\right) + (1-f)^2 L_x^2 \left(\frac{a^2 - b^2}{(\epsilon_1^{In_2O_3})^2} - \frac{2a}{\epsilon_1^{In_2O_3}} + 1\right) \quad \text{Equation(5.16)}$$

$$\beta = \frac{2(1-f)L_x b}{\epsilon_1^{In_2O_3}} + 2(1-f)^2 L_x^2 \left(\frac{ab}{(\epsilon_1^{In_2O_3})^2} - \frac{b}{\epsilon_1^{In_2O_3}}\right) \quad \text{Equation(5.17)}$$

then, the effective dielectric tensor becomes

$$\frac{\gamma^{eff}}{f} = \frac{c + id}{\alpha + i\beta} = \frac{(c + id)(\alpha - i\beta)}{\alpha^2 + \beta^2} \quad \text{Equation(5.18)}$$

where the real and imaginary parts of the effective dielectric tensor of Co in In_2O_3 host matrix are

$$Re(\gamma^{eff}) = f \left(\frac{c\alpha + d\beta}{\alpha^2 + \beta^2} \right) \quad \text{Equation(5.19)}$$

$$Im(\gamma^{eff}) = f \left(\frac{d\alpha - c\beta}{\alpha^2 + \beta^2} \right) \quad \text{Equation(5.20)}$$

The real and imaginary parts of the effective dielectric tensor of Co in a In_2O_3 host matrix mentioned in Equ.5.19 and Equ.5.20 are plotted in Fig.5.2.

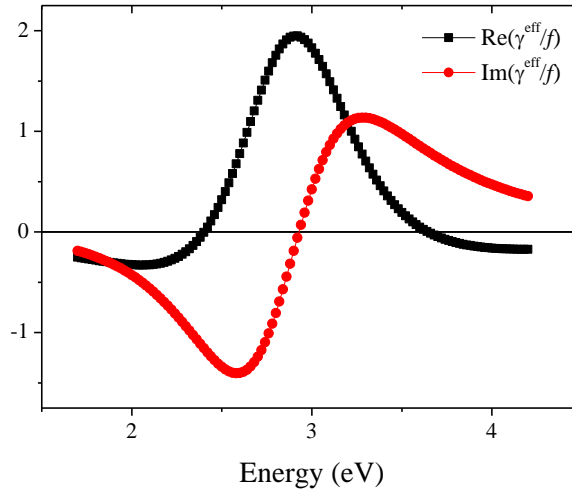


Figure 5.2: The real and imaginary parts of the effective dielectric tensor of Co in In_2O_3 host matrix, where, $\epsilon'_1 = n^2$, $\epsilon''_1 = 0$, $f = 0.1$ and $L_x = 0.333$.

The expressions for the off diagonal elements components of the dielectric tensor (Equ.1) for cobalt are in the form of Equ.5.19 and Equ.5.20 but experimentally are related to the Faraday MCD and Faraday rotation, as follows:

$$Re(\gamma^{Co}) \approx \frac{\lambda n}{\pi l} \theta_F \quad \text{Equation(5.21)}$$

$$Im(\gamma^{Co}) \approx \frac{\lambda n}{\pi l} \eta_F \quad \text{Equation(5.22)}$$

Since the absorption of indium oxide is ignored within the transparency region below the band gap, then, $\epsilon_1^{In_2O_3} = n^2(\lambda)$ where the wavelength dependence of the normal refractive index n of In_2O_3 was taken to be in the form

$$n(\lambda) = A + B/\lambda^2 + C/\lambda^4 \quad \text{Equation(5.23)}$$

where λ is the wavelength of the light used in (μm) units, and the fitted values of Cauchy's parameters are $A = 1.81$, $B = 0.0121$, and $C = -0.00019$.

The real and imaginary parts of γ were calculated using the measured Faraday rotation (θ_F) and the Faraday ellipticity (η_F) respectively fitted with $Re(\gamma^{eff})$ and the $Im(\gamma^{eff})$ spectra were calculated theoretically as a function of energy using Equ.5.19 and Equ.5.20 to determine the fraction of metallic Co f and the contribution of metallic Co to the total MCD signal as shown in Fig.5.3.

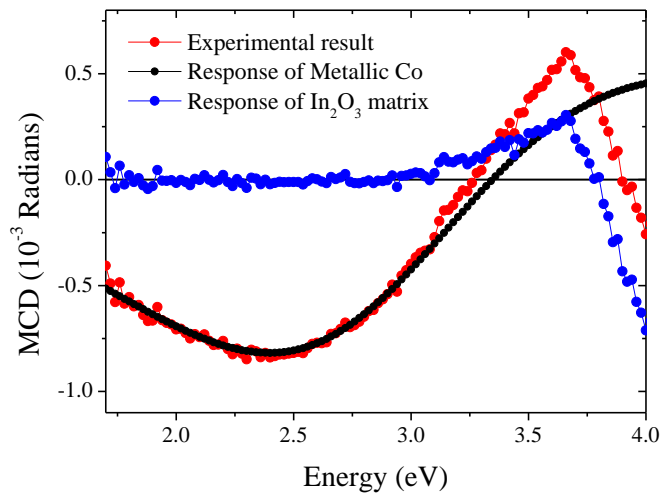


Figure 5.3: MCD spectrum of Co-doped In_2O_3 thin film fitted using Maxwell-Garnett theory to determine the fraction and the contribution of Co nanoparticles to the host material.

5.3 Fe_3O_4 Nanoparticles

In order to distinguish between the MCD spectra that represent the response of the In_2O_3 oxide matrix and those related to the response of the Fe_3O_4 nanoparticles and to determine the fraction of the Fe_3O_4 nanoparticles in these thin films, I have extended the Maxwell-Garnett (M-G) theory to include the contribution of the Fe_3O_4 nanoparticles and the host In_2O_3 . Therefore, the response of the Fe_3O_4 nanoparticles was fitted to the Maxwell-Garnett theory in the region $E < 2.7\text{eV}$. In this case, the expression for the elements of the dielectric tensor for Fe_3O_4 is

$$\tilde{\varepsilon} = \begin{pmatrix} \tilde{\varepsilon}_{xx} & i\tilde{\varepsilon}_{xy} & 0 \\ -\tilde{\varepsilon}_{xy} & \tilde{\varepsilon}_{xx} & 0 \\ 0 & 0 & \tilde{\varepsilon}_{zz} \end{pmatrix} \quad \text{Equation(5.24)}$$

and the effective dielectric function for light propagation along the direction of magnetization, z, is given by

$$\tilde{\varepsilon}_{xy}^{eff} = \tilde{\varepsilon}_{xy}^{In_2O_3} + \frac{f(\tilde{\varepsilon}_{xy}^{Fe_3O_4} - \tilde{\varepsilon}_{xy}^{In_2O_3})}{\left[1 + (1-f) \frac{L_{xx}}{\tilde{\varepsilon}_{xx}^{In_2O_3}} (\tilde{\varepsilon}_{xx}^{Fe_3O_4} - \tilde{\varepsilon}_{xx}^{In_2O_3})\right]^2} \quad \text{Equation(5.25)}$$

where

$$\tilde{\varepsilon}_{xx}^{In_2O_3} = \varepsilon'_{xx} + i\varepsilon''_{xx} \quad \text{Equation(5.26)}$$

$$\varepsilon'_{xx} = n^2 - k^2, \quad \varepsilon''_{xx} = 2nk \quad \text{Equation(5.27)}$$

Since $k = 0$ below the optical band gap, therefore, Equ.5.27 becomes

$$\varepsilon'_{xx} = n^2, \quad \varepsilon''_{xx} = 0 \quad \text{Equation(5.28)}$$

Substituting Equ.5.28 in Equ.5.26 leads to

$$\tilde{\varepsilon}_{xx}^{In_2O_3} = n^2(\lambda) \quad \text{Equation(5.29)}$$

f is the fraction of Fe_3O_4 nanoparticles in the sample and usually is very small $f \ll 1$; therefore, $(1-f) \sim 1$. L_{xx} is the demagnetising factor. Both f and L_{xx} are treated as fitting parameters. The fitted value of f is then compared with the value obtained from EXAFS. Equ.5.25 becomes

$$\tilde{\varepsilon}_{xy}^{eff} = \tilde{\varepsilon}_{xy}^{In_2O_3} + \frac{f(\tilde{\varepsilon}_{xy}^{Fe_3O_4} - \tilde{\varepsilon}_{xy}^{In_2O_3})}{\left[1 + \frac{L_{xx}}{n^2} (\tilde{\varepsilon}_{xx}^{Fe_3O_4} - n^2)\right]^2} \quad \text{Equation(5.30)}$$

If we assume $\tilde{\varepsilon}_{xy}^{In_2O_3}$ is very small, then, $\tilde{\varepsilon}_{xy}^{Fe_3O_4} - \tilde{\varepsilon}_{xy}^{In_2O_3} = \tilde{\varepsilon}_{xy}^{Fe_3O_4}$; therefore, Equ.5.30 becomes

$$\tilde{\varepsilon}_{xy}^{eff} = \tilde{\varepsilon}_{xy}^{In_2O_3} + \frac{f(\tilde{\varepsilon}_{xy}^{Fe_3O_4})}{\left[1 + \frac{L_{xx}}{n^2} (\tilde{\varepsilon}_{xx}^{Fe_3O_4} - n^2)\right]^2} \quad \text{Equation(5.31)}$$

Since we are interested in the imaginary part of the dielectric tensor, Equ.5.31 becomes

$$Im\tilde{\varepsilon}_{xy}^{eff} = Im\tilde{\varepsilon}_{xy}^{In_2O_3} + Im \left\{ \frac{f(\tilde{\varepsilon}_{xy}^{Fe_3O_4})}{\left[1 + \frac{L_{xx}}{n^2}(\tilde{\varepsilon}_{xx}^{Fe_3O_4} - n^2)\right]^2} \right\} \quad \text{Equation(5.32)}$$

For Fe ions

$$\tilde{\varepsilon}_{xx}^{Fe} = \varepsilon'_{xx} + i\varepsilon''_{xx} \quad \text{Equation(5.33)}$$

$$\tilde{\varepsilon}_{xy}^{Fe} = \varepsilon'_{xy} + i\varepsilon''_{xy} \quad \text{Equation(5.34)}$$

By rewriting Equ.5.32 taking into consideration Equ.9:

$$Im\tilde{\varepsilon}_{xy}^{eff} = Im\tilde{\varepsilon}_{xy}^{In_2O_3} + Im \left\{ \frac{f\varepsilon'_{xy} + if\varepsilon''_{xy}}{\left[1 + \frac{L_{xx}}{n^2}(\varepsilon'_{xx} + i\varepsilon''_{xx}) - L_{xx}\right]^2} \right\} \quad \text{Equation(5.35)}$$

By letting

$$a = 1 - L_{xx}, \quad b = \frac{L_{xx}}{n^2} \quad \text{Equation(5.36)}$$

Equ.5.35 becomes

$$Im\tilde{\varepsilon}_{xy}^{eff} = Im\tilde{\varepsilon}_{xy}^{In_2O_3} + Im \left\{ \frac{f\varepsilon'_{xy} + if\varepsilon''_{xy}}{[a + b\varepsilon'_{xx} + ib\varepsilon''_{xx}]^2} \right\} \quad \text{Equation(5.37)}$$

By considering new variables $\alpha_1, \alpha_2, \alpha_3,$ and α_4 where

$$\alpha_1 = a + b\varepsilon'_{xx} \quad \text{Equation(5.38)}$$

$$\alpha_2 = b\varepsilon''_{xx} \quad \text{Equation(5.39)}$$

$$\alpha_3 = f\varepsilon'_{xy} \quad \text{Equation(5.40)}$$

$$\alpha_4 = f\varepsilon''_{xy} \quad \text{Equation(5.41)}$$

By substituting Equ.5.38, 5.39, 5.40, and 5.41 in Equ.5.37

$$Im\tilde{\varepsilon}_{xy}^{eff} = Im\tilde{\varepsilon}_{xy}^{In_2O_3} + Im \left\{ \frac{\alpha_3 + i\alpha_4}{[\alpha_1 + i\alpha_2]^2} \right\} \quad \text{Equation(5.42)}$$

Solving Equ.5.42 for the imaginary part of $Im\tilde{\varepsilon}_{xy}^{eff}$ leads to

$$\begin{aligned} Im\tilde{\varepsilon}_{xy}^{eff} &= Im\tilde{\varepsilon}_{xy}^{In_2O_3} + Im \left\{ \frac{\alpha_3 + i\alpha_4}{[\alpha_1 + i\alpha_2]^2} \right\} \\ &= Im\tilde{\varepsilon}_{xy}^{In_2O_3} + Im \left\{ \frac{\alpha_3 + i\alpha_4}{\alpha_1^2 + 2i\alpha_1\alpha_2 - \alpha_2^2} \right\} \end{aligned} \quad \text{Equation(5.43)}$$

By putting $\alpha_5 = \alpha_1^2 - \alpha_2^2$, the part $\left\{ \frac{\alpha_3 + i\alpha_4}{\alpha_1^2 + 2i\alpha_1\alpha_2 - \alpha_2^2} \right\}$ in Equ.5.43 becomes

$$\begin{aligned}
\left\{ \frac{\alpha_3 + i\alpha_4}{\alpha_1^2 + 2i\alpha_1\alpha_2 - \alpha_2^2} \right\} &= \frac{\alpha_3 + i\alpha_4}{\alpha_5 + 2i\alpha_1\alpha_2} \\
&= \frac{\alpha_3 + i\alpha_4}{\alpha_5 + 2i\alpha_1\alpha_2} \times \frac{\alpha_5 - 2i\alpha_1\alpha_2}{\alpha_5 - 2i\alpha_1\alpha_2} \\
&= \frac{\alpha_3\alpha_5 - 2i\alpha_1\alpha_2\alpha_3 + i\alpha_4\alpha_5 + 2\alpha_1\alpha_2\alpha_4}{\alpha_5^2 + 4\alpha_1^2\alpha_2^2} \\
&= \frac{\alpha_3\alpha_5 + 2\alpha_1\alpha_2\alpha_4 + i(\alpha_4\alpha_5 - 2\alpha_1\alpha_2\alpha_3)}{\alpha_5^2 + 4\alpha_1^2\alpha_2^2}
\end{aligned} \tag{Equation(5.44)}$$

By putting Equ.5.44 in Equ.5.43, then

$$\begin{aligned}
Im\tilde{\varepsilon}_{xy}^{eff} &= Im\tilde{\varepsilon}_{xy}^{In_2O_3} + \\
&Im \left\{ \frac{\alpha_3\alpha_5 + 2\alpha_1\alpha_2\alpha_4 + i(\alpha_4\alpha_5 - 2\alpha_1\alpha_2\alpha_3)}{\alpha_5^2 + 4\alpha_1^2\alpha_2^2} \right\}
\end{aligned} \tag{Equation(5.45)}$$

$$Im\tilde{\varepsilon}_{xy}^{eff} = Im\tilde{\varepsilon}_{xy}^{In_2O_3} + \left\{ \frac{\alpha_4\alpha_5 - 2\alpha_1\alpha_2\alpha_3}{\alpha_5^2 + 4\alpha_1^2\alpha_2^2} \right\} \tag{Equation(5.46)}$$

Since we assumed that $\tilde{\varepsilon}_{xy}^{In_2O_3}$ is very small, the part $Im\tilde{\varepsilon}_{xy}^{In_2O_3}$ can be ignored. As a result, Equ.5.46 becomes

$$Im\tilde{\varepsilon}_{xy}^{eff} = \frac{\alpha_4\alpha_5 - 2\alpha_1\alpha_2\alpha_3}{\alpha_5^2 + 4\alpha_1^2\alpha_2^2} \tag{Equation(5.47)}$$

The values of a and b are calculated from Equ.13, where, L_{xx} is a fitting parameter and the index of refraction as a function of energy is obtained from the Swanepoel method, explained in section 3.9, for pure In_2O_3 thin film grown under the same growth conditions, which in this case was at low oxygen pressure, as given in chapter 4. The values of α_1 and α_2 are calculated from the real (ε'_{xx}) and imaginary (ε''_{xx}) part of the diagonal element of the dielectric tensor of Fe_3O_4 as mentioned in Equ.5.33, Equ.5.38 and Equ.5.39, where the real (ε'_{xx}) and imaginary (ε''_{xx}) parts of the diagonal element of the dielectric tensor of Fe_3O_4 are a function of energy, as shown in Fig.5.4.

Removed
by the author
for copyright reasons

Figure 5.4: The real (ϵ'_{xx}) and imaginary (ϵ''_{xx}) part of the diagonal element of the dielectric tensor of Fe_3O_4 [12].

The values of α_3 and α_4 were calculated from the values of the real (ϵ'_{xy}) and imaginary (ϵ''_{xy}) parts of the off-diagonal element of the dielectric tensor of Fe_3O_4 using Equ.5.40, and Equ.5.41. The spectra of the real (ϵ'_{xy}) and imaginary (ϵ''_{xy}) parts of the off-diagonal element of the dielectric tensor of Fe_3O_4 as a function of energy are shown in Fig.5.5.

Removed
by the author
for copyright reasons

Figure 5.5: The real (ϵ'_{xy}) and imaginary (ϵ''_{xy}) parts of the off-diagonal element of the dielectric tensor of Fe_3O_4 [12].

Determination of the values of $\alpha_1, \alpha_2, \alpha_3, \alpha_4,$ and α_5 , paves the way for calculating the value of $Im\tilde{\epsilon}_{xy}^{eff}$ as a function of energy theoretically. However, experimentally, the following form of the dielectric tensor is used.

$$\hat{\epsilon} = \begin{pmatrix} \epsilon_1 & +i\gamma & 0 \\ -i\gamma & \epsilon_1 & 0 \\ 0 & 0 & \epsilon_2 \end{pmatrix} \quad \text{Equation(5.48)}$$

Each element is complex. Below the band gap, the absorption of indium oxide is ignored; therefore, $\epsilon_1' = n^2$ and $\epsilon_1'' = 0$. Above the band gap energy of indium oxide, this approximation will not be valid. If ϵ_{xy} is defined as above, then

$$\gamma = \gamma' + i\gamma'' \quad \text{Equation(5.49)}$$

where

$$\gamma' \approx \frac{\lambda n}{\pi d} \theta_F \quad \text{Equation(5.50)}$$

$$\gamma'' \approx \frac{\lambda n}{\pi d} \eta_F \quad \text{Equation(5.51)}$$

For our Fe_3O_4 nanoparticles in In_2O_3 samples, the wavelength dependence of the normal refractive index n was taken as in equ.5.23. The real part of γ was calculated at each photon energy step using the measured Faraday rotation (θ_F). Similarly, the imaginary part of γ was calculated at each photon energy step using the Faraday ellipticity (η_F).

The spectrum of $Im\tilde{\epsilon}_{xy}^{eff}$ as a function of energy was calculated theoretically using Equ.5.47 and fitted to the spectrum of γ'' obtained experimentally as a function of energy over the energy range 1.5 to 2.7 eV, where the magneto-optical response from the In_2O_3 is expected to be negligible, using f , and L_{xx} as free parameters. The spectra of the off-diagonal element $Im\tilde{\epsilon}_{xy}^{eff}$ and γ'' are shown in Fig.5.6.

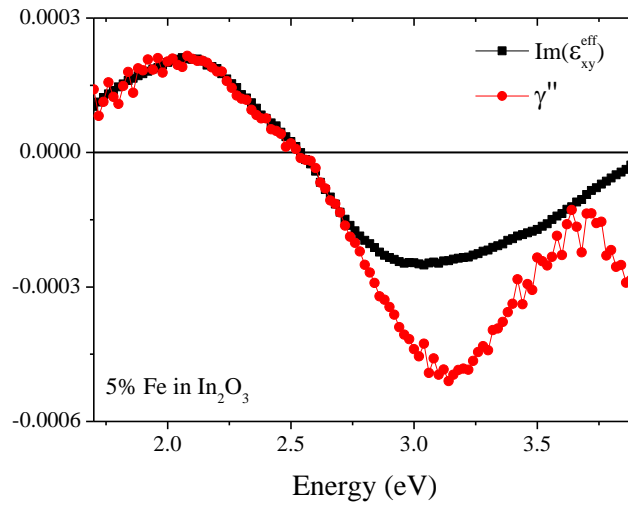


Figure 5.6: The imaginary ($\tilde{\epsilon}_{xy}^{eff}$) part calculated theoretically, which represents the response of Fe_3O_4 nanoparticles fitted to the imaginary (γ'') part of the off-diagonal element measured experimentally.

Fig.5.6 shows the imaginary part of the off-diagonal dielectric constant calculated theoretically which represents the response of the Fe_3O_4 nanoparticles, whereas the imaginary part of the off-diagonal dielectric constant deduced from Faraday ellipticity measurements represents the overall response of In_2O_3 plus that of the Fe_3O_4 nanoparticles. The contribution of the indium oxide matrix to the MCD signal can be obtained from the fitting, as shown in Fig.5.7.

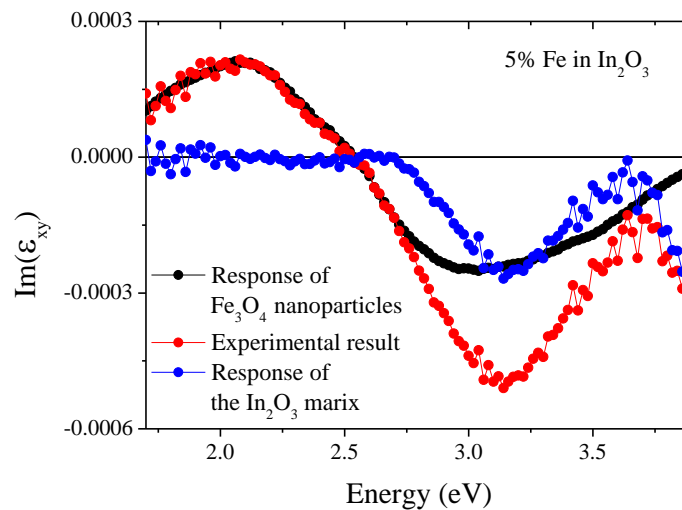


Figure 5.7: MCD spectra of Fe-doped In_2O_3 (red line) fitted with black line using Maxwell-Garnett theory to determine the fraction and the contribution of the Fe_3O_4 nanoparticles to the host material, while the blue line is the actual contribution corresponding to the In_2O_3 matrix.

In Fig.5.7, the response of the Fe₃O₄ nanoparticles is shown as a black line, while, the blue line represents the MCD signal due to the contribution of the Indium oxide matrix concentrated below the optical absorption edge. At this stage, the demagnetizing factor of the inclusions L_{xx} and the fraction f of the Fe₃O₄ nanoparticles are determined.

5.4 Conclusion

This chapter develops magneto-optical method as a lab-based alternative to EXAFS for determining the fraction, the magnetization and the magneto-optical responses of Co and Fe₃O₄ nanoparticles in SMS thin films. This was achieved by developing Maxwell-Garnett (M-G) theory. EXAFS measurements tell us whether the thin films contain nanoparticles or not, but do not give the fraction of these nanoparticles or the contribution of these nanoparticles of the overall magnetization or magneto-optical response. The magneto-optical method is cheaper where there is no cyclotron system required, safer where there is no involvement with X-ray radiation, quantitative, and more accurate than the EXAFS method.

5.5 References

1. J. Y. Kim, J. H. Park, B. G. Park, H. J. Noh, S. J. Oh, J. S. Yang, D. H. Kim, S. D. Bu, T. W. Noh, H. J. Lin, H. H. Hsieh and C. T. Chen, *Physical Review Letters* **90**, 017401 (2003).
2. J. M. D. Coey, A. P. Douvalis, C. B. Fitzgerald and M. Venkatesan, *Applied Physics Letters* **84**, 1332-1334 (2004).
3. J. M. D. Coey, M. Venkatesan and C. B. Fitzgerald, *Nat Mater* **4**, 173-179 (2005).
4. C. Clavero, B. Sepúlveda, G. Armelles, Z. Konstantinovi, M. G. d. Muro, A. Labarta and X. Batlle, Vol. **100**. 2006: AIP. 074320.
5. D. Stroud, *Physical Review B* **12**, 3368 (1975).
6. J. S. Ahn, K. H. Kim, T. W. Noh, D. H. Riu, K. H. Boo and H. E. Kim, *Physical Review B* **52**, 15244 (1995).
7. P. B. Johnson and R. W. Christy, *Physical Review B* **6**, 4370 (1972).
8. N. D. Fatti, F. Vallée, C. Flytzanis, Y. Hamanaka and A. Nakamura, *Chemical Physics* **251**, 215-226 (2000).
9. G.S. Krinchik, Vol. **35**. 1964: AIP. 1089-1092.
10. R. Carey and B. W. J. Thomas, *Journal of Physics D: Applied Physics* **7**, 2362 (1974).
11. C. Clavero, A. Cebollada, G. Armelles, Y. Huttel, J. Arbiol, F. Peiró and A. Cornet, *Phys Rev* **72**, 02441 (2005).
12. W. F. J. Fontijn, P. J. V. D. Zaag, M. A. C. Devillers, V. A. M. Brabers and R. Metselaar, *Physical Review B* **56**, 5432 (1997).

Chapter 6 – Co Doped In₂O₃

6.1 Introduction

The transition metal (TM) doped semiconductor oxide was found to show ferromagnetism at room temperature [1-10]. The ferromagnetism in semi magnetic semiconductors (SMS) is usually attributed to the interaction between the host *s*, *p* bands carriers and the localized *3d* electrons in doped transition metal elements. Several theoretical models have been suggested based on the *s(p)-d* interactions feature, and these fall into two categories: the first category is the carrier-mediated models like the Zener model and the Ruderman-Kittel-Kasuya-Yosida (RKKY) model [11, 12]. In the carrier-mediated models, the coupling between magnetic ions is achieved through the mobile carriers, i.e., holes in the valence band or electrons in the conduction band. The second category is the super exchange models like the double-exchange model [13-16]. In super exchange models, the coupling is achieved between magnetic ions through the localized carriers.

This chapter investigates the optical and magneto optical response of the Co-doped In₂O₃ thin films deposited in different growth conditions, and compares the result with that obtained previously for a pure In₂O₃ thin film in order to assess the effect of the Co doping. The Maxwell-Garnett (M-G) theory discussed in last chapter is used to determine the fraction and the magneto-optical response of metallic Co in some thin films where the existence of metallic Co is confirmed. The influence of co-doping In₂O₃ with Co plus Sn simultaneously is also covered.

6.2 Experiment Details, Results, and Discussion

In order to investigate the influence of Co doping content on the optical and magneto-optical properties of In₂O₃, Five thin films of (In_{1-x}Co_x)₂O₃ with *x* = 0.01, 0.02, 0.03, 0.04, 0.05 were deposited by A. Hakimi in the University of Cambridge.

The thin films were grown in a highly oxygen deficient environment using dc magnetron sputtering on sapphire substrate at 300 °C. Pure In₂O₃ thin films were also grown at the same time under the same conditions as the Co-doped samples and served as a set of control samples. The data described in this section have been published [17]. The deposition details are shown in Table.6.1.

SAMPLE	CONTENT	THICKNESS (nm)	PRESSURE (mTorr)	TEMPERATURE (°C)	DEPOSITION	
					METHOD	SUBSTRATE
016	In ₂ O ₃	200	0.562	330	dc. magnetron sputtering	Al ₂ O ₃ (0001)
006	(In _{0.99} Co _{0.01}) ₂ O ₃	200	0.562			
007	(In _{0.98} Co _{0.02}) ₂ O ₃	200	0.562			
008	(In _{0.97} Co _{0.03}) ₂ O ₃	200	0.562			
009	(In _{0.96} Co _{0.04}) ₂ O ₃	200	0.562			
010	(In _{0.95} Co _{0.05}) ₂ O ₃	200	0.562			

Table 6.1: Growth details of (In_{1-x}Co_x)₂O₃ thin films.

An energy dispersive x-ray spectroscopy (EDX) compositional analysis revealed that the actual contents of Co were 1.6, 3.1, 4.7, 6.4, and 8.1% and the films were uniformly doped. XRD measurements performed by A. Hakimi confirmed the bixbyite cubic structure of (In_{1-x}Co_x)₂O₃ thin films, which implies that Co-doping up to 8.1% has no effect on the bixbyite cubic structure of pure In₂O₃. The XRD analysis given in Fig.6.4 (a) shows no detectable peaks corresponding to any secondary phases of oxides of Co or metallic Co. Also, a shift in the In₂O₃ (222) and (400) diffraction peaks towards higher values of 2θ with an increase of Co content implies the substitution of Co²⁺ ions (ionic radius 0.74 Å) with In³⁺ ions (ionic radius 0.94 Å) at In sites rather than the formation of a defect phase; this was confirmed afterward by EXAFS measurements as shown in Fig.6.4 (b).

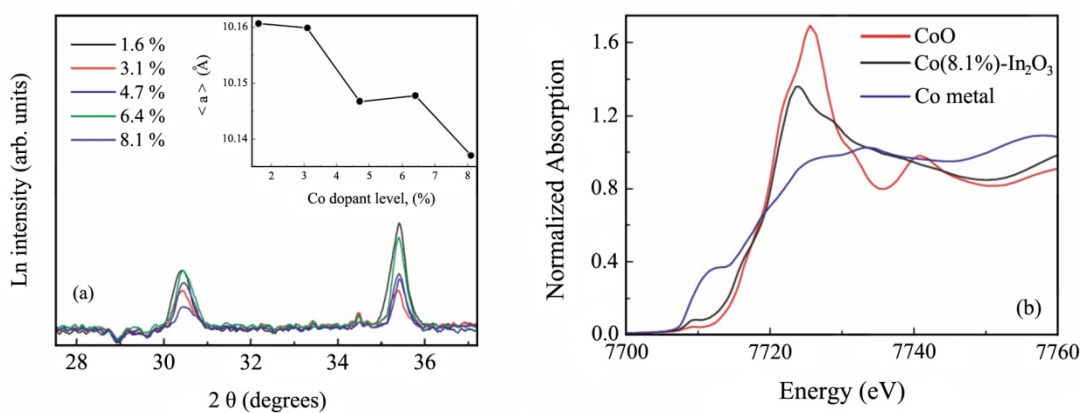


Figure 6.1: (a) XRD data where the lattice constant decreases with the increase of Co content. (b) Normalized Co near-edge EXAFS spectra of the In₂O₃ thin film doped with 8.1% Co compared with CoO and Co metal [17].

The EXAFS measurements were performed at the Advanced Photon Source by S. M. Heald. The EXAFS data was for In_2O_3 thin film doped with 8.1% Co compared with CoO and Co metal. The position of the EXAFS spectra edges in Fig.6.4 (b) indicates that the Co is predominately Co^{2+} . The increased pre-edge feature near 7710 eV indicates the presence of a small amount of Co metal. However, Heald reported that the thin films have very small grains and there is no evidence of metallic Co nanoparticles. The resistance of $(\text{In}_{1-x}\text{Co}_x)_2\text{O}_3$ thin films as a function of temperature follows the typical resistance (R) versus T curve of semiconductor materials, where the resistivity of the semiconductor increases with decreases in temperature. Variation of resistance of 1.6% of Co thin film with temperature is shown in Fig.6.2 (a).

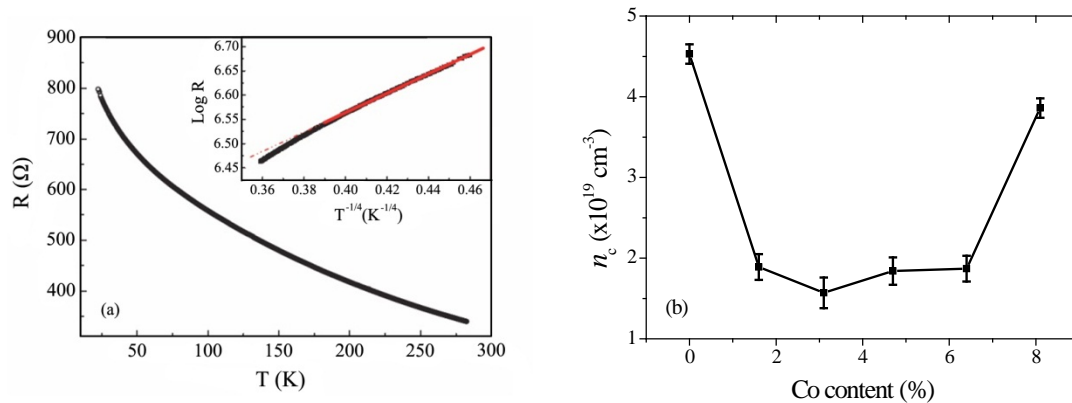


Figure 6.2: (a) Resistance, R , versus temperature curve for an In_2O_3 film doped with 1.6% Co. Inset: $\log R$ versus $T^{-1/4}$ plot for temperatures below 50 K. (b) Variation of carrier density n_c with an increases of Co-doping content [17].

Variation of carrier concentration n_c with Co content is shown in Fig.6.2 (b). The carrier concentration of $(\text{In}_{1-x}\text{Co}_x)_2\text{O}_3$ thin films dropped with doping with cobalt comparing with that of pure In_2O_3 ; thus, the carrier concentration decreases with increases in the cobalt content, and the carrier concentration of 8.1% Co-doped In_2O_3 increases to be equal to the carrier concentration of pure In_2O_3 . The carrier's density measured at room temperature is not linearly dependent on the concentration of Co^{2+} ions.

Magnetic properties were investigated using the superconducting quantum interference device (SQUID) magnetometer in the temperature range of 5–300 K in

magnetic fields up to 1 Tesla. Variations of the magnetic moment with an applied magnetic field displayed clear evidence of ferromagnetism in each of the Co-doped In_2O_3 films up to and above room temperature as shown in Fig.6.3. The substrates were repeatedly measured at both low and high temperature and consistently gave a diamagnetic response. The complete data for magnetization, carrier concentration, and mobility can be found in the paper [17].

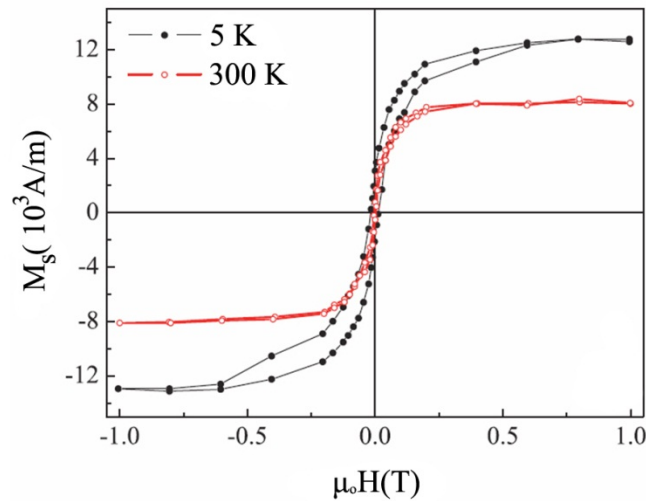


Figure 6.3: Ferromagnetic hysteresis loops for an 8.1% Co-doped In_2O_3 thin film at 5 and 300 K [17].

The optical properties of $(\text{In}_{1-x}\text{Co}_x)_2\text{O}_3$ thin films were measured at room temperature over the range of energy of 1.7eV to 4.5eV. The optical transmission spectra as a function of cobalt concentration are shown in Fig.6.4.

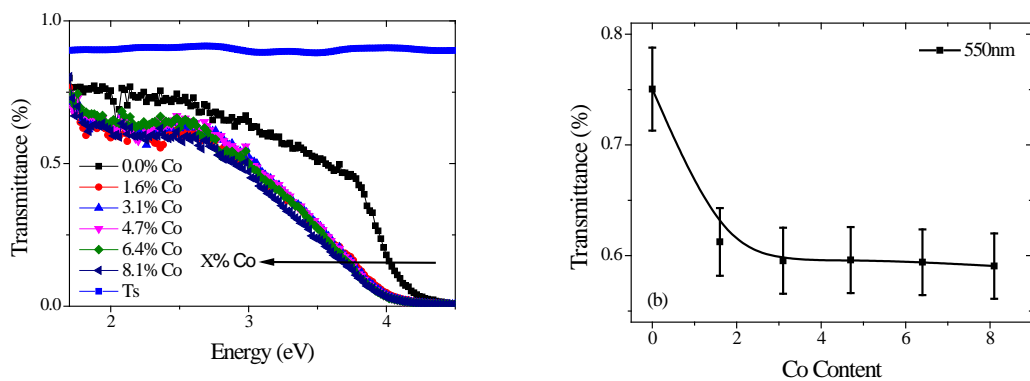


Figure 6.4: (a) Shows the optical transmission spectra of $(\text{In}_{1-x}\text{Co}_x)_2\text{O}_3$ thin films measured at RT. (b) The optical transmission spectrum at 550 nm, 2.3eV, as a function of Co content.

The optical transmission spectra illustrated in Fig.6.4 show a decrease in the transmission light and a shift in the optical absorption edge toward low energy with an increase in Co content. There is evidence of the formation of oxygen vacancy levels below the optical band gap at 3.3eV for pure and Co-doped In_2O_3 thin films, where the transmission at 3.3eV is much lower than that at 2.0eV. This gives an indication that there are transitions only between the valance band and the oxygen vacancy levels around 3.3eV, whereas no transmission occurs around 2.0eV, implying that there is no metallic Co formed in these thin films [18, 19]. The density of oxygen vacancy levels increases with increases in Co-doping, whereas the transmission of pure In_2O_3 drops sharply with Co doping at 3.3eV. The shift of the optical absorption edge toward low energy with an increase in Co content implies the decrease in carrier concentration with increases in Co content, which is in accordance with what has been found previously in Fig.6.2 (b). The variations in the absorption spectra with Co content are shown in Fig.6.5.

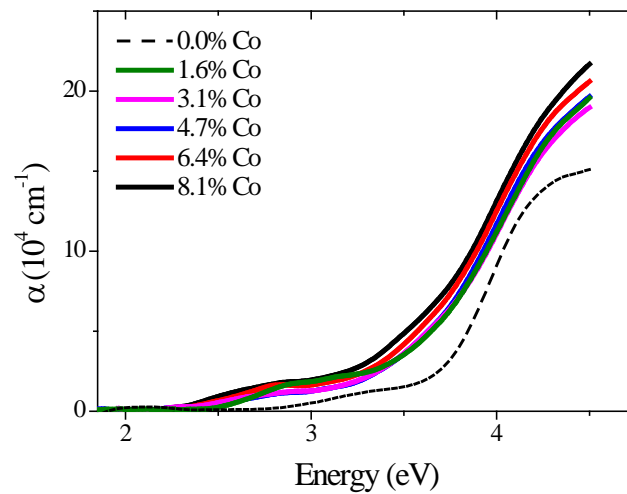


Figure 6.5: Variations in the optical absorption spectra of $(\text{In}_{1-x}\text{Co}_x)_2\text{O}_3$ thin films with Co content measured at RT.

The optical absorption spectra of the sputtered $(\text{In}_{1-x}\text{Co}_x)_2\text{O}_3$ thin films show non-zero absorption within the optical band gap energy range starting from 2.5eV to the optical absorption edge. The absorption of pure In_2O_3 thin film deposited under the same conditions, starting around 2.8eV, implies that NBE oxygen vacancy levels are formed as long as the thin film is deposited at low oxygen pressure. The density of the oxygen vacancy levels increases with an increase in Co content and goes deeper

within the optical band gap as shown in Fig.9 for those samples doped with Co. The optical band gap is higher for pure In_2O_3 than that for Co-doped In_2O_3 . The optical band edge is shifting toward lower energy with an increase in Co content due to the expansion of the lattice in order to fit the doped Co atoms. The variation of $\alpha^2 E^2$ and the optical band gap energy with Co content is shown in Fig.6.6.

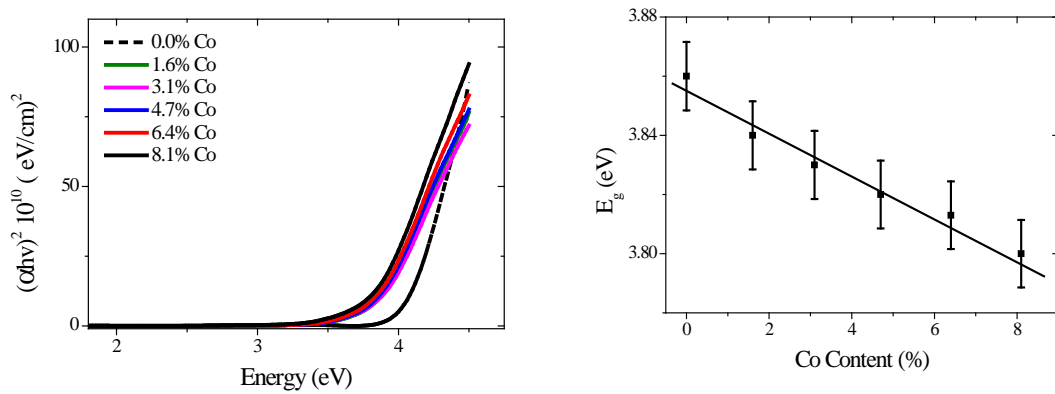


Figure 6.6: Variations in $(\alpha h\nu)^2$ and the optical band gap energy with Co content.

The variations in the optical band gap energy with an increase in Co content in $(\text{In}_{1-x}\text{Co}_x)_2\text{O}_3$ thin films show that, the band gap energy decreases with Co doped and decreases further with an increase in Co content. The variations in MCD spectra of $(\text{In}_{1-x}\text{Co}_x)_2\text{O}_3$ thin films with Co content are shown in Fig.6.7.

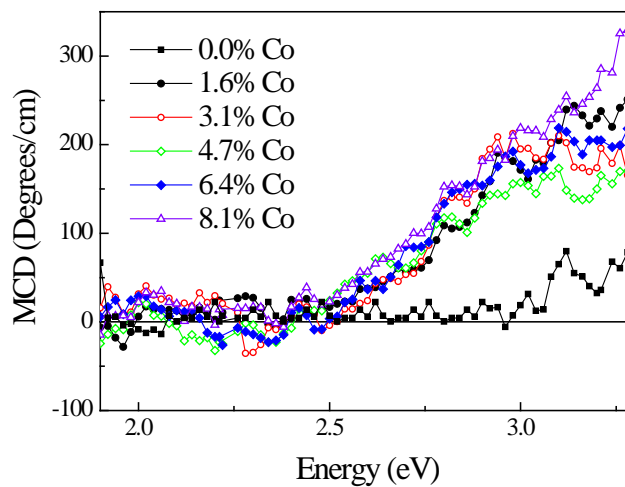


Figure 6.7: Variations in MCD spectra with Co content of $(\text{In}_{1-x}\text{Co}_x)_2\text{O}_3$ thin films.

The data illustrated in Fig.6.7 was measured at RT and a magnetic field of 1.8Tesla. The optical band gap energies fall within the range of energy between 3.80eV and 3.86eV, as shown in Fig.6.7. The MCD shown in Fig.6.8 shows an MCD feature at 3.3eV located below the optical band gap energy of the $(\text{In}_{1-x}\text{Co}_x)_2\text{O}_3$ thin films. This MCD feature appeared for both pure and Co-doped In_2O_3 thin films and the MCD features initialized from the sample energy where the absorption in Fig.6.5 became non-zero, implying the increasing numbers of allowed transitions from the valence band to the oxygen defects bands were a consequence of the broken symmetry introduced by Co doping. The observation of MCD signals rising at energies above 2.5 eV demonstrates these transitions involve spin-polarized states. The MCD of the pure In_2O_3 sample and the Co-doped samples are consistent with the strength of absorption spectra shown in Fig.10. The MCD contribution of the sapphire substrate was subtracted from all the thin films' MCD spectra. Usually, the existence of Co^{2+} ions in a thin film leads to a dispersive MCD signal around 2eV. The MCD spectrum does not show any peak at 2eV and it could be too weak to be detected. The observed MCD signal at 3.3eV shows the correct dependence on cobalt concentration, and the shape of the MCD spectrum at 300K does not indicate any contribution from metallic cobalt [20] or CoO [21], as is shown in the next section. The variation of the MCD spectrum at 3.3eV and the saturation magnetization, M_s , with an increase in Co content is shown in Fig.6.8. (The data were plotted so the values agree at 8%).

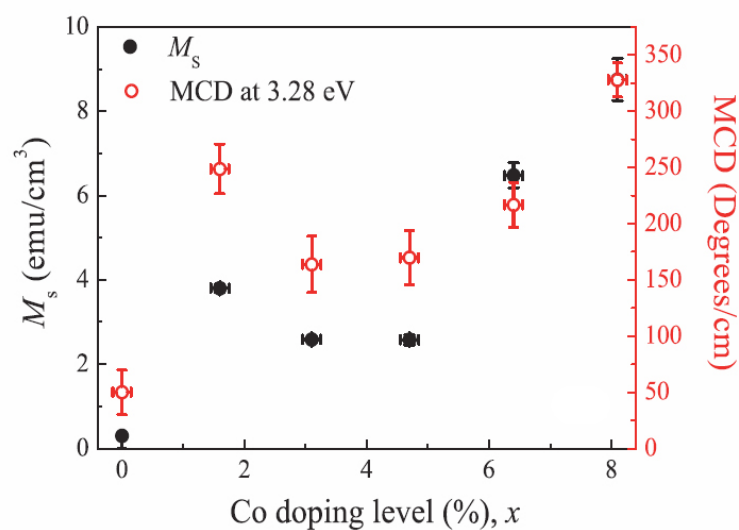


Figure 6.8: Room temperature MCD (taken at 3.28 eV) and saturation magnetization, M_s , as a function of Co doping level [17].

The agreement between the MCD data and the saturation magnetization data provides strong evidence that these donor states are related to the ferromagnetism. Investigating the temperature dependence of the MCD spectrum provided more details about the origin of the MCD signal. Therefore, the MCD spectrum of 8.1% Co-doped In_2O_3 thin film as a function of temperature was measured at a magnetic field of 0.5 Tesla. The variation of the MCD spectrum with temperature is shown in Fig.6.9.

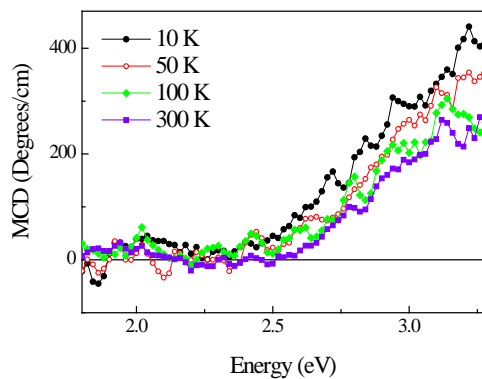


Figure 6.9: Temperature dependence of the MCD spectrum of 8.1% Co-doped In_2O_3 thin film measured at a magnetic field of 0.5 Tesla.

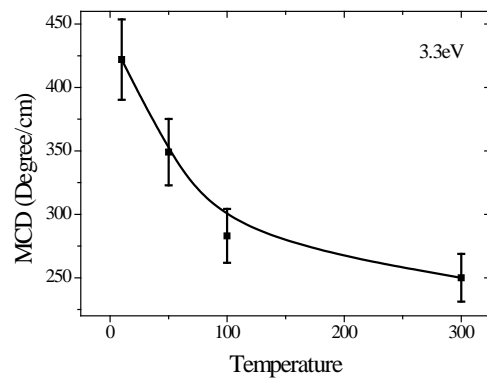


Figure 6.10: Variation of the MCD spectrum at 3.3 eV with an increase in temperature of 8.1% Co-doped In_2O_3 thin film measured at 0.5 Tesla.

Fig.6.9 illustrated that, The change in the strength of the MCD between 5 and 300 K at the same magnetic field implies the independence of the MCD signal from any increase in the paramagnetic component. The variation of MCD signals with an increase in temperature is shown in Fig.6.10. The ratio of the magnitude of the MCD at 10 and 300 K agrees very well with the reduction of the magnetization between 5 and 300 K given in Fig.6.3. The MCD and the magnetization have the same temperature, and concentration dependence is strong evidence to support the contention that the observed ferromagnetism originates from the same donor states as those involved in the optical transitions. The ferromagnetic origin of the band edge MCD is confirmed further by the observation of an open MCD hysteresis loop for the Co-doped films.

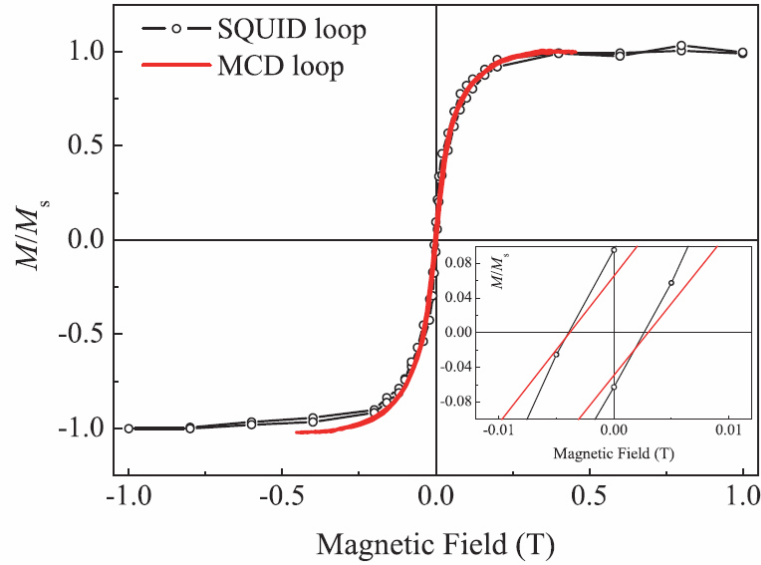


Figure 6.11: Hysteresis loops for an 8.1% Co-doped In_2O_3 film using a SQUID magnetometer and using MCD taken at 3.2 eV at room temperature. In both cases, the background signal from the substrate was subtracted[17].

Fig.6.11 shows that, the MCD loop of an 8.1% Co-doped In_2O_3 sample was superimposed upon a magnetic hysteresis loop for the same film measured using a SQUID at room temperature. The shapes of the loops are very similar, and the coercive fields are almost identical (inset, Fig. 6.11).

Ali films were deposited using sputtering system has no metallic Co while thin films gown using PLD system containing an amount of metallic Co. Typical that film characteristic is very sensitive to the exact conditions of fabrication.

In order to investigate the variation of optical and magneto-optical properties of Co-doped In_2O_3 with oxygen partial pressure, annealing in vacuum process, and doping with Tin, KACST engineers S. Alfahad and M. Alotibi deposited thin films of $(\text{In}_{1-x-y}\text{Co}_x\text{Sn}_y)_2\text{O}_3$ on sapphire (Al_2O_3) substrates using the PLD system. The data of some representative thin films will be given. The annealed thin films were in a vacuum for half an hour. The substrate temperature of these thin films was sustained at 600 °C and the oxygen partial pressure was varied between 2×10^{-3} mTorr and 10mTorr. The growth details are shown in Table 6.2.

SAMPLE	CONTENT	THICKNESS (nm)	PRESSURE (mTorr)	ANNEALING for 30 Min °C	TEMPERATURE (°C)	LASER ENERGY (mJ)	DEPOSITION METHOD	SUBSTRATE Al ₂ O ₃ (0001)
355T79 SP	(In _{0.95} Co _{0.05}) ₂ O ₃	152	2x10 ⁻³	No	600	300	PLD	
368T79SP		240	10					
356T79SP		151	2x10 ⁻³	300				
357T79SP		143	2x10 ⁻³	400				
358T79SP		141	2x10 ⁻³	500				
486T80SP	(In _{0.90} Co _{0.05} Sn _{0.05}) ₂ O ₃	186	2x10 ⁻³	No	600	300	PLD	
487T81SP	(In _{0.85} Co _{0.05} Sn _{0.10}) ₂ O ₃	174	2x10 ⁻³					

Table 6.2: Growth details of (In_{0.95}Co_{0.05})₂O₃ thin film at different oxygen partial pressures.

The EXAFS measurements by Heald for Co-doped In₂O₃ thin film un-annealed and annealed at 500°C compared with CoO and Co metal are shown in Fig.6.12.

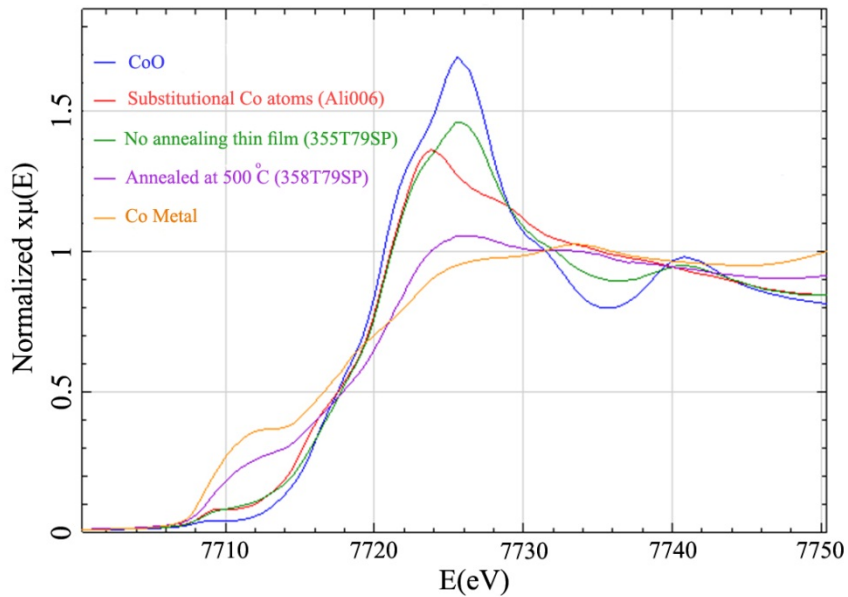


Figure 6.12: Normalized Co near-edge EXAFS spectra of the un-annealed and grown at low oxygen pressure and annealed In₂O₃ thin films at 500°C compared with CoO, Co metal, and substitutional Co atoms in In₂O₃ matrix.

The increased pre-edge EXAFS feature of un-annealed and annealed thin films near 7710 eV at 500°C indicates the presence of Co metal in annealed thin film as is implied by the shift of the purple spectrum line toward the Co metal orange spectrum line.

The ferromagnetic hysteresis loops measured at RT and a magnetic field of 1 Tesla by Al Qahtani using a SQUID magnetometer as shown in Fig.6.13 (a) for thin films grown at different oxygen partial pressure and shown in Fig.6.13 (b) for thin films annealed in vacuum at different temperature.

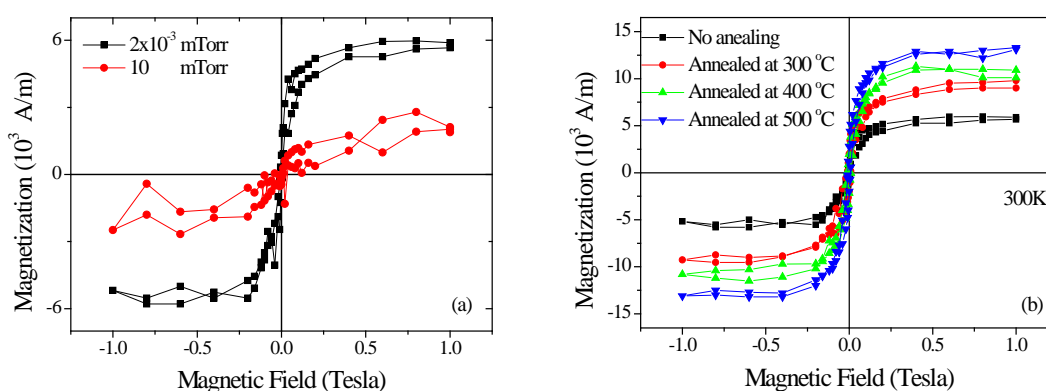


Figure 6.13: Variation of magnetization of $(\text{In}_{0.95}\text{Co}_{0.05})_2\text{O}_3$ thin films with (a) Oxygen partial pressure, (b) Annealing in vacuum at different temperatures.

Fig.6.13 provides clear evidence of ferromagnetism in each of the Co-doped In_2O_3 thin films up to and beyond room temperature. The magnetic moment increases with decreases in oxygen partial pressure, as shown in Fig.6.13 (a), due to the increase of oxygen vacancy density and the magnetic moment increases with an increase in the annealing in vacuum temperature, as shown in Fig.6.13 (b) due to the increase of oxygen vacancy density plus the increase of the fraction of metallic Co with annealing temperature.

The variation of the optical transmission spectra with oxygen partial pressure and annealing in vacuum temperature are shown in Fig.6.14 (a) and Fig.6.14 (b) respectively.

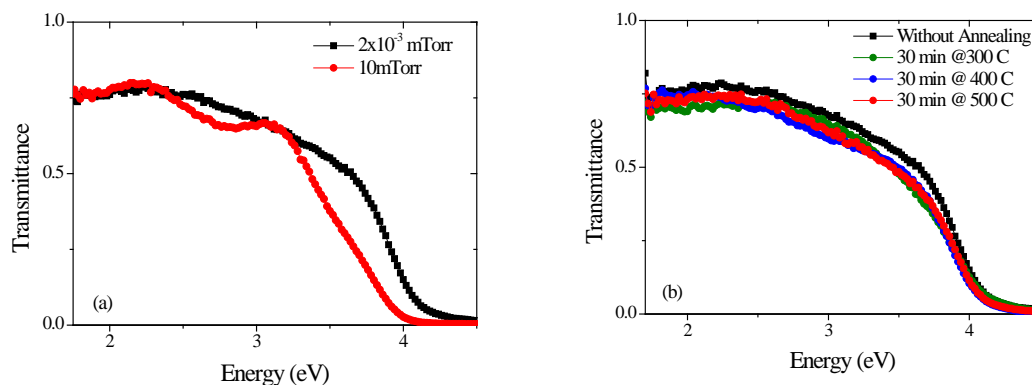


Figure 6.14: Variation in the optical transmission spectra of $(\text{In}_{0.95}\text{Co}_{0.05})_2\text{O}_3$ thin films with (a) Oxygen partial pressure, (b) Annealing in vacuum temperature.

The transmission spectra of $(\text{In}_{0.95}\text{Co}_{0.05})_2\text{O}_3$ thin films grown at 2×10^{-3} mTorr and 10 mTorr are illustrated in Fig. 6.14 (a); this shows that the transmission within the transparent region of the spectrum reaches 78%, which is lower than that observed for pure In_2O_3 thin films, as discussed in chapter 4, which reach 89%. The difference in oxygen partial pressure has no effect on the transmission spectrum at low energy, especially below 2.5 eV. Above this energy and to the absorption edge, a notable wide impurity band is formed below the optical absorption edge for the sample deposited at oxygen partial pressure of 2×10^{-3} mTorr. There is a shift in the optical absorption edge toward high energy with a decrease in oxygen partial pressure which concurs with what has been seen for pure In_2O_3 thin films. The difference that the Co ions made in these samples is that the transmission decreased over all the range of energy compared with pure In_2O_3 thin films and the impurity band that formed below the band gap edge looks larger and wider for the thin film grown at 2×10^{-3} mTorr in comparison with the pure sample grown at the same oxygen partial pressure. Fig. 6.15 (b) shows that, the transmission spectrum decreases with the increase in annealing temperature. This behaviour is the opposite of the variation of transmittance with the increase in annealing temperature for un-doped In_2O_3 discussed previously. This drop in transparency of the samples implies the formation of clusters of Co nanoparticles in these films due to the annealing process, as confirmed by EXAFS measurements shown in Fig. 6.13. The variation of the optical absorption coefficient with oxygen partial pressure and annealing in vacuum temperature are shown in Fig. 6.15 (a) and Fig. 6.15 (b) respectively.

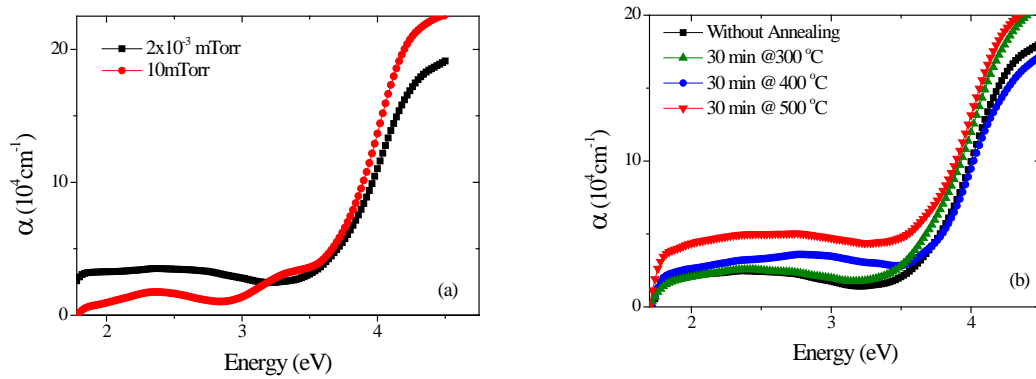


Figure 6.15: Variation in the optical absorption coefficient of $(\text{In}_{0.95}\text{Co}_{0.05})_2\text{O}_3$ with (a) Oxygen partial pressure, (b) Annealing in vacuum temperature.

Fig.6.15 (a) shows two absorption features seen at 2.3eV and 3.3eV in both samples. The feature at 2.3eV did not exist before in the optical absorption spectrum of pure In_2O_3 discussed in chapter 4, which means that this feature is related to the TM-doped material (cobalt). In fact, the feature at 2.3eV implies the formation of Co nanoparticles in both thin films and the density of the Co nanoparticles is greater in the sample deposited at base pressure; this explains the high and wide absorption seen at this energy. The source of these peaks can be explored in greater depth through the magneto-optical measurement. Fig.6.15 (b) shows that, the optical absorption coefficient is annealing-temperature dependent. The absorption spectra show continuous transitions from 1.8eV to around 3.9eV where the band gap is. These continuous transitions are due to the formation of defect bands below the band gap energy and due to the contribution of metallic Co. The variation in the absorption coefficient squared and the optical band gap with oxygen partial pressure and annealing in vacuum temperature are shown in Fig.6.16 (a) and Fig.6.16 (b) respectively.

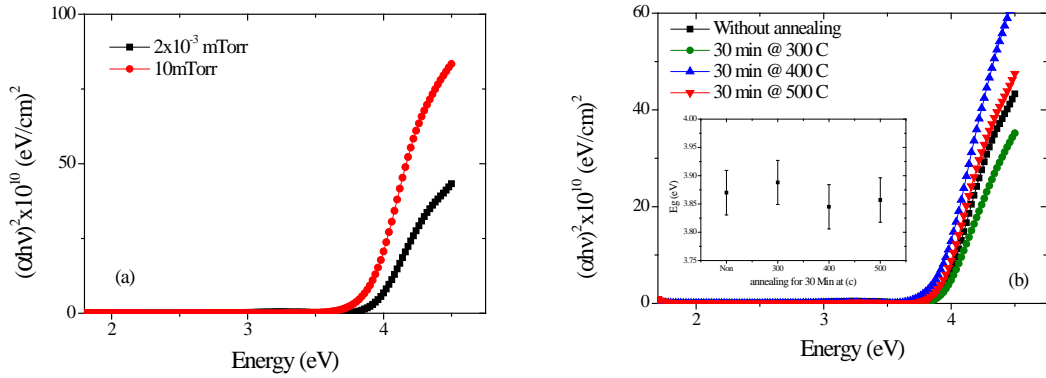


Figure 6.16 : Variation in the optical band gap energy of $(\text{In}_{0.95}\text{Co}_{0.05})_2\text{O}_3$ thin films with (a) oxygen partial pressure, (b) Annealing in vacuum temperature.

Fig.6.16 (a) shows that, the optical band gap energy of $(\text{In}_{0.95}\text{Co}_{0.05})_2\text{O}_3$ thin films increases with decreases in oxygen partial pressure. The same behaviour was observed in pure In_2O_3 thin films, and doping In_2O_3 with up to 5% of cobalt has no effect on the variation of the optical band gap of In_2O_3 semiconductor with oxygen partial pressure. Fig.6.16 (b) shows that, the optical band gap energy is annealing-temperature independent within the error range, which indicates that these thin films had been grown with very high crystallization, and no enhancement occurs due to the annealing process. It is expected that the optical band gap energy will shift toward higher energy as seen before for pure In_2O_3 , but in annealed $(\text{In}_{0.95}\text{Co}_{0.05})_2\text{O}_3$ thin films, the carrier density seems to decrease with the annealing process due to the Co doping. The MCD spectrum of $(\text{In}_{0.95}\text{Co}_{0.05})_2\text{O}_3$ thin films are shown in Fig.6.17.

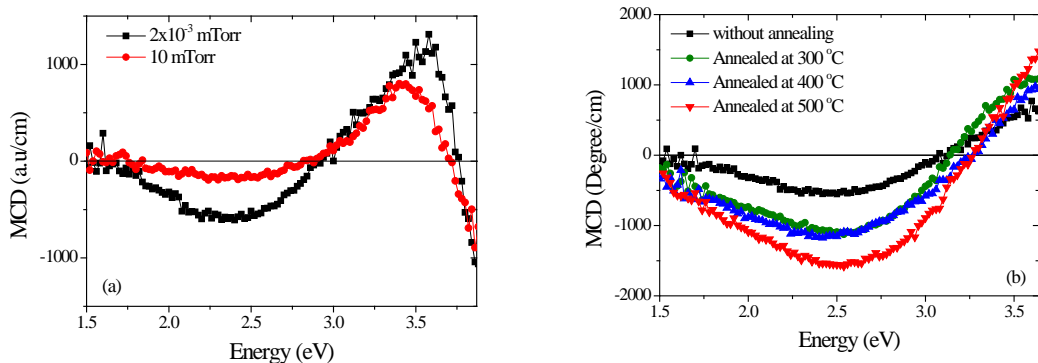


Figure 6.17 : Variation in MCD spectrum of $(\text{In}_{0.95}\text{Co}_{0.05})_2\text{O}_3$ thin films with (a) oxygen partial pressure, (b) Annealing in vacuum temperature.

The variation in the MCD spectrum of $(\text{In}_{0.95}\text{Co}_{0.05})_2\text{O}_3$ thin films with oxygen partial pressure and annealing in vacuum temperature are shown in Fig.6.17 (a) and Fig.6.17 (b) respectively and the data was measured at RT and a magnetic field of 1.8Tesla. Fig.6.17 (a) shows that, both thin films exhibit a negative MCD feature at 2.3eV and a positive MCD feature at 3.4eV. The magnetic circular dichroism spectra are comparable with the imaginary (ϵ''_{xy}) part of the off diagonal element of the dielectric tensor of Co nanoparticles studied by Clavero [22-24]; this confirms the formation of metallic Co in these samples, a claim that was supported by the EXAFS measurements. Fig.6.17 (b) also shows two MCD features at 2.5eV and 3.6eV. Both MCD signals are located below the optical band gap energy, which is 3.8eV. These two features were observed in Fig.6.17 (a) but the location of these two features is shifted with annealing to higher energy by 0.2eV, and the feather at 2.5eV is much larger than that seen before. The MCD feature at 2.3eV is completely due to the metallic Co, and the metallic Co density is oxygen partial pressure and annealing in vacuum dependent and increases with a decrease in oxygen partial pressure or increase in annealing in vacuum temperature. The MCD feature at 3.4eV reflects the response of the metallic Co in addition to the response of the indium oxide matrix. The feature at 2.5eV in Fig.6.17 (b) is completely related to the metallic Co and the appearance of this feature for the un-annealed sample implies the formation of metallic Co is not only an outcome of the annealing process but also due to other growth conditions, most probably the high substrate temperature. The Maxwell-Garnett theory was used to determine the fraction and the contribution of metallic Co.

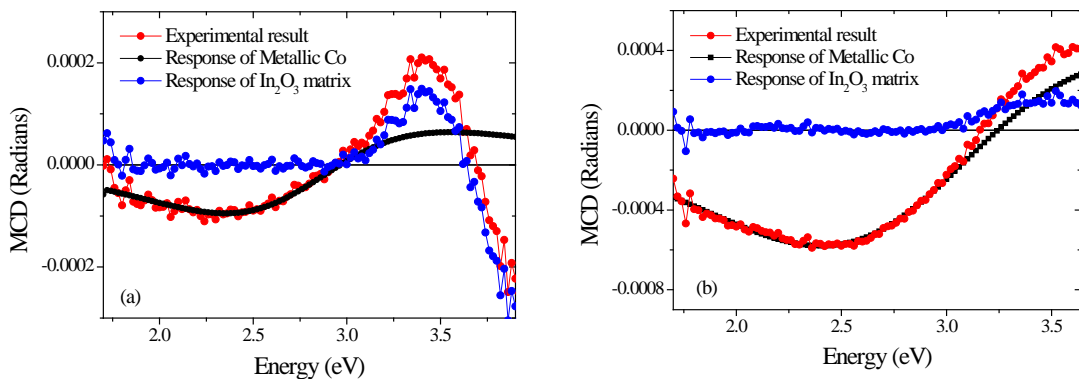


Figure 6.18: Maxwell-Garnett fitting of the MCD spectrum of $(\text{In}_{0.95}\text{Co}_{0.05})_2\text{O}_3$ thin film (a) deposited at 10mTorr. (b) Annealed at 300 °C.

The Maxwell-Garnett theory was used to determine the variation of MCD response and the fraction of metallic Co with Oxygen partial pressure and with the annealing temperature as shown in Fig.6.18. The MCD spectrum due to the response of In_2O_3 matrix is identical to that measured for substitutional Co atoms in the In_2O_3 matrix measured previously and shown in Fig.6.8. The fitting demagnetizing factor L_{xx} was found to be equal to 0.33. The variation in the MCD amplitude due to the metallic Co and the MCD due to the indium oxide matrix with oxygen partial pressure and annealing in vacuum temperature are shown in Fig.6.19 (a) and Fig.6.19 (b) respectively.

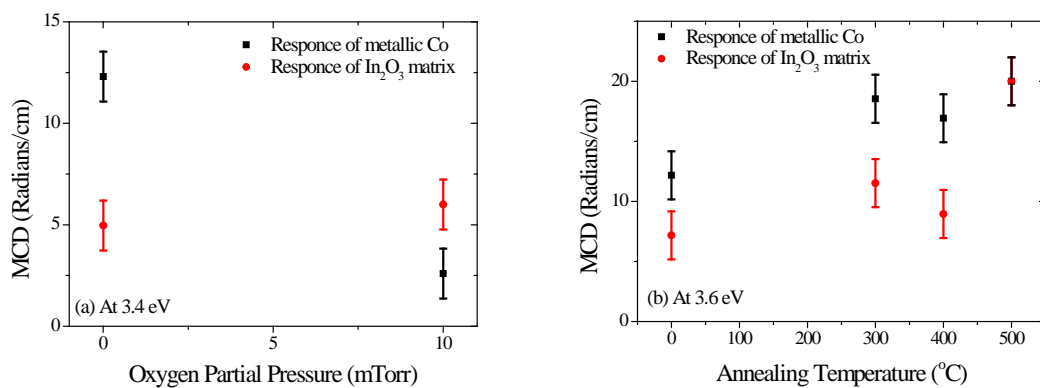


Figure 6.19: Variation in MCD amplitude at 3.4eV of $(\text{In}_{0.95}\text{Co}_{0.05})_2\text{O}_3$ thin films with (a) oxygen partial pressure, (b) Annealing in vacuum temperature.

Fig.6.19 (a) illustrates the MCD signal due to the metallic Co and the MCD signal due to the In_2O_3 matrix at 3.4eV as a function of oxygen partial pressure. In general, the overall MCD amplitude decreases with an increase in oxygen partial pressure due to the decrease in the density of carriers and the density of metallic Co. In Co-doped In_2O_3 thin film grown at 10mTorr, the MCD response of the In_2O_3 matrix is dominant, whereas the MCD response of metallic Co is dominant in the thin film deposited at a low oxygen partial pressure of 2×10^{-3} mTorr, which implies that the thin film deposited at low oxygen partial pressure is rich in metallic Co. Fig.6.20 (b) shows that, the MCD signal is annealing-temperature dependent. The MCD signal due to the metallic Co and the MCD signal due to the In_2O_3 matrix increase with an increase in annealing temperature. The increase in the metallic Co MCD signal with an increase in annealing temperature is due to the increase in metallic Co density with

an increase in annealing temperature whereas the increase in the In_2O_3 matrix MCD signal is due to the increase in oxygen vacancy density with the increase in annealing temperature in a vacuum. Fig.6.19 (b) shows that the contribution of metallic Co to the MCD signal is dominant in all thin films except for those annealed at 500 °C, in which case the contribution of metallic Co and the contribution of the oxide matrix become equal. The variation of the fraction of the metallic Co (f) with oxygen partial pressure and annealing in vacuum temperature are shown in Fig.6.20 (a) and Fig.6.20 (b) respectively.

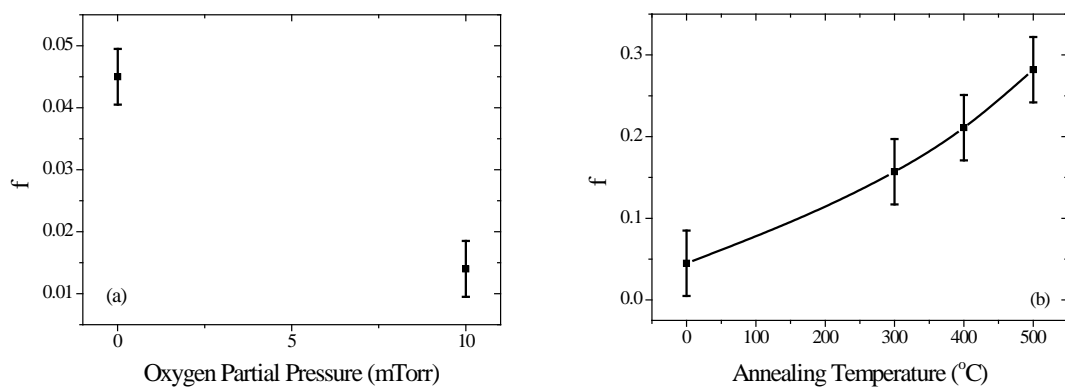


Figure 6.20: Variation in metallic Co fraction co-exists in Co-doped In_2O_3 thin films with (a) oxygen partial pressure, (b) Annealing in vacuum temperature.

Fig.6.20 shows that the fraction of metallic Co is oxygen partial pressure and annealing-temperature dependent. The fraction of metallic Co in the thin film deposited at low oxygen pressure is 0.045 while the fraction in the thin film deposited at 10mTorr is 0.017. Therefore, the density of metallic Co increases as the oxygen partial pressure decreases. In Fig.6.20 (b), the un-annealed thin film has a fraction of metallic Co of 0.045, and this fraction is increased during the annealing process where the fraction of metallic Co in the thin film annealed at 500 °C is 0.28. Therefore, the density of metallic Co increases with the annealing process up to a factor of 6 at an annealing temperature of 500 °C.

In order to investigate the influence of tin doping on Co-doped In_2O_3 , thin films of $(\text{In}_{0.95-y}\text{Co}_{0.05}\text{Sn}_y)_2\text{O}_3$ were deposited as shown in table 6.2. In fact, not all the Co atoms in these thin films substitute indium atoms in the lattice matrix. Some fraction of metallic Co was detected using EXAFS measurements. The variation in

the optical transmission and reflection of $(\text{In}_{0.95-y}\text{Co}_{0.05}\text{Sn}_y)_2\text{O}_3$ thin films with tin content is shown in Fig.6.21.

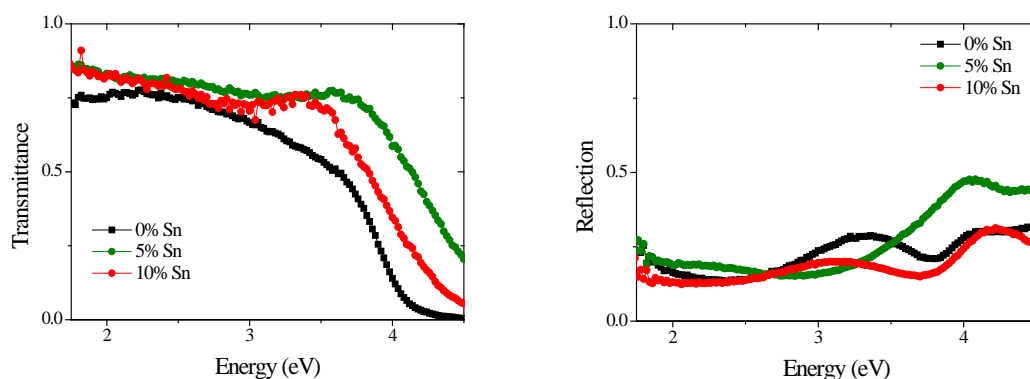


Figure 6.21: Variation in the optical transmission and reflection of $(\text{In}_{0.95-y}\text{Co}_{0.05}\text{Sn}_y)_2\text{O}_3$ thin films with tin content, where metallic Co in these thin film is detected.

The transmission increases with an increase in tin content, which is in agreement with the same result obtained for the pure In_2O_3 thin films discussed in chapter 4. The optical absorption edge is shifted toward higher energy with an increase in tin content of up to 5% of tin; then, the optical absorption edge is shifted toward low energy due to the un-embedded tin atoms of tin in the In_2O_3 lattice where the density of un-embedded tin atoms increases with an increase in tin content of more than 5%. The transmission at 550nm and the optical absorption coefficient spectra as a function of tin content are shown in Fig.6.22.

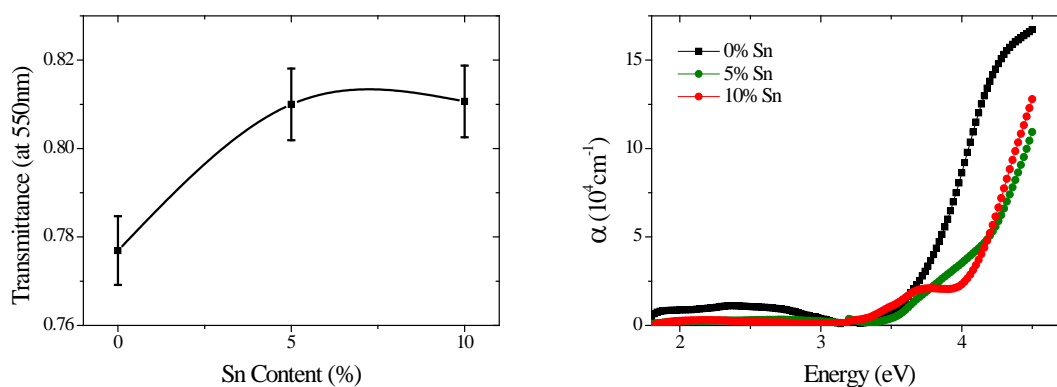


Figure 6.22: Variation in the optical transmission at 550nm, 2.3eV, and the optical absorption coefficient of $(\text{In}_{0.95-y}\text{Co}_{0.05}\text{Sn}_y)_2\text{O}_3$ thin films with tin content.

The absorption coefficient spectra of un-doped-with-tin thin film show two transitions, the first at 2.4eV and the second below the optical absorption edge at 3.5eV. The first transition, at 2.4eV, is due to the metallic Co. This transition feature disappears when the thin film is doped with tin. The thin films doped with tin show just one transition feature at 3.4eV and the behaviour of the optical absorption edge with tin is in agreement with what was observed in the transmission spectra, as shown in Fig.6.21. The absorption coefficient is non-zero at 3.3eV and increases with an increase in energy up to the absorption band edge. The area between 3.3eV and the optical band gap energy is where the energy states of defects are formed. Therefore, it is obvious that the formation of energy states by defects increases with an increase in tin content. Increasing tin content leads to a shift of the optical absorption coefficient spectrum toward high energy. When the doping with tin is increased to above 5%, the interstitial Sn atoms in the lattice start to exist; this, in turn, causes the shift in absorption of the coefficient spectra toward low energy. The variation of the optical absorption coefficient squared and the optical band gap with tin content are shown in Fig.6.23.

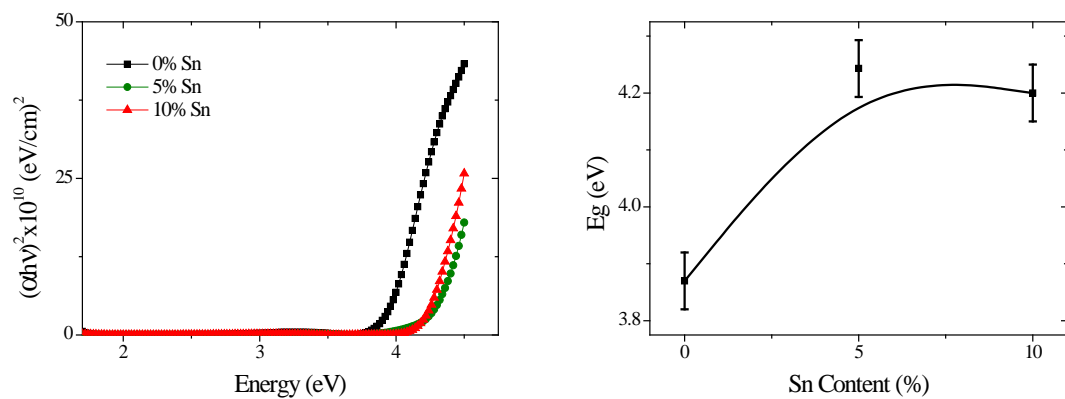


Figure 6.23: Variation in the optical absorption coefficient squared and the optical band gap with tin content of $(\text{In}_{0.95-y}\text{Co}_{0.05}\text{Sn}_y)_2\text{O}_3$ thin films.

Fig.6.23 shows that, the optical band gap energy of $(\text{In}_{0.95-y}\text{Co}_{0.05}\text{Sn}_y)_2\text{O}_3$ thin films is tin-content dependent. The optical band gap energy increases with an increase in tin content of up to 5% then it decreases afterwards, confirming that with more than 5% of tin, the tin atoms are not soluble in the lattice, which affects all the optical properties of these thin films. The increase in the optical band gap energy is due to the

increase in carrier density, where each extra tin atom donates one extra electron to the system. The MCD spectra of $(\text{In}_{0.95-y}\text{Co}_{0.05}\text{Sn}_y)_2\text{O}_3$ thin films were measured at room temperature and a magnetic field of 1.8 Tesla. The variation in MCD spectra with tin content over the range of energy of 1.7 eV to 4.2 eV is shown in Fig.6.24.

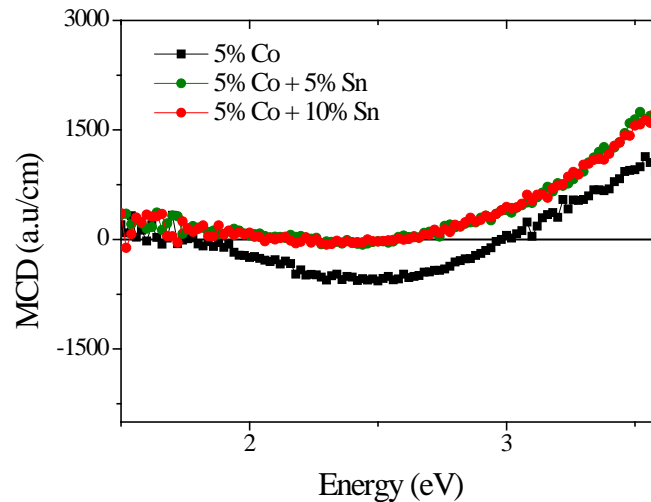


Figure 6.24: Variation in MCD spectra of $(\text{In}_{0.95-y}\text{Co}_{0.05}\text{Sn}_y)_2\text{O}_3$ thin films with tin content measured at RT and a magnetic field of 1.8 Tesla.

The MCD spectrum shows MCD features at 2.5 eV and at 3.6 eV are consistent with the absorption spectra given in Fig.6.23. For un-doped with tin thin film, there are two MCD features. The MCD feature at 2.5 eV is evidence of the formation of the metallic Co in this thin film, and the feature at 3.6 eV is a combination of the MCD originating from the metallic Co and the MCD originating from the oxide matrix. For the other thin films doped with tin, the feature at 2.5 eV, which is related to the metallic Co, disappears and a small MCD feature at 1.7 eV is initialized, which is related to the *d-d* transitions among tin atoms. This MCD feature falls in the error range of the system and might not be real. Also, there is an MCD feature at 3.6 eV, which is related to the transition of carriers from the valance band to the oxygen vacancy levels formed within the forbidden band gap by vacancy defects. The disappearance of the MCD peak at 2.5 eV for the Sn-doped thin films implies that doping with tin leads to an increase in the solubility of Co atoms in the host In_2O_3 lattice and prevents the formation of metallic Co.

6.3 Conclusion

This chapter investigated the influence of Co-doping on the optical and magneto-optical properties of In_2O_3 thin films. The results provide compelling evidence that the observed ferromagnetism in SMS is due to the polarized electrons in localized donor states associated with the oxygen vacancies. Magnetometry and magneto-optical measurements show that Co-doped In_2O_3 is ferromagnetic beyond room temperature. The density of impurity donor states formed below the band gap edge is due to the oxygen vacancies and increases and widens with decreases in oxygen partial pressure, with an increase in Co content, and with doping with Sn as confirmed by magneto-optical measurements.

EXAFS measurements confirmed that some thin films contain metallic Co nanoparticles. Therefore, the magnetization and the magneto-optics' behaviours will be a mix of that due to the response of metallic Co and that due to the response of the semiconductor matrix. However, the EXAFS measurements could not give the fraction of these nanoparticles. Magneto-optical measurements were found to be more accurate and quantitative in this field.

The fraction and the MCD response of metallic Co that co-exist in some thin films and the MCD response of In_2O_3 matrix were found to increase with a decrease in the oxygen partial pressure or with an increase in the annealing temperature in a vacuum. The vacuum annealing process improves the magnetization, the magneto-optical responses of metallic Co and the In_2O_3 matrix.

Although the oxygen partial pressure and the annealing process lead to an increase in the fraction of metallic Co, there is no evidence that the oxygen partial pressure or the annealing process is responsible for the existence of metallic Co in these thin films where the metallic Co is observed in thin films deposited at high oxygen partial pressure and in un-annealed thin films. Therefore, the responsibility for the existence of metallic Co is most likely to be the substrate temperature, which is as high as 600°C in all thin films containing metallic Co, or due to the high laser power used to prepare the thin films.

Doping with tin up to 5% increases the transparency and the carrier concentration of the samples whereas doping with a fraction of tin of more than 5%

leads the interstitial Sn ions to form and act as scattering centres. The amplitude of the MCD signal is in accordance with the carrier density and the density of the oxygen vacancy bands, which implies that the carrier density and the impurity donor states are responsible for the observed MCD signal and the transitions within the forbidden band gap energy. The metallic Co does not appear in Sn-doped thin films, indicating that doping with tin leads to an increase in the solubility of Co atoms in the host In_2O_3 lattice and prevents the formation of metallic Co.

6.4 References

1. N. H. Hong, J. Sakai, W. Prellier and A. Hassini, *J. Phys. : Condens. Matter* **17**, 1697 (2005).
2. J. M. D. Coey, A. P. Douvalis, C. B. Fitzgerald and M. Venkatesan, *Appl. Phys. Lett.* **84**, 1332-1334 (2004).
3. S. B. Ogale, R. J. Choudhary, J. P. Buban, S. E. Lofland, S. R. Shinde, S. N. Kale, V. N. Kulkarni, J. Higgins, C. Lanci, J. R. Simpson, N. D. Browning, S. D. Sarma, H. D. Drew, R. L. Greene and T. Venkatesan, *Phys. Rev. Lett.* **91**, 077205 (2003).
4. M. Venkatesan, C. B. Fitzgerald, J. G. Lunney and J. M. D. Coey, *Phys. Rev. Lett.* **93**, 177206 (2004).
5. N. H. Hong, J. Sakai, W. Prellier, A. Hassini, A. Ruyter and F. Gervais, *Phys. Rev. B* **70**, 195204 (2004).
6. Z. Wang, J. Tang, L. D. Tung, W. Zhou and L. Spinu, *J. Appl. Phys.* **93**, 7870-7872 (2003).
7. G. Peleckis, X. L. Wang and S. X. Dou, *J. Magn. Magn. Mater.* **301**, 308-311 (2006).
8. P. F. Xing, C. Y. Xue, T. M. Jian, Y. S. Shen, L. G. Lei, M. L. Mo and J. Jun, *Chinese Physics Letters* **26**, 117503 (2009).
9. X. Meng, L. Tang and J. Li, *J. Phys. Chem. C* **114**, 17569-17573 (2010).
10. G. Peleckis, X. Wang and S. X. Dou, *Appl. Phys. Lett.* **89**, 022501 (2006).
11. T. Dietl, H. Ohno and F. Matsukura, *Phys. Rev. B* **63**, 195205 (2001).
12. T. Dietl, A. Haury and Y. D. A. Merle, *Phys. Rev. B* **55**, R3347 (1997).
13. H. Akai, *Phys. Rev. Lett.* **81**, 3002 (1998).
14. P. G. D. Gennes, *Phys. Rev.* **118**, 141 (1960).
15. M. V. Schilfgaard, and O. N. Mryasov, *Phys. Rev. B* **63**, 233205 (2001).
16. P. W. Anderson, and H. Hasegawa, *Phys. Rev.* **100**, 675 (1955).
17. A. M. H. R. Hakimi, M. G. Blamire, S. M. Heald, M. S. Alshammari, M. S. Alqahtani, D. S. Score, H. J. Blythe, A. M. Fox and G. A. Gehring, *Phys. Rev. B* **84**, 085201 (2011).
18. D. S. Score, M. Alshammari, Q. Feng, H. J. Blythe, A. M. Fox, G. A. Gehring, Z. Y. Quan, X. L. Li and X. H. Xu, *J. Phys. : Conference Series* **200**, 062024 (2010).

19. G. A. Gehring, H. J. Blythe, F. Qi, D. S. Score, A. Mokhtari, M. Alshammari, M. S. Al Qahtani and A. M. Fox, *Magnetics, IEEE Transactions on* **46**, 1784-1786 (2010).
20. C. Clavero, A. Cebollada, G. Armelles, Y. Huttel, J. Arbiol, F. Peiró and A. Cornet, *Phys. Rev. B* **72**, 024441 (2005).
21. M. A. White, S. T. Ochsenbein and D. R. Gamelin, *Chem. Mater.* **20**, 7107-7116 (2008).
22. A. G. Clavero, J. Margueritat, J. Gonzalo, M. G. D. Muro, A. Labarta and B. X, *Appl. Phys. Lett.* **90**, 182506 (2007).
23. C.A. Clavero, G. Armelles, Y. Huttel, J. Arbiol, F. Peiró and A. Cornet, *Phys Rev* **72**, 02441 (2005).
24. C. Clavero, B. Sepúlveda, G. Armelles, Z. Konstantinović, M. García del Muro, A. Labarta, and X. Batlle, *J. Appl. Phys.* **100**, 074320 (2006).

Chapter 7 – Fe Doped In₂O₃

7.1 Introduction

Iron (Fe) is one of the TMs that show high magnetic moments when used as a doping material in an In₂O₃ semiconductor, as seen in Fig.2.16. This chapter investigates the optical and magneto-optical properties of the Fe-doped In₂O₃. It covers the effect of variations in Fe content, oxygen partial pressure, annealing and tin doping on the optical and magneto-optical properties of Fe-doped In₂O₃. The Maxwell–Garnett theory is used for the first time in history to determine the fraction, magnetic and magneto-optical response of Fe₃O₄ nanoparticles present in some of Fe-doped In₂O₃ thin films.

7.2 Experiment Details, Results, and Discussion

In order to investigate the influence of Fe content, vacuum annealing and doping with tin on the optical and magneto-optical properties of In₂O₃ thin films, Thin films were prepared as shown in Table 7.1.

SAMPLE	CONTENT	THICKNESS (nm)	PRESSURE (mTorr)	ANNEALING for 30 min C°	T&S SEPARATION (mm)	TEMPERATURE (°C)	LASER ENERGY (mJ)	DEPOSITION METHOD	SUBSTRATE
133T53SP	(In _{0.99} Fe _{0.01}) ₂ O ₃	336	2x10 ⁻³	ANNEALING for 30 min C°	T&S SEPARATION (mm)	TEMPERATURE (°C)	LASER ENERGY (mJ)	DEPOSITION METHOD	Al ₂ O ₃ (0001)
132T52SP	(In _{0.98} Fe _{0.02}) ₂ O ₃	294	2x10 ⁻³						
131T51SP	(In _{0.97} Fe _{0.03}) ₂ O ₃	258	2x10 ⁻³						
130T50SP	(In _{0.96} Fe _{0.04}) ₂ O ₃	200	2x10 ⁻³						
129T49SP	(In _{0.95} Fe _{0.05}) ₂ O ₃	156	2x10 ⁻³	No	32	600	250	PLD	
329T49SP	(In _{0.95} Fe _{0.05}) ₂ O ₃	170	2x10 ⁻³	500	32	600	250	PLD	
330T49SP	(In _{0.95} Fe _{0.05}) ₂ O ₃	174	2x10 ⁻³	400	32	600	250	PLD	
331T49SP	(In _{0.95} Fe _{0.05}) ₂ O ₃	179	2x10 ⁻³	300	32	600	250	PLD	
328T49SP	(In _{0.95} Fe _{0.05}) ₂ O ₃	178	2x10 ⁻³	No	32	600	250	PLD	
362T62SP	(In _{0.90} Fe _{0.05} Sn _{0.05}) ₂ O ₃	162	2x10 ⁻³	No	32	600	250	PLD	
435T93SP	(In _{0.85} Fe _{0.05} Sn _{0.10}) ₂ O ₃	196	2x10 ⁻³	No	32	600	250	PLD	

Table 7.1: Growth details of In₂O₃ thin films grown at different Fe content, annealing temperature, and doping with Tin content.

Thin films of $(\text{In}_{1-x-y}\text{Fe}_x\text{Sn}_y)_2\text{O}_3$ with different concentrations of Fe_3O_4 varying from 1% to 5%, and different concentrations of Sn were prepared by S. Alfahad and M. Alotibi from the National Center of Nanotechnology at KACST. The oxygen partial pressure was sustained at 2×10^{-3} mTorr during the growth process. The influence of oxygen partial pressure will be investigated separately where the related thin films grown in China not in KACST.

Starting with the influence of the Fe content, the XRD analysis by Hakimi shows that, the thin films are very crystalline, prefer IO(222) orientation and the Fe_3O_4 nanoparticles were also present.

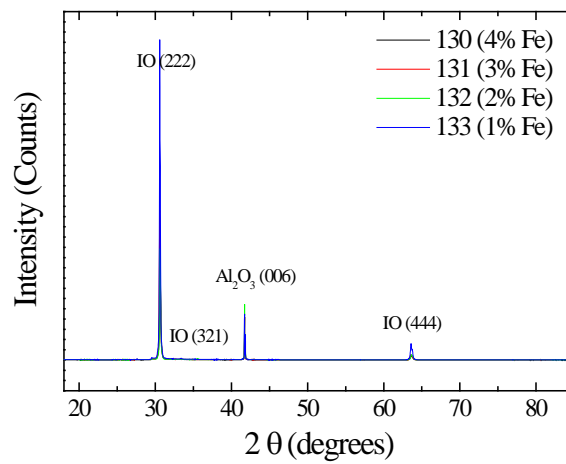


Figure 7.1: XRD data of $(\text{In}_{1-x}\text{Fe}_x)_2\text{O}_3$ thin films where In_2O_3 (222) and (444) reflection peaks do not shift with Fe concentrations, implying that not all Fe ions are substitutional.

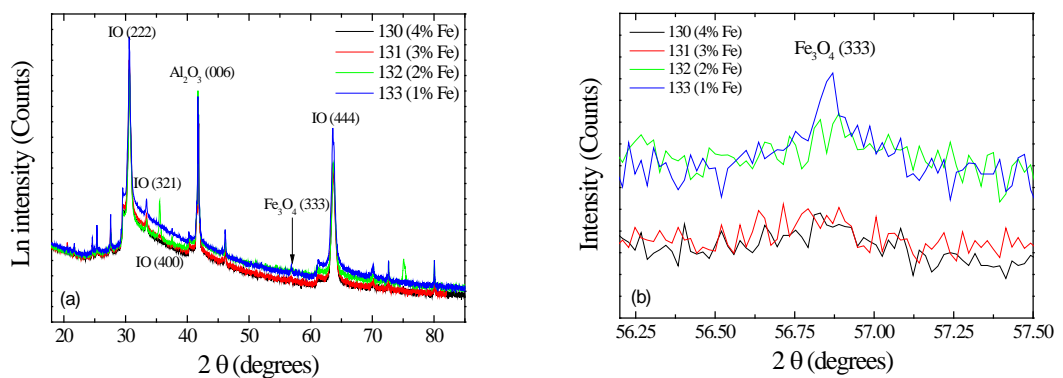


Figure 7.2: a) High resolution XRD data of $(\text{In}_{1-x}\text{Fe}_x)_2\text{O}_3$ thin films where Fe_3O_4 nanoparticles can be seen. b) High resolution XRD data in the range from 56 to 57, which confirm the existence of Fe_3O_4 nanoparticles in all the thin films; its fraction increases with Fe-doping content.

The lattice constant fluctuates as shown in Fig.7.3, and does not show any strong dependence on the level of Fe doping, which suggests that the Fe is not doping substitutionally.

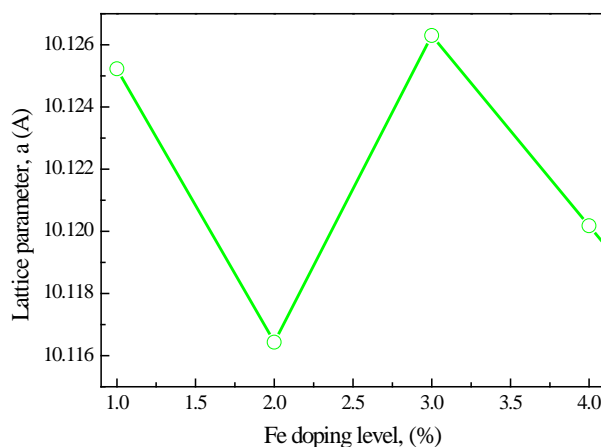


Figure 7.3: Fluctuation of the lattice constant with an increase in Fe content.

The EXAFS measurements performed by Heald on In_2O_3 thin film doped with 5% Fe compared with magnetite (Fe_3O_4) are shown in Fig.7.4.

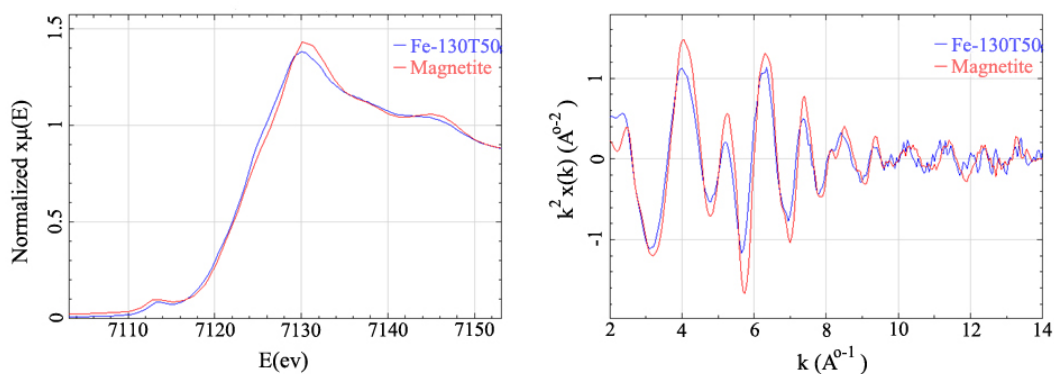


Figure 7.4: Normalized Fe near-edge EXAFS spectra of the In_2O_3 thin film doped with 4% Fe compared with Fe_3O_4 .

The EXAFS measurements confirmed the formation of nanoparticles of magnetite in the In_2O_3 thin films. Variation of the resistance with temperature is shown in Fig.7.5

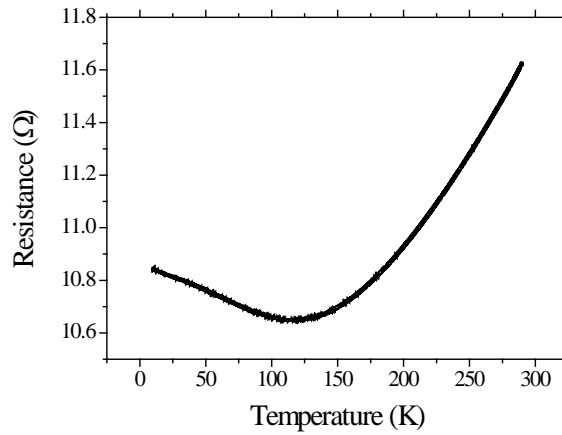


Figure 7.5: Resistance, R , versus temperature curve for an In_2O_3 film doped with 2% Fe.

The resistance of $(\text{In}_{1-x}\text{Fe}_x)_2\text{O}_3$ thin films as a function of temperature agrees over most of the range of typical resistance (R) versus T curve of metallic materials, where the resistivity of the metallic increases with an increase in temperature. The variation of resistance of 2% of Fe-doped In_2O_3 thin film with temperature is shown in Fig.7.5 where this thin film has the lowest carrier concentration among the others, as shown in Fig.7.6, where the variations in the carrier concentration and the mobility with an increase in Fe-doping content were measured at 10K and 300K.

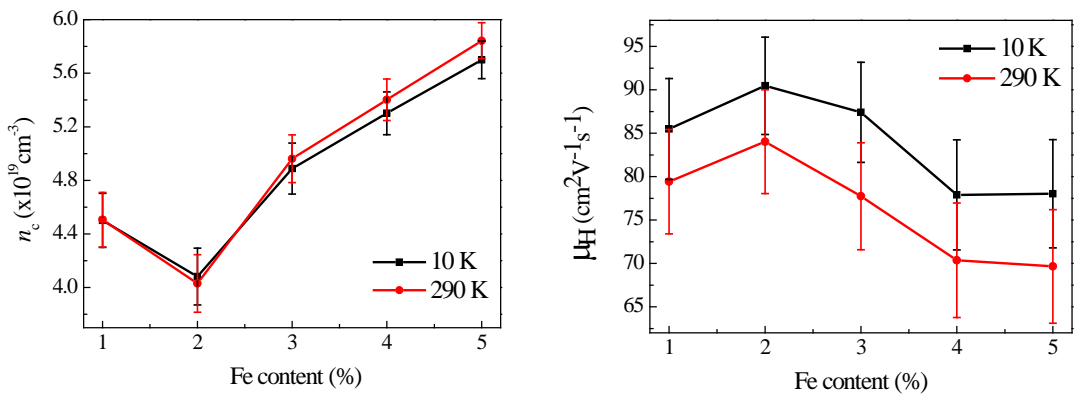


Figure 7.6: Variations in carrier concentration (n_c), and mobility (μ) with Fe-doping content.

The carrier concentration of $(\text{In}_{1-x}\text{Fe}_x)_2\text{O}_3$ thin films dropped with doping with Fe to 2%; however, the carrier concentration increased with an increase in Fe content. The mobility is consistent with the variation of the carrier concentration with Fe

content until it is saturated above 4% of Fe content. Magnetic properties were investigated using a SQUID magnetometer in the temperature range of 5–300 K in magnetic fields up to 1 Tesla. Variation of magnetic moment with applied magnetic field displayed ferromagnetism in each of the Fe-doped In_2O_3 films above room temperature due to the formation of Fe_3O_4 nanoparticles as shown in Fig.7.7.

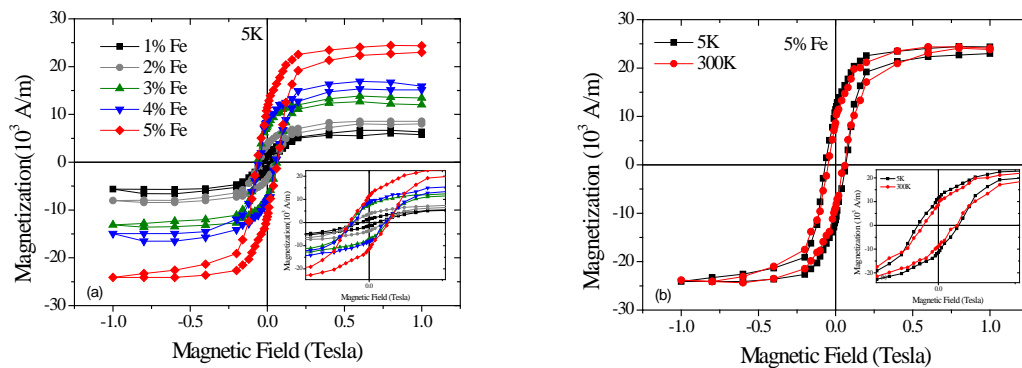


Figure 7.7: a) Ferromagnetic hysteresis loops of a Fe-doped In_2O_3 thin film at 5 K.
b) Hysteresis loops of 5% Fe-doped In_2O_3 thin film at 5K and 300K.

The magnetization increases with an increase in Fe content and in agreement with the carrier concentration, as shown in Fig.7.6 except that 2% of Fe thin film shows a higher magnetization than that of 1% thin film, while the carrier concentration of 2% thin film is lower than that of 1%, which was not expected due to correlation between the magnetization and the carrier concentration. The optical transmission and optical reflection spectrum of $(\text{In}_{1-x}\text{Fe}_x)_2\text{O}_3$ thin films as a function of energy were measured at RT and are shown in Fig.7.8.

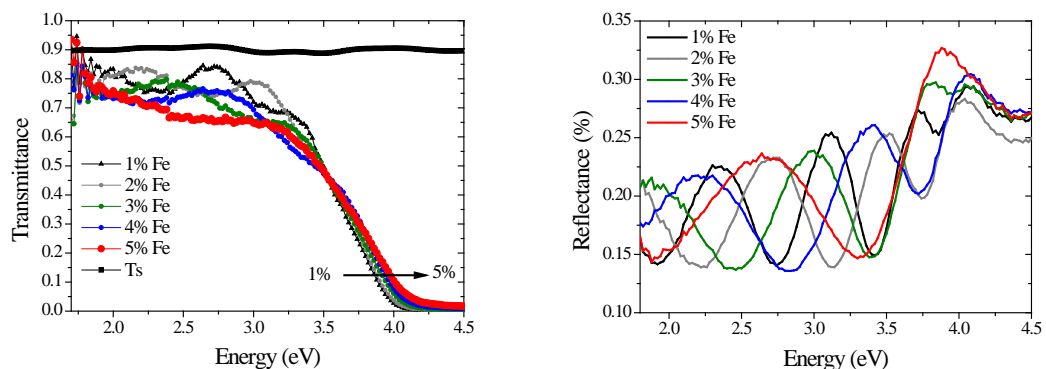


Figure 7.8: Variation in the optical transmission, and reflection spectrum with Fe ions content.

Fig.7.8 illustrated the variation in the optical transmission, and optical reflection spectrum of $(\text{In}_{1-x}\text{Fe}_x)_2\text{O}_3$ thin films with Fe ions content. The transmission spectra show high transparency and perfect interference fringes in the infrared and visible region for samples with Fe content below 5%. For the thin film with 5% Fe content, the transmission spectrum shows no interference fringes due to the low thickness of the sample and due to an increase in the absorption coefficient. The reflection spectrum displays perfect interference fringes in the transparent region of the sample for all content, but shows high reflection above the optical absorption edge. The optical absorption edge of the transmission spectra is shifted to higher energy with an increase in Fe content. The difference in the interference fringes observed in the infrared and visible region in both spectra is due to the difference in thickness and to the variation of indices of refraction with Fe content. The variation in the optical absorption coefficient and the optical gap energy with Fe content is shown in Fig.7.9.

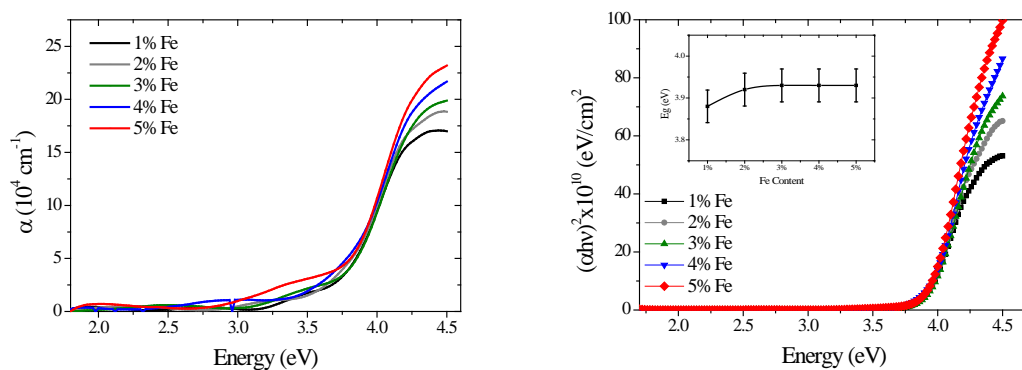


Figure 7.9: Variation in the optical absorption coefficient and the optical band gap with Fe content for $(\text{In}_{1-x}\text{Fe}_x)_2\text{O}_3$ thin films.

Fig.7.9 shows absorption below the optical absorption edge around 3.3eV for all the thin films. At this energy, the formation of oxygen vacancy bands is expected. However, the thin film with 5% Fe shows that another absorption occurs at 2.0eV. The origin of these absorption bands was investigated carefully using a magneto-optics approach. The optical absorption edge shifted to higher energy when more Fe content was added, which is consistent with the same shift observed in the

transmission spectra. Variations in the optical band gap with an increase in Fe content are shown in the inset of Fig.7.9. The variation in the optical band gap energy with Fe content can be explained by the Moss–Burstein effect [1], where the optical band gap expands as the carrier density increases.

The electronic structure of the samples was investigated through the measurement of the MCD spectra. The MCD spectra were measured with an applied magnetic field up to 1.8 Tesla in the Faraday configuration, and the MCD spectrum of the substrate was subtracted. The variation of the MCD spectra with Fe content is shown in Fig.7.10.

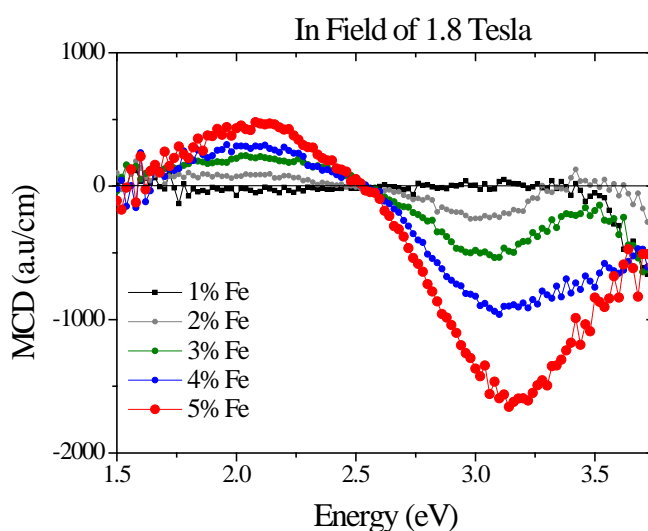


Figure 7.10: MCD spectrum of $(\text{In}_{1-x}\text{Fe}_x)_2\text{O}_3$ thin films grown by a PLD system at oxygen pressure of 2×10^{-6} mTorr on sapphire substrates and measured in a magnetic field of 1.8 Tesla.

Fig.7.10 illustrates the MCD spectra as a function of Fe concentration in In_2O_3 with characteristic features near 2.0 eV and 3.2 eV. The feature near 2.0 eV could be due to the Fe^{2+} ions and the feature near 3.2 eV could be due to the formation of oxygen vacancy bands near the band edge. However, based on EXAFS measurements, the two features together are due to the Fe_3O_4 nanoparticles. As a result, the MCD spectrum at 2.0eV is completely due to d - d transitions between the Fe_3O_4 nanoparticles, as reported by P. van der Zaag *et al.* and P. Wachter *et al.* [2, 3], whereas the feature at 3.2eV is due to a combination of contributions originating from Fe_3O_4 nanoparticles and the oxide matrix near the band edge. In order to distinguish between the MCD spectra that represent the response of the In_2O_3 oxide matrix and

those related to the response of the Fe_3O_4 nanoparticles and to determine the fraction of the Fe_3O_4 nanoparticles in these thin films, the Maxwell–Garnett (M–G) theory explained in chapter 5 used. Therefore, the response of the Fe_3O_4 nanoparticles was fitted to the Maxwell-Garnett theory in the region $E < 2.7\text{eV}$. The imaginary part of the off-diagonal dielectric constant calculated theoretically represents the response of the Fe_3O_4 nanoparticles, whereas the imaginary part of the off-diagonal dielectric constant deduced from Faraday ellipticity measurements on the thin film sample at 300K and a magnetic field of 1.8 Tesla represents the overall response of In_2O_3 plus that of the Fe_3O_4 nanoparticles. The contribution of the indium oxide matrix to the MCD signal can be obtained from the fitting, as shown in Fig.7.11.

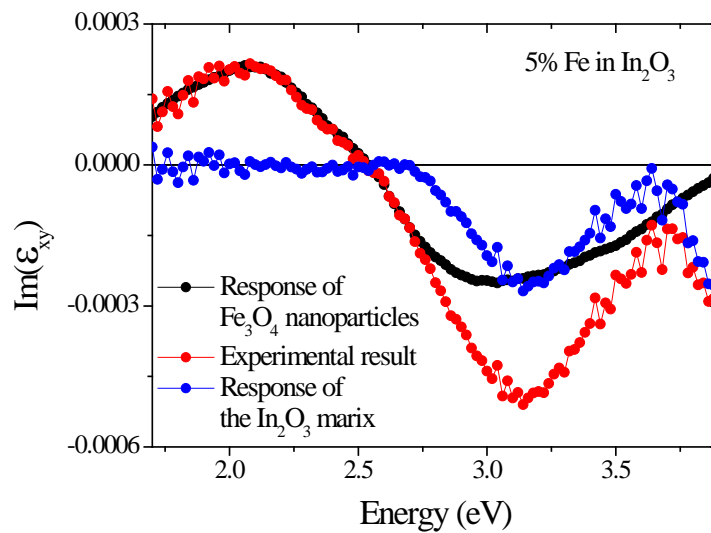


Figure 7.11: MCD spectra for $(\text{In}_{0.95}\text{Fe}_{0.05})_2\text{O}_3$ thin film (red line) fitted using Maxwell-Garnett theory to determine the fraction and the contribution of Fe_3O_4 nanoparticles (black line), while the blue line is the contribution corresponding to the In_2O_3 matrix.

In Fig.7.11, the response of the Fe_3O_4 nanoparticles is shown as a black line, while, the blue line represents the MCD signal due to the contribution of the Indium oxide matrix concentrated below the optical absorption edge, which confirms the existence of the polarized carriers in these thin films. The value of the demagnetizing factor of the inclusions L_{xx} was 0.333 in all the fitted thin films. The demagnetizing factor of the inclusions L_{xx} is Fe content independent, which implies the spherical inclusions of Fe_3O_4 nanoparticles. The contribution of Fe_3O_4 nanoparticles and the

contribution of the oxide matrix as a function of Fe content at 3.2eV are shown in Fig.7.12.

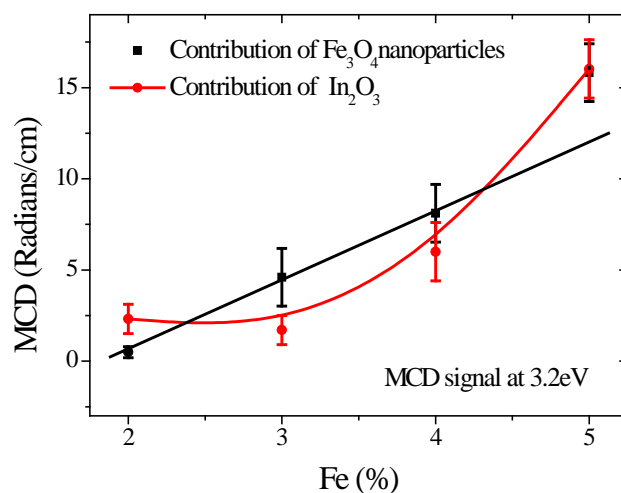


Figure 7.12: Variation in MCD amplitude at 3.2eV with Fe content for Fe_3O_4 nanoparticles in In_2O_3 thin film measured at RT and magnetic field of 1.8 Tesla. The red line shows the variation of In_2O_3 matrix contribution to the total MCD signal. The black line is to guide the eye and shows the contribution corresponds to the Fe_3O_4 nanoparticles to the total MCD signal at 3.2eV.

Fig.7.12 illustrates the contribution of Fe_3O_4 nanoparticles and the In_2O_3 matrix to the total MCD signal amplitude at 3.2eV. In the thin film with 1% Fe in In_2O_3 , there is no MCD signal detected. At 2% Fe, the contribution corresponding to the In_2O_3 matrix is larger than that corresponding to the Fe_3O_4 nanoparticles. Increasing the Fe content leads to an increase in the MCD contribution related to Fe_3O_4 nanoparticles, which implies the increase in the density of the Fe_3O_4 nanoparticles. At low content of Fe, the MCD signal is dominated by the contribution of the In_2O_3 matrix, whereas, with a content of Fe higher than 2%, the MCD signal is dominated by the contribution of Fe_3O_4 nanoparticles up to 5% of Fe where these two components become equal. It is notable that both contributions increase with an increase in Fe content. All the thin films were deposited at low oxygen pressure of 2×10^{-6} Torr, which leads to the increase of oxygen vacancy density, as discussed in section 4.3. Increasing the Fe content leads to a decrease in the In_2O_3 fraction to the benefit of Fe_3O_4 nanoparticles, and so the contribution of Fe_3O_4 becomes dominant. The fraction of Fe_3O_4 nanoparticles as a function of Fe content is shown in Fig.7.13.

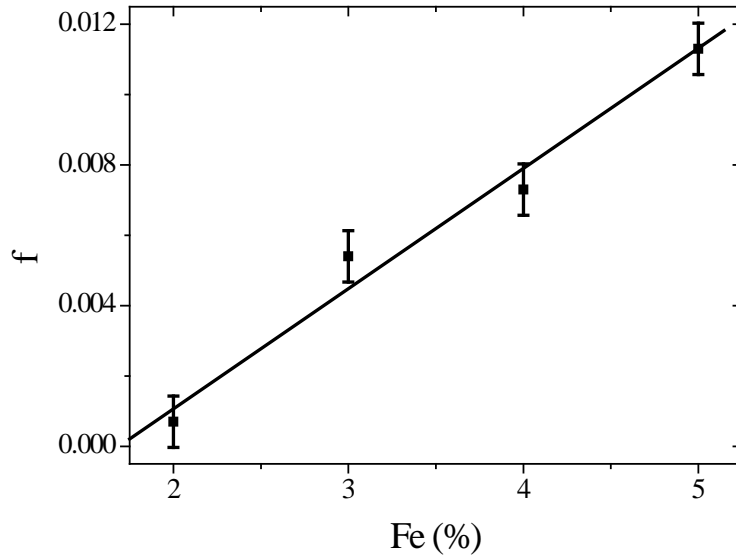


Figure 7.13: Fraction of Fe_3O_4 nanoparticles as a function of Fe content, where the black line is guide to the eye.

Fig.7.13 illustrates the fraction of Fe_3O_4 nanoparticles in the sample f , where in 2% Fe-doped In_2O_3 thin film, 0.05% of Fe content fraction was changed to Fe_3O_4 nanoparticles. The fraction of Fe_3O_4 nanoparticles increases with an increase in Fe content, where at 5% doped In_2O_3 , the fraction of Fe_3O_4 nanoparticles reaches 0.011%. In fact, this is the first time that the fraction of Fe_3O_4 nanoparticles embedded in a semiconductor host is determined using the magneto-optics approach.

The ferromagnetic hysteresis loops of Fe-doped In_2O_3 thin films measured at 5K and 300K indicated a remanence in these thin films, as shown in the inset of Fig.7.7. Therefore, the MCD spectrum as a function of Fe concentration in remanence was measured. Such a measurement leads to MCD spectra without any paramagnetic contributions, like the one that originated from the substrate. It is notable that the amplitude of the MCD signals at 2.0 eV and 3.2eV for the MCD spectra measured at remanence, shown in Fig.7.14 (a), is lower than that measured in field shown in Fig.7.10 due to the absence of any contribution activated by the field. The MCD spectra as a function of Fe concentration in remanence are shown in Fig.7.14 (a).

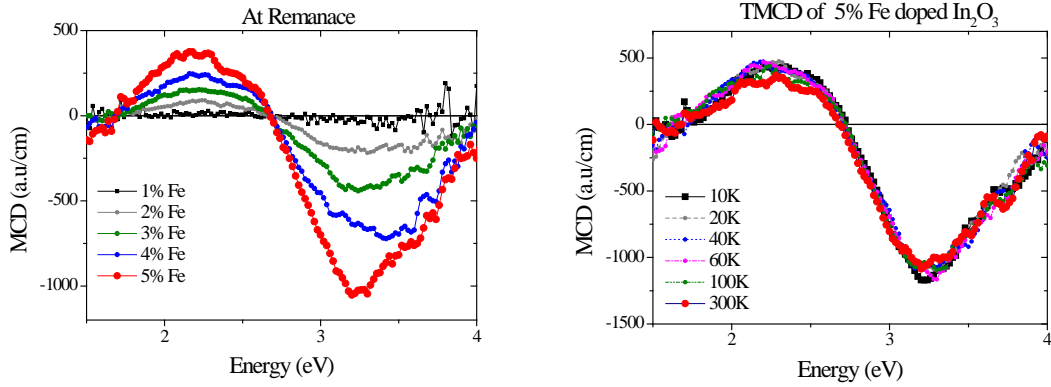


Figure 7.14: a) MCD spectra at remanence of $(\text{In}_{1-x}\text{Fe}_x)_2\text{O}_3$ thin films. b) Temperature dependence of MCD spectrum of $(\text{In}_{0.95}\text{Fe}_{0.05})_2\text{O}_3$ thin film measured at remanence.

The MCD spectrum of $(\text{In}_{0.95}\text{Fe}_{0.05})_2\text{O}_3$ is quite temperature independent and does not show any MCD peaks other than that due to the Fe_3O_4 nanoparticles and that due to the oxygen impurity levels where the influence of Fe_3O_4 nanoparticles is dominant. The MCD spectra of $(\text{In}_{0.95}\text{Fe}_{0.05})_2\text{O}_3$ were measured in field and measured at remanence and are shown in Fig.7.15, where the only difference between the two spectra is seen at 3.3eV and is due to the oxygen impurity levels in the In_2O_3 matrix. This indicates that there is no paramagnetic contribution, as any paramagnetic contribution activated by the magnetic field would be shown in the whole range of spectra, not just at 3.3eV.

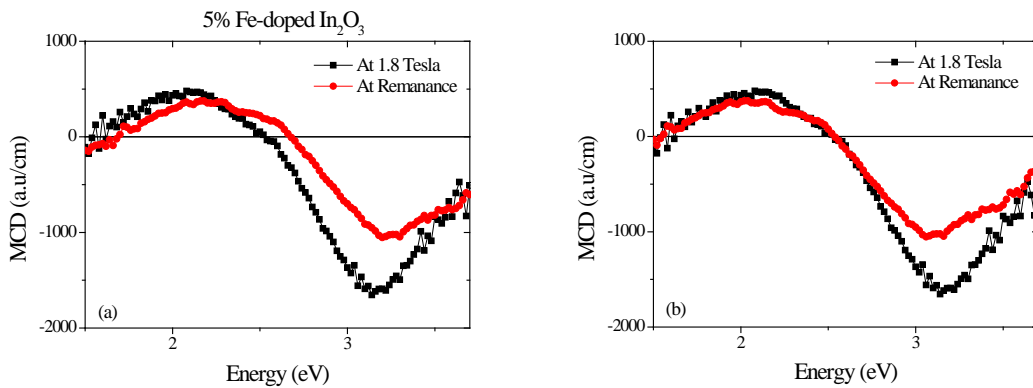


Figure 7.15: a) MCD spectra in field and at remanence for $(\text{In}_{0.95}\text{Fe}_{0.05})_2\text{O}_3$ thin film, b) The scaled MCD spectra over each other in order to show the difference.

Observation of MCD spectra from the oxygen impurity bands in these thin films implies that the localized carriers located in the oxygen vacancy bands are

polarized, which is confirmed by the Hall effect measurements of $(\text{In}_{0.95}\text{Fe}_{0.05})_2\text{O}_3$ thin film, as shown in Fig.7.16.

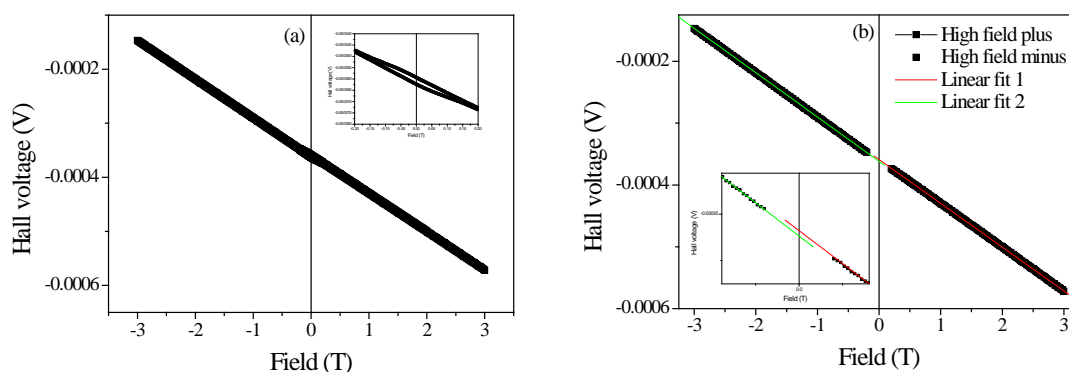


Figure 7.16: a) Raw data before any linear (Ordinary Hall effect) is subtracted. b) Linear fits to the high field data show an offset Therefore, AHE is genuine.

In order to investigate the influence of the annealing process on the structure and physical properties of Fe-doped In_2O_3 , several thin films were deposited under the same growth conditions as shown in Table 7.1, and the signs of formation of Fe_3O_4 nanoparticles appeared again in these samples. None of the samples discussed in last section were used again in this experiment, but all the samples were grown from same target at same time. One sample was not annealed and the others were annealed at 300 °C, 400 °C, and 500 °C, for 30 minutes in a vacuum after the deposition process. The XRD analysis by Hakimi for the thin film that was annealed at 500 °C is shown in Fig.7.17 where the peak of the Fe_3O_4 nanoparticles in these thin films is observed.

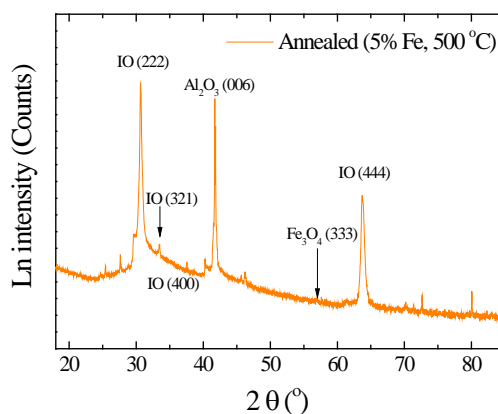


Figure 7.17: XRD data of thin film annealed at 500 °C where the Fe_3O_4 nanoparticles is observed.

The magnetic properties of these thin films were investigated by Alqahtani using a SQUID magnetometer. The hysteresis loops were measured at 5 and 300 K at a magnetic field of up to 1 Tesla where the diamagnetic contribution from the substrate has been subtracted. The variation in magnetic moment with an increase in annealing temperature in a vacuum is shown in Fig.7.18.

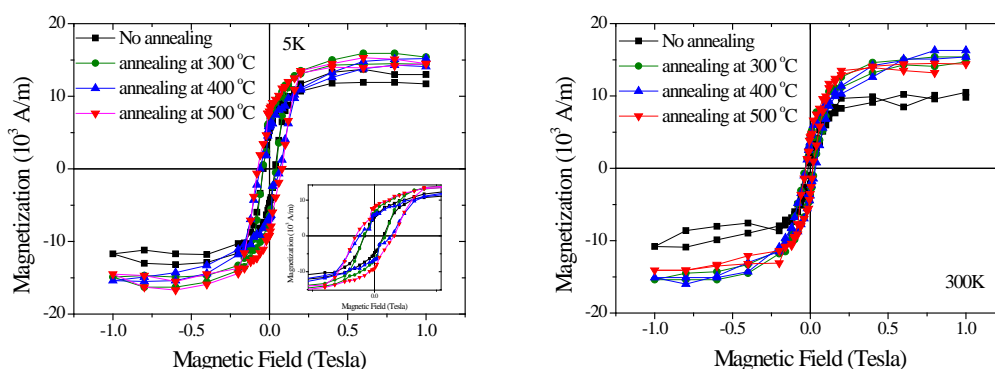


Figure 7.18: Variation in magnetic moment with an increase in annealing temperature in a vacuum of $(\text{In}_{0.95}\text{Fe}_{0.05})_2\text{O}_3$ thin films prepared by the PLD system.

The magnetic moment increases with the vacuum annealing process. However, the magnetic moments are annealing-temperature independent implying that no more oxygen atoms can be removed from the system; therefore, the magnetization is saturated. The optical transmission and the optical absorption were measured at RT and the variation in transmittance and the absorption spectra with annealing temperature are shown in Fig.7.19.

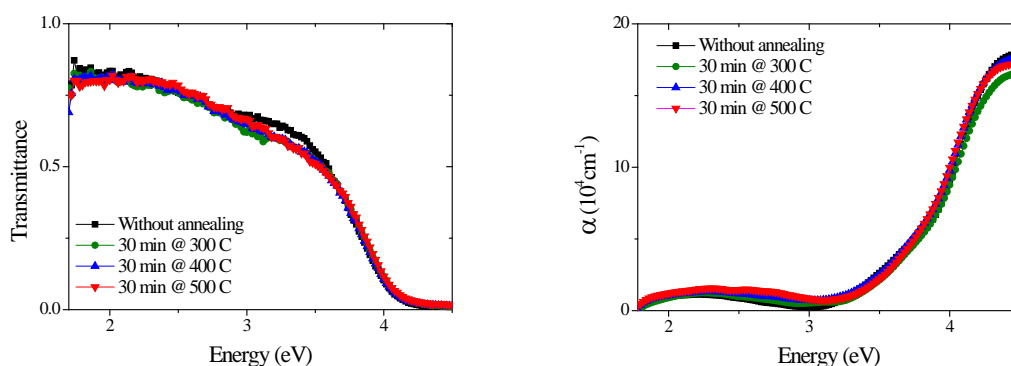


Figure 7.19: Variation in the optical transmission and the optical absorption coefficient spectra of $(\text{In}_{0.95}\text{Fe}_{0.05})_2\text{O}_3$ with annealing temperature.

The transmittance of pure sapphire substrate is about 0.89 in an energy range of 1.7 to 4.5eV. The transmittance spectra, given in Fig.7.19, show a reduction in transmittance especially in the range of 3.0eV to 3.75eV due to the formation of oxygen vacancy bands below the band gap energy with the annealing process, which is also confirmed by the reflection spectra where the maximum to minimum decreases with an increase in annealing in the same range of energy. The absorption spectra show two optical transitions features occurring below the band gap around 2.2eV and 3.3eV. These transitions increase with an increase in annealing temperature. As discussed previously, the transition around 3.3eV is due to the formation of defect bands below the band gap energy in addition to a formation of Fe₃O₄ nanoparticles, as confirmed by XRD measurement shown in Fig.7.17. The transitions around 2.3eV are entirely due to the Fe₃O₄ nanoparticles. The variations in the absorption coefficient squared and the optical band gap with an increase in annealing temperature are shown in Fig.7.21.

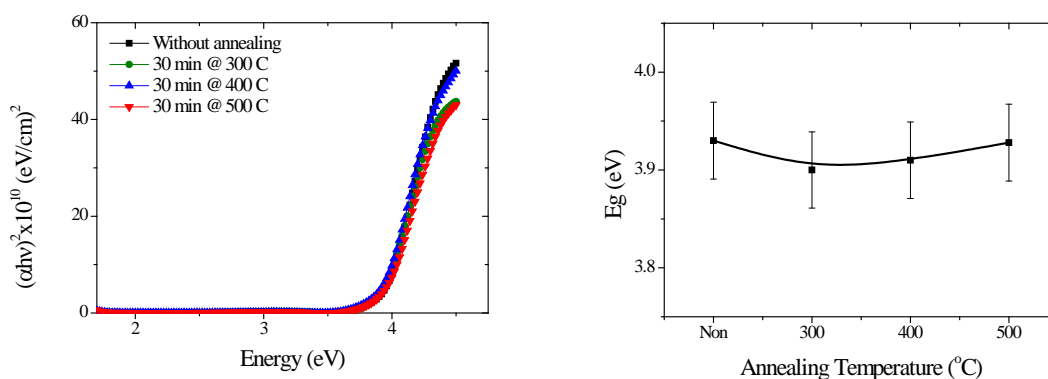


Figure 7.20: Variations in the optical absorption coefficient squared and the optical band gap with an increase in annealing temperature.

The band gap energy is shown to be annealing-temperature independent within the error range, which means that the films have been grown with the optimum crystallite quality. The absorption at 2.2eV and 3.3eV, shown in Fig.7.19, is explained by the MCD spectra that appear at same energies, as shown in Fig.7.21.

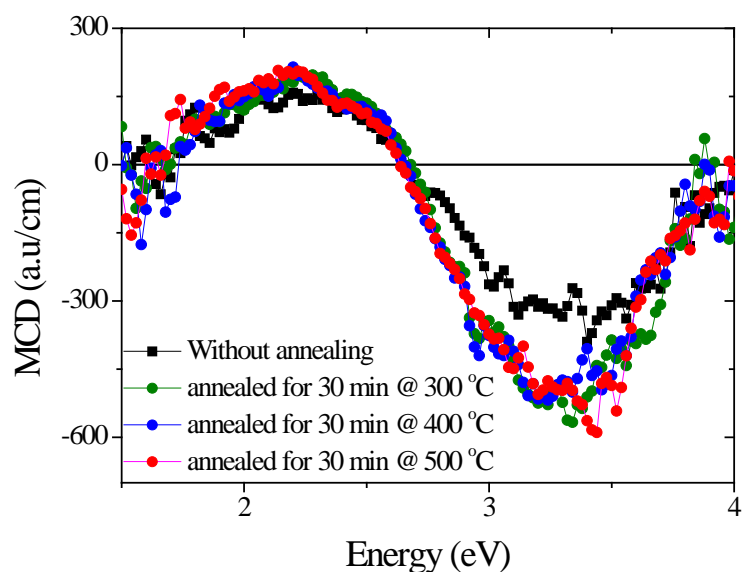


Figure 7.21: MCD spectra of $(\text{In}_{0.95}\text{Fe}_{0.05})_2\text{O}_3$ thin films annealed at different temperature.

Due to the existence of Fe_3O_4 nanoparticles in these films, the MCD spectra shown in Fig.7.21 are a combination of the MCD signal that originated from Fe_3O_4 nanoparticles and the MCD signal that originated from the In_2O_3 semiconductor. The appearance of a 2.2eV feature of Fe_3O_4 nanoparticles for the un-annealed sample indicates that the formation of Fe_3O_4 nanoparticles is due to the high substrate temperature (600°C) during the growth of the samples. However, the density of the Fe_3O_4 nanoparticles increases with annealing, which explains the increase in MCD magnitude at 2.2eV. The Maxwell-Garnett theory discussed in chapter 5 was used to assess the variation in the ratio and contribution of the Fe_3O_4 nanoparticles with annealing temperature. The variation in the contribution of the Fe_3O_4 nanoparticles and the contribution of the oxide matrix to the total MCD spectra and the fraction of Fe_3O_4 nanoparticles as a function of the annealing temperature are shown in Fig.7.22 (a) and (b) respectively.

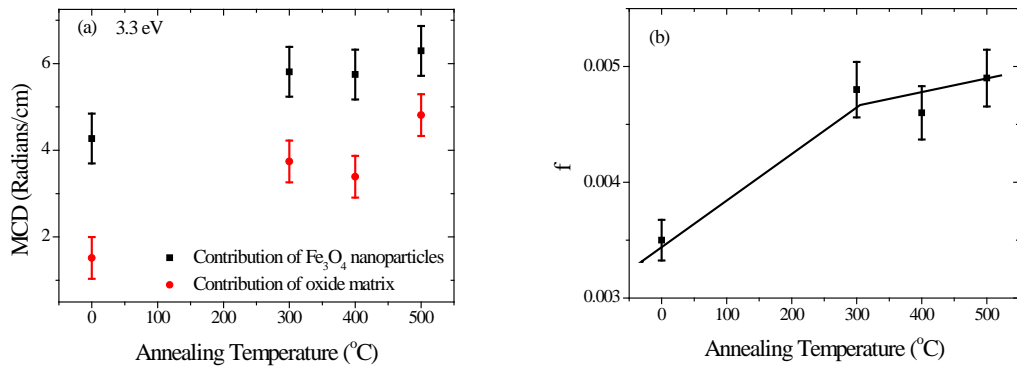


Figure 7.22: a) Variation in MCD amplitude at 3.3eV with annealing temperature. b) Variation in the fraction of Fe₃O₄ nanoparticles with annealing temperature, where the data point at 0K represents the the un-annealed sample and the black line is a guide for the eye.

Fig.7.22 (a) illustrates the MCD signal's amplitude at 3.3eV, where the MCD spectrum increases with an increase in annealing temperature. The contribution of the Fe₃O₄ nanoparticles to the total MCD signal is larger than that of the oxide matrix. The MCD signal related to the Fe₃O₄ nanoparticles is saturated with an increase in annealing temperature, which is in agreement with the variation in the fraction of Fe₃O₄ nanoparticles with an increase annealing temperature shown in Fig.7.22 (b). The vacuum annealing process leads to some enhancement in MCD signal of the oxide matrix supported by the increases in the oxygen vacancy density. The fraction of Fe₃O₄ nanoparticles increases with an increase in annealing temperature. The fraction of Fe₃O₄ nanoparticles seems to be saturated at 0.5%.

In order to explore the effect of tin doping on the optical and magneto-optical properties of Fe-doped In₂O₃, three iron doped indium oxide (In_{0.95}Fe_{0.05})₂O₃ thin films doped with 0, 5 and 10% of tin were deposited using the PLD system as shown in Table 7.1. The magnetic properties of these thin films were not measured. The variation of the optical transmission spectra and the optical band gap energy with tin content are shown in Fig.7.23 and Fig.7.24 respectively.

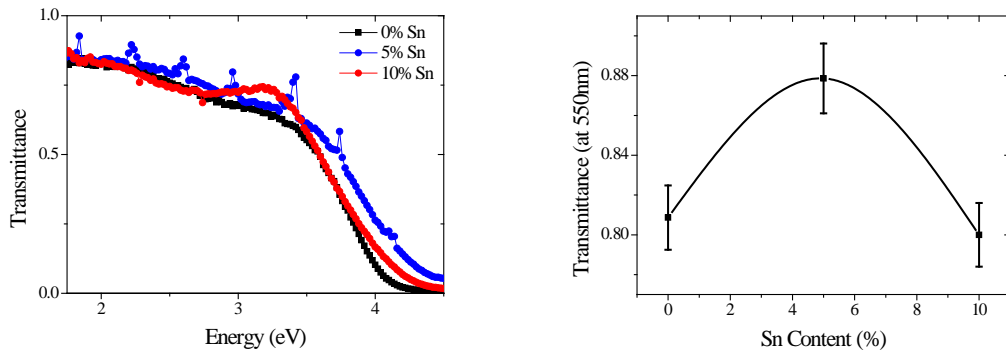


Figure 7.23: Variation in the optical transmission and the optical transmission at 550nm, 2.3eV, spectra of $(\text{In}_{0.95}\text{Fe}_{0.05})_2\text{O}_3$ thin films doped with different content of tin.

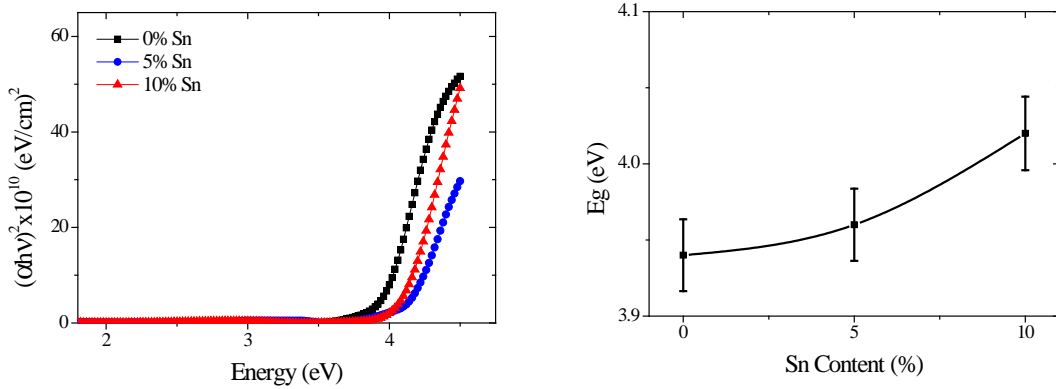


Figure 7.24: Variation in $(\alpha h\nu)^2$ and the band gap of $(\text{In}_{0.95-y}\text{Fe}_{0.05}\text{Sn}_y)_2\text{O}_3$ with an increase in tin content.

Fig.7.23 illustrate that, the transmission increases with an increase in tin content up to 5% and decreases afterwards, especially in the range of 3.5 to 4.5 eV. The optical band gap energy increases with increases in tin content, which is in agreement with what was seen for pure In_2O_3 . The decreases in optical transmission at 550nm with tin content above 5% of tin is due to the increase in the density of un-embedded tin atoms in the In_2O_3 lattice. The high band gap energy seen in the un-doped with tin sample spectrum is due to the growth at low oxygen pressure, and adding more tin leads to an increase in the band gap energy. The influence of tin doping on the MCD spectra of $(\text{In}_{0.95}\text{Fe}_{0.05})_2\text{O}_3$ thin films is shown in Fig.7.25.

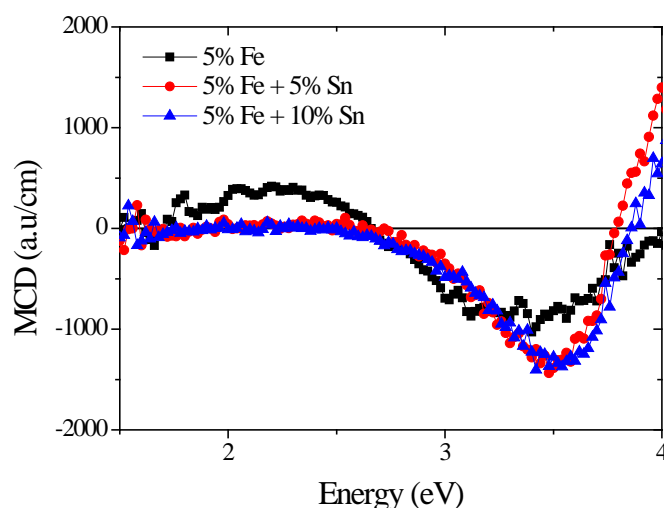


Figure 7.25: Variation in MCD spectrum of $(\text{In}_{0.95}\text{Fe}_{0.05})_2\text{O}_3$ thin films with tin content.

As found previously, the MCD feature seen at 2.2eV for un-doped thin film is related to Fe_3O_4 nanoparticles. It is surprising that for the thin films doped with tin, the 2.2eV feature totally disappears, which implies that adding tin may help the Fe atoms to embed within the In_2O_3 lattice and prevent the formation of nanoparticles. This result supports our previous observation, specifically, that metallic Co disappears also for thin films doped with tin, as discussed in chapter 6. The feature at 3.4eV for the un-doped with tin sample is a combination of the MCD coming from the Fe_3O_4 nanoparticles and the MCD coming from the states of oxygen vacancies produced by the growth at low oxygen pressure. For tin doped samples, the MCD feature at 3.4eV increased when tin was added to the oxide matrix and the optical absorption edge shifted to higher energy as expected and as was stated previously for pure and Co-doped In_2O_3 . The contribution of tin atoms to the MCD spectrum is increasing the carrier concentration and, most probably, fighting the formation of cluster and nanoparticles to the benefit of the oxygen vacancy bands which are formed below the optical absorption edge.

In order to explore the variation in the optical and magneto-optical properties of Fe-doped In_2O_3 with oxygen partial pressure, two $(\text{In}_{0.95}\text{Fe}_{0.05})_2\text{O}_3$ thin films were deposited on sapphire (Al_2O_3) substrates using pulsed laser ablation. The samples were prepared by Xiao-Hong Xu's group from Shanxi Normal University, China; this

means they were totally different from those prepared in KACST, which were discussed earlier. A full paper about the structure, magnetism, transport, and optical and magneto-optical properties of these thin films has been published (see Jiang *et al* [4]). The substrate used was the single-side polished type; the temperature during the growth process was maintained at 600 °C and the oxygen partial pressure was varied between the two samples. One sample was prepared at 5×10^{-3} mTorr and the other sample was prepared at 100 mTorr. The EXAFS measurements by Heald show no Fe_3O_4 nanoparticles in these thin films. The XRD measurement was performed by Xu and shown in Fig7.26 (a). The XRD analysis of the Fe-doped In_2O_3 films fabricated at low oxygen partial pressure shows the well known single-phase cubic un-doped In_2O_3 structure, well-oriented (222) and with no extra peaks relating to metallic Fe clusters or Fe oxide secondary phases, which implies that Fe ions are incorporated into the In^{3+} sites of the In_2O_3 lattice without changing the cubic bixbyite structure.

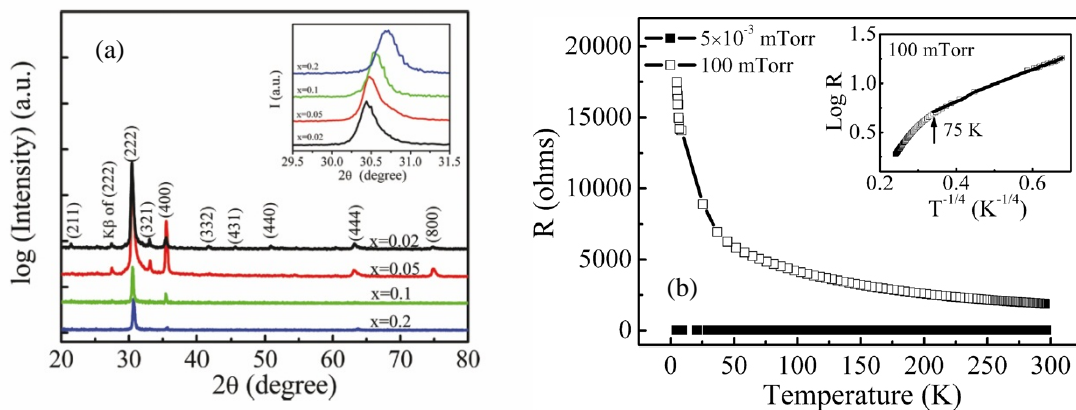


Figure 7.26: a) XRD patterns and b) the variation in resistance with temperature for the sample fabricated at 5×10^{-3} mTorr and 100mTorr. The inset shows $\log R$ vs $T^{-1/4}$ for the sample fabricated at 100mTorr (published [4]).

The value of the lattice constant at d (222) increases with increases in oxygen partial pressure until 10 mTorr and then decreases. This behaviour can be explained based by the fact that the increase in P_{O_2} during film growth leads to a reduction in oxygen vacancy density, associated with the oxidation of Fe^{2+} ions to Fe^{3+} ions. A decrease in the density of oxygen vacancies leads to an increase of $d(222)$, while an increase in the number of Fe^{3+} ions leads to a decrease of $d(222)$, because the radius of Fe^{3+} (0.79 Å) is small compared with both Fe^{2+} (0.92 Å) and In^{3+} (0.94 Å). Thus, the effect of changing the density of the oxygen vacancies dominates between 5×10^{-3}

mTorr and 10 mTorr, while the effect of changing the ionization state of Fe dominates for pressures between 10 and 100 mTorr, as confirmed by the XPS analysis [5]. The variation of resistance with temperature of the sample grown at 100 mTorr shows a metallic behaviour, whereas the sample grown at 5×10^{-3} mTorr shows classic semiconductor behaviour, as shown in Fig.7.26 (b).

The transport properties using the Van der Pauw four-point configuration and the Hall effect measurements were investigated by Xu. The carrier concentration (n_c) measured at RT is $2.40 \times 10^{18} \text{ cm}^{-3}$ and $4.27 \times 10^{20} \text{ cm}^{-3}$ for the thin films deposited at 100 mTorr and 5×10^{-3} mTorr respectively. The resistivity (ρ) is $2.06 \times 10^{-1} \Omega \cdot \text{cm}$ and $9.25 \times 10^{-4} \Omega \cdot \text{cm}$ for the thin films deposited at 100 mTorr and 5×10^{-3} mTorr respectively. Therefore, the carrier concentration decreases while the resistivity increases with an increase in oxygen partial pressure. The dependence of resistivity and carrier density on oxygen partial pressure is due to the variation in the concentration of oxygen vacancies and Fe^{2+} ions in these films. This variation is because the thin film fabricated at high oxygen pressure of 100 mTorr lies in the insulating regime, whereas the thin film fabricated at low oxygen pressure of 5×10^{-3} mTorr lies in the metallic regime.

The magnetic measurements were performed by my colleague Alqahtani using a SQUID magnetometer. The hysteresis loops were measured at 5 and 300 K for both samples; the hysteresis loops for the sample fabricated at 5×10^{-3} mTorr are shown in Fig.27 (a) and those for the one fabricated at 100 mTorr are shown in Fig.27 (b). The diamagnetic contribution from the substrate has been subtracted from the loops.

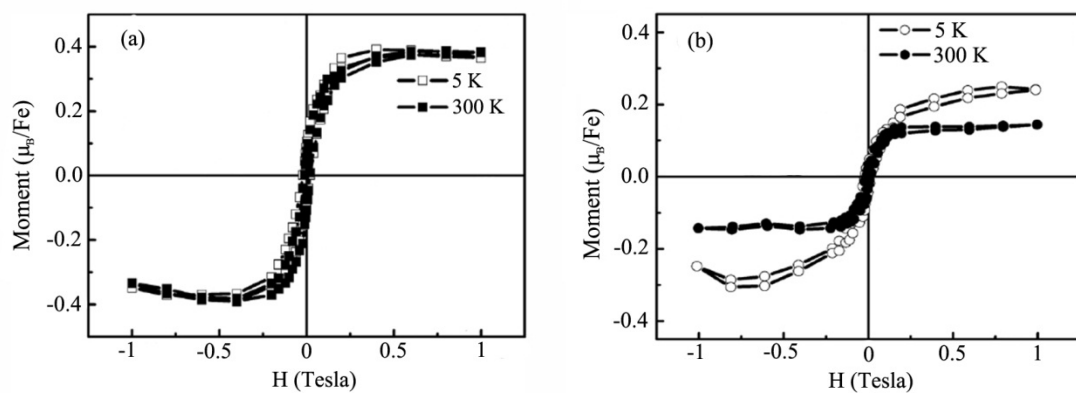


Figure 7.27: The hysteresis loops for the samples fabricated at (a) 5×10^{-3} mTorr and (b) 100mTorr. (published [4] in Oe unit).

The samples exhibit a clear RT ferromagnetic behaviour. The magnetization of the sample fabricated at 5×10^{-3} mTorr shows temperature independent behaviour, which indicates that the Curie temperature T_c of the sample is above RT, which is required for developing practical spintronic devices. In contrast, the magnetization of the sample fabricated at 100 mTorr shows temperature dependent behaviour, which mean that in addition to the ferromagnetic moment there is also a paramagnetic contribution. The influence of oxygen partial pressure on the electronic structure is revealed through the study of the optical properties of these films. Variation in the optical absorption spectra with temperature for both samples was measured. The temperature dependence of the absorption spectra of the sample fabricated at 5×10^{-3} mTorr is given in Fig.28 (a) and for the samples fabricated at 100 mTorr is given in Fig.28 (b).

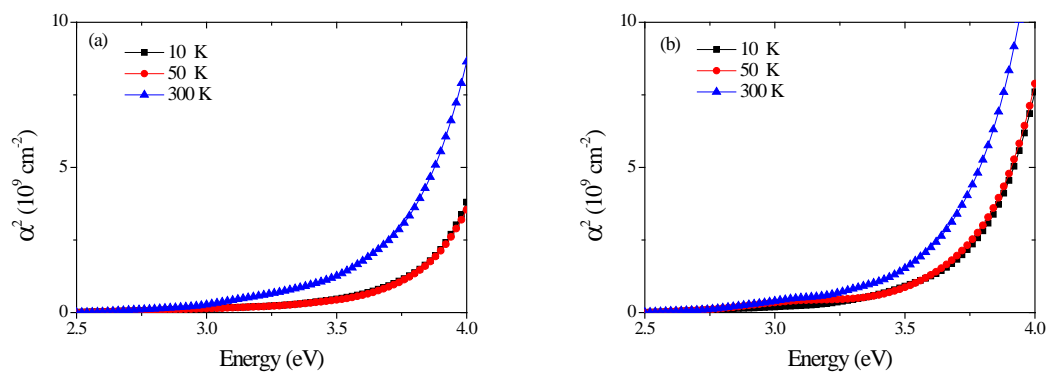


Figure 7.28: Variation in the absorption coefficient squared with energy for the sample fabricated at (a) 5×10^{-3} mTorr and (b) 100mTorr [4] (published in different format).

The absorption is temperature dependent in both samples due to the activation of phonons at RT. However, the absorption is more temperature dependent for the sample fabricated at 5×10^{-3} mTorr, which implies that at low temperatures, the localized states present in the sample fabricated at 100 mTorr activate the transition more effectively than do the delocalized impurity band states in the sample fabricated at 5×10^{-3} mTorr. The optical band gap was calculated using the Tauc plot method and the variation in optical band gap energy with oxygen partial pressure is shown in Fig.7.29.

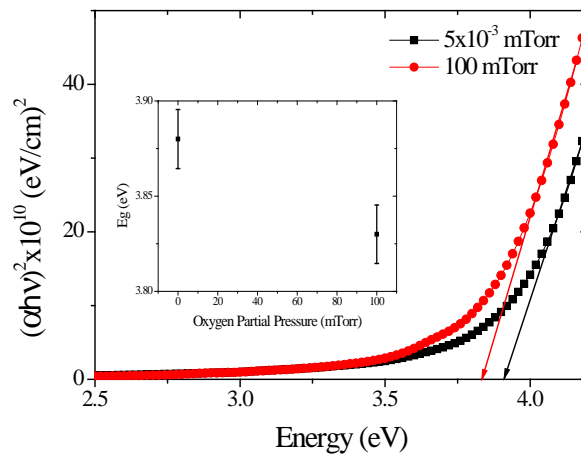


Figure 7.29: Variation in the optical band gap energy of $(\text{In}_{0.95}\text{Fe}_{0.05})_2\text{O}_3$ thin films with oxygen partial pressure.

The optical band gap increases with a decrease in oxygen partial pressure, which is consistent with a previous result for pure In_2O_3 . Growth at low oxygen partial pressure leads to an increase in carrier density; therefore, the optical band gap energy increased. The MCD was measured with the applied magnetic field up to 1.8 Tesla in Faraday geometry as a function of temperature. The MCD spectra were obtained after the subtraction of the MCD spectra of the substrate. The magneto-optic spectrum measured shows an MCD signal from the film fabricated at 5×10^{-3} mTorr only located below the band gap energy as shown in Fig.7.30.

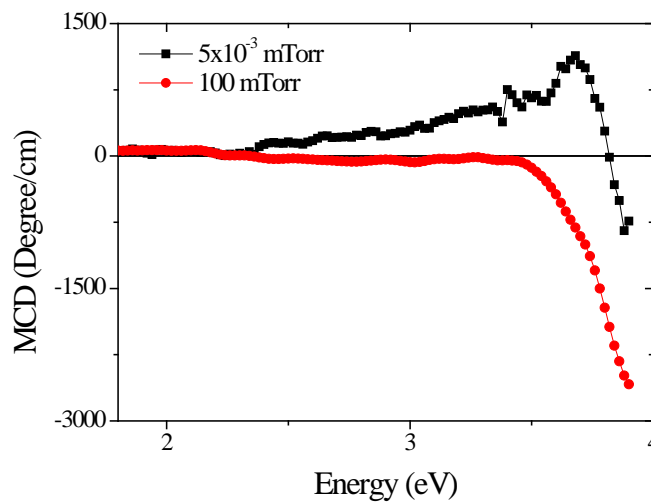


Figure 7.30: Variation in MCD spectra of 5% Fe-doped In_2O_3 with oxygen partial pressure measured at RT and a magnetic field of 1.8 Tesla.

Fig.7.30 shows that the film fabricated at 100 mTorr exhibits no MCD signal whereas the film fabricated at 5×10^{-3} mTorr displays a positive MCD signal originated from the forbidden transitions states in the energy range $2.75 < E < 3.70$ eV. The MCD signal measured the difference in the density of states at the Fermi energy level. Therefore, in the case of the film fabricated at 100 mTorr, the energy states near the Fermi energy level are localized; thus, the energy density is potential dependent, but not energy dependent. As a result, any spin splitting of these localized states does not lead to unequal densities of states at the Fermi energy level. In contrast, the film fabricated at 5×10^{-3} mTorr is metallic and contains a fraction of Fe^{2+} ions. Fe^{2+} ions act as acceptors that will generate a spin-polarized conduction band. The density of states in a conduction band is strongly energy dependent. As a result, the spin splitting of these states leads to unequal densities of states at the Fermi energy level, which results in the strong MCD spectrum.

7.3 Conclusion

This chapter investigated the influence of Fe-doping content, oxygen partial pressure, vacuum annealing process, and doping with tin on the optical and magneto-optical properties of Fe-doped In_2O_3 thin films. XRD and EXAFS measurements show that some thin films contain a fraction of Fe_3O_4 nanoparticles. Therefore, the Maxwell-Garnett theory was used for the first time to measure the fraction of Fe_3O_4 nanoparticles and to distinguish between the MCD response of the host matrix and that of Fe_3O_4 nanoparticles. The magneto-optical measurements method was found to be more accurate and quantitative than the EXAFS measurements. The magneto-optical measurements revealed that the fraction of Fe_3O_4 nanoparticles increases linearly with an increase in Fe content and the density of the oxygen vacancy bands increases with an increase in Fe content. The MCD is due to responses of the Fe_3O_4 nanoparticles which, in turn, are due the responses of In_2O_3 matrix; the density of these polarized carriers increases with an increase in Fe content. Also, the fraction of Fe_3O_4 nanoparticles increases with an increase in the annealing in a vacuum temperature. This fraction can be reduced by doping with tin, as Sn-doping prevents the formation of Fe_3O_4 nanoparticles and increases the density of carriers and the oxygen vacancy bands. The vacuum annealing process leads to an increase in the MCD response due to the Fe_3O_4 nanoparticles and that related to the In_2O_3 matrix.

However, the vacuum annealing process is not responsible for the formation of Fe_3O_4 nanoparticles, as the Fe_3O_4 nanoparticles have been observed in un-annealed samples.

Ferromagnetism at room temperature was observed in Fe-doped In_2O_3 thin films that did not contain any Fe_3O_4 nanoparticles. The observed ferromagnetism is due to the substitution of Fe for In and does not arise from the presence of either metallic Fe clusters or Fe oxides secondary phases in the films. We found that the ferromagnetism, carrier concentration, and the density of oxygen vacancies depend sensitively on oxygen partial pressure during the growth, where the density of oxygen vacancy increases with decreases in oxygen partial pressure.

7.4 References

1. E. Burstein, Phys. Rev. **93**, 632 (1954).
2. W. F. J. Fontijn, P. J. V.D. Zaag, M. A. C. Devillers, V. A. M. Brabers and R. Metselaar, Phys. Rev. B **56**, 5432 (1997).
3. X. Zhang, J. Schoenes and P. Wachter, Solid State Commun. **39**, 189-192 (1981).
4. F. X. Jiang, X. H. Xu, J. Zhang, X. C. Fan, H. S. Wu, M. Alshammari, Q. Feng, H. J. Blythe, D. S. Score, K. Addison, M. Al-Qahtani and G. A. Gehring, J. Appl. Phys. **109**, 053907 (2011).
5. M. Descostes, F. Mercier, N. Thromat, C. Beaucaire and M. Gautier-Soyer, Appl. Surf. Sci. **165**, 288-302 (2000).

Chapter 8 Multiferroic GdMnO₃

8.1 Introduction

The rare-earth elements, from lanthanum (La) to lutetium (Lu), are an example of incomplete inner f shells, but their outer electrons are almost identical. The rare earth elements exhibit a strong paramagnetism at room temperature and above and have a large net magnetic moment. The total magnetic moment of these elements originates from the electrons of unfilled $4f$ shells due to both orbital and spin motions. The $4f$ shell is a deep shell and the outer electron shells work to shield against the other ions in the field. Therefore, the orbital moments remain unquenched. At low temperatures, the magnetic behaviour of the rare earth elements is complex. All the rare earth elements show ferromagnetic or antiferromagnetic behaviour over a range of temperatures. The RMnO₃ rare-earth manganites are one of the well-known multiferroic materials which exhibit ferromagnetic and ferroelectric properties at the same time in the same phase. One of the rare-earth elements is gadolinium, which is discussed in this chapter. This chapter begins with a review of the multiferroic materials and focuses on GdMnO₃; then, the optical and magneto-optical properties of GdMnO₃ are presented. The data presented in this chapter have been submitted for publication.

8.2 Literature Review

Multiferroic materials have attracted considerable attention due to their intriguing physical properties. These materials exhibit ferromagnetic and ferroelectric properties simultaneously in the same phase. The idea is to control the magnetization of multiferroic materials by an electric field and to control their electrical properties by the induction of polarization by a magnetic field. This phenomenon provides another route for linking magnetic and electric properties for a single material, which is called the magnetoelectric effect or magnetoelectric coupling [1-4]. Thus, the magnetoelectric effect can be used as a key parameter to develop novel magnetoelectric and magneto-optical devices. These novel devices require suitable materials in thin film forms, rather than in bulk forms but, until the present time, there have not been enough studies on multiferroic thin films [5].

The magnetoelectric effect has a long history starting from its discovery by Rontgen in 1888, when a moving dielectric became magnetized when placed in an electric field. This discovery was followed by contributions from Curie, Debye and others until today. A comprehensive history of magnetoelectrics can be found in a topical review called *Revival of the magnetoelectric effect* by Manfred Fiebig [6]. Recently, an extraordinary renaissance of magnetoelectric effect publications has been observed, as shown in Fig.8.1.

Removed
by the author
for copyright reasons

Figure 8.1: Publications per year with ‘magnetoelectric’ in the title [6].

The revival of multiferroics has been powered by many factors, such as the fabrication of high-quality single crystalline samples [3, 7], the improvement of first-principles computational techniques [8], and the developments in thin-film growth techniques, which have allowed the properties of existing materials to be modified by strain engineering [9]; this was unachievable by traditional methods.

In ferroic and multiferroic materials, the magnetic field H controls the magnetization M , where the magnetization is spontaneously formed to produce ferromagnetism. The electric field E controls the polarization P , where the polarization is spontaneously formed to produce ferroelectricity. The stress σ controls the strain ϵ , where the strain is spontaneously formed to produce ferroelasticity. Therefore, in multiferroic materials, the coexistence of at least two ferroic forms of ordering leads to additional interactions. Thus, in a magnetoelectric multiferroic, an electric field E may control M or a magnetic field H may control P [10].

Removed
by the author
for copyright reasons

Figure 8.2: Phase control in ferroics and multiferroics[10].

The RMnO₃ rare-earth manganites (where R= Pr, Nd, Sm, Eu, Gd, and Tb) have attracted more attention than the other multiferroic materials, not only for their magnetoelectric properties but also for their crystal structure. Depending on the rare-earth ionic radius, the RMnO₃ form either an orthorhombic phase or a hexagonal phase. Orthorhombic RMnO₃ has ferroelectric and magnetic properties below the Néel temperature ($T_N \sim 41$ K) [3, 11, 12], which is quite a low temperature, and charge, spin, orbital, and lattice subsystems are linked very tightly. Thus, the strain in the thin films of these materials plays an important role in the formation of their properties. Therefore, the effects of the strain need to be clarified. On the other hand, hexagonal RMnO₃ or (hexa-RMnO₃) has ferroelectric and magnetic properties up to 590 K [13], but the magnetoelectric coupling for hexa-RMnO₃ is still smaller than that of orthorhombic RMnO₃ [1, 13, 14].

Removed
by the author
for copyright reasons

Figure 8.3: Phase diagram of GdMnO₃ for magnetic fields applied along the b axis. Shaded areas signal regions of strong hysteresis [15, 16].

The influence of magnetic field, pressure and temperature upon the magnetization and the dielectric properties in bulk single crystals of GdMnO_3 has been investigated [15-18]. It has been found that a magnetic field is necessary to induce multiferroicity in GdMnO_3 , and H-T phases are field orientations along a, b, and c axis dependent. In Fig. 3, the first transition occurs at 42K between the paramagnetic (PM) phase and an incommensurate antiferromagnetic (ICAFM) phase. At 20K and fields greater than 2T, the ICAFM transforms into a canted A-type antiferromagnet (cAFM). At 12K, a transition to a ferroelectric (FE) phase occurs. On the other hand, below ~20K and fields smaller than 2T there is strong hysteresis so that several phases can coexist. These phases are very dependent on pressure due to the existence of a ferroelectric phase. The phase boundaries depend on both the magnitude and the direction of the magnetic field, which means the magnetic structure of GdMnO_3 needs to be determined unambiguously. Because the H-T phases are field-orientation dependent, one might consider that, for thin films of the manganites and using the epitaxial strain, the physical properties can be changed [19] and the magnetic and electronic phases can be controlled [20]. The optical absorption spectra of RMnO_3 thin films at room temperature are shown in Fig.8.4.

Removed
by the author
for copyright reasons

Figure 8.4: Absorption spectra of RMnO_3 thin films at room temperature shows intersite transition peak at 2 eV [21].

The optical absorption spectra for RMnO_3 manganites shown in Fig.8.4 illustrated a clear peak occurring near 2eV [21]; this has been confirmed for LaMnO_3 and NdMnO_3 [22]. This absorption peak is caused by the charge transfer excitation

between Mn ions due to the different canting of the Mn *d*-orbitals and is dependent on the directions of the Mn spins. Magneto-optical studies on TbMnO₃ single crystal in a magnetic field have also shown a strong feature occurring near 3eV[23]. This chapter investigates the effect of strain caused by lattice mismatch to different substrates on the magnetic and magneto-optical properties of GdMnO₃.

8.3 Experiment Details, Results, and Discussion

Stoichiometric mixtures of Gd₂O₃ and MnO₂ were used to prepare a target of GdMnO₃. Then, the target was used to grow GdMnO₃ thin films on LaAlO₃ and SrTiO₃ substrates using dc magnetron sputtering. The GdMnO₃ thin films were deposited in a mixture of Ar and O₂ environments at a pressure of 1-2 mTorr. The substrates' temperature was sustained at 650°C with the [110]-direction parallel to the plane of the substrate. The thickness of the thin films varied between 100-200 nm. The structures of the thin films were characterized by x-ray diffraction, as shown in Fig.8.5. The growth of the thin films and the XRD measurements were done by Ya. Mukovskii from the National University of Science and Technology, Moscow, Russia.

Removed
by the author
for copyright reasons

Figure 8.5: X-ray data of GdMnO₃ films on the SrTiO₃ and LaAlO₃ substrates.

The XRD diffraction pattern in Fig.8.5 shows epitaxial growth, and some peaks appear at 2θ values 22° and 47° arising from GdMnO₃ planes. The relatively stronger peak intensity at $2\theta = 47^\circ$ is indicative of the preferential (431) orientation of GdMnO₃ thin films. In fact, the LaAlO₃ substrate was found to be heavily twinned, and the SrTiO₃ substrate undergoes a structural transition at $\sim 100\text{K}$; this may produce

further strains on the film in the temperature range where the magnetic ordering occurs.

Magnetic characterization was performed by Alqahtani in the University of Sheffield using a SQUID magnetometer. Measurements were carried out in the temperature range of 5-300 K in a magnetic field of 10 KOe. The contribution from the diamagnetic substrates was subtracted and the hysteresis loops of GdMnO₃ film on SrTiO₃ substrate at 5K and 300K are shown in Fig.8.6.

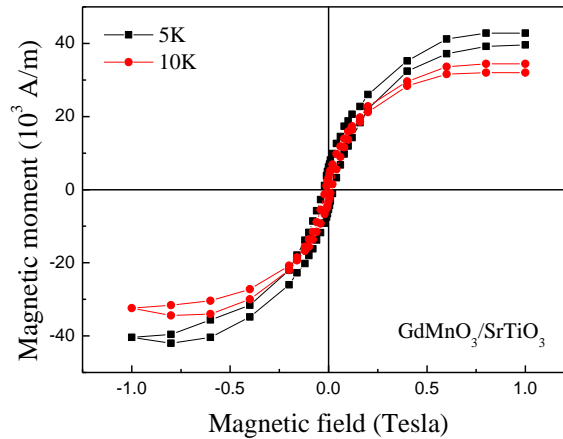


Figure 8.6: Hysteresis loops of GdMnO₃ film on SrTiO₃ substrate at 5K and 10K.

The field cooled and the zero field cooled magnetization measurement leads to the determination of the Néel temperature of these thin films where, at the Néel temperature, the transition from the paramagnetic phase to the antiferromagnetic phase occurs. The Néel temperature in TbMnO₃ is $T_N \sim 40$ K and the Néel temperature of GdMnO₃ is expected to be larger than that because the T_N for rare-earth orthoferrites, titanites, vanadites, and chromites increases with the increasing radius of the lanthanon [24]. Therefore, the transition from the paramagnetic phase to the antiferromagnetic phase for bulk GdMnO₃ occurs at the temperature of 47K, while for GdMnO₃ nanoparticles, was observed at the temperature of 44K [24]. In these thin films, the transition from the paramagnetic phase to the antiferromagnetic phase occurs at 44K for the films on the SrTiO₃ substrate and at 40K for the film on the LaAlO₃ substrate and shifted to a lower temperature, which indicates that the exchange interactions between the Mn ions are very sensitive to the strain [3] and the

strain induced by the substrates is important in reducing T_N . The optical transmission, reflection and absorption spectra of the GdMnO_3 thin films on LaAlO_3 and SrTiO_3 substrates were measured at room temperature. The data of the LaAlO_3 substrate was excluded because of the birefringence behaviour, as will be explained later. The optical transmission spectra of the SrTiO_3 substrate and the GdMnO_3 thin films on LaAlO_3 and SrTiO_3 substrates are shown in Fig.8.7 (a).

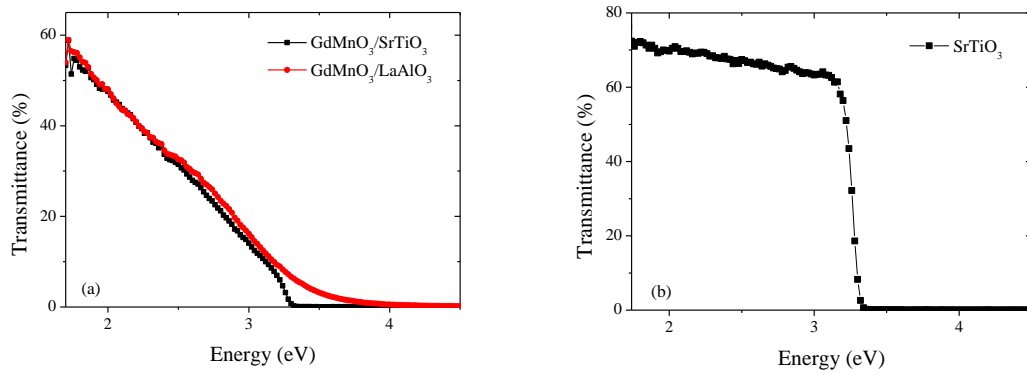


Figure 8.7: The optical transmission of a) the GdMnO_3 thin films on LaAlO_3 and SrTiO_3 substrates. b) The SrTiO_3 substrate alone.

The transmission spectrum of the SrTiO_3 substrate shows no transmission light above 3.2 eV, but below 3.2 eV, the transmission increases sharply to 60%, whereas the transmission spectrum in the presence of the GdMnO_3 thin film increases with a decrease in energy by way of the optical band gap. The optical absorption coefficient for the GdMnO_3 on LaAlO_3 and SrTiO_3 substrates is shown in Fig.8.8 (a).

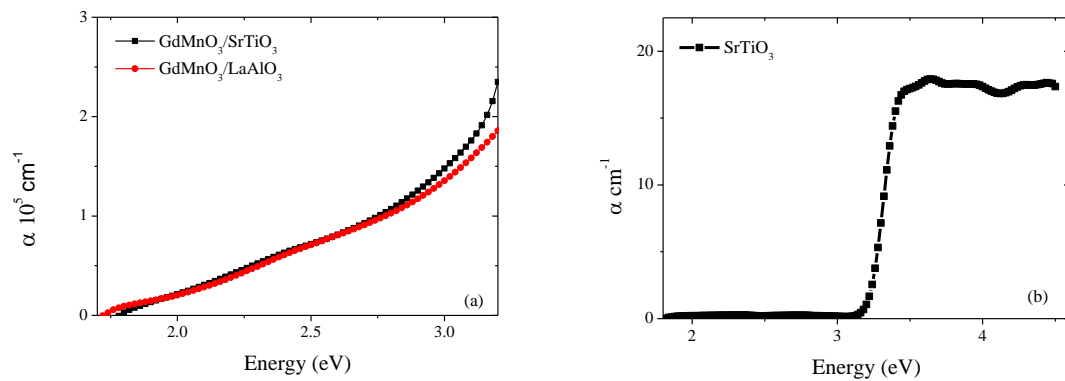


Figure 8.8: The optical absorption coefficient of a) the GdMnO_3 thin films on LaAlO_3 and SrTiO_3 substrates. b) The SrTiO_3 substrate alone.

Fig.8.8 (a) confirms the formation of a shoulder of absorption below the optical band gap energy 3.25eV; this shoulder of absorption does not exist in the absorption spectrum of SrTiO₃ substrate shown in (b). Above the optical band gap energy, the absorption is dominated by the substrate absorption edge [25]. The absorption of GdMnO₃ on the LaAlO₃ substrate shows a longer shoulder of absorption up to the optical band gap ~3.48eV and then rises beyond. With the existence of the GdMnO₃ thin film, the absorption between the band gap energy and higher energies is due to charge transfer transitions from the oxygen 2*p* band to the unoccupied Mn *d* states.

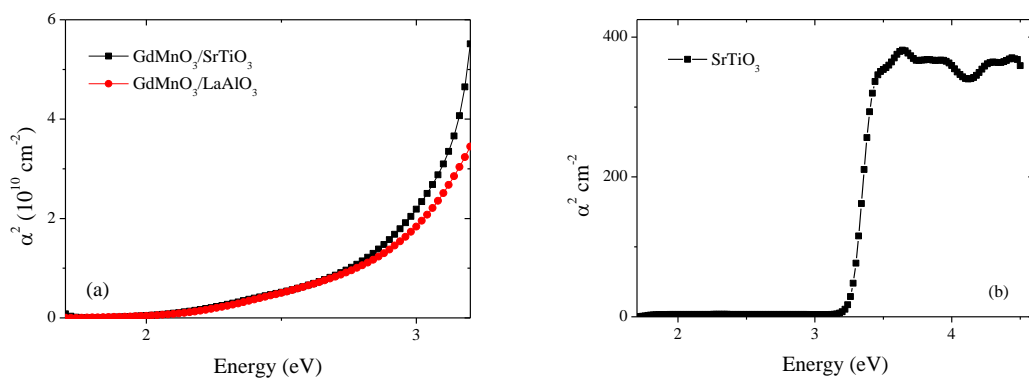


Figure 8.9: The absorption squared for a) the GdMnO₃ thin films on LaAlO₃ and SrTiO₃ substrates taken at room temperature. b) The SrTiO₃ substrate.

The MCD spectra at room temperature for both films are shown in Fig.8.10.

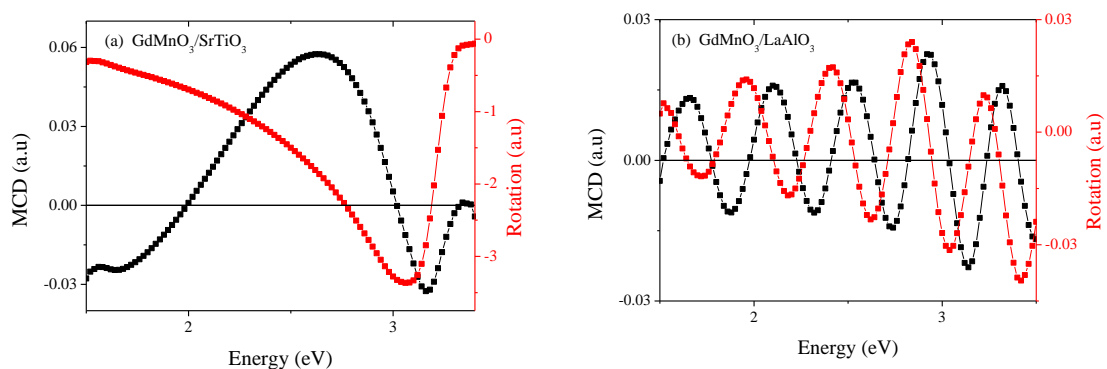


Figure 8.10: MCD and rotation spectra for (a) GaMnO₃ on SrTiO₃ (b) GaMnO₃ on LaAlO₃ where the substrate contribution is included. The measurement was taken at room temperature and a magnetic field of 1.8Tesla.

The MCD spectra of GdMnO_3 thin films on LaAlO_3 and SrTiO_3 substrates illustrated in Fig.8.10 were measured at room and low temperatures in Faraday geometry. The magnetic field was applied normally to the plane of the thin films and was 1.8Tesla and 0.5Tesla at room and low temperature measurements respectively. The room temperature MCD spectra of both GaMnO_3 thin films are dominated by the contribution from their substrates. Therefore, the temperature dependence of MCD spectra from blank SrTiO_3 and LaAlO_3 substrates was measured and subtracted from the temperature dependence of MCD spectra of the GaMnO_3 thin films in order to obtain the contribution from the GaMnO_3 films only.

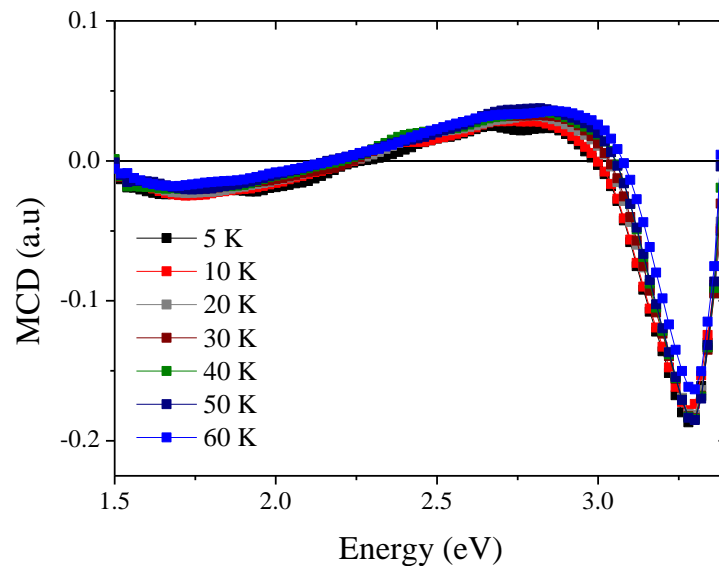


Figure 8.11: MCD spectra of SrTiO_3 substrate as a function of temperature measured in a magnetic field of 0.5 Tesla.

The MCD spectrum of the GdMnO_3 on LaAlO_3 substrate shows birefringence, as shown in Fig.10 (b), and there is no way to avoid it. Therefore, the MCD spectrum from this sample is ignored. The MCD spectrum as a function of the temperature of the GdMnO_3 on SrTiO_3 substrate was detected after a high care orientation of the substrate in order to make the E vector of the light travel along the optical axis to avoid the birefringence arising from the SrTiO_3 substrate below 100K [26]; this is shown in Fig.11. When the substrate contribution is subtracted, the MCD temperature

dependent spectrum from GdMnO₃ on SrTiO₃ substrate is revealed, as shown in Fig.8.12.

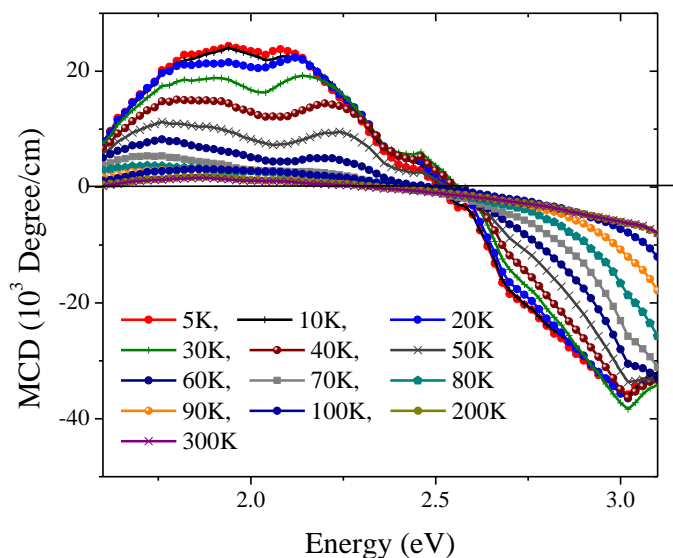


Figure 8.12: The MCD spectrum as a function of the temperature of GdMnO₃ on SrTiO₃ taken at 0.5T. The contribution from a blank SrTiO₃ substrate has been subtracted from this data.

The origin of the peak at 2 eV has been studied by several groups; they have reported that the peak at 2.0 eV comprises three separate peaks at roughly 1.9, 2.3, and 2.6 eV[23]. This peak is related to the transitions to the Mn *d* orbitals, where the allowed transitions are dominated by the spin occupations of the Mn *d* orbitals. Transitions to unoccupied *d* levels with opposite spin are higher in energy by the Hubbard energy, $J_H \sim 1\text{eV}$, and so would appear at different parts of the spectrum. The strength of the MCD peak at 2.0eV decreases rapidly with an increase in temperature and is suppressed almost to zero at 60K. The MCD peak at 3eV peak is due to the remaining contribution of the SrTiO₃ substrate, as shown in Fig.8.11. The variation of the MCD with temperature is shown in Fig.8.13.

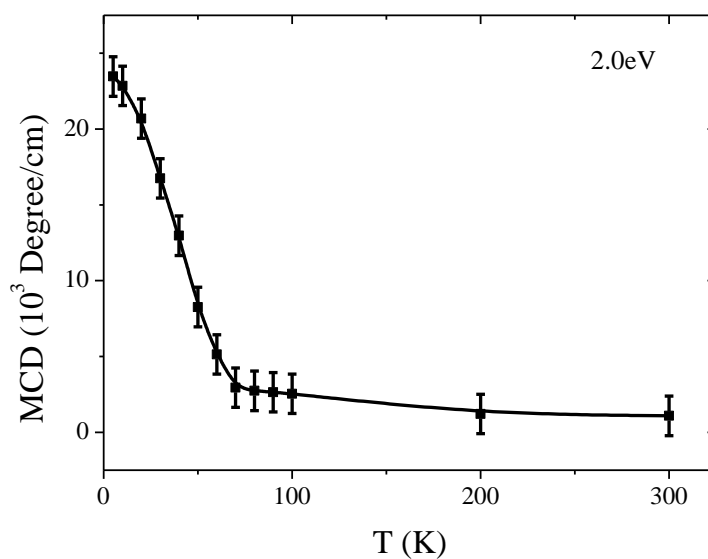


Figure 8.13: The intensity of this MCD signal at 2.0eV as a function of temperature.

The MCD peak at 2.0eV can be studied much better using MCD at remanence than in any other mode because other features are absent. Thus, the MCD spectrum at remanence was measured at 0.5Tesla, as shown in Fig.8.14.

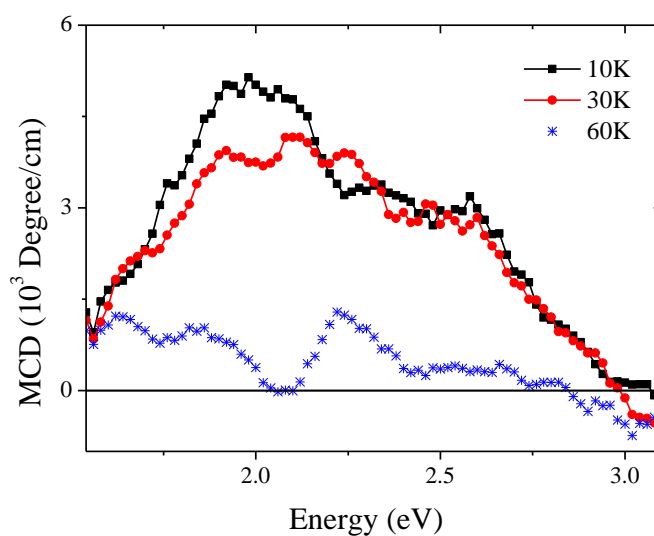


Figure 8.14: The MCD spectrum taken at remanence for GdMnO_3 on SrTiO_3 . There is a finite spectrum at 10K and 30K; the spectrum at 60K is almost zero.

The MCD spectra in field (Fig.8.12) and in zero magnetic field (Fig.8.14) give two optical features with different temperature and field dependencies. Usually, the MCD spectrum measured in zero magnetic field has the same shape as the spectrum measured in field but with lower magnitude. The MCD of GdMnO₃ on SrTiO₃ in field and in zero magnetic field are not alike, which is a unique occurrence. The peak at ~2eV at 10K in the zero magnetic field spectrum has been reduced by a factor of ~5 relative to its value in field. Nonetheless, it is very surprising to obtain such a high remanence spectrum at 30K. It is possible that the strain in the film induces a canted phase already at TN. This peak at 2.0eV is due to a charge transfer excitation between Mn ions and has been observed in the spectrum of LaMnO₃ [21-23].

8.4 Conclusion

The optical and magneto-optical properties of an epitaxial film of GdMnO₃ grown on SrTiO₃ were investigated in order to obtain detailed information on the magnetic polarisation of the electronic states. Two features in the optical spectrum, well known from bulk studies, the charge transfer transition between Mn *d* states at ~2eV and the band edge transition from the oxygen *p* band to the *d* states at ~3eV, were observed in the optical absorption and the magnetic circular dichroism (MCD). The MCD peak at 2eV was not visible as a distinct peak in the absorption but showed very clearly in the MCD spectrum, especially at remanence. The MCD at ~2eV correlates well with the Mn spin ordering and the three peak structure observed in the absorption spectrum of LaMnO₃ also re-emerged and was observed in these data. The MCD peak at 3eV is due to the STO substrate.

8.5 References

1. T. Lottermoser, T. Lonkai, U. Amann, D. Hohlwein, J. Ihringer and M. Fiebig, *Nature* **430**, 541-544 (2004).
2. N. Hur, S. Park, P.A. Sharma, J. S. Ahn, S. Guha and S. W. Cheong, *Nature* **429**, 392-395 (2004).
3. T. Kimura, T. Goto, H. Shintani, K. Ishizaka, T. Arima and Y. Tokura, *Nature* **426**, 55-58 (2003).
4. W. Prellier, M. P. Singh and P. Murugavel, *J. Phys.: Condens. Matter* **17**, R803 (2005).
5. R. Ramesh, and N. A. Spaldin, *Nat Mater* **6**, 21-29 (2007).
6. F. Manfred, *J. Phys. D: Appl. Phys.* **38**, R123 (2005).
7. N. Ikeda, H. Ohsumi, K. Ohwada, K. Ishii, T. Inami, K. Kakurai, Y. Murakami, K. Yoshii, S. Mori, Y. Horibe and H. Kito, *Nature* **436**, 1136-1138 (2005).
8. C. Ederer, and N. A. Spaldin, *Current Opinion in Solid State and Materials Science* **9**, 128-139 (2005).
9. D. G. Schlom, J. H. Haeni, J. Lettieri, C. D. Theis, W. Tian, J. C. Jiang and X. Q. Pan, *Mater. Sci. Eng. B* **87**, 282-291 (2001).
10. N. A. Spaldin, and M. Fiebig, *Science* **309**, 391-392 (2005).
11. T. Goto, T. Kimura, G. Lawes, A. P. Ramirez and Y. Tokura, *Phys. Rev. Lett.* **92**, 257201 (2004).
12. T. Kimura, G. Lawes, T. Goto, Y. Tokura and A.P. Ramirez, *Phys. Rev. B* **71**, 224425 (2005).
13. W. S. Choi, D. G. Kim, S. S. A. Seo, S. J. Moon, D. Lee, J. H. Lee, H. S. Lee, D. Y. Cho, Y. S. Lee, P. Murugavel, J. Yu and T. W. Noh, *Phys. Rev. B* **77**, 045137 (2008).
14. M. Fiebig, T. Lottermoser, D. Frohlich, A. V. Goltsev and R. V. Pisarev, *Nature* **419**, 818-820 (2002).
15. J. Baier, D. Meier, K. Berggold, J. Hemberger, A. Balbashov, J. A. Mydosh and T. Lorenz, *J. Magn. Magn. Mater.* **310**, 1165-1167 (2007).
16. J. Baier, D. Meier, K. Berggold, J. Hemberger, A. Balbashov, J. A. Mydosh and T. Lorenz, *Phys. Rev. B* **73**, 100402 (2006).

17. K. Noda, S. Nakamura, J. Nagayama and H. Kuwahara, *J. Appl. Phys.* **97**, 10C103 (2005).
18. J. Hemberger, S. Lobina, H. A. Krug von Nidda, N. Tristan, V. Y. Ivanov, A. A. Mukhin, A. M. Balbashov and A. Loidl, *Phys. Rev. B* **70**, 024414 (2004).
19. Y. Okimoto, Y. Konishi, M. Izumi, T. Manako, M. Kawasaki and Y. Tokura, *J. Phys. Soc. Jpn.* **71**, 613
20. Y. Konishi, Z. Fang, M. Izumi, T. Manako, M. Kasai, H. Kuwahara, M. Kawasaki, K. Terakura and Y. Tokura, *J. Phys. Soc. Jpn.* **68**, 3790
21. M. W. Kim, S. J. Moon, J. H. Jung, J. Yu, S. Parashar, P. Murugavel, J. H. Lee and T.W. Noh, *Phys. Rev. Lett.* **96**, 247205 (2006).
22. M. W. Kim, P. Murugavel, S. Parashar, J. S. Lee and T. W. Noh, *New J. Phys.* **6**, 156 (2004).
23. M. Bastjan, S. G. Singer, G. Neuber, S. Eller, N. Aliouane, D. N. Argyriou, S. L. Cooper, Uuml and M. Bhausen, *Phys. Rev. B* **77**, 193105 (2008).
24. X. L. Wang, D. Li, T. Y. Cui, P. Kharel, W. Liu and Z. D. Zhang, *J. Appl. Phys.* **107**, 09B510 (2010).
25. K.V. Benthem, C. Elsasser and R. H. French, *J. Appl. Phys.* **90**, 6156-6164 (2001).
26. M. A. Geday, and A. M. Glazer, *J. Phys.: Condens. Matter* **16**, 3303 (2004).

Chapter 9 - Conclusions

9.1 Thesis Review

This study investigated the optical and magneto-optical properties of pure and transition metal doped In_2O_3 in order to find a suitable material for the new generation of spin-based electronics. In_2O_3 (IO) was chosen for the excellent combination of magnetism, transport, optical and magneto-optical properties it has when doped with Sn and transition metal.

Optical systems were developed to achieve a high accuracy, with low noise level in addition to managing the low temperature measurements. Python, C++, Microsoft.Net and LabView program were used to build up drivers to control the two optical systems, and to acquire the data. Software was programmed to analyse the obtained data. The absorption system was rebuilt in order to manage low temperature measurements where new items, such as temperature controller, cryostat, vacuum pump, were added to the system and new drivers were programmed to control the temperature controller through the computer. Without these developments, obtaining the optical and magneto-optical data seen in this study would have not been possible.

These systems were used to perform the first optical and magneto-optical measurements on pure and doped In_2O_3 thin films. The optical and magneto-optical properties of pure and (Cr, Mn, Fe, Co, Ni, Sn)-doped In_2O_3 were investigated at different transition metal concentrations and at different growth conditions. However, only selective and representative data have been included in this study. This study is considered the first attempt that investigated the optical and magneto-optical properties of pure and transition metal doped In_2O_3 . The optical and magneto-optical measurements showed that there was a group of energy states formed within the forbidden range of the optical band gap energy of In_2O_3 and located closed lower the conduction band. The origin of these states was found to be due to the defect states associated with oxygen vacancies as confirmed by the absorption measurements at low temperature. The density of the oxygen vacancy impurity states increases and expands to a deeper level of energy toward the valance band with a decrease in oxygen partial pressure during the growth, or with doping with tin, or with annealing

in a vacuum. Tuning the density of the oxygen vacancy impurity states gives control over the carrier concentration density in the system. This achievement of controlling the carrier concentration density leads the In_2O_3 semiconductor to show insulator or metallic behaviours.

Magnetometry and the magneto-optical measurements of transition-metal doped In_2O_3 revealed the origin of the magnetism in the class of the magnetic oxides. The observed ferromagnetism in magnetic oxides was due to the polarized electrons in localized donor states associated with oxygen vacancies.

Extended X-ray Absorption Fine Structure (EXAFS) measurements showed that some of the transition-metal doped In_2O_3 thin films contain transition metal nanoparticles. In this study, a new complementary technique to the EXAFS was developed to identify the existence of magnetic nanoparticles in addition to providing the fraction and contribution of these nanoparticles to the magnetisation and magneto-optical properties. The Maxwell-Garnett analysis of magnetic circular dichroism was developed to obtain quantitative measures of the amount of defect phases present for Co metal. Similar to Maxwell-Garnett analysis, a new equation for Fe_3O_4 nanoparticles was developed in this study. The magneto-optical method is cheaper where there is no cyclotron system required, safer where there is no involvement with X-ray radiation, quantitative, and more accurate than the EXAFS method.

The fraction of transition metal nanoparticles was found to decrease with doping with tin whereas metallic Co nanoparticles in Co-doped In_2O_3 thin films and Fe_3O_4 nanoparticles in Fe-doped In_2O_3 thin films disappeared when these thin films were doped with tin indicating that doping with Sn not only introduces more carriers but also inhibits the growth of defect phases in semi magnetic semiconductor thin films. This might be because of screening from the carriers as a side effect of changing the crystal strain as a result of doping with Sn.

9.2 Future Work

Completion of the current work on (Cr, Mn, Ni, Zn)-doped In_2O_3 is necessary to have a comprehensive overview about the properties of transition metal doped

In_2O_3 , and to be more confident about the source of magnetisation in semi magnetic semiconductors. More measurements need to be done, including an accurate assessment of the composition of thin films, and the percentage of spin polarisation using an Andreev reflection and whether there are second phases or transition metal nanoparticles present using extended X-ray absorption fine structure EXAFS measurements.

It would be really interesting to grow two thin films, one pure In_2O_3 , and one transition metal doped In_2O_3 , with the same carrier concentration or with the same oxygen vacancy density which could be measured through the absorption spectra to assess whether they show the same magnetic and magneto-optical properties in order to determine the role of the transition metal itself in semi magnetic semiconductors.

We believe that role of the transition metal in semi magnetic semiconductors is simply to cause an imbalance in the density of polarized carriers in oxygen vacancy bands, which leads to a positive or a negative magnetic circular dichroism signal, where Cr-, Fe-, and Co-doped In_2O_3 show a positive magnetic circular dichroism signal, while Ni-doped In_2O_3 shows a negative magnetic circular dichroism signal. In fact, we tried to investigate Zn-doped In_2O_3 to check this point, but we faced some difficulties which delayed the project. However, the difference between the densities of the polarized carriers in oxygen vacancy bands is responsible for the magnetisation in semi magnetic semiconductors, which indeed needs to be investigated in the future.

Appendix A: Development of computer program

A.1 Introduction

The aim of this software is to calculate the absorption coefficient from the experimental transmittance data alone using Swanepoel Method [1] As mentioned previously, in section 3.9, Swanepoel shows that the transmittance is given by

$$T = \frac{Ax}{B - Cx \cos \varphi + Dx^2} \quad \text{Equation(A.1.1)}$$

where

$$A = 16n^2s \quad \text{Equation(A.1.2)}$$

$$B = (n + 1)^3(n + s^2) \quad \text{Equation(A.1.3)}$$

$$C = 2(n^2 - 1)(n^2 - s^2) \quad \text{Equation(A.1.4)}$$

$$D = (n - 1)^3(n - s^2) \quad \text{Equation(A.1.5)}$$

$$\varphi = 4\pi d/\lambda \quad \text{Equation(A.1.6)}$$

$$x = \exp(-\alpha d) = 1 - \gamma \quad \text{Equation(A.1.7)}$$

As explained earlier, the values of n , s , and d can be achieved by fitting experiment data in the transparent region. Using Microsoft Excel, the parameters A , B , C , D and φ can be calculated as a function of wavelength. Therefore, at every point of wavelength, there are different values for these parameters. The program will use these parameters at every wavelength to calculate the value of transmittance based on equ.A.1. The program starts by assuming $\gamma = 0$ and then computes the value of transmittance. Then, the program matches the value of the calculated transmittance with that measured experimentally. If these values are the same, then the γ value is recorded and saved. If the calculated and measured values of the transmittance are not the same, then the γ value is increased by $\gamma = \gamma_0 + 0.0001$; and the transmittance recalculated and compared again and so on. The result is spectra of γ as a function of energy, which can be used to calculate the absorption coefficient.

A.2 Program Structure

A modular structure was used to develop the program in order to simplify it so it would be easy to understand and follow for future use and for improvements to be made. The program consists of multi-central loops in order to read data, do the calculation for gamma, and to record the results. This modular structure is shown in Fig.1.

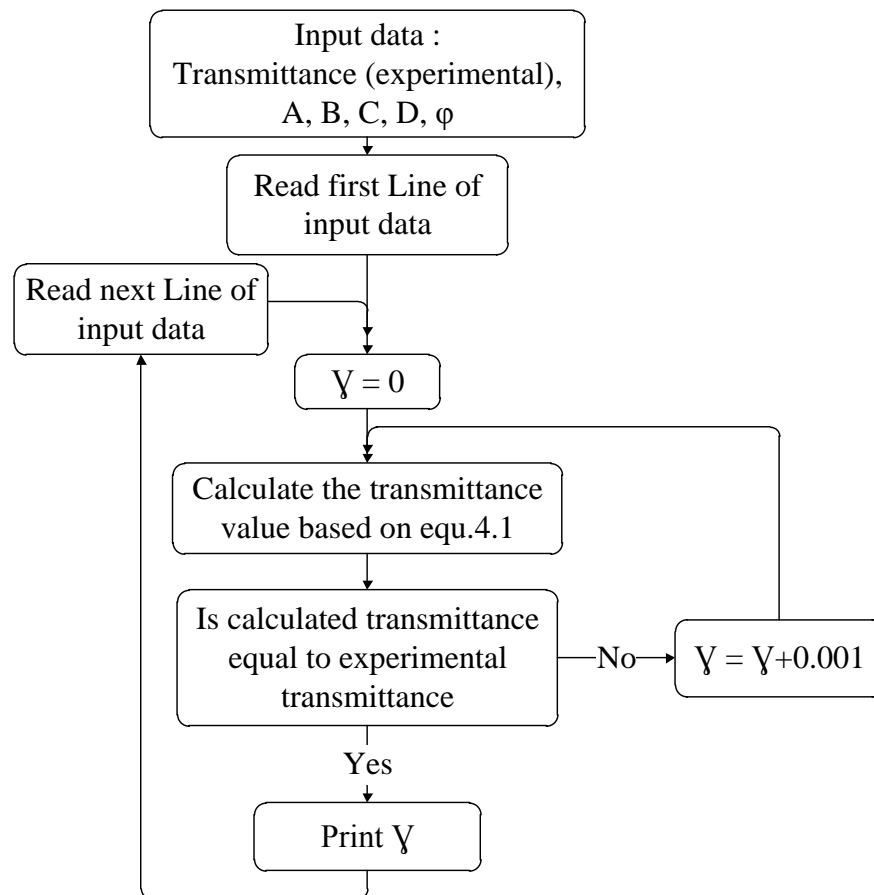


Figure 1: The modular structure used to develop the program.

A.3 Program Code

```
import wx
import math
import time

class MainFrame(wx.Frame):
    def __init__(self, parent, id):

        wx.Frame.__init__(self, parent, id, 'Gamma Hunter', size=(950,400))
        panel = wx.Panel(self, -1)

        status = self.CreateStatusBar()
        menubar = wx.MenuBar()
        first = wx.Menu()
        second = wx.Menu()
        third = wx.Menu()
        fourth = wx.Menu()

        first.Append(wx.NewId(), "New Indow", "This is a new window")
        first.Append(wx.NewId(), "Open ..", "This will open a new window")
        first.Append(wx.NewId(), "Exit", "This will close the program")
        menubar.Append(first, "File")

        second.Append(wx.NewId(), "Select All", "Select All..")
        second.Append(wx.NewId(), "Cut", "Cut..")
        second.Append(wx.NewId(), "Copy", "Copy..")
        second.Append(wx.NewId(), "Paste", "Paste..")
        second.Append(wx.NewId(), "Clear", "Clear..")
        menubar.Append(second, "Edit")

        third.Append(wx.NewId(), "Start Fitting", "Start Fitting..")
        menubar.Append(third, "Run")

        fourth.Append(wx.NewId(), "About Gamma Hunter", "Select All..")
        menubar.Append(fourth, "Help")

        self.SetMenuBar(menubar)

        wx.StaticText(panel, -1, 'Ex. Tran :', (20,20))
        wx.StaticText(panel, -1, 'A: ', (150, 20))
        wx.StaticText(panel, -1, 'B: ', (280, 20))
        wx.StaticText(panel, -1, 'C: ', (410, 20))
        wx.StaticText(panel, -1, 'D: ', (540, 20))
        wx.StaticText(panel, -1, 'Phi: ', (670, 20))
        wx.StaticText(panel, -1, 'Gamma: ', (800, 20))
        wx.StaticText(panel, -1, 'Data points :', (20,165))
```

```

#self.sc = wx.SpinCtrl(self, -1, '', (150, 75), (60, -1))
#self.sc = wx.TextCtrl(self, -1, 1, (150, 75), (60, -1), style=wx.TE_MULTILINE)
self.ExTran = wx.TextCtrl(panel, -1, '', (20,40), (120, 120), style=wx.TE_MULTILINE)
self.A = wx.TextCtrl(panel, -1, '', (150,40), (120, 120), style=wx.TE_MULTILINE)
self.B = wx.TextCtrl(panel, -1, '', (280,40), (120, 120), style=wx.TE_MULTILINE)
self.C = wx.TextCtrl(panel, -1, '', (410,40), (120, 120), style=wx.TE_MULTILINE)
self.D = wx.TextCtrl(panel, -1, '', (540,40), (120, 120), style=wx.TE_MULTILINE)
self.Phi = wx.TextCtrl(panel, -1, '', (670,40), (120, 120), style=wx.TE_MULTILINE)
self.Gamma = wx.TextCtrl(panel, -1, '', (800,40), (120, 200), style=wx.TE_MULTILINE)
#self.sc.SetValue(0)

VariablesList = ['Choose box to Clear','Tran.', 'A', 'B', 'C','D','Phi','Gamma']
self.choice1 = wx.Choice(panel, 1, choices=VariablesList, pos=(20, 180))
self.choice1.SetSelection(0)
self.choice1.Bind(wx.EVT_CHOICE, self.choice1_click, id=1)

count_btn = wx.Button(panel, 1, 'Check', (185, 230))
count_btn.SetFocus()
fitting_btn = wx.Button(panel, 2, 'Start Fitting', (280, 230))
clearAll_btn = wx.Button(panel, 3, 'Clear All', (185, 260))
close_btn = wx.Button(panel, 4, 'Close', (280, 260))
clear_btn = wx.Button(panel, 5, 'Clear', (20, 205))

self.Bind(wx.EVT_BUTTON, self.onCheck, id=1)
self.Bind(wx.EVT_BUTTON, self.onFitting, id=2)
self.Bind(wx.EVT_BUTTON, self.OnClearAll, id=3)
self.Bind(wx.EVT_BUTTON, self.OnClose, id=4)
self.Bind(wx.EVT_BUTTON, self.OnClear, id=5)

self.Bind(wx.EVT_CLOSE, self.OnClose)

def choice1_click(self, event):
    self.Toclear = self.choice1.GetStringSelection()
def OnClear(self, event):
    #print self.Toclear
    if self.Toclear == 'Tran.':
        self.ExTran.Clear()
    elif self.Toclear == 'A':
        self.A.Clear()
    elif self.Toclear == 'B':
        self.B.Clear()
    elif self.Toclear == 'C':
        self.C.Clear()
    elif self.Toclear == 'D':
        self.D.Clear()
    elif self.Toclear == 'Phi':
        self.Phi.Clear()
    elif self.Toclear == 'Gamma':
        self.Gamma.Clear()

```

```

def onCheck(self, event) :
    NTr = str(self.ExTran.GetNumberOfLines())
    NA = str(self.A.GetNumberOfLines())
    NB = str(self.B.GetNumberOfLines())
    NC = str(self.C.GetNumberOfLines())
    ND = str(self.D.GetNumberOfLines())
    NP = str(self.Phi.GetNumberOfLines())

    wx.StaticText(self, -1, NTr , (100,165))
    wx.StaticText(self, -1, NA , (230,165))
    wx.StaticText(self, -1, NB , (360,165))
    wx.StaticText(self, -1, NC , (490,165))
    wx.StaticText(self, -1, ND , (620,165))
    wx.StaticText(self, -1, NP , (750,165))

def onFitting(self, event):
    Num = self.ExTran.GetNumberOfLines()
    #fahr = self.ExTran.GetLineText(0)
    #self.Gamma.Replace(0, 0, fahr)
    #self.celsius.SetLabel(str(fahr))

    i = 0
    while i < Num:

        ExTV = self.ExTran.GetLineText(i)
        AV = self.A.GetLineText(i)
        BV = self.B.GetLineText(i)
        CV = self.C.GetLineText(i)
        DV = self.D.GetLineText(i)
        PHIV = self.Phi.GetLineText(i)

        #print len(self.ExTran.GetLineText(i))
        if len(ExTV) < 1: # IF impty string
            break
        if len(AV) < 1: # IF impty string
            break
        if len(BV) < 1: # IF impty string
            break
        if len(CV) < 1: # IF impty string
            break
        if len(DV) < 1: # IF impty string
            break
        if len(PHIV) < 1: # IF impty string
            break

        ExTV = float(ExTV)
        AV = float(AV)
        BV = float(BV)
        CV = float(CV)
        DV = float(DV)
        PHIV = float(PHIV)

```

```

Gamma_value = 0

while ExTV:

    X = 1 - Gamma_value
    Tc = AV*X/(BV-CV*X*math.cos(PHIV)+ DV*X**2)
    if( Tc < (ExTV+0.001) and Tc > (ExTV-0.001)):
        if Gamma_value > 1 :
            Gamma_value = 0
        Ga = repr(round(Gamma_value,6))
        self.Gamma.AppendText(Ga + "\n")
        break

    Gamma_value = Gamma_value + 0.001

    i=i+1

def OnClose(self, event):
    self.Destroy()
def OnClearAll(self, event):
    self.ExTran.Clear()
    self.A.Clear()
    self.B.Clear()
    self.C.Clear()
    self.D.Clear()
    self.Phi.Clear()
    self.Gamma.Clear()

class MyApp(wx.App):
    def OnInit(self):
        dlg = MyDialog(None, -1, 'Gamma Huner')
        dlg.Show(True)
        dlg.Centre()
        return True

#app = MyApp(0)
#app.MainLoop()

if __name__ == '__main__':
    app=wx.PySimpleApp()
    Frame=MainFrame(None, -1)
    Frame.Show()
    app.MainLoop()

```

When the code is executed, the program initializes and shows the interface of the software as shown in Fig.2.

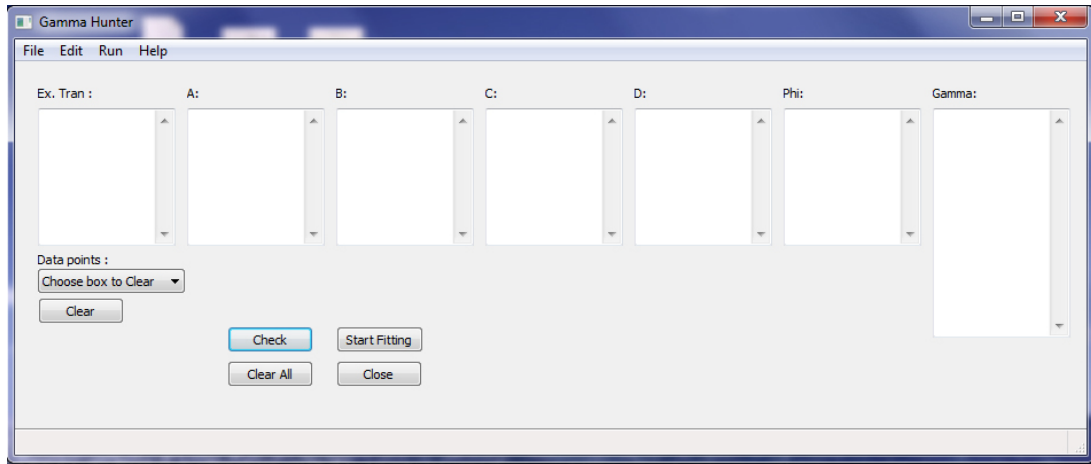


Figure 2: The software interface used to calculate Gamma values

Each variable piece of data can be pasted into the corresponding parameter box. The ‘clear’ button is used to clear any box selected from the drop down menu named “choose box to clear”. The ‘clear all’ button will discard any data pasted or calculated in all the boxes. The ‘check’ button will count the data point in every box and show the number of data points below the related box, as shown in Fig.3. The ‘start fitting’ button will generate the values of Gamma.

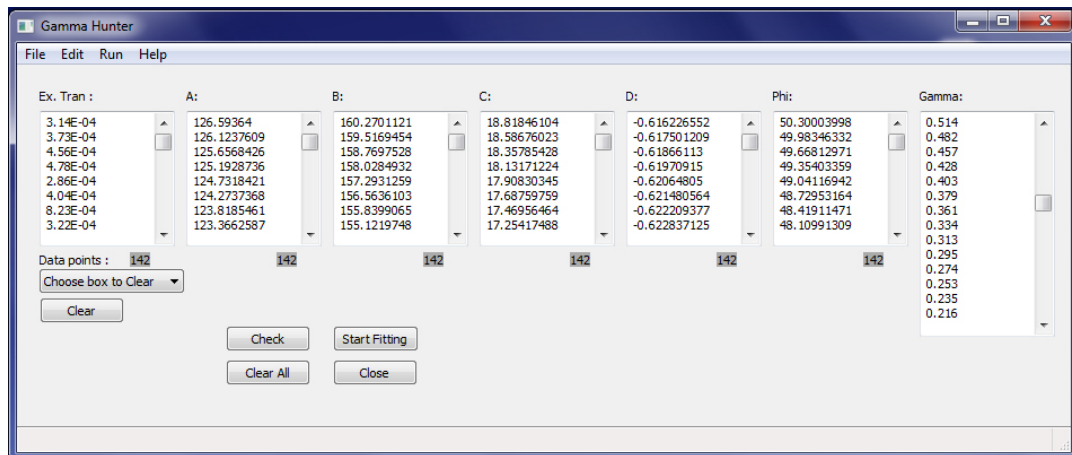


Figure 3: The software while running to calculated Gamma values.

Fig.4 shows experimental transmittance spectra fitted using the software. The fitted spectra are based on the absorption values calculated using the software.

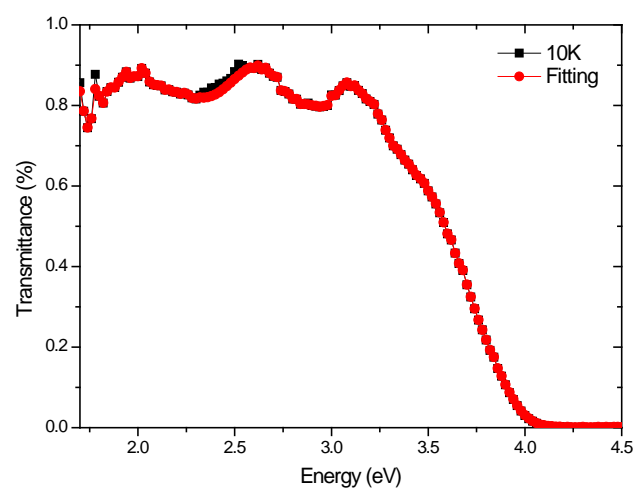


Figure 4: Transmittance spectra fitted using the software.

A.4 References

1. R. Swanepoel, J. Phys. E: Scientific Instruments, 1983. **16**(12): p. 1214.

Appendix B: Abbreviations

CB	Conduction band
CL	Cathodoluminescence spectra
DL	Deep-level states
DMSs	Dilute magnetic semiconductors
EDAX	Energy-dispersive X-ray spectroscopy
E_F	Fermi energy level
EXAFS	X-ray absorption fine structure
GPIB	General Purpose Interface Bus
H_c	Coercive field or coercivity
ITO	Indium-tin-oxide
KACST	King Abdulaziz City for Science and Technology
LabVIEW	Laboratory Virtual Instrumentation Engineering Workbench
LCD	Liquid crystal display
LCP	Left circularly polarized light
MAX	The Measurement and Automation
MBE	Molecular beam epitaxy
MCD	Magnetic circular dichroism
M-G	Maxwell-Garnett theory
M_r	Remaining magnetization, or remanence
M_s	Saturation magnetization
NBE	Near-band-edge states
OLED	Organic light emitting diode
PLD	Pulse laser deposition
RCP	Right circularly polarized light
RKKY	Ruderman-Kittel-Kasuya-Yosida model
SMS	Semi magnetic semiconductors
SQUID	Superconducting quantum interference device
T_c	Curie temperature
TM	Transition element

T_N	Néel temperature
VB	Valence band
XMCD	X-ray magnetic circular dichroism
XRD	X-ray diffraction